Structure and functional properties of epitaxial $PbZr_xTi_{1-x}O_3$ films

Kurt Vergeer

STRUCTURE AND FUNCTIONAL PROPERTIES OF EPITAXIAL $PBZR_XTI_{1-X}O_3$ FILMS

Graduation committee

Chairman and secretary

Prof. dr. ir. J.W.M. Hilgenkamp	University of Twente

Supervisors

Prof. dr. ing. A.J.H.M Rijnders	University of Twente
Prof. dr. ir. G. Koster	University of Twente

Members

Prof. dr. A.J. Bell	University of Leeds
Prof. dr. W.A. Groen	TU Delft
Dr. F. Blom	Océ-Technologies
Prof. dr. ir. W.G. van der Wiel	University of Twente
Prof. dr. ir. H.J.W. Zandvliet,	University of Twente
Dr. ir. E.P. Houwman	University of Twente

The research described in this dissertation was carried out in the Inorganic Materials Science Group at the MESA+ Institute for Nanotechnology, Faculty of Science and Technology at the University of Twente in Enschede, the Netherlands. The research work was done in collaboration with Océ.

This research was carried out under project number M62.3.10404 in the framework of the Research Program of the Materials innovation institute (M2i) in the Netherlands (www.m2i.nl).

Printed by: Gildeprint, Enschede
ISBN: 978-90-365-4305-7
DOI: 10.3990/1.9789036543057
Copyright © Kurt H. Vergeer

STRUCTURE AND FUNCTIONAL PROPERTIES OF EPITAXIAL $PBZR_XTI_{1-X}O_3$ FILMS

DISSERTATION

to obtain the degree of doctor at the University of Twente,
on the authority of rector magnificus,
prof. dr. T.T.M. Palstra
on account of the decision of the graduation committee,
to be publicly defended
on Friday the 17th of February 2017 at 12:45

by

Kurt Vergeer

born on the 9th of July, 1984
Wanroij, The Netherlands

This dissertation has been approved by:

Prof.dr.ing. A.J.H.M. Rijnders

Prof.dr.ir. G. Koster

Contents

1.Introduction 1
1.1 Piezoelectricity 2
1.2 Stress free PZT 3
1.3 PZT films 5
1.3.1 Tetragonal PZT 6
1.4 Models 7
1.5 Piezoelectric characteristics 7
1.6 Thesis outline: 8
References: 10

2.Fabrication and Characterization methods 13
2.1 Introduction 14
2.2 Thin film fabrication 15
2.2.1 Pulsed Laser Deposition (PLD) 15
2.2.2 PLD setup 16
2.3 Sample Structure 17
2.3.1 Substrate 17
2.3.2 Electrodes and PZT 19
2.3.3 Metal Deposition 21
2.3.4 Etching and structuring 22
2.4 Characterization: 24
2.4.1 Crystal structure: 24
2.4.2 Electrical and Optical Characterization 28
2.4.3 Surface characteristics 31

References 33

3. Thermodynamic energy model of strained dense epitaxial PZT 37

3.1 Introduction 38

3.2 Gibbs and Helmholtz free energy model 38

3.2.1 Gibbs free energy 38

3.2.2 Helmholtz free energy 41

3.2.3 Poly-domain Helmholtz free energy equation 43

3.3 Misfit strain 47

3.3.1 The basic lattice parameter and the atomic and thermal misfit strain 47

3.3.2 Misfit strain in the model 52

3.4 Simplification of the poly-domain Helmholtz free energy 53

3.4.1 Full poly-domain Helmholtz free energy equation 55

3.4.2 Poly-domain Helmholtz free energy equation 56

3.4.3 Single domain Helmholtz free energy equation 57

3.5 Conclusion: 58

References 59

4.Functional properties of poly-domain ferroelectric oxide films. 61

4.1 Introduction 62

4.1.1 Unclamped bulk PZT 63

4.1.2 External parameters of clamped PZT films 66

4.1.3 Crystal phases in clamped PZT films 68

4.2 Analytical approach of a clamped tetragonal poly-domain PZT film . 70

4.2.1 Domain fraction (Analytical approach) 71

4.2.2 Polarization and Stress (Analytical approach) 71
4.2.3 Material properties near zero field (Analytical approach) 73
4.2.4 Unit cell lattice parameters (Analytical approach) 76
4.2.5 Piezoelectric Coefficients (Analytical approach) 77
4.3 Numerical Analysis 79
4.3.1 PZT phase diagram (Numerical approach) 80
4.3.2 Domain Fraction and Stress (Numerical approach) 83
4.3.3 The Unit Cell Polarization (Numerical approach) 84
4.3.4 Dielectric constant and piezoelectric coefficients (Numerical approach) 87
4.4 Conclusion 88
References 90

5. Determination of the contributions to the piezoelectric coefficient of polydomain 001 tetragonal $Pb(Zr_{40}Ti_{60})O_3$ thin film by XRD methods. 93
5.1 Introduction 94
5.2 Analytical determination of the average piezoelectric coefficient. ... 95
5.2.1 Model Parameters 98
5.2.2 Model Misfit Strain 98
5.3 Basic Lattice Parameter 100
5.3.1 Out of plane lattice parameter 101
5.3.2 Discussion on the origin of difference between Model and Experiment 103
5.3.3 Electric field and strain: 107
5.3.4 Domain Fraction 109
5.3.5 Resulting d_{33} 114
5.4 Misfit strain 119

5.5 Discussion on Model Corrections 121
5.5.1 Discrepancies 121
5.5.2 Corrections 121
5.6 Conclusions 125
References 127

6.Determination of the origin of high piezoelectric coefficients in clamped dense 001 single crystal PZT films. 131
6.1 Introduction 132
6.2 Bulk single crystal PZT 133
6.2.1 Polarization rotation 133
6.2.2 Phase change 135
6.2.3 Dense clamped PZT film 139
6.3 Experimental comparison 145
6.31 Misfit strain in dense clamped PZT film. 145
6.3.2 Columnar PZT growth 148
6.4 Discussion 149
6.5 Conclusion: 150
References: 151

7. Domain wall structure and motion in dense clamped tetragonal (001) PZT films. 155
7.1 Introduction 156
7.1.1 DWs in PZT films with a tetragonal crystal structure 158
7.1.2 DWs in unclamped bulk tetragonal PZT 158
7.1.3 DWs in clamped tetragonal 2D PZT films. 161
7.2 TEM analysis of 2D films 165

7.2.1 Tilting and the domain fraction 166

7.2.2 Discussion on 2D films 172

7.3 3D PZT films 173

7.3.1 DWs in clamped tetragonal 3D PZT films. 173

7.3.2 Domain structure observed using XRD 175

7.3.3 Polarization switching and domain reconstruction 177

7.3.4 PFM: Surface structure 183

7.4 Discussion 185

7.5 Conclusion 188

References 190

Appendix 193

References: 196

Acknowledgements: 197

1.Introduction

Sensor and actuating properties of silicon based micro electro mechanical systems (MEMS) can be greatly increased by incorporating piezoelectric films[1-4]. Since the early 90's, piezoelectric films of various types have been studied intensively and improved methods to prepare them have been developed[5]. $PbZr_xTi_{x-1}O_3$ (PZT) films have proven to be a promising material for MEMS technology due to its strong ferroelectric and piezoelectric properties[1][6]. New products, such as piezo-MEMS printing heads, are envisioned and, currently, technology is being developed for the integration of piezoelectric films into MEMS on an industrial scale. Further device miniaturization will require moving to thinner layers (under 1 micrometer). While leading to cost reduction and processing simplification, this transition introduces several complications. For example it was observed that properties and film lifetime decrease with film thickness[6].

To better understand the decrease in properties of a PZT film it is important to understand how the characteristics deviate from an ideal PZT layer. The ferroelectric and piezoelectric properties are highly dependent on the crystalline quality. Epitaxial films have been shown to have improved properties over textured and polycrystalline films[7]. It has however been difficult to create high quality, dense, epitaxial PZT films on silicon substrates[8-10], whereas PZT layers grown on other substrates such as perovskite $SrTiO_3$, $KTaO_3$ and $DyScO_3$ have shown to result in high quality epitaxial films[11][12]. Once the high quality epitaxial PZT films are made these can be used to better understand the relation between structure and properties of epitaxial films. This knowledge, if turned into a general model, can help to predict the piezoelectric and ferroelectric characteristics for a wide range of situations. Any deviation of these characteristics can give an indication of the effects of structural differences of a less high quality film compared to high quality epitaxial films.

1.1 Piezoelectricity

A piezoelectric material is a material in which an electric charge is built up due to an applied mechanical stress (Nm^{-2}). Piezoelectric materials also show the opposite effect, called converse piezoelectric effect, where the application of an electrical field creates mechanical deformation in the crystal. The piezoelectric effect is understood as the linear electromechanical interaction between the mechanical and the electrical state in crystalline materials with non-centrosymmetric crystal structure[13]. Piezoelectricity was discovered by Jacques and Pierre Curie in 1880[14]. They demonstrated the effect on a variety of crystals. Among these materials the naturally occurring quartz (SiO_2) is one of the most widely used piezoelectric materials. Presently one of its most common uses is as a crystal oscillator, where the mechanical resonance of a vibrating crystal creates an electric signal with a very precise frequency. This is used to keep track of time in a variety of products such as integrated circuits, wristwatches and radios.

Nowadays, due to the possibilities of fabricating synthetic crystals, there is a wide variety of piezoelectric materials to choose from. Among these a few well-known ceramic materials are zinc oxide (ZnO), barium titanate ($BaTiO_3$ or BTO) and lead zirconate titanate ($PbZr_xTi_{1-x}O_3$ or PZT). In crystalline form these materials can exhibit a very strong piezoelectric effect. Traditionally these materials came as powders, which were sintered into blocks of small crystals. These were then grinded or cut into pieces and functionalized by gluing them into place. Due to the demand for high quality materials much research was done on the properties of these bulk polycrystalline materials.

As technology moved towards smaller scale into the field of micro-electro-mechanical systems (MEMS) the bulk samples proved difficult to integrate. A different approach was developed whereby a layer of piezoelectric material was deposited onto a substrate material. This allowed for the mass production of piezo-MEMS materials on silicon. The low cost, high sensitivity and low power consumption has led to a large range of applications. Here, the direct piezoelectric effect is employed for sensing, energy harvesting or ignition, used in sound wave detectors, touch screens,

pressure sensors, lighters and piezoelectric energy harvesters. The converse piezoelectric effect is used for actuators including inkjet printing, auto-focusing for smartphone cameras, valves in microfluidics, ultrasonic micromotors and atomic- (AFM) and piezo- (PFM) force microscopy[1]. In some applications both effects are used simultaneously, as for example in medical ultrasonography transducers and cantilevers for chemical sensing in gas and liquid[15][16].

1.2 Stress free PZT

In this work PZT is chosen as the material of focus. It is the most common piezoelectric ceramic in use today and many other piezoelectric materials are based upon the same perovskite crystal structure such as (1-x)$PbMg_{1/3}Nb_{2/3}O_3$-(x)$PbTiO_3$ (PMN-PT) and $Pb_xLa_{(1-x)}Zr_yTi_{(1-y)}$ O_3 (PLZT). PZT is the acronym for a range of material compositions ranging from $PbTiO_3$ (PTO or PZT (x=0)) to $PbZrO_3$ (PZO or PZT (x=1)). PZT is a solid solution of $PbTiO_3$ and $PbZrO_3$. PZT has a perovskite crystal structure with a Pb ion at the A site, either a Zr or Ti ion on the B site and O ions at the C site, see figure 1.1. At room temperature all PZT compositions are piezoelectric. On a unit cell level the compositions are however different (figure 1.2). At room temperature stress free (not clamped) PZT with a high Ti content ($x<0.45$) results in a tetragonal crystal structure (*P4mm*) [17][18], while a high Zr content ($x>0.49$) results in a rhombohedral structure (*R3m*). An even higher Zr content results in an anti-ferroelectric orthorhombic phase. On the border between the two competing tetragonal and rhombohedral structures there is a region commonly referred to as the morphotropic phase boundary (MPB). The MPB composition has been of great interest to industry and research due to its remarkable piezoelectric and dielectric properties, see figure 1.2. Using synchrotron neutron diffraction it was found that this region contains monoclinic and/or tetragonal phases and that an applied electric field can switch the crystal between these phases [18][17].

Next to being piezoelectric, PZT is also ferroelectric. Ferroelectric materials are piezoelectric materials in which a spontaneous polarization is present. This spontaneous polarization can be switched by using an external electric field, giving rise to a polarization hysteresis loop (Fig.2.7). Although PZT devices, except in the case of memory applications, are usually used in a region where the material does not switch its polarization, the ferroelectric switching can have an effect on the piezoelectric characteristics.

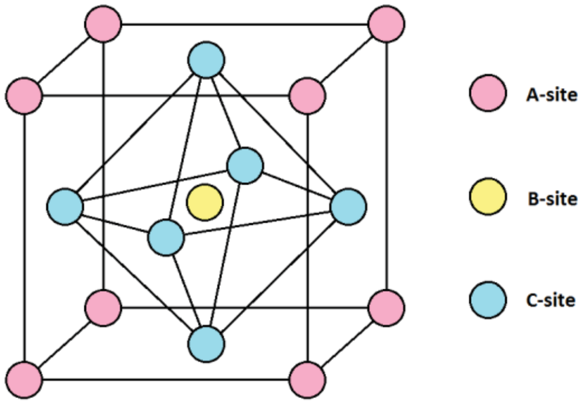

Figure 1.1: Basic perovskite unit-cell structure with A, B and C-site ions.

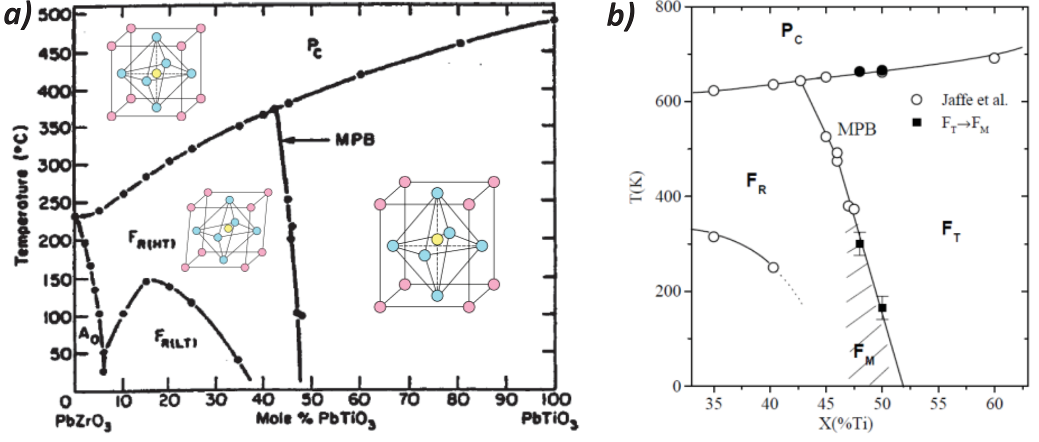

Figure 1.2: Phase diagrams of PZT showing the phase at a given composition and temperature. The figures show the para-electric cubic P_c, high/low temperature ferroelectric rhombohedral $F_{R(HT/LT)}$, ferroelectric tetragonal F_T, anti-ferroelectric orthorhombic A_T and the ferroelectric monoclinic phase. a) PZT phase diagram after *Jaffe et al.*[19][26]. b) PZT phase diagram around the morphotropic phase boundary (MPB) [20].

1.3 PZT films

PZT films can be fabricated using a variety of methods. Some of the common methods are solution gelation (Sol-gel), chemical vapor deposition (CVD), sputtering, thermal evaporation and pulsed laser deposition[5][21][11][22]. Deposition of a PZT film has the additional properties/consequences that the substrate can have an effect on the crystal structure of the film. If the out-of-plane crystal orientation of every crystallite in the film is aligned perpendicular to the substrate surface and the in-plane orientation is random, the film is called textured. This allows one to maximize piezoelectric properties, which are dependent on the optimal orientation, improving the overall film characteristics. With the right substrate and deposition conditions the film can also be epitaxial. A film is epitaxial if its crystal structure has some preferential orientation related to the substrate's crystal structure. One of the advantages of an epitaxial film is the low number of grain boundaries between grains. This minimizes the leakage current and ion transport. These mechanisms degrade the crystal, and decrease the film's lifetime. Epitaxial films are also less complicated to study due to its single crystal nature, which is ideal for diffraction studies and the lack of defects, allowing one to observe the effect of a fully strained PZT film.

Substrate materials can also cause a misfit strain in the epitaxial film. For a film to be epitaxial the substrate's unit cell must, over a large range, cause the film's unit cell to grow in a preferred in-plane orientation. This is usually only the case when the unit cell lattice parameters of the substrate and film in both in-plane orientations are nearly similar. Any small difference between the unit cell sizes will have to be solved by the film through a strain. This is the epitaxial strain (section 3.3). Samples dominated by this type of strain will be referred to as epitaxially strained films (ESF). When a thicker film is deposited, the film can become relaxed during growth through defects. If these defects are sparse the newly grown films will be able to relax to its stress free lattice parameter values at the growth temperature, while still being epitaxial. If the film is thick enough most of the film will be in this relaxed state and have no epitaxial strain. However, when these samples are cooled, the substrate and clamped film, having

different thermal expansion coefficients, can again cause a strain in the film. This strain is called the thermal misfit strain and is influenced mostly by the type of substrate material that is used, see section 2.3. Samples like these that lack epitaxial strain but do have thermal strain will be referred to as thermally strained films (TSF). Note that ESFs have both thermal strain and epitaxial strain. Both types of strain can have a large influence on the piezoelectric characteristics, especially because they restrict a change in strain even when an electric field is applied. Epitaxial strain and misfit strain can change the phase of a material compared to the phase of its unclamped structure but can also prevent phase changes. Both effects influence the characteristics of the film.

1.3.1 Tetragonal PZT

For PZT with a tetragonal crystal structure the thermal misfit strain usually causes the film to form three types of domains (section 4.1.4). The domains in PZT are distinguished through their polarization, and consequently their elongation, orientation of the unit-cells. The out-of-plane orientation of the film coincides the out-of-plane crystal direction (001) of the cubic substrate and is referred to as the 3-direction. A domain with unit cells, which have an out-of-plane polarization (P_3), is referred to as a *c*-domain, see figure 1.3. The two other domains have unit-cells with an in-plane polarization along the (100) and (010) crystal direction of the substrate, referred to as the 1- and 2-direction, respectively. Domains containing unit-cells with the main polarization component in the 1- and 2-direction are referred to as the *a*- and *b*-domain , respectively.

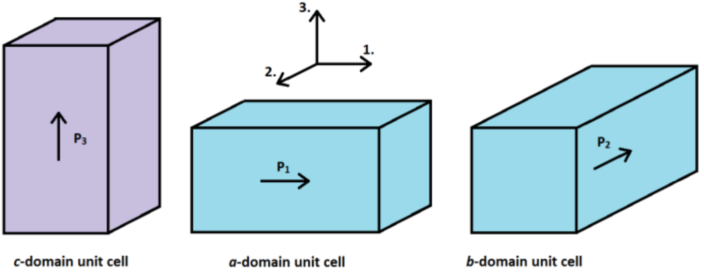

Figure 1.3: The three domains which are considered in thermally strained tetragonal PZT films.

1.4 Models

Many properties of unclamped or film PZT for all compositions, misfit strains and at any temperature can be understood with the use of the thermodynamic Landau-Devonshire (LD) theory. These phenomological models are used to study ferroelectric phase transitions and domain pattern formation. By locally minimizing the total free energy it is possible to find the resulting internal crystal parameters such as polarization and stress. This approach has been used by Haun et al. for single domain unclamped PZT[23] and was later expanded by Pertsev and Kukhar[24][25] to predict the behavior of epitaxial films with a single or poly-domain polarization and crystal structure[24][25]. This model for clamped films allows for a tetragonal PZT film with only 2 domains. However, the film structure and characteristics predicted by the model for clamped tetragonal PZT films are not visible in the domain structure observed using atomic force microscopy (AFM) or in the lattice parameter measurements done using X-ray diffraction (XRD) (chapter 3). The model proposed in this work is derived in a similar manner but has been expanded upon to allow for a 3 domain structure in an attempt to better fit the experimental data.

1.5 Piezoelectric characteristics

For piezoelectric materials the parameters of most interest are the piezoelectric coefficients, d_{ij} and e_{ij}[1]. Here, *i* and *j* stand for directions given in Voigt notation. Coefficient d_{ij} either refers to a piezoelectric material's change in electric displacement (D_i) for a change in the stress (σ_j) while the applied electric field (E) remains constant (corresponding to the direct piezoelectric effect) or to the change in strain (S_j) for a change in the electric field (E_i) while the stress (σ) remains constant (corresponding to the converse piezoelectric effect), see equation 1.1. As an example, the value for d_{31}, in the case when we are interested in the converse piezoelectric effect, shows the strain change of the material in the in-plane direction (1-direction) due to an out-of-plane (3-direction) electric field in the absence of an applied stress. The d_{ij} is the most important coefficient since it shows the change in shape of the material due to an applied field, or visa versa.

The coefficient e_{ij} refers to the change in electric displacement (D_i) for a change in the strain (S_j) while the electric field (E) remains constant (direct piezoelectric effect) or to the change in stress (σ_j) for a change in the electric field (E_i) while the strain (S) remains constant (converse piezoelectric effect), see equation 1.2. This parameter is important for understanding the stress exerted on a layer when it is clamped.

$$d_{ij} = \left(\frac{\partial \mathrm{D}_i}{\partial \sigma j}\right)^E = \left(\frac{\partial \mathrm{S}_j}{\partial E_i}\right)^\sigma \tag{1.1}$$

$$e_{ij} = \left(\frac{\partial \mathrm{D}_i}{\partial S_j}\right)^E = -\left(\frac{\partial \sigma_j}{\partial E_i}\right)^S \tag{1.2}$$

More details about how these parameters can be found theoretically and experimentally will be covered in chapters 4 and 5.

1.6 Thesis outline:

The work described in this thesis is focused on the characterization and understanding of epitaxial, clamped, dense $PbZr_xTi_{x-1}O_3$ (PZT) films. The properties of the films are analyzed using a phenomenological model in order to understand the origin of the material properties. The thesis consists of 7 chapters. Chapter 1 is an introduction to PZT and its application. Chapter 2 will focus on the fabrication of epitaxial films and how these films are characterized.

A thermodynamic model has been developed to simulate properties of clamped PZT films. The model allows us to describe the change of unit cell lattice parameters when affected by different constraints or external forces of which substrate misfit strain, applied electric field and temperature are the most common. Chapter 3 describes the origin of the model and what improvements and modifications were made to existing models presented in literature. A free energy equation is provided which can be used to describe epitaxial, clamped and dense PZT films.

In chapter 4 the results and predictions of the model are shown. Here, most focus is on the piezoelectric coefficients, stress, strain, polarization and crystal phase. In this chapter an analytical approximation will be given that provides a relationship between important parameters allowing for simple predictions without the use of numerical calculations.

Experimental work done on tetragonal poly domain $PbZr_{40}Ti_{60}O_3$ films is shown in chapter 5. The clear tetragonal poly-domain nature, as observed by X-ray diffraction, provides extensive information, which can be compared to the theoretical predictions. Measured piezoelectric coefficients, polarization and strain are all compared to the predictions of the model and give insight into the validity and shortcomings of the model.

The origin of high piezoelectric coefficients is discussed in chapter 6. Here, the effect of misfit strain on the characteristics of the PZT films close to the morphotropic phase boundary (MPB) will be investigated. The idea of separating the intrinsic piezoelectric coefficient of the unit cell of different domains and the effect of phase change for obtaining a general piezoelectric coefficient is explored. This allows us to determine how much of the characteristics of PZT are governed by its intrinsic values and how much by external factors.

In chapter 7 the structure of the domains and domain walls (DWs) in tetragonal PZT will be explored. How domains walls interact and how the large scale domain and DW structure change due to applied fields is analyzed using AFM, PFM and TEM methods. The domain and DWs structure, in a poly-domain phase in tetragonal PZT films, play an important role in better understanding how films can locally relax the stress induced by the misfit strain between the film and substrate.

References:

[1] P. Muralt, *"Ferroelectric thin films for micro-sensors and actuators: a review"*. Journal of Micromechanics and Microengineering vol.10, pp.136-146, (2000).

[2] S. Trolier-McKinstry and P.Muralt, "*Thin Film Piezoelectrics for MEMS*". Journal of Electroceramics vol.12, pp.7-17, (2004).

[3] R. A. Dorey and R.W.Whatmore. "Electroceramic Thick Film Fabrication for MEMS". Journal of Electroceramics vol.12, pp.19-32 (2004).

[4] J. Baborowski, "Microfabrication of Piezoelectric MEMS", Journal of Electroceramics vol.12, pp.33-51 (2004).

[5] Gene H. Haertling , "Ferroelectric Ceramics: History and Technology", Journal of American Ceramic Society vol.82 issue 4, pp797-818, (1999).

[6] J. F. Scott and C.A. Paz de Araujo, *"Ferroelectric Memories"*, Science 246, pp.1400-1405 (1989).

[7] D. Akai, M. Yokawa, K. Hirabayashi, K. Matsushita, K. Sawada and M. Ishida, *"Ferroelectric properties of sol-gel delivered epitaxial $Pb(Zr_xTi_{1-x})O_3$ thin films on Si using epitaxial γAl_2O_3 Layers"*. Applied Physics Letters. 86. 2005.

[8] Byung-Eun Park et al., "Fabrication of PbZrxTi1-xO3 Films on Si Structures Using Y2O3 Buffer Layers", Japanese Journal of Applied Physics 37, 5145, (1998).

[9] M. Dekkers et al. "Ferroelectric properties of epitaxial Pb (Zr , Ti) O 3 thin films on silicon by control of crystal orientation", Applied Physics Letters, 95, 012902, (2009).

[10] Chang Jung Kim et al., “Electrical characteristics of (100), (111), and randomly aligned lead zirconate titanate thin films”, Journal of Applied Physics 76, pp.7478-7482, (1994).

[11] D. Walker et al. “A comprehensive investigation of the structural properties of ferroelectric $PbZr_{0.2}Ti_{0.8}O_3$ thin films grown by PLD”, Physica Status Solidi A 206, pp.1799-1803, (2009).

[12] R. Steenwelle, “Strain and Composition Effects in Epitaxial PZT Thin Films”, Thesis University of Twente, (2012), ISBN 978-94-6191-293-0.

[13] "Piezoelectric Crystal Classes". Newcastle University, UK. Retrieved 8 March 2015 from https://www.staff.ncl.ac.uk/j.p.goss/symmetry/PP_Piezo.html.

[14] Curie, Jacques; Curie, Pierre (1880). "Développement par compression de l'électricité polaire dans les cristaux hémièdres à faces inclinées" [Development, via compression, of electric polarization in hemihedral crystals with inclined faces]. Bulletin de la Société minérologique de France. 3: 90–93

[15] Yi-Chu Hsua et al., “Demonstration and characterization of PZT thin-film sensors and actuators for meso- and micro-structures”, Sensors and Actuators A 116, 369, (2004).

[16] M. D. Nguyen et al. “Characterization of epitaxial Pb(Zr,Ti)O3 thin films deposited by pulsed laser deposition on silicon cantilevers”, Journal of Micromechanics and Microengineering. 20, 085022, (2010).

[17] D. E. Cox, B. Noheda and G. Shirane,“Low temperature phases in $PbZr_{0.52}Ti_{0.48}O_3$: A neutron powder diffraction study”, Physical Review B 71, 134110, (2005).

[18] B. Noheda and D. E. Cox, "Bridging phases at the morphotropic boundaries of lead oxide solid solutions", Cornell University Library, arXiv:cond-mat/0511256 [cond-mat.mtrl-sci], (2005)

[19] B. Noheda et al., "A monoclinic ferroelectric phase in the $Pb(Zr_{1-x}Ti_x)O_3$ solid solution", Applied Physics Letters, vol 74-14, pp.2059-2061, (1999).

[20] B. Noheda et al."The monoclinic phase in PZT: new light on the morphotropic phase boundaries", Cornell University Library, arXiv:cond-mat/0002409 [cond-mat.mtrl-sci], (2000).

[21] Tao Yu et al., "Epitaxial $Pb(Zr_{0.53}Ti_{0.47})O_3/LaNiO_3$ heterostructures on single crystal substrates", Applied Physics Letters 69, 2092, (1996).

[22] Hee-Chul Lee and Won-Jong Lee, "Characterization of Pb (Zr, Ti) O 3 thin films fabricated by plasma enhanced chemical vapor deposition on Ir-based electrodes", Journal of vacuum science & Technology A 20, 1939, (2002).

[23] M. J. Haun, Z. Q. Zhuang, E. Furman, S. J. Jang and L. E. Cross, "*Electrostrictive Properties of the lead zirconate titanate solid-solution system"*, Journal of the American Ceramic Society, Volume 72,7-1140, (1989).

[24] N. A. Pertsev, V.G. Kukhar, H. Kohlstedt and R. Waser, "*Phase diagrams and physical properties of single-domain epitaxial $Pb(Zr_{1-x}Ti_x)O_3$ thin films"*, Physical Review B 67, 054107 (2003).

[25] V. G. Kukhar, N. A. Pertsev, H. Kohlstedt and R. Waser, "*Polarization states of polydomain epitaxial $Pb(Zr_{1-x}Ti_x)O_3$ thin films and their dielectric properties"*, Physical Review B 73, 214103 (2006).

[26] T. Yamamoto, "*Crystallographic, Dielectric and Piezoelectric Properties of PbZrO3 –PbTiO3 System by Phenomenological Thermodynamics*", Japanese Journal of Applied Physics, 37 6041, (1998).

2.Fabrication and Characterization methods

Abstract:

In this chapter the fabrication and analysis methods of the epitaxial $PbZr_xTi_{1-x}O_3$ (PZT) films investigated in this work will be discussed. The fabrication steps needed to create a capacitor structure formed by an epitaxial PZT film on $SrTiO_3$ (STO) and $KTaO_3$ (KTO) single crystal substrates with a top and bottom conductive $SrRuO_3$ (SRO) electrode using pulsed laser deposition (PLD) are shown. To obtain information about the crystal structure a variety of methods, such as X-ray diffraction (XRD), atomic force microcopy (AFM) and transmission electron microscopy (TEM), are used. PZT is not only a piezoelectric material but also a ferroelectric. Electrical measurements, such as polarization hysteresis loops, are used to obtain information about the films, such as polarization and switching voltage.

2.1 Introduction

High quality epitaxial PZT films are necessary to observe the intrinsic properties of the crystal structure of a fully strained film. For textured films with mixed orientations it is difficult to examine the crystal structure of PZT and high defect densities will relax strain induced by the substrate in an uncontrollable way, affecting every part of the PZT crystal differently. The word epitaxy has its origin in the two Greek words epi (”above”) and taxis (”an ordered manner”)[1]. In material science epitaxial growth refers to the deposition of a crystalline film on a crystalline substrate. For the film to be epitaxial the crystal structure of the film has to have some preferential orientation related to the crystal structure of the substrate. In XRD terms a film is epitaxial if the film has in-plane or asymmetrical diffraction peaks. Textured films have no in-plane crystal orientation preference and the out-of-plane crystal orientation is related to the surface plane of the substrate (not to its crystal structure) and are therefore not epitaxial. Currently many PZT film fabrication techniques are used to obtain a high-crystalline quality. These range from physical methods such as sputter deposition, evaporation, pulsed laser deposition and molecular beam epitaxy and chemical methods such as chemical vapour deposition and sol-gel processes. However, although a high crystalline quality improves the piezoelectric characteristics of the film, the presence of grain boundaries still has a large influence on the piezoelectric characteristics. If single crystal grains are free standing (not mechanically connected) the material can easily deform under an applied electric field. However, when the film is used to apply a stress to the substrate it is preferred to have a dense and defect free crystal film. This can be achieved by fabricating epitaxial films in which the lateral size of the crystal is (much) larger than the film thickness. In addition, dense films and films with a few grain boundaries generally have a low leakage current, increasing the lifetime[25][26] of the film in applications.

2.2 Thin film fabrication

2.2.1 Pulsed Laser Deposition (PLD)

All PZT films discussed in this work were grown using PLD in order to obtain a dense, epitaxial layer. The basic principle of PLD is the use of laser pulses to ablate material from a target that is subsequently deposited on a substrate, see figure 2.1.

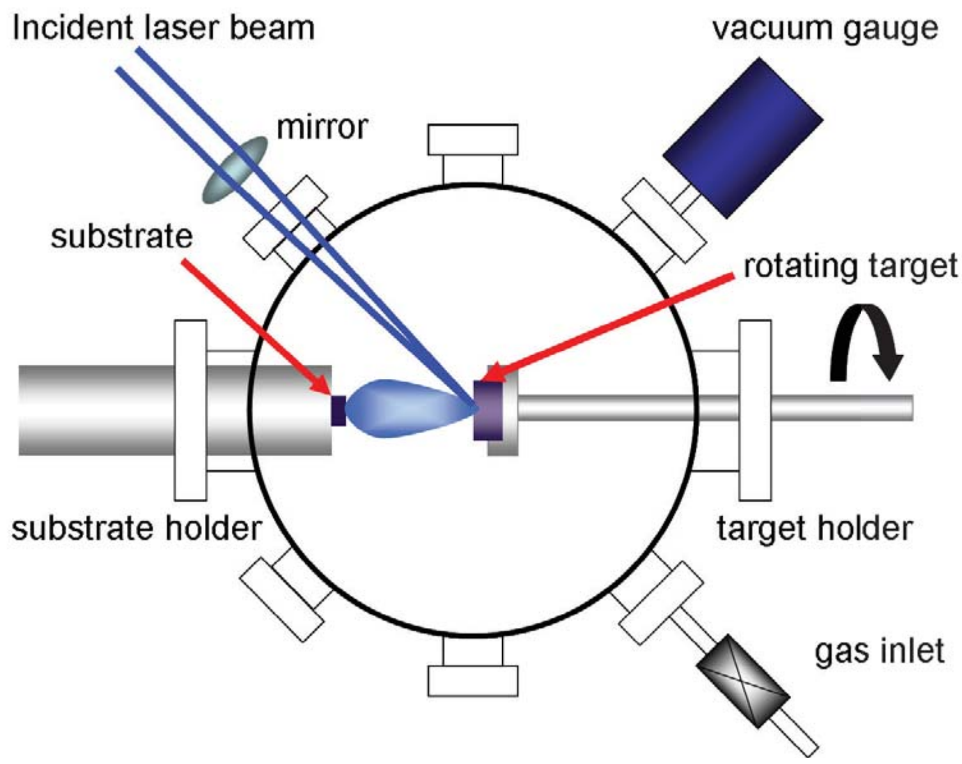

Figure 2.1: Schematic overview of the PLD system[2].

First, a high power short laser pulse is generated and focused onto the target material. The absorbed energy of the pulse heats the material locally to a very high temperature creating a plasma of high velocity particles. The plasma quickly expands forming a visible plume of target material. This plume travels through the background gas to the preheated substrate. Depending on the background gas and its pressure, a mix of charged and uncharged particles and molecules is deposited onto the substrate. The substrate is usually heated using a heating element in the substrate holder. The temperature of the substrate influences the growth process since it

allows the material to diffuse over the surface, slowly forming a thin film with a composition roughly equal to that of the target material. If the lattice parameter of the film closely matches that of the substrate the unit cells of the film material can grow in a long range crystalline structure, resulting in an epitaxial layer[3].

2.2.2 PLD setup

In our experimental PLD setup a KrF eximer laser is used, which emits short 30ns (full-width at half maximum, FWHM) ultraviolet pulses with a wavelength of 248nm, at a repetition rate between 4 and 10 Hz. Using optics the spot size on the target is set to 2.7 mm^2 with a fluence on the target of 2.5 J/cm^2. A mask is used to insure a homogeneous energy density distribution over the laser spot. The target is mounted so that the laser hits it at an angle of 45°. The substrate and heater are mounted directly in front of the target at a distance of 57 mm. To improve thermal contact with the heater the substrate is glued using silver paste. The chamber is pumped down using a turbo pump to a base pressure between 10^{-5} and 10^{-6} mbar. While pumping the substrate is heated to the deposition temperature of 600^oC. After the chamber has been pumped down to base pressure the turbo pump valve is closed and a bypass valve is opened to lower the pumping speed. An oxygen flow of 10 ml/min is introduced and the bypass valve is regulated in order to obtain a 0.10-0.13 mbar O_2 background pressure in the chamber. This gas slows down and oxidizes the particles in the plume [4][5] and ensures that enough oxygen is present for the crystalline growth of the oxide materials.

The target is continuously rotated in order to ensure a large, continuously ablated area on the target. The target is first pre-ablated for 2 min at 4Hz, while the substrate is protected, this is done to remove surface contaminations and to create a stoichiometrically correct deposition, correcting for the initial difference in ablation speeds of the different atoms and reaching a steady state. After the pre-ablation the shutter is opened and the film is grown using the deposition parameters, given in table 2.1. These values are optimized for the best crystallinity of the PZT capacitor on a perovskite substrate.

Table 2.1: PLD parameters for SRO and PZT.

	$SrRuO_3$ (SRO)	$Pb(Zr_xTi_{1-x})O_3$
Energy Density (J/cm^2)	2.5	2.5
Spot size (mm^2)	2.7	2.7
Laser Frequency (Hz)	4	10
Oxygen Pressure (mbar)	0.13	0.10
Target substrate distance (mm)	57	57
Substrate Temperature (^oC)	600	600

2.3 Sample Structure

2.3.1 Substrate

As for most microelectronic devices silicon (Si) substrates are widely used in MEMS applications. However, deposition of epitaxial PZT films on Si substrates has been notoriously difficult. This is mostly due to the fact that Si readily reacts with oxygen, which creates a thin amorphous SiO_2 layer on top of the substrate. This amorphous layer makes epitaxial growth difficult to achieve. Much work has gone into using a variety of pre-etching and buffer layers in order to access the crystalline Si underneath and allow for an epitaxially grown layer[6][7][8]. Generally for devices the goal of achieving an epitaxial layer has been abandoned and much work is done to improve the textured PZT layer in order to meet the desired high in-plane piezoelectric coefficient. It should be mentioned that single crystal Si/STO substrates have been prepared using molecular beam epitaxy (MBE), prepared by the Schlom group at Cornell University, and also through nanosheets deposited on Si as a seeding layer[9]. In chapter 6 the material properties of PZT films grown on Si will be explored. However, textured films, due their grain boundaries, are not ideal for studying the idealized situation required for testing the accuracy of models aimed at strained films. For this the PZT film should ideally be completely strained, 100% dense, free of grain boundaries, in short single crystalline. To achieve these conditions we have chosen to use STO as the substrate because it has been

shown to allow epitaxial PZT growth[10] and because of extensive knowledge in the Inorganic Materials Science (IMS) group on substrate preparation. Next to STO, KTO was also used as a substrate. Both substrate types have lattice parameters close to those of SRO and PZT (at the deposition temperatures[11]), see table 2.2. The thermal misfit strain (see section 3.3) of the substrates compared to that of PZT is also of importance for the characteristics of the epitaxial film. Using X-ray diffraction measurements it was found that all PZT compositions deposited in this work have an estimated unit cell lattice parameter at 600°C of approximately a_{600}=4.07 ±0.03 Å[12] [13][11].

Table 2.2: Lattice parameters (a) of the substrate and buffer materials found in this thesis at room temperature and 600°C. The lattice parameter values are for unclamped (stress-free) samples which are taken from literature if a reference is given. The arrows represent the range of lattice parameters expected for PZT compositions between $PbZr_{0.37}Ti_{0.63}O_3$ and $PbZr_{0.55}Ti_{0.45}O_3$.

Material	a_{RT} (Å)	a_{600} (Å)
$SrTiO_3$	3.905	3.93
Si	5.43 ($a/\sqrt{2}$=3.84)	5.45 ($a/\sqrt{2}$=3.85)
$KTaO_3$	3.99	4.00
$SrRuO_3$	3.93	3.97
$PbZr_{0.20}Ti_{0.80}O_3$	(Tetragonal) a_{short}=3.95[10] a_{long}=4.15[10]	(Cubic) 4.02 [10]
$PbZr_{0.37}Ti_{0.63}O_3$	(Tetragonal) a_{short}=4.00[10] a_{long}=4.15[10]	(Cubic) 4.06 ± 0.01
⇕	⇕	⇕
$PbZr_{0.55}Ti_{0.45}O_3$	(Rhombohedral) 4.08±0.01[13]	(Cubic) 4.08 ± 0.01

The substrates of STO (001) and KTO (001) were available as 0.5mm thick 5mmx5mm samples and were supplied by CrysTec. The Si (001) substrates were cut down to either 5mmx5mm or 10mmx10mm samples. The substrates were cleaned using acetone and ethanol in an ultrasonic bath both for 10 minutes. The KTO samples were then annealed in an oven for 120 min at 500°C with an oxygen flow of 150 mL/min. The STO is ultrasonicated in DEMI-water for 40 min and then transferred to a beaker glass with 20% buffered hydrofluoric acid (BHF) and ultrasonicated for 30 s. To stop the BHF etching process the substrate is then directly moved to beaker glasses with DEMI water, in the 1st for 10 s in the 2nd for 10 s and the 3rd for 30 s. After blow drying, the STO substrate is moved to a tube oven and annealed at 950°C with a dwell time of 90 min and an oxygen flow of 150 mL/min at ambient pressure.

2.3.2 Electrodes and PZT

To be able to apply an electric field across the PZT film's top and bottom electrodes are required. SRO is used because of its high conductivity[14]. It has been shown that SRO can be grown epitaxially on both STO and KTO single crystal substrates and allows for the epitaxial growth of materials such as PZT[10]. At the deposition temperature stress free SRO has a tetragonal crystal structure with lattice size a_c=7.91Å (a_c/2=3.955Å) and a_a=5.58 ($a_a/\sqrt{2}$=3.948Å)[15]. From XRD measurements it is found that the SRO film (≈100nm) grows epitaxially strained, which can be seen from the similar Q_x values (Chapter 2) found between the STO and SRO peaks (Fig.2.2), on the STO substrate. The PZT also grows epitaxially. The out-of-plane crystal orientation of the PZT unit-cell is identical to that of SRO and STO, see figure 2.2a. However, although PZT grows epitaxially strained initially, as the film gets thicker (>25 nm)[16] the in-plane lattice parameter of the PZT crystal relaxes to its stress free state through defect formations. The bulk of the (1 μm) PZT film is not epitaxially strained in-plane, which can be seen from the difference in Q_x values found in the (013) reciprocal space map (Fig. 2.2b). The SRO films of about 100 nm are grown with PLD in 20 min using the deposition parameters in table 2.1. SRO at room

temperature has a pseudocubic perovskite structure with a pseudocubic lattice parameter of 3.93 Å[14]. The epitaxially strained SRO film on STO is also subject to thermal misfit strain at room temperature causing a strain on the crystal resulting in out-of-plane and in-plane lattice parameters of 3.95 Å and 3.90 Å, respectively. The top electrode is grown with the same deposition parameter setting but is strained slightly differently due to the underlying PZT film, resulting in different lattice parameters and therefore giving a XRD diffraction peak location different from that of the bottom electrode (Fig. 2.5).

Room temperature lattice parameter values of stress free (unclamped) PZT depend on the PZT composition. Close to the morphotropic phase boundary (MPB) the PZT can contain rhombohedral, tetragonal and monoclinic phases [13]. The lattice parameters of PZT compositions used in this work are assumed to be between those of tetragonal $PbZr_{0.37}Ti_{0.63}O_3$ with a_a= 4.00 Å and a_c= 4.15 Å and rhombohedral $PbZr_{0.55}Ti_{0.45}O_3$ with a_r=4.08 Å[13][17][11] and around a_{short}=3.95 Å and a_{long}=4.15 Å[10] for $PbZr_{0.20}Ti_{0.80}O_3$. The lattice parameters of epitaxial PZT films depend on the composition, but are also influenced by the substrate material and the deposition temperature and will be given in the appropriate chapter. At deposition temperature all used PZT compositions have, if stress free, a cubic crystal with a cubic lattice parameter in the range of 4.04-4.10 Å. The PZT films deposited by PLD grow epitaxially because of the small difference in lattice parameter with SRO and STO at 600°C, figure 2.2b. The PZT films are grown for 50-60 min using the deposition parameters in table 1 resulting in film thicknesses of 700-900 nm.

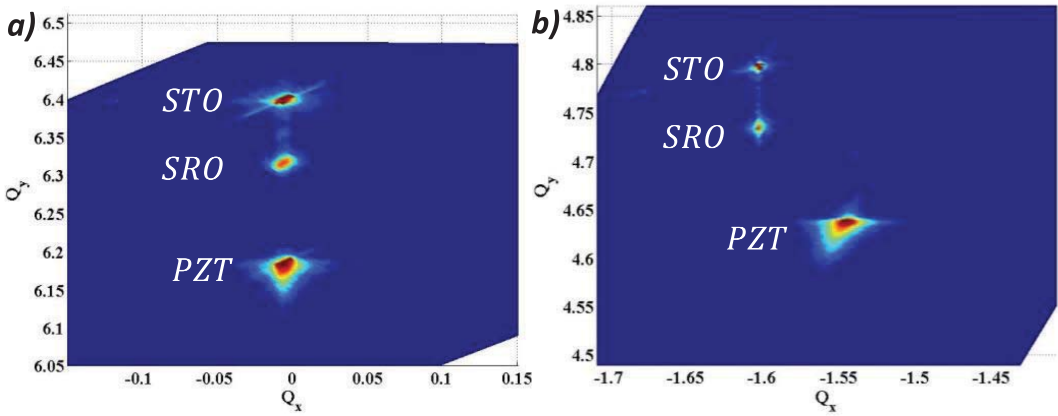

Figure 2.2 XRD reciprocal space maps of the (004) and (013) diffraction peaks of a STO/SRO (100nm)/PZT (x=0.4) (1 μm) at deposition temperature (600°C). For extra information see section 2.4. (a) The (004) peaks show that that the out-of-plane crystal direction of SRO and PZT is in line with that of the STO substrate. The identical Q_x value of SRO and STO in both (a) and (b) indicate that the in-plane lattice parameter are indentical and that SRO is grown epitaxially strained. Note that the out of plane lattice parameters are not identical. The (013) peak of PZT shows that the majority of the PZT layer is not epitaxially strained to the substrate but has a different constant in-plane lattice parameter indicating the unit cell is completely unstrained.

2.3.3 Metal Deposition

In this work amorphous conductive metal films were often used as a protective layer during wire-bonding for the SRO top electrode and in chapter 7 also as thin film top electrodes. The SRO top electrode is protected from the short pulse of ultrasonic force needed for wire bonding. An approximately 100nm thick Au top electrode was deposited using radio frequency (RF) sputtering on a Perkin Elmer 3 sputter machine. Target substrate distance, background pressure, argon pressure, voltage, power, deposition time and deposition rate were respectively 3.8 cm, $1\cdot10^{-6}$ mbar, $2\cdot10^{-2}$ mbar, 1100 V, 150 W, 3 min, and 40 nm/min. In chapter 7 we study domain wall structures with AFM using a thin (<10nm) film of conductive material as a top electrode. For these films Pt and Au were used with a 2 nm Ti adhesion layer in order to improve the metal contact with the main PZT film.

2.3.4 Etching and structuring

To allow contact to the bottom electrode, the top electrode needed to be structured. To achieve this, the sample was first prepared using photolithography methods and then dry etched to remove the top electrode from parts of the sample. The photolithography process took place in the MESA+ Nanolab cleanroom. The sample was cleaned in an acetone and ethanol ultrasonic bath both for 10 min. Due to the bad adhesion between the photoresist and the gold top layer a hexamethyldisilazane (HMDS) adhesion layer is used. The HMDS is spun at 4000rpm for 30 seconds. Then positive photoresist is spun at 4000 rpm for 30 sec, and subsequently baked on a hot plate at 100°C for 1 min, resulting in a 1.7 µm thick photoresist layer. A ultraviolet (UV) source in combination with a mask is used to expose parts of the photoresist layer. The photoresist is developed in OPD 4262 for 1 min, followed by rinsing with deionized water to stop the development process. The sample is dried and finally checked with an optical microscope and then etched using a large area (11 cm in diameter) ion beam etcher, which removes the top electrode, leaving the bottom electrode intact. The photoresist is removed using acetone and the sample is cleaned with ethanol and blown dry. Silver paste on the side of the sample was used to contact the back electrode while the top electrode was either contacted using wire-bonding or conductive probes.

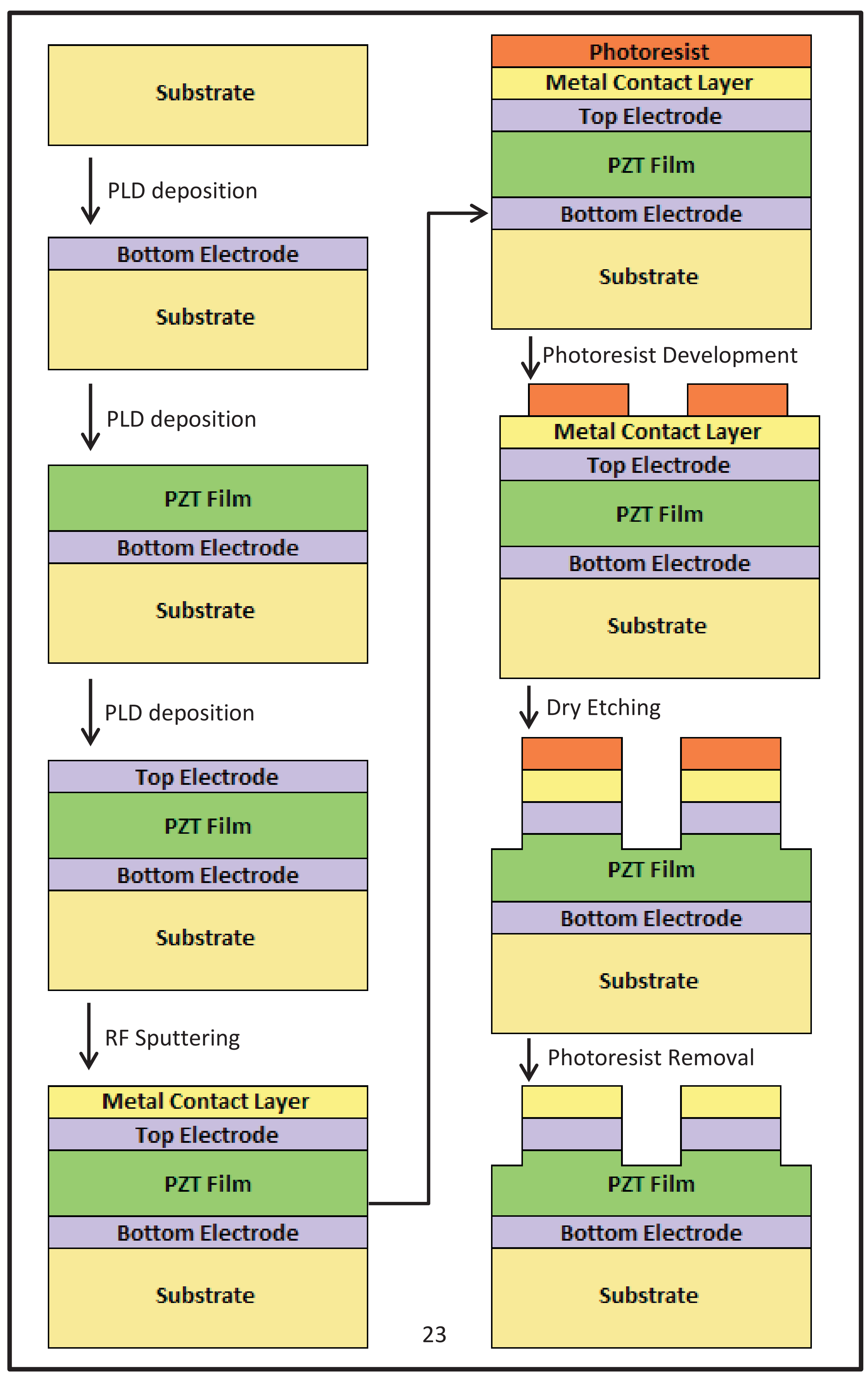
Substrate
PLD deposition
Bottom Electrode
Substrate
PLD deposition
PZT Film
Bottom Electrode
Substrate
PLD deposition
Top Electrode
PZT Film
Bottom Electrode
Substrate
RF Sputtering
Metal Contact Layer
Top Electrode
PZT Film
Bottom Electrode
Substrate
Photoresist
Metal Contact Layer
Top Electrode
PZT Film
Bottom Electrode
Substrate
Photoresist Development
Metal Contact Layer
Top Electrode
PZT Film
Bottom Electrode
Substrate
Dry Etching
PZT Film
Bottom Electrode
Substrate
Photoresist Removal
PZT Film
Bottom Electrode
Substrate

2.4 Characterization:

2.4.1 Crystal structure:

XRD is a common tool for analyzing crystal structures. This is done by measuring the angles and intensities of diffracted beams from a sample due to an incident X-ray beam. In this work XRD is used to obtain out-of-plane and in-plane crystal lattice distances, tilting of the lattice of the films with respect to the substrate and domain fractions of polarization domains in the film. Depending on the type of information required different types of XRD scans are used.

Unless specified, all measurements were made using a Panalytical MRD machine, which includes a Gobel parabolic mirror, 4 bounce Ge (220) monochromator and a large area Pixcel area detector. The line focused Cu X-Ray source (45 kV, 40 mA) in combination with the monochromator gives a Cu K-Alpha1 (λ=1.5406 Å) incident beam. A divergence slit of 0.5^o is used given a beam of width of about 1 mm. The MRD has an Anton Paar stage allowing for measurements in a temperature range between room temperature and 950^oC. Any changes in the machine setup will be given in the appropriate chapter.

To get information about the out-of-plane lattice distance of films and substrate $2\theta\omega$-scans are used, where 2θ is the angle between the incoming beam and the detector and ω is the angle between the sample and the incoming beam, see figure 2.4a. With angling or tilting in the film we refer to the angle between the out-of-plane lattice vector [001] of the film with respect to that of the [001] lattice vector of the cubic substrate, see figure 2.4b. In $2\theta\omega$-scans the 2θ angle is changed and at the same time ω is kept equal to θ. The detector consists of multiple small detectors (pixels) arranged along a line in the width direction of the detector. The scans can either be “0D” or “1D”, where the former method counts the X-Rays, summing the signal from all detectors when its center is at the correct 2θ location, while the latter method stores the data of every pixel separately allowing the summing up of each separate pixel with the same 2θ value. The 1D method is better for obtaining 2θ values since it is not influenced by

the ω value of the diffraction peaks but has a negative impact from X-Ray scattering and incident beam width. The distance between crystal planes can be obtained from the 2θ value of the diffraction peak via Bragg's law:

$$n\lambda = 2d\sin\theta \tag{2.1}$$

where *n* is a positive integer, λ is the wavelength of the X-rays and *d* is the distance between the crystal planes. Extracting the 2θ value of a substrate peak from a scan is usually simple, because of the long scale ordering and low defect density in the substrate, resulting in a narrow diffraction peak width, especially in 0D scans. To find the 2θ diffraction peaks related to the film we usually resort to fit with either a Gaussian fit or a Voigt fit, which combines a Lorentzian and Gaussian peak fit[18].

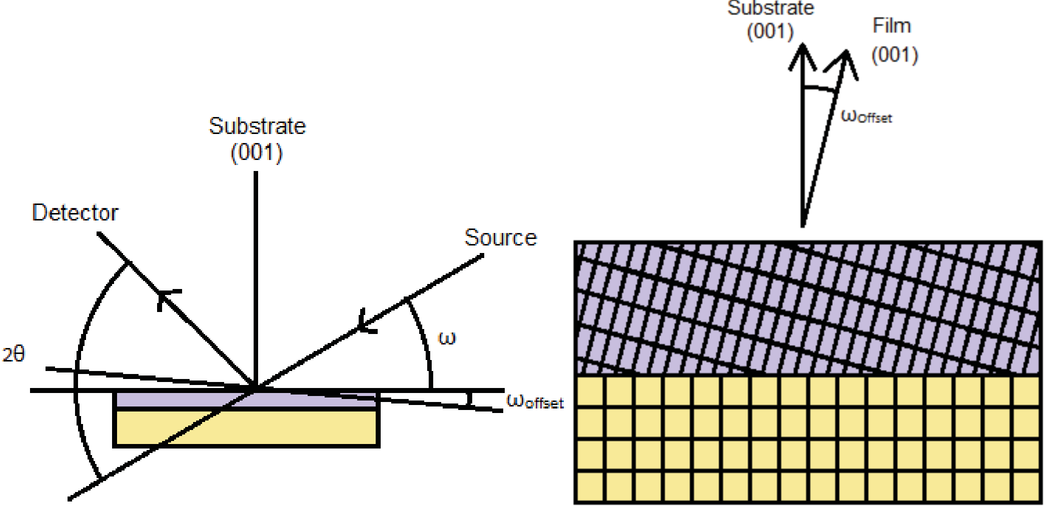

Figure 2.4: (a) Overview of the definition of the 2θ and ω angles in XRD. The ω and ω_{offset} angles are set relative to the out-of-plane crystal orientation (001) of the substrate. (b) Shows the possible ω_{offset} between the out-of-plane crystal orientation (001) of the unit-cells in the film compared to those of the substrate. In this work the (001) direction of the substrate is always set at ω_{offset}=0.

To obtain information about the angle (or tilt) between the out-of-plane lattice parameter orientation of the film and substrate, ω–scans are used. Here a constant 2θ is used, corresponding to the out-of-plane lattice parameter of the relevant peak, and a scan is made along the ω direction. If additional information about the angling in the χ direction is needed, where

χ is the sample tilt angle perpendicular to the ω direction, ω-χ-scans can be made. The disadvantage of the ω-χ-scan is that a scan along the χ direction usually holds less accurate information because of the finite angular divergence of the incoming beam in the χ-direction and the long scan time (of ω-χ-scans) due to the many line scans required for a two axis scan, see figure 2.6. Both ω and χ are given in degrees, where ω is not used in the axis of the graph, but rather the offset value ω_{offset}, see equation 2.2, so that the zero values of both the χ and ω_{offset} axis represent a direction that corresponds to the out-of-plane direction of the substrate diffraction peak along the symmetrical axis. A reciprocal space map (RSM), see figure 2.4, is made by scanning both 2θ and ω independently. Although usually requiring several hours for one scan it has the advantage that it gives a better overview of the diffraction peaks, see figure 2.5, and also allows one to obtain the in-plane lattice parameters of the film by scanning several different asymmetrical diffractions peaks. Exact settings for all XRD measurements are given in the appropriate chapter. RSMs are represented in momentum space (Q-space) where the momentum vectors Q_{100} (in-plane) and Q_{001} (out-of-plane) are given by equation 2.3 and 2.4, respectively. Q_{010} represents the other (in-plane) direction but is generally not used to represent data in this work.

$$\omega_{offset} = \omega - \theta \tag{2.2}$$

$$Q_x = Q_{100} = \frac{4\pi}{\lambda}\sin(\theta)\sin(\omega_{offset}) \tag{2.3}$$

$$Q_y = Q_{001} = \frac{4\pi}{\lambda}\sin(\theta)\cos(\omega_{offset}) \tag{2.4}$$

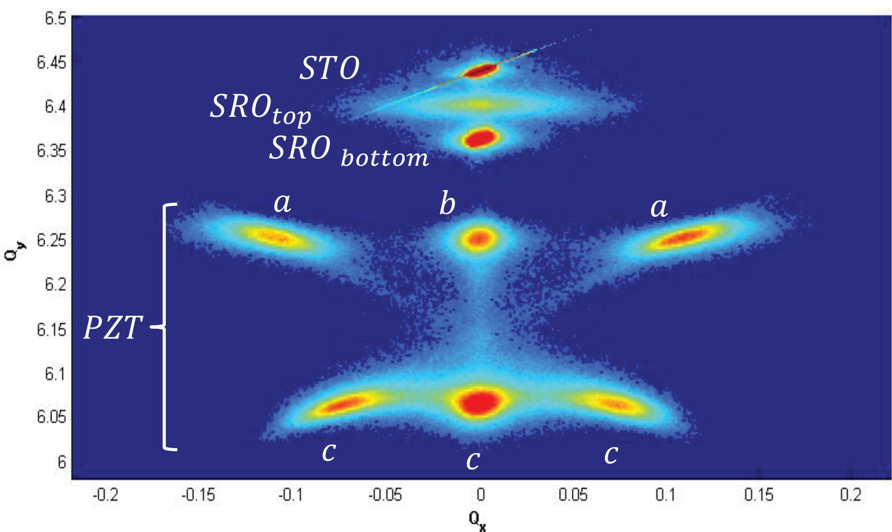

Figure 2.5: Example of a typical RSM of a STO/SRO(100 nm)/PZT (x=0.4)(1μm)/SRO(100 nm) system showing the 004 diffraction peaks. From the top the diffraction peaks correspond to the STO substrate, SRO (top electrode), SRO (bottom electrode), 4 (3 are distinguishable) PZT *a*- and *b*-domains and 4 (3 are distinguishable) PZT *c*-domains (see section 1.3).

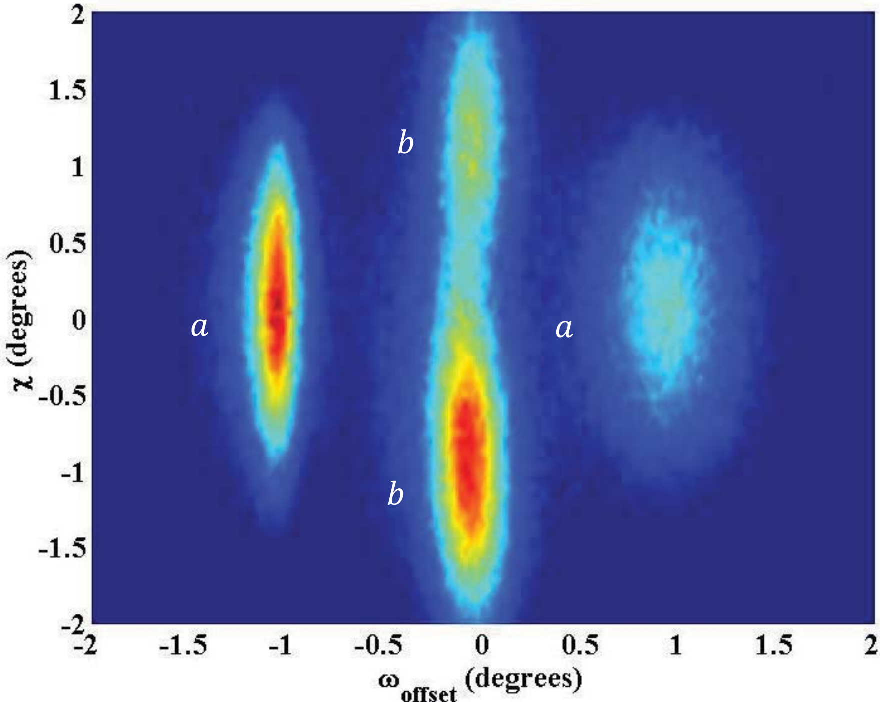

Figure 2.6: Example of a ω-χ-scans at the location of the *a*-domains (figure 2.5) at Q_y=6.25 (2θ≈ 100°). It reveals that the 3 peaks in the RSM are actually 2 *a*- and 2 *b*-domain peaks. It also shows that the tetragonal crystal structure has 4 different domains, tilted symmetrically over about 1 degree in four different directions in the in-plane [100] and [010] directions, with respect to the substrate out-of-plane direction. A similar scan can be made around the c-domain peaks at Q_y=6.05.

To gather more information about the local crystal structure transmission electron microscopy (TEM) was used (chapter 7). In TEM electrons are used to obtain a resolution in the range of the materials crystal unit cell because of the small de Broglie electron wavelength compared to light. For more detailed information on TEM see [23]. For the electrons to pass through the material a sample thickness in the range of about 65 to 100 nm is required. This is done by several grinding and polishing steps until the sample is below 5 µm thick, followed by ion milling to reach the desired final thickness. Note that in this work the grinding and polishing is done from the side of the samples in order to have a thin slice containing both substrate and film (Fig. 7.5). In order to save time, two different samples were imaged together by using epoxy to glue them together at their surface (Fig. 7.7a). To avoid damage to the samples during the processing they are glued on top of Si wafers and then glued inside a Cu holding ring. The epoxy glue was applied at 120°C, which could cause some thermal stress on the material. The ion milling creates a lens shape making the thickness over a larger range not completely uniform. In this work a Philips CM300ST FEG TEM was used for all TEM measurements[19].

2.4.2 Electrical and Optical Characterization

A common measurement for a ferroelectric material such as PZT is a polarization hysteresis loop, see figure 2.7a. In this measurement a triangular voltage signal is applied across the capacitor, see figure 2.7b, and the resulting current is measured. All loops are measured after a pre-polarization loop to ensure polarization switching during the measurement. The current measurement made during these loops allows us to extract the charge transport due to the polarization switch of the ferroelectric material. This gives information about the switching field, switching speed and out-of-plane polarization at each electric field strength for a chosen measurement frequency[20].

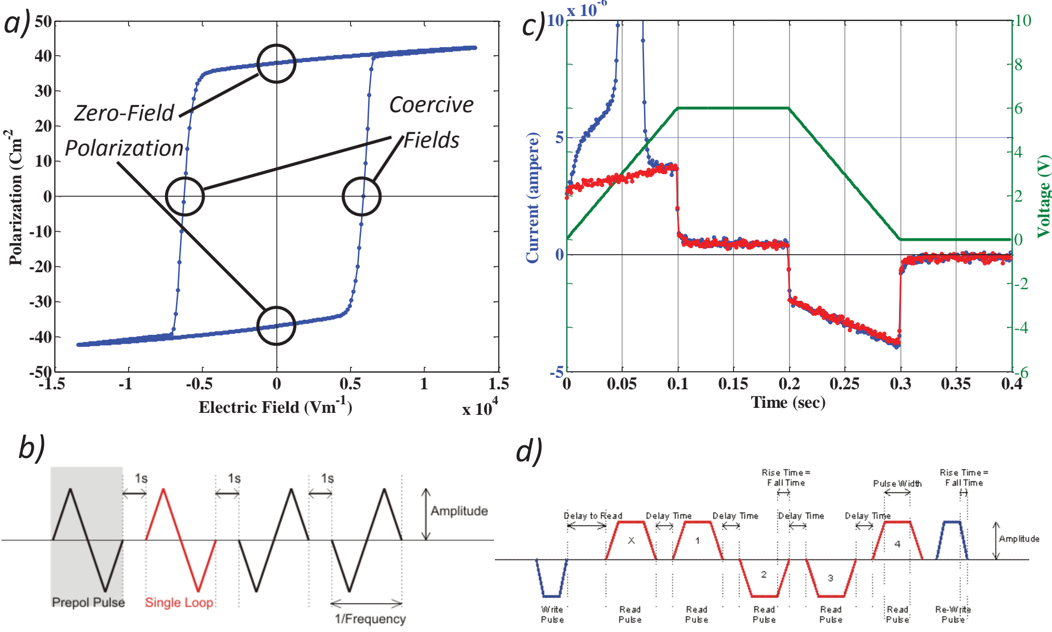

Figure 2.7: (a) Example of a hysteresis loop obtained from a dense strained epitaxial 1 µm PZT film with an area of ≈11 mm^2. The voltage was swept between -12 V and +12 V at a rate of 10Hz. The data was averaged over 3 loops. (b) Voltage signal applied by the apparatus for obtaining the hysteresis loop. (c) Example showing the PUND measurement of the first two voltage ramps (6V). The measured current difference between a sample with a polarization switch (blue) and no switch (red). A clear current peak is visible where the polarization switches (blue). Between 0.1 and 0.2 s an indication of the leakage current can be found. (d) PUND voltage signal.

Although most information of interest can be extracted from the hysteresis loops other measurements allow for more focus on a particular characteristic. Leakage current measurements can be important for checking the quality of samples, especially those with large electrodes where the probability of a significant defect in the crystal is higher. Large leakage currents are easily noticeable in hysteresis measurements and generally point to a conductive channel through the PZT film, which will not allow for an applied electric field across the sample. Small leakage currents can have a more subtle influence on a hysteresis loop usually by opening up the loop vertically, influencing the polarization measurements. Leakage measurements are useful to distinguish between a leakage currents and a time dependent switching mechanism, which both affect a polarization loop

similarly, and check the sample quality. Leakage current measurements were performed by applying a constant voltage for 2 s where the current data was measured between 1.4 and 1.8 s. The measurements were repeated every 0.5 V over a range between -6 and +6 V.

It is found that all samples used in this work, for which the polarization information is used, had a very low leakage current, which had a negligible effect on polarization measurements for the frequencies used. Additionally, unless otherwise mentioned, the measured out-of-plane polarization at zero field (found during a polarization loop), the remnant polarization (found in the sample after some time) and the saturation polarization (the theoretical maximum polarization obtained from an extrapolation of the polarization at higher fields to zero field) are all found to be identical for the hysteresis measurements performed throughout this work (figure 2.7a).

To obtain a better insight into the origin of the measured polarization (i.e. the origin of current or charge build up) PUND measurements were used, figure 2.7c. PUND measurements show the difference in current measured between the situations when a ferroelectric layer switches its polarization and when it does not. The measurement voltage signal can be found in figure 2.7d. All pulses have a trapezoid shape with a linear voltage ramp up and down of 0.1 s and a constant voltage in between with a duration of 0.1 s. Information about the capacitance of the capacitor was collected by using a CV measurements. Here, the voltage is increased and decreased linearly similar to a hysteresis loop at a frequency of 0.2Hz. On top of this base voltage a 4kHz AC voltage with an amplitude of 50mV is used to measure the capacitic response at every voltage point.

All electrical measurements were done using an aixACCT TF Analyzer 2000HS. The apparatus comes with a double beam laser interferometer (DBLI), which, if the sample is polished on both sides, allows one to measure thickness changes of the sample under varying applied voltage. This is especially useful for large electrodes which can slightly bend the substrate making measurements done only on the surface, such as vibrometer and white light interferometer, less reliable. The DBLI only measures the total thickness change. This method is used to obtain

information about the out-of-plane piezo electric coefficient of the PZT films (chapter 5).

2.4.3 Surface characteristics

The surface structural properties of the substrate and films were obtained by scanning probe microscopy, see figure 2.9. Our main tool for imaging the surface is tapping mode AFM. In tapping mode AFM a tip with a radius of around 8nm[21] is used to scan the surface locally. The tip taps the surface close to the resonance frequency of the cantilever, which is piezo-electrically actuated. Interaction of the tip with the surface changes the resonance frequency and phase of the cantilever oscillations, which can be read out via a laser reflected off the back of the cantilever. This primarily gives information about small local height changes of the samples. The main application of AFM in this work is to observe domain walls (DWs) and the difference in tilt between domains in tetragonal PZT (Chapter 7). All AFM measurements are done using the Bruker Icon using TESPA V2 tips. Next to AFM the apparatus also allows for piezo force microscopy (PFM) measurements, which are done using a conductive tip, Bruker R11C24. Here, an AC voltage is applied on the tip creating an electric field near it. This electric field interacts with the surface of the ferroelectric material. The resulting movement can be detected either as a tilt along the cantilever or perpendicular to it. Both of these tilts give information about the local polarization strength and direction. In this work PFM is mainly used to gain information about the polarization orientation of the different domains found in tetragonal PZT (Chapter 7).

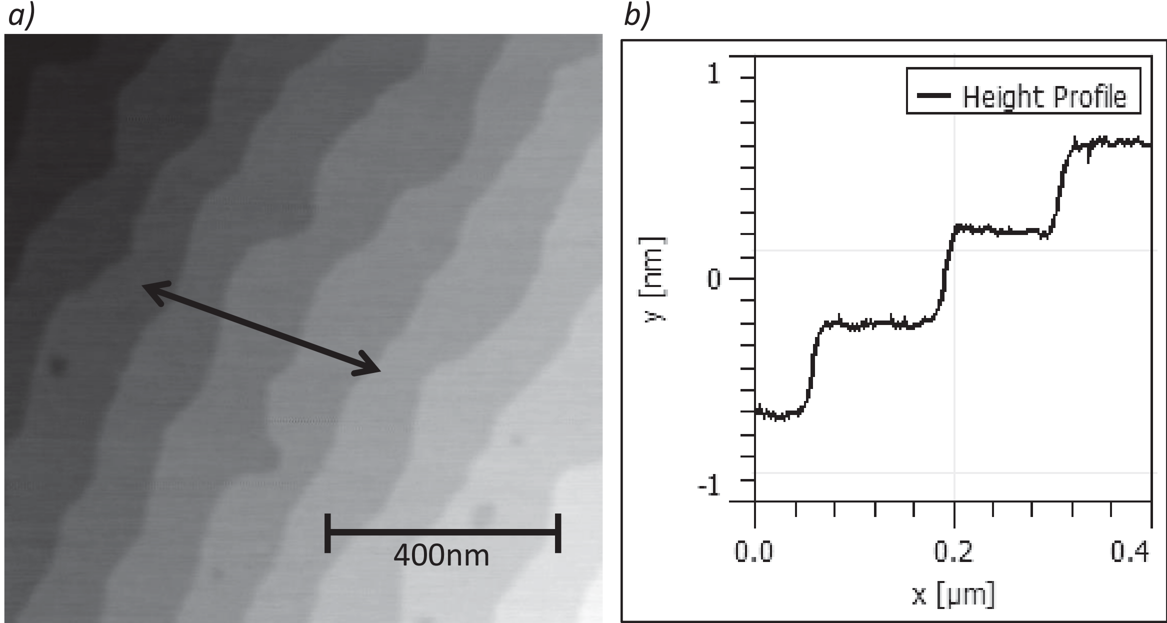

Figure 2.9: (a) AFM height profile of cleaned and annealed STO substrate. (b) Step height of about 4 Å coinciding with the unit cell thickness indicating that all terraces have the same termination. In this case we expect a TiO_2 termination.

Surface information was also gathered using high resolution scanning electron microscopy (HR-SEM). HR-SEM is a method for obtaining surface structure and compositional information on the nanometer scale. More information on the basics of SEM can be found in [24]. In this work HR-SEM was used to measure the film thickness and gain information about surface structures, grain structure and crystallinity and growth inhomogeneities at the nanometer scale. Unless otherwise mentioned, all SEM images were made using the Zeiss Merlin FEG HRSEM [22].

References

[1] M. Ohring, "*Materials Science of thin films (Second Edition)*", ISBN: 978-0-12-524975-1, p417-418, (2002).

[2] K. Wang (2013). Laser Based Fabrication of Graphene, Advances in Graphene Science, Dr. M. Aliofkhazraei (Ed.), InTech, DOI: 10.5772/55821. Available from: http://www.intechopen.com/books/advances-in-graphene-science/laser-based-fabrication-of-graphene

[3] M. Ohring, "*Material Science of Thin Films*", (2001), ISBN:978-0-12-524975-1.

[4] K, Orsel et al. ,"*Influence of the oxidation state of SrTiO3 plasmas for stoichiometric growth of pulsed laser deposition films identified by laser induced fluorescence*", APL Materials 3, 106103, (2015).

[5] R. Groenen et al. ,"*Research Update: Stoichiometry controlled oxide thin film growth by pulsed laser deposition*", APL materials 3, 070701, (2015).

[6] M. Dekkers et al., "*Ferroelectric properties of epitaxial Pb(Zr,Ti)O3 thin films on silicon by control of crystal orientation*", Applied Physics Letters 95, 012902 (2009).

[7] S. Mi et al., "*Atomic structure of the interface between $SrTiO_3$ thin films and Si(001) substrates*", Applied Physics Letter 93, 101913, (2008).

[8] S. Baek and C. Eom, "*Epitaxial integration of perovskite-based multifunctional oxides on silicon*", Acta Materialia V.61 8, p.2734-2750, (2013).

[9] M. Nguyen et al., "*Highly Oriented Growth of Piezoelectric Thin Films on Silicon Using Two-Dimensional Nanosheets as Growth Template Layer*", *ACS Appl. Mater. Interfaces*, (2016), 8 (45), pp

31120–31127.

[10] R. Steenwelle, "*Strain and Composition Effects in Epitaxial PZT Thin Films*", Thesis University of Twente, (2012), ISBN 978-94-6191-293-0.

[11] I.N. Andryushinan et al., "*The PZT system ($PbTi_xZr_{1-x}O_3$, , $0≤x≤1.0$): High temperature X-ray diffraction studies. Complete x-T phase diagram of real solid solutions (Part 3)*". Ceramics international. Vol. 39-3. (2013).

[12] B. Noheda et al. "*A monoclinic ferroelectric phase in the $Pb(Zr_{1-x}Ti_x)O_3$ solid solution*". Applied Physics letters, vol. 74-14. (1999).

[13] B. Noheda, D. E. Cox and G. Shirane. "*Stability of the monoclinic phase in the ferroelectric perovskite $PbZr_{x-1}Ti_xO_3$*". Physical review B, vol. 63-014103. (2000).

[14] G. Koster, L. Klein, W. Siemons et al. "*Structure, physical properties, and applications of SrRuO3 thin films*". Reviews of modern physics. Vol. 84-1. (2012).

[15] Kennedy, B. J., and B. A. Hunter. "*High-temeprature phases of $SrRuO_3$*". Physical review B 58, 653. (1998).

[16] Boota et al., "*Epitaxial Pb(Mg1/3Nb2/3)O3-PbTiO3 (67/33) thin films with large tunable self-bias field controlled by a PbZr1−xTixO3 interfacial layer*", Applied Physics Letters, 104, 182909 (2014).

[17] G. Shirane, K. Suzuki and A. Takeda. "*Phase transitions in solid solutions of $PbZrO_3$ and $PbTiO_3$ (II) X-ray study*". Journal of the physical society of Japan. Vol. 7-1. (1952).

[18] S. Enzo, G. Fagherazzi, A. Benedetti and S. Polizzi. "*A profile-fitting procedure for analysis of broadened X-ray diffraction peaks. I. Methodology*". Journal of Applied Crystallography 21, pp.536-542. (1988)

[19] MESA+ Nanolab, Transmission Electron Microscope specifications, https://www.utwente.nl/mesaplus/nanolab/analyselab/Analysis_Facilities/TEM/

[20] M. Nyguyen, "Ferroelectric and Piezoelectric properties of epitaxial PZT films and devices on silicon", Thesis University of Twente, (2010), ISBN 978-90-365-3047-7.

[21] MESA+ Nanolab, Transmission Electron Microscope specifications, https://www.brukerafmprobes.com/images/product/specPDF/3844.pdf

[22] MESA+ Nanolab, Scanning Electron Microscope specifications, https://www.utwente.nl/mesaplus/nanolab/analyselab/Analysis_Facilities/SEM/

[23] D. Williams and C. Carter, "*Transmission electron microscopy*", p.5-17, Plenum Press, New York, (1996), ISBN: 0-306-45247-2.

[24] P. Goodhew, J. Humphreys and R. Beanland, "*Electron Microscopy and Analysis*", Taylor & Francis, New York and London, (2001), ISBN: 0-7484-0968-8

[25] M. Dekkers et al., "*Ferroelectric properties of epitaxial Pb(Zr,Ti)* O_3 *thin films on silicon by control of crystal orientation*", Applied Physics Letters 95, 012902, (2009).

[26] M.D. Ngyugen et al., "*Highly Oriented Growth of Piezoelectric Thin Films on Silicon Using Two-Dimensional Nanosheets as Growth Template Layer*", ACS Applied Materials and Interfaces, (2016), 8 (45), pp 31120–31127

3. Thermodynamic energy model of strained dense epitaxial PZT

Abstract:

In this chapter the origin of our thermodynamic energy model for a dense, clamped single crystal $PbZr_xTi_{1-x}O_3$ film is described. We derive the full Helmholtz free energy equations for the new boundary conditions and equation, required to derive material properties, such as unit cell strain, from the model. In addition, for more idealized conditions, a simplified free energy equation is derived with a smaller number of variables. This simplification also allows for Helmholtz free energy equations related to a specific phase state of the PZT material. The different Helmholtz free energy equations derived in this chapter will be used throughout this thesis to better understand experimental results of clamped PZT films and help predict material properties for films under different conditions such as temperature, electric field and strain variations.

3.1 Introduction

In this work we have created a thermodynamic model to better understand dense strained epitaxial PZT films. The model has its origin in the Landau theory, which is a phenomenological model. Devonshire adapted this model for ferroelectric materials. This led to the Landau-Devonshire phenomenological theory, which was used to explain phase transitions at the morphotropic phase boundary observed in PZT[2]. Haun *et al.*[1-6] continued this work, which was hampered by the lack of coefficients required for the free energy formulation, and gave a full Gibbs free energy equation used to describe solid solutions of PZT[1-6]. Pertsev *et al.* adapted the work done by Haun for dense, fully clamped PZT films[7-9]. For this, the Gibbs free energy was reformulated into the Helmholtz free energy and several boundary conditions were added that were thought to be important in order to allow the model to better predict the properties of PZT films.

In this work both the Gibbs free energy and Helmholtz free energy formulas are used to better understand the behavior of dense epitaxially grown PZT on substrates with different misfit strains. X-ray diffraction (XRD) and atomic force microscopy (AFM) results (Section 3.2.3) are used to see how PZT behaves in practice, which allows us to adapt the boundary conditions used by Pertsev et al. to better fit the experimental results.

3.2 Gibbs and Helmholtz free energy model

3.2.1 Gibbs free energy

The thermodynamic model for PZT crystals has its origin in the Gibbs and Helmholtz free energy equations for gases. The Gibbs free energy originates from the thermodynamic study of gases where the formula gives the energy contained in a system at a given pressure and temperature. More information about the terms and symbols can be found in the glossary (see Appendix).

$$G_0(p,T) = H - TS = U + pV - TS_e \tag{3.1}$$

The energy formula can be adjusted so that it can also be used for solid materials such as crystals and is referred to as the elastic Gibbs free energy density. For our crystal the Gibbs free energy gives the energy contained in a system at a constant stress and temperature. Note that the stress has separate directions unlike pressure in a gas. This formula, equation 3.2, is used for bulk material where we have a clearly defined external stress and temperature. To solve the equation we have to minimize the energy term.

Using the 6th order expansion of the polarization energy one obtains the Gibbs free energy density formula for a single domain crystal[2]:

$$\begin{aligned}
&G(\sigma, T) = \\
&+\alpha_1(P_1^2 + P_2^2 + P_3^2) + \alpha_{11}(P_1^4 + P_2^4 + P_3^4) + \alpha_{111}(P_1^6 + P_2^6 + P_3^6) \\
&+\alpha_{12}(P_1^2P_2^2 + P_3^2P_2^2 + P_1^2P_3^2) + \alpha_{123}(P_1^2P_2^2P_3^2) \\
&+ \alpha_{112}\left(P_1^4(P_2^2 + P_3^2) + P_2^4(P_1^2 + P_3^2) + P_3^4(P_2^2 + P_1^2)\right) \\
&-0.5s_{11}(\sigma_1^2 + \sigma_2^2 + \sigma_3^2) - s_{12}(\sigma_1\sigma_2 + \sigma_1\sigma_3 + \sigma_2\sigma_3) \\
&-0.5s_{44}(\sigma_4^2 + \sigma_5^2 + \sigma_6^2) \\
&-Q_{11}(\sigma_1 P_1^2 + \sigma_2 P_2^2 + \sigma_3 P_3^2) \\
&-Q_{12}(\sigma_1(P_2^2 + P_3^2) + \sigma_2(P_1^2 + P_3^2) + \sigma_3(P_1^2 + P_2^2)) \\
&-Q_{44}(\sigma_4 P_2 P_3 + \sigma_4 P_1 P_3 + \sigma_4 P_1 P_2)
\end{aligned} \tag{3.2}$$

The first three lines of the formula, using the dielectric stiffness constants (α_i, α_i and α_{iii}), give the internal energy of the crystal, which is dependent on the polarization and temperature. Temperature is introduced though α_1, which is not a material constant, defined by: $\alpha_1 = (T - \theta)/2\varepsilon_0 C$, where T, θ, ε_0 and C are the temperature, Curie Weiss temperature, permittivity of free space and the Curie constant, respectively[3]. Note that the Curie Weiss temperature is not always equal to the phase transition temperature, but for the PZT compositions used throughout this work ($0.3 \leq x \leq 0.6$) the Curie temperature is equal to the transition temperature. More details on this can be found in [3]. The elastic energy put into the system through the external application of stress is described by the terms with the elastic compliance coefficients (s_{ij}). Because the stress is applied externally the energy terms are negative, lowering the free energy. The electrostrictive constant (Q_{ij}) introduce the energy terms representing the interaction

between the crystals polarization and the applied stress and is defined such that the strain induced by the polarization is given by $S_j = Q_{ij} P_i^2$.

Haun *et al.*[0][1][2] use the full Gibbs free energy formula, which includes parameters for octahedral tilting which is a tilt of the oxygen ion location octahedra with respect to the lead ion locations[5]. This is used for rhombohedral and anti-ferroelectric orthorhombic unit cells. The octahedral tilting is given by the parameters θ_1, $\theta_2$and θ_3, see [2]. Haun *et al.* make a difference between the high temperature rhombohedral phase, which has zero tilting, and the low temperature phase with non-zero angling (Fig. 1.2). However, in case of the low temperature rhombohedral phase the material constants are only given if the unit cell is perfectly rhombohedral (P_1=P_2=P_3). This is usually not true in clamped thin films in both the work done by Pertsev *et al.* [8][9] and our work. Although not explicitly stated, Pertsev *et al.* only consider the high temperature rhombohedral phase[8] and also do not require the out-of-plane and in-plane polarization to be equal (P_1=P_2≠P_3). In this work we also use the high temperature rhombohedral phase, and allow the material to take any polarization (P_1≠P_2≠P_3). Because the parameters given by Haun *et al.* only work for where the polarizations are equal, these will not be included in this work. The low temperature rhombohedral phase occurs in PZT with a high Zr content ($x \geq 0.7$) at temperatures below 150°C[5][2]. All compositions discussed in this work, experimental and theoretical, have a high temperature rhombohedral case ($x \leq 0.6$) and, therefore, the octahedral tilt parameter in both the Gibbs and Helmholtz free energy equations can be considered to be zero.

3.2.2 Helmholtz free energy

The Gibbs free energy density equation can be used to model unclamped bulk PZT crystals, which is common for powder PZT crystals. For a clamped PZT film the equation for the Helmholtz free energy density is required. The Helmholtz Free Energy gives the energy of a system at a given volume and temperature. For a gas system it is:

$$F(V,T) = \mathrm{U} - \mathrm{TS}_e = \mathrm{G(p,T)} - pV \tag{3.3}$$

In order to apply this to clamped crystals the constant volume condition represents a constant strain or constant deformation condition. To obtain from the Gibbs free energy the Helmholtz free energy, one needs to subtract the equivalent of pV, which for a solid crystal is the sum of the stress multiplied by the strain, separate for each direction.

$$pV \rightarrow -\sum_{i=1}^{6} \sigma_i S_i \tag{3.4}$$

Due to this transformation the stress is no longer external but internal, which implies an increase in energy for an increase in stress. The strain can be found by differentiating the Gibbs free energy with respect to the stress.

$$S_{\mathrm{i}} = -\frac{dG_0}{d\sigma_i} \tag{3.5}$$

$$\begin{aligned}
S_1 &= s_{11}\,\sigma_1 + s_{12}(\sigma_2 + \sigma_3) + Q_{11}\,P_1^2 + Q_{12}\,(P_2^2 + P_3^2) \\
S_2 &= s_{11}\,\sigma_2 + s_{12}(\sigma_1 + \sigma_3) + Q_{11}\,P_2^2 + Q_{12}\,(P_1^2 + P_3^2) \\
S_3 &= s_{11}\,\sigma_3 + s_{12}(\sigma_1 + \sigma_2) + Q_{11}\,P_3^2 + Q_{12}\,(P_1^2 + P_2^2) \\
S_4 &= s_{44}\,\sigma_4 + Q_{44}\,P_2P_3 \\
S_5 &= s_{44}\,\sigma_5 + Q_{44}\,P_1P_3 \\
S_6 &= s_{44}\,\sigma_6 + Q_{44}\,P_1P_2
\end{aligned}$$

The Helmholtz free energy density of a film with a single domain (or symmetrical domains such as *a*- and *b*- domains) is then given by:

$$F(S,T) = \mathrm{G}(\sigma,T) + \sum_{i=1}^{6} \sigma_i \frac{dG_0}{d\sigma_i} \tag{3.6}$$

$$\begin{aligned}
F(S,T) = & \\
& +\alpha_1(P_1^2 + P_2^2 + P_3^2) + \alpha_{11}(P_1^4 + P_2^4 + P_3^4) + \alpha_{111}(P_1^6 + P_2^6 + P_3^6) \\
& +\alpha_{12}(P_1^2 P_2^2 + P_3^2 P_2^2 + P_1^2 P_3^2) + \alpha_{123}(P_1^2 P_2^2 P_3^2) \\
& + \alpha_{112}\left(P_1^4(P_2^2 + P_3^2) + P_2^4(P_1^2 + P_3^2) + P_3^4(P_2^2 + P_1^2)\right) \\
& +0.5 s_{11}(\sigma_1^2 + \sigma_2^2 + \sigma_3^2) + s_{12}(\sigma_1\sigma_2 + \sigma_1\sigma_3 + \sigma_2\sigma_3) \\
& +0.5 s_{44}(\sigma_4^2 + \sigma_5^2 + \sigma_6^2)
\end{aligned}$$

The stress is now an internal stress in response to the externally applied strain conditions of a clamped thin film. For poly-domain materials the total Helmholtz Free energy formula will be the summation of the corresponding Helmholtz free energy terms of the separate domains multiplied with a factor for their fraction (ϕ). In this work the domain fraction is only used for tetragonal, poly-domain films, which are modeled as having two domains. The *c*-domain with an out-of-plane polarization and an *a*-domain, with a predominantly in-plane polarization. The domain fractions are ϕ_c and $\phi_a (= 1 - \phi_c)$, respectively (see eqs 3.15 and 3.16). *b*-domains with an in-plane polarization perpendicular to the *a*-domain are taken into account, but it appears that it is not necessary to introduce separate terms for the b-domains in the free energy equation, due to its symmetry with *a*-domains. The *a*-domain fraction (ϕ_a) is assumed to be a combination of 50% *a*-domain and 50% *b*-domain.

The Helmholtz free energy formula allows us to apply a strain constraint. This is the most important difference between a bulk material (constant stress) and a clamped film (constant strain). Next to the applied strain and temperature we also require an electric field effect. The electric field energy term ($\mathcal{E}_{Electric\ Field}$) is dependent on the polarization of the material and is negative as the electric field does work on the film (similar to an applied stress). The associated energy term is added to both the Gibbs

Free energy and the Helmholtz Free energy and can be split up into the decrease in free energy due to the interaction with polarization and due to the electric field energy in a vacuum for a capacitor[8][9]. Due to the capacitor system layout the applied electric field in our work is always in the out-of-plane direction (3-direction) and therefore written as E_3 and only interacts with the out-of-plane polarization vector P_3. The added energy terms are:

$$\mathcal{E}_{Electric\ Field} = \int \mathcal{E} dV = -\int \vec{E}\,\vec{D} dV \quad \text{where} \quad \mathrm{D} = \vec{P} + \varepsilon_0 \vec{E} \qquad (3.7)$$

$$\mathcal{E}_{Electric\ Field\ 3}\ (E_3, P_3) = -E_3 P_3 - 0.5 \varepsilon_0 E_3^2$$

One expects that the out-of-plane polarization increases when the electric field increases so that the free energy decreases. The capacitor energy term is negligible compared to the polarization energy term for the electric fields used in our experiments (usually $E_3 < 3.0 \cdot 10^7$ Vm^{-1}).

Besides the material constants the Gibbs free energy equation requires a stress, temperature and electric field input, while the Helmholtz free energy equation requires extra constraints since the in-plane stress is no longer an input value, but rather a reaction of the material in order to minimize the free energy. The required constraint is the in-plane strain in the film due to the clamping to the substrate through misfit strain (Section 3.3).

3.2.3 Poly-domain Helmholtz free energy equation

The Helmholtz free energy equation used by Pertsev *et al.* for a single domain film is identical to equation 3.6. The differences between the models arise only in the poly-domain film state. In this section it will be assumed that the only situation requiring the poly-domain Helmholtz free energy formula is for tetragonal unit cells consisting of *c*- and *a*-domains. We will explain further on why this is.

Much work has been done by notably Pertsev and Kukhar into the formulation and use of the Helmholtz free energy in PZT films in order to model the film structure (e.g. crystal phase) and properties (e.g. dielectric

coefficient). Here, the assumptions made by Pertsev *et al.* for a poly-domain tetragonal crystal structure will be discussed in order to clarify the largest changes between the two models.

Tetragonal crystal structures with different domains, with an orthogonal polarization, have 90° domain walls (DWs) oriented at an angle of about 45° with the out-of-plane (001) axis. These DWs allow the different unit cells to fit next to each other without a discontinuity or defect in the crystal structure (Fig. 7.1). If the DW is between a *c*-domain ($P_3 \neq 0$) and an *a*-domain ($P_1 \neq 0$) it will require the strain in the (010) 2-direction (S_2) to be equal for the lattice to be continuous. Therefore, Kukhar *et al.* have set a constraint for their model, requiring S_2 of the *a*- and *c*-domains to be equal. This constraint makes it impossible to introduce a *b*-domain ($P_2 \neq 0$), since its S_2 value is different from that of the other domains due to its polarization (Fig. 3.4). This limits the model to having only two tetragonal domain types in the film, referred to as the *c/a/c/a*-phase, with all domain walls oriented in-plane, in the 2-direction.

The reason for a change in the model originates largely from three points.
- The large discontinuities in the dielectric constants and piezoelectric coefficients as a function of the misfit strain with the substrate predicted by Kukhar *et al.*, that are not observed in experimental work[9][10].

- The local mixing of domain walls in the 1- and 2-direction observed in AFM data indicating the local presence of *c/a*- and *c/b*- domain structures, see figure 3.1. The word local is used because the 4-fold symmetry structure in the AFM plots is generally smaller than the film thickness (1 µm). This indicates that the different domain structures should not be considered separately.

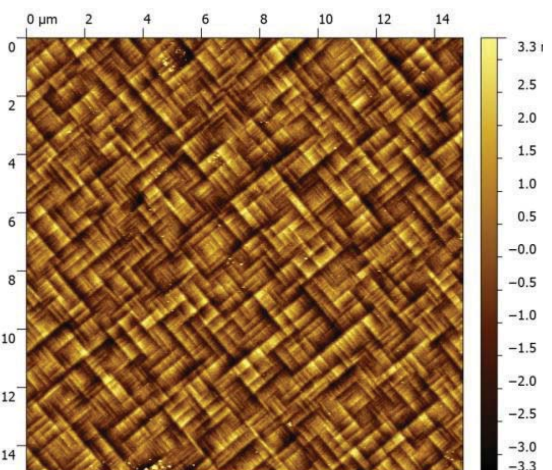

Figure 3.1: Surface information obtained using AFM. The 1µm film is PZT x=0.4 is grown on STO using PLD. The lines represent domain walls which are visible in AFM due to the tilting of the domains caused by domains walls in poly-domain tetragonal materials (see chapter 7). The <1µm 4-fold symmetry indicates a local influence between *c/b*- and *c/a*-domains.

- The presence of *c*-, *b*- and *a*-domains (*c/b/a*-phase), observed in XRD data (Fig. 3.2) and the lack of a strain difference in the short axis of the *c*-, *b*- and *a*- domains. Such a strain difference is for a *c/a/c/a*-phase with a misfit strain ranging between S_m=-0.005 and 0, see figure 3.3[9]. For a c/a/c/a domain structure the strain difference between the two short axes is predicted to be between 0.005 and 0.01. Our XRD experiments show (Fig. 3.4) shows the low strain difference between the short axis with a largest strain difference of at the most 0.0015 (table 3.1).

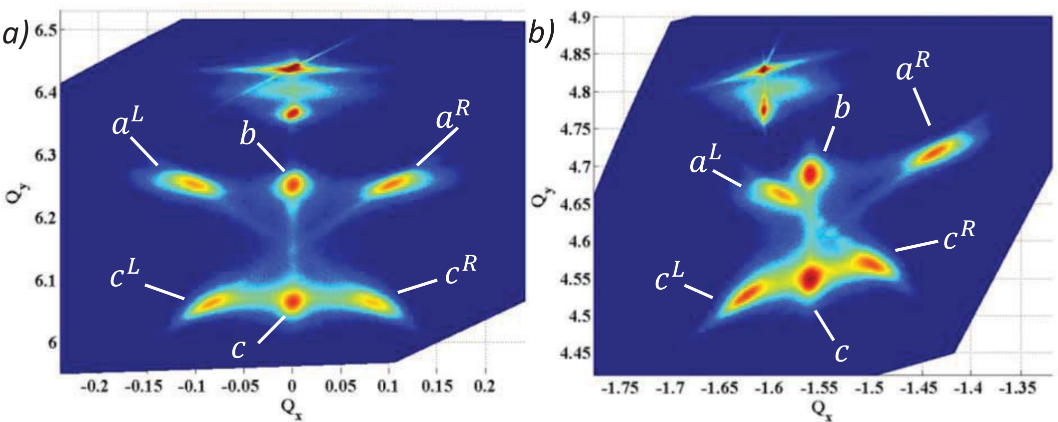

Figure 3.2: Reciprocal space maps obtained with XRD diffraction of a PZT x=0.4 film (tetragonal crystal structure). Showing (a) (004) and (b) (013) diffraction peaks both containing *c*-, *b*- and *a*- domains. The (004) and (013) peaks allow for the extraction of out-of-plane and in-plane lattice parameters, table 3.1, using equations 2.1-2.5. The peaks are labeled indicating the domain type and either a left (L) or right (R) tilt. The *b*- domain is tilted to the front and back, showing only one peak. The domain regions consist of either c/b- or c/a domains. The tilt of the *b*- or *a*- domain are connected with the oppositely tilted c-domain by a faint streak, indicating gradual tilt change in the connecting DW from for example the cL domain into a aR domain. Other than an in-plane rotation the *a*- and *b*- domains are identical.

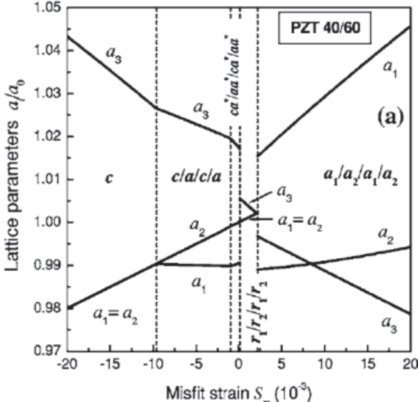

Figure 3.3: Unit cell lattice parameters calculated with the model of Kukhar *et al.* [9]. The strain difference between the short axis, a_1 and a_2, in the *c/a/c/a*-region is expected to be between 0.01 and 0.005 for the misfit strain range expected for PZT x=0.4 on STO as calculated via the thermal expansion coefficients.

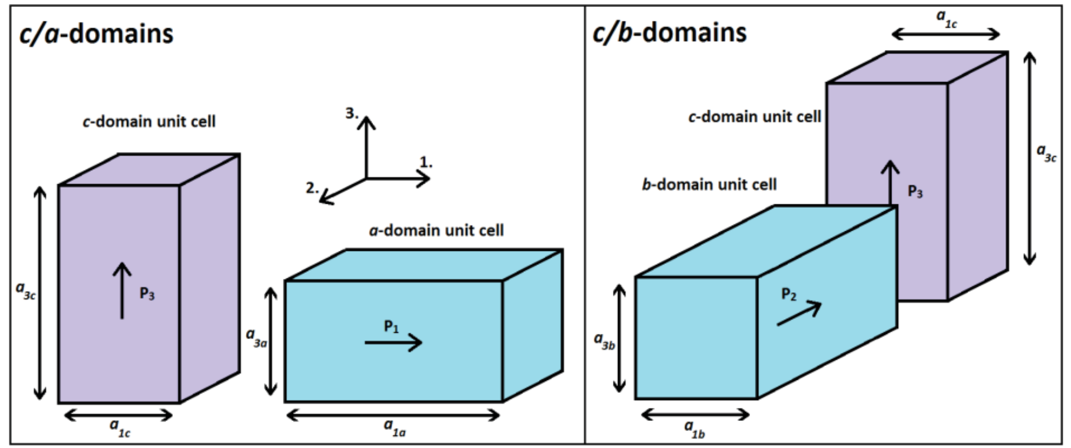

Figure 3.4: In-plane (100) and out-of-plane (001) lattice parameters obtained from figure 3.2. The tilt is not considered.

Table 3.1: The resulting lattice parameters for the c/b- and c/a- domain regions. Here the left tilted *a*- and right tilted *c*- domain are used.

c/a-region	*c/b*-region
a_{3c} =4.1460	a_{3c} =4.1445
$\boldsymbol{a_{1c}}$ **=4.0178**	$\boldsymbol{a_{1c}}$ **=4.0214**
$\boldsymbol{a_{3a}}$ **=4.0206**	$\boldsymbol{a_{3b}}$ **=4.0225**
a_{1a} =4.1472	$\boldsymbol{a_{1b}}$ **=4.0232**

To allow for all three domains to coexist the S_2 constraint introduced by Kukhar *et al.* was removed. Effectively all microscopic restrictions related to the connection between unit cells of different domains at the DWs are removed. With only macroscopic constraints our model effectively removes any interaction between the domains except through the domain fraction. The macroscopic boundary conditions used in this model are misfit strain (section 3.3) and stress and strain conditions due to the assumption of a rigid substrate and lack of stress on the surface of the film (section 3.4).

3.3 Misfit strain

3.3.1 The basic lattice parameter and the atomic and thermal misfit strain

The term misfit strain is used to describe the effect of a substrate on the film grown on top of it. There are two main types of misfit strain, referred to as epitaxial misfit strain (EMS) and thermal misfit strain (TMS). The first often applies to very thin films without misfit dislocations. The second applies to thick films, where in the bulk of the film all epitaxial misfit strain is relieved by dislocations in the initial growth phase of the layer arising at deposition temperature. Then the misfit strain arises from a temperature change. Note that thin films with an epitaxial misfit strain still experience thermal misfit strain as well.

To understand misfit strain one first needs to understand the concept of the basic lattice parameter, a_0. From here, it will be assumed that our crystal is grown in the (001) direction on a cubic substrate with a (001) orientation. The basic lattice parameter of a unit cell is the atomic lattice distance that a unit cell would have if there was no strain presented, meaning zero stress and zero polarization (Eq. 3.5). The actual lattice parameters arise from strain on the basic unit cell lattice parameter, $a_x = a_0(S_x + 1)$. Assuming an isotropic thermal expansion the basic lattice parameter changes with temperature through the average thermal expansion coefficient, α. Giving $a_0(T) = a_0(T_0)(1 + \alpha)$. The average of the thermal expansion is calculated over the temperature interval between T and T_0. Therefore, a change in the lattice parameter, for example due to an applied electric field, causes a strain, while a change in temperature corresponds to a change in the basic lattice parameter, which is not a strain. Note that at the deposition temperatures used in this work (T_d=600°C), PZT is para-electric, which, if unstressed at that temperature, has cubic atomic lattice parameters equal to the basic lattice parameter. However, if a unit cell becomes polarized the actual lattice parameters are no longer equal to the basic lattice parameter. Note that for a non-ferroelectric, cubic substrate (i.e. STO between RT and T_d) the actual lattice parameter is always equal to the basic lattice parameter.

Although one can use the model to calculate the strain of a unit cell this value cannot be translated into an actual lattice parameter without a_0. It is possible to estimate a_0 using the measured lattice parameters and assuming that the volume of a strained unit cell is equal to that of an unstrained cell giving: $a_0 = \sqrt[3]{V}$, with V, the volume of the unit cell determined from the measured lattice parameters. This is not ideal since it assumes incorrectly that polarization or stress does not change the unit cell volume. This will be discussed in section 5.3. However, the error made through this assumption is usually small and the method is straightforward, not requiring further knowledge about the stress and polarization state of the unit cell.

The epitaxial misfit strain describes a film that is grown epitaxially on a substrate, where during growth the in-plane lattice parameter of the film continues on the in-plane lattice parameter of the substrate. This type of misfit strain usually occurs when the in-plane lattice parameters of the two materials are very close to one another and when the film is very thin. If the temperature changes the in-plane lattice parameter of the film will, if the film can withstand the thermally induced stress, follow the in-plane lattice parameter of the substrate. The actual misfit is described by the difference between the basic lattice parameter of the film (a_0) and substrate (a_s) and does not have to be zero at growth temperature:

$$S_m^{Epitaxial} = \frac{a_s - a_0}{a_0} \tag{3.8}$$

The thermal misfit strain describes the strain in a film, which is grown relaxed (stress free), but becomes strained due to the difference in thermal expansion of the film and substrate after a temperature change. This type of misfit strain best describes thicker epitaxially grown films. For thicker films the material can still be epitaxial, but usually due to defects the material is only epitaxially strained initially and the main part of the film can best be described as relaxed, i.e. it has its unclamped bulk lattice parameter at deposition temperature. As the materials cool down, the substrate shrinks more or less than the film causing the film to be strained, see figure

3.5. Considering material A (substrate) and material B (Film) it is possible to calculate the misfit strain at room temperature by using:

$$S_{m\,(RT)}^{Thermal} = -\Delta T(<\alpha_A> - <\alpha_B>) \qquad (3.9)$$

Where ΔT is the change in temperature and $<\alpha_A>$ and $<\alpha_B>$ are the average thermal expansion coefficients over the temperature range. Note that the thermal expansion coefficients are defined with respect to the basic unit cell lattice parameters at deposition temperature. Assuming measurements are made at room and deposition temperature the misfit strain can be written as:

$$S_{m(RT)}^{Thermal} = \left(\frac{a_{0A}^{Dep} - a_{0A}^{RT}}{a_{0A}^{Dep}} - \frac{a_{0B}^{Dep} - a_{0B}^{RT}}{a_{0B}^{Dep}}\right) \qquad (3.8)$$

Note that the thermal misfit strain is zero at deposition temperature and that it depends on the deposition temperature. Changing the deposition temperature, therefore, changes the misfit strain at room temperature.

Films can be in-between or be subject to both types of misfit strain, but usually researchers work with materials and thicknesses that allow the film to be subject to either epitaxial misfit strain or a thermal misfit strain. In this work the PZT film is only considered to have a thermal misfit strain due to the fact that the film thicknesses used (>>100nm) result in most of the film to be stress free during growth (Fig. 3.2).

The substrate material used here is usually (001) STO, which has a cubic lattice. STO is para-electric in the range of temperatures (RT-600°C) used in this work. The PZT film is also para-electric and cubic at deposition temperatures but becomes tetragonal, for high Ti compositions, when cooled due the phase transition to the polarized state. The unit cells of PZT at room temperature are strained, due to self-strain caused by polarization. The tetragonal unit cell of the *c*-domain has both short axis (shorter than the basic lattice parameter) in-plane, thus the *c*-unit cell has an overall negative in-plane strain. The *a/b* domain region unit cell has a short and long axis in-plane thus negative self-strain in the short axis direction and positive self-strain in the long axis direction. A thermal misfit strain of zero

would force the film to have a certain number of *c*-domain and *a/b*-domain unit cells in the (010) and (100) direction in order to exactly cancel their individual in-plane strain effects. This is why the thermal misfit strain strongly influences the domain fraction (ϕ_c) (Fig. 3.5c). If the thermal misfit strain has a value equal to the negative in-plane strain of the *c*- domain it would result in a film made up of only *c*-domain unit cells. An even more negative misfit strain cannot be resolved by a change in domain fraction and the film will have to change the stress and polarization of the *c*-domains in order to make the in-plane strain of the *c*-domain more negative. Similarly for a large positive thermal misfit strain only *a*- and *b*-domains will be present that become tensile strained with increasing thermal misfit strain.

Thermal Misfit Strain

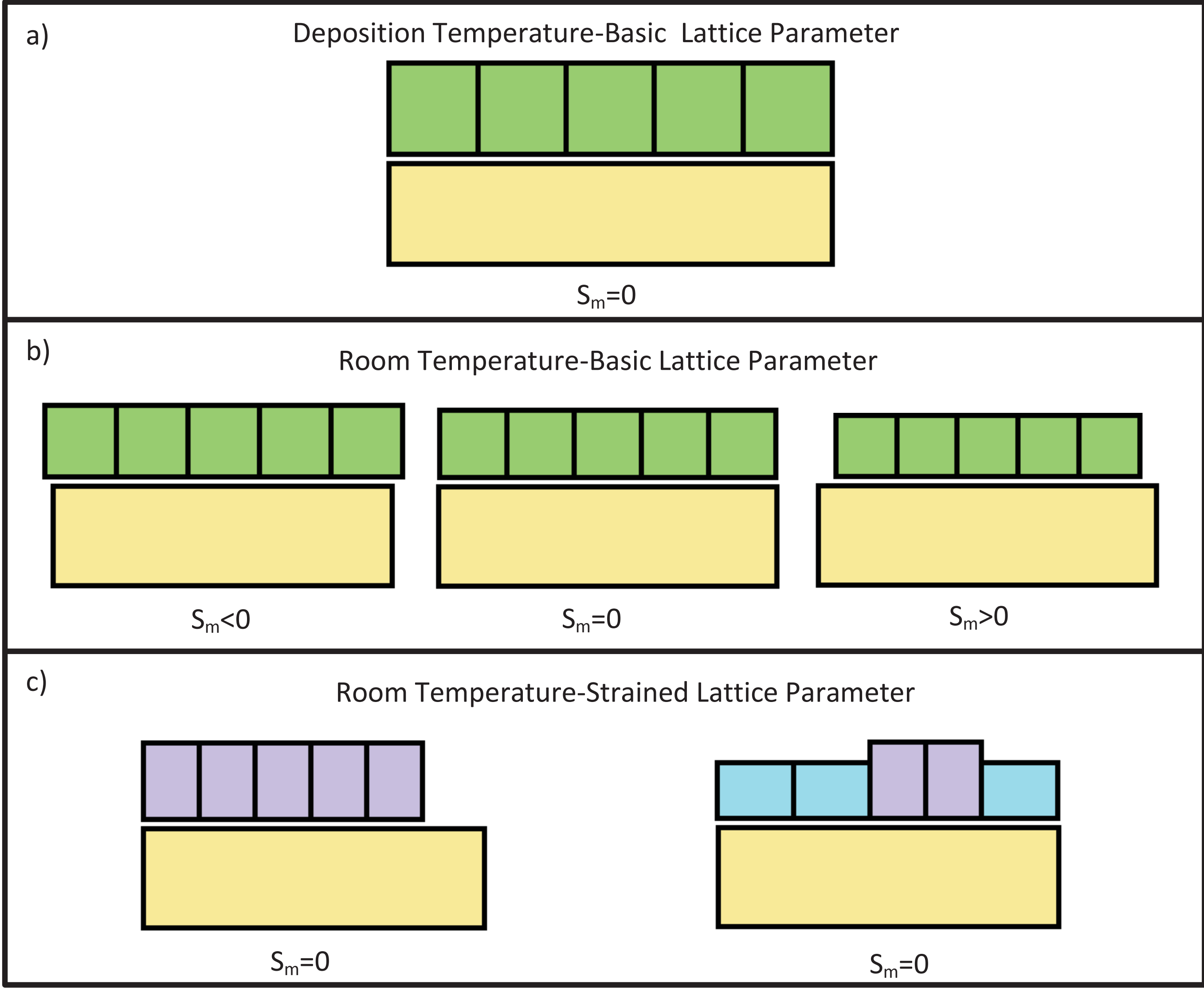

Figure 3.5. SChematic showing thermal misfit strain. a) The paraelectric cubic film (green) is grown relaxed (i.e. without any stress) on a paraelectric cubic substrate (yellow) at deposition temperature, resulting in no thermal misfit strain in the film. b) At lower temperatures a difference in thermal expansion coefficient results in the basic unit cells of the film either covering too much or too little area resulting in a negative or positive misfit strain with respect to the substrate, respectively. The film has to resolve this misfit. c) For tetragonal unit cells the misfit strain is still fully defined by the basic lattice parameter as in b. Here, as an example, we have assumed a misfit strain of zero. The tetragonal unit cells have to cover the substrate area and can, if the misfit strain larger is not too extreme, be achieved by creating a poly-domain film consisting of a certain fraction of a/b and c domains.

3.3.2 Misfit strain in the model

The misfit strain in our model is based on the thermal misfit strain. The meaning of this parameter is given by equation 3.8. The model predicts strains but without a value for the basic lattice parameter (a_0) these strains cannot be translated into actual lattice parameters. For the model the misfit strain is in short the average strain the film is required to have in order to cover a specific area of the substrate. The area that has to be covered is defined for a single domain (or in-plane symmetrical) film by:

$$(1+S_m)^2 = (1+S_1)(1+S_2) \tag{3.9}$$

For the poly-domain model each individual domain requires its own Helmholtz free energy function. For the *c/b/a*-phase the formula can be simplified through some available symmetries. Firstly the *a*- and *b*- domains are symmetrical in-plane, requiring that their domain fractions are equal. This allows us to write down the Helmholtz free energy formula for the film with the same energy function for the *b*- and *a*-domain. Therefore the *c/b/a*-phase requires only two energy functions, one proportional to ϕ_c and the other to $\phi_a = (1-\phi_c)$. Note that it is assumed that ϕ_a consist of equal parts of *a*- and *b*-domains. For a poly-domain tetragonal film the misfit strain is related to the strain in the *c*- and the *a*-domain as:

$$(1+S_m)^2 = \phi_c\big((1+S_{1c})(1+S_{2c})\big) + \big(1-\phi_c\big)\big((1+S_{1a})(1+S_{2a})\big) \tag{3.10}$$

It is expected that even at the extremes of the applicability of our model the strains are still fairly small (maximum strain ≈0.04). This allows equation 3.9, which is for a single domain film, to be simplified to:

$$2S_m = S_1 + S_2 \tag{3.11}$$

For a poly-domain tetragonal film equation 3.10 can also be simplified:

$$2S_m = \phi_c(S_{1c}+S_{2c}) + \big(1-\phi_c\big)(S_{1a}+S_{2c}) \tag{3.12}$$

Note that the in-plane strain relation implies that ϕ_c is independent of the out-of-plane stress on the unit cells. This can be seen by combining

equations 3.5, 3.14 and the fact that the average out-of-plane stress ($<\sigma_3>$) is zero. The poly-domain relation (Eq. 3.12) is used to define the domain fraction as:

$$\phi_c = \frac{(\,2S_m - (S_{1a} + S_{2a})\,)}{(S_{1a} + S_{2c}) - (S_{1a} + S_{2a})} \qquad (3.13)$$

In the poly-domain Helmholtz free energy formula equation 3.13 is used to replace ϕ_c in order to introduce the misfit strain dependence in the free energy formulation.

3.4 Simplification of the poly-domain Helmholtz free energy

The poly-domain Helmholtz free energy formula requires the minimization with respect to 19 variables, even after combining variables of the *a*- and *b*-domains. The formula is minimized to a local minimum, which is required for electric field switching, forcing us to minimize from multiple starting values in order to find the energy of other locally stable crystal phases for comparison requiring multiple minimizations per data point. This large number of variables makes further simplifications of the energy function useful to obtain numerical and analytical results. The basic formula will however still be important for the introduction of extra constraints such as the introduction of domain interactions and depolarizing fields, which are explored in chapter 5.

First, the boundary conditions are introduced for dense fully strained epitaxial films. Since the film is not limited in the out-of-plane direction the average out-of-plane stress is zero ($<\sigma_3>=0$). Similarly, since the top of the film is free to move, the related average in-plane shear stresses are zero ($<\sigma_4>=0, <\sigma_5>=0$).

The out-of-plane stress is zero for a single domain film since the material is always free to move in that direction. For a poly-domain film the domains can compensate out-of-plane stress requiring only the average stress to be zero. This allows us to express $\sigma_{3\mathrm{a}}$ in $\sigma_{3\mathrm{c}}$ through:

$$\phi_c \sigma_{3\mathrm{c}} = -(1-\phi_c)\sigma_{3\mathrm{a}} \tag{3.14}$$

If we write out equation 3.12 into polarization and stress terms and express $\sigma_{3\mathrm{a}}$ in terms of $\sigma_{3\mathrm{c}}$ it appears that ϕ_c is independent of $\sigma_{3\mathrm{c}}$. This can be used to show that the in-plane stresses in the Helmholtz free energy terms of the *c*-domain and *a*-domain are related in the same way to the out-of-plane stress and minimization shows that the energy is minimized for $\sigma_{1\mathrm{c}} = \sigma_{2\mathrm{c}}$ and $\sigma_{1\mathrm{a}} = \sigma_{2\mathrm{a}}$.

We have not been able to prove analytically that all in-plane stresses are equal but all simulations have shown that this is always the case. Therefore it will be assumed that $\sigma_{1\mathrm{c}} = \sigma_{2\mathrm{c}} = \sigma_{1\mathrm{c}} = \sigma_{2\mathrm{c}} = \sigma_{12}$. Rewriting the poly-domain Helmholtz free energy formula with σ_{12} shows that energy minimization is only obtained for $\sigma_{3\mathrm{c}} = 0$ and thus $\sigma_{3\mathrm{a}} = 0$.

From the simulation it is also found that the *c*-domains never obtains an in plane polarization ($P_{1c} = P_{2c} = 0$) component nor that the *a*-domains obtain a (010) polarization component ($P_{2a} = 0$). The *a*-domain does develop an out-of-plane polarization component ($P_{3a} \geq 0$) when a nonzero electric field is introduced. Such an *a*-domain with a tilted polarization vector is referred to as an *ac**-domain. Minimization of the shear stresses makes them zero since s_{44} in the Helmholtz free energy formula is positive giving $\sigma_4 = \sigma_5 = \sigma_6 = 0$. The simplifications show that when one allows for unequal (010) directed strains (S_2) in the *a*- and *c*-domain and no other interactions between the domains than through the domain fraction this results in two separate domains with equal in-plane stresses.

Using the equation for the domain fraction (Eq. 3.13) it is possible to obtain the full Helmholtz free energy density equation for a clamped crystalline film (section 3.4.1). For the numerical simulations this equation is not reduced using the simplifications found in section 3.4. This allows one to add additional energy terms. We will see that these additional energy terms may result in non-zero out of plane stresses in the *c*- or *a*- domains, as well as in non-homogeneous in-plane stresses. This equation is used in section 5.5, where additional energy terms are used to improve the model predictions, which point towards the presence of additional constraints for the clamped films.

3.4.1 Full poly-domain Helmholtz free energy equation

The total energy of a strained poly-domain film, with only $<\sigma_3>=0$, $<\sigma_4>=0, <\sigma_5>=0, <\sigma_6>=0$ as boundary conditions, is:

$$\begin{aligned}
&F_{Total\ Basic} = \\
&\phi_c[\alpha_1(P_{1c}^2+P_{2c}^2+P_{3c}^2)+\alpha_{11}(P_{1c}^4+P_{2c}^4+P_{3c}^4)+\alpha_{111}(P_{1c}^6+P_{2c}^6+P_{3c}^6) \\
&+\alpha_{12}(P_{1c}^2P_{2c}^2+P_{3c}^2P_{2c}^2+P_{1c}^2P_{3c}^2)+\alpha_{123}(P_{1c}^2P_{2c}^2P_{3c}^2) \\
&+\alpha_{112}\left(P_{1c}^4(P_{2c}^2+P_{3c}^2)+P_{2c}^4(P_{1c}^2+P_{3c}^2)+P_{3c}^4(P_{2c}^2+P_{1c}^2)\right) \\
&+0.5s_{11}(\sigma_{1c}^2+\sigma_{2c}^2+\sigma_{3c}^2)+s_{12}(\sigma_{1c}\sigma_{2c}+\sigma_{1c}\sigma_{3c}+\sigma_{2c}\sigma_{3c}) \\
&-E_3P_{3c}\ ] \\
&(1-\phi_c) \\
&[\alpha_1(P_{1a}^2+P_{2a}^2+P_{3a}^2)+\alpha_{11}(P_{1a}^4+P_{2a}^4+P_{3a}^4)+\alpha_{111}(P_{1a}^6+P_{2a}^6+P_{3a}^6) \\
&+\alpha_{12}(P_{1a}^2P_{2a}^2+P_{3a}^2P_{2a}^2+P_{1a}^2P_{3a}^2)+\alpha_{123}(P_{1a}^2P_{2a}^2P_{3a}^2) \\
&+\alpha_{112}\left(P_{1a}^4(P_{2a}^2+P_{3a}^2)+P_{2a}^4(P_{1a}^2+P_{3a}^2)+P_{3a}^4(P_{2a}^2+P_{1a}^2)\right) \\
&+0.5s_{11}(\sigma_{1a}^2+\sigma_{2a}^2+\sigma_{3a}^2)+s_{12}(\sigma_{1a}\sigma_{2a}+\sigma_{1a}\sigma_{3a}+\sigma_{2a}\sigma_{3a}) \\
&-E_3P_{3a}] \\
&-0.5\varepsilon_0E_3^2 \qquad (3.15)
\end{aligned}$$

The misfit strain is introduced through ϕ_c and σ_{3a}, defined by equations 3.13 and 3.14, respectively. The strains are defined by equations 4.18-4.23. The variables for which the formula has to be minimized is $P_{1c}, P_{2c}, P_{3c}, P_{1a}, P_{2a}, P_{3a}, \sigma_{1c}, \sigma_{2c}, \sigma_{1a},\ \sigma_{2a}$ and σ_{3c}. Eq. 3.15 is used to introduce extra constraints arising from, for example, domain interactions and interactions between film and substrate.

3.4.2 Poly-domain Helmholtz free energy equation

The basic poly-domain Helmholtz free energy formula (3.15) can be simplified though the use of the analytically and numerically found simplifications mentioned in section 3.4. The simplified equations allow for shorter calculation times and both simplifications are used in chapter 4 to derive analytical solutions for PZT film properties. Using these simplifications the free energy equation for tetragonal poly-domain PZT film (containing *c*- and *ac**- domains) can be written as:

$$
\begin{aligned}
&F_{Total\ ac^*} = \\
&\phi_c[\alpha_1(P_{3c}^2) + \alpha_{11}(P_{3c}^4) + \alpha_{111}(P_{3c}^6) \\
&+s_{11}(\ \sigma_{12}^2) + s_{12}(\sigma_{12}^2) - E_3 P_{3c}] \\
&\left(1-\phi_c\right)[\alpha_1(P_{1a}^2 + P_{3a}^2) + \alpha_{11}(P_{1a}^4 + P_{3a}^4) + \alpha_{111}(P_{1a}^6 + P_{3a}^6) \\
&+\alpha_{12}(P_{1a}^2 P_{3a}^2) +\ \alpha_{112}\left(P_{1a}^4(P_{3a}^2) + P_{3a}^4(P_{1a}^2)\right) \\
&+s_{11}(\ \sigma_{12}^2) + s_{12}(\sigma_{12}^2) - E_3 P_{3a}] \\
&-0.5\varepsilon_0 E_3^2 \qquad\qquad (3.16)
\end{aligned}
$$

Here ϕ_c is defined similar as for the basic formula, but now with equal in-plane stresses. This formula requires the minimization of only four variables, P_{3c}, P_{1a}, P_{3a} and σ_{12}.

3.4.3 Single domain Helmholtz free energy equation

Next to the poly-domain solution one can also derive the equation for a single domain with an arbitrary polarization direction:

$$
\begin{aligned}
&F_{Total\ Single\ Domain} = \\
&+\alpha_1(P_1^2+P_2^2+P_3^2)+\alpha_{11}(P_1^4+P_2^4+P_3^4)+\alpha_{111}(P_1^6+P_2^6+P_3^6) \\
&+\alpha_{12}(P_1^2P_2^2+P_3^2P_2^2+P_1^2P_3^2)+\alpha_{123}(P_1^2P_2^2P_3^2) \\
&+\alpha_{112}\left(P_1^4(P_2^2+P_3^2)+P_2^4(P_1^2+P_3^2)+P_3^4(P_2^2+P_1^2)\right) \\
&+s_{11}(\sigma_1^2)+s_{12}(\sigma_1^2)-E_3P_3-0.5\varepsilon_0E_3^2 \qquad (3.17)
\end{aligned}
$$

Note that the assumption that the formula is for a single domain does not mean that the material is in a one-domain state. The formula also describes cases of multiple symmetrical domains with the same energy density formula. For example, the *a/b*-phase has *a*- and *b*-domains but can be described with the single domain formula due to the fact that both domains have the same free energy formula. Similarly rhombohedral unit cells can have four different in-plane polarization components with the same P_3 component and for symmetry reasons with the same domain fraction and can therefore also be described by equation 3.17. In the single domain formula ϕ_c is no longer a variable.

The misfit strain is defined in terms of σ_{12} through equations 3.5 and 3.11 as:

$$
\sigma_{12}=\frac{S_m-0.5Q_{11}(P_1^2+P_2^2)-0.5Q_{12}(P_1^2+P_2^2+2P_3^2)}{(s_{11}+s_{12})} \qquad (3.18)
$$

Substituting σ_{12} in $F_{Total\ Single\ Domain}$ results in an energy equation for which the variables P_1, P_2 and P_3 have to be minimized. The single domain energy formulas for the *a/b*-domain structures (*a*-domain) ($P_1 \neq 0, P_3 \ll P_1, P_2 = 0$), single domain rhombohedral ($P_1 = P_2\ P_3 \neq 0$) and single tetragonal *c*-domain ($P_1 = P_2 = 0,\ P_3 \neq 0$) can be simplified further when these conditions on the polarization are substituted into equation 3.17. These simplifications essentially force the model to adopt a certain crystal phase and are used to compare the energy difference between the

different phases. A zero (or small) energy difference may imply that a crystal can show multiple phases simultaneously. This analysis is performed in chapter 6.

3.5 Conclusion:

In this chapter it has been shown that a previous model made for clamped PZT films by Kukhar and Pertsev *et al.*[7-9][11], based on the work done by Haun *et al.*[1-6] on PZT solid solutions, does not accurately predict experimental results for the tetragonal poly-domain phase. A 4-fold symmetry observed using AFM on tetragonal PZT films grown on STO, indicates a local *c/b/a*-phase that was not predicted by the previous *c*/*a*-phase model. In addition, XRD experiments on the same films show that there is no large difference between the in-plane strains (S_{2c} and S_{1c}) in the *c*-domain unit cells as is also predicted.

It has been possible to derive new Helmholtz free energy equations for clamped films using new boundary conditions. The main change to the model, proposed in this chapter, is the removal of any restrictions that limit or influence the interaction between different domains. In addition the model allows for any polarization orientation of the unit cell. The resulting thermodynamic Helmholtz free energy equations allows one to model a clamped, dense, epitaxial, single and poly-domain PZT film under an electric field, orthogonal to the films plane, at a given temperature (chapter 4). The basic equation (Eq. 3.15) allows the introduction of addition energy terms (chapter 5), while equations 3.16 and 3.17 allow for faster calculations but require the validity of additional simplifications used in deriving them. Note that so far all Helmholtz free energy equations given in this chapter do not include interactions between the domains via domain walls or domain tilting and do not restrict the film in any way other than through the global film-substrate thermal misfit strain.

References

[1] M. J. Haun, Z. Q. Zhuang, E. Furman, S. J. Jang and L. E. Cross, "*Electrostrictive Properties of the lead zirconate titanate solid-solution system"*, Journal of the American Ceramic Society, Volume 72,7-1140, (1989).

[2] M. J. Haun, E. Furman, S. J. Jang, L. E. Cross, "*Thermodynamic theory of the lead zirconate-titanate solid solution system, part I: Phenomenology"*, Ferroelectrics,99:1,13-25. (1989).

[3] M. J. Haun, E. Furman, H. A. McKinstry, L. E. Cross, "*Thermodynamic theory of the lead zirconate-titanate solid solution system, part II: Tricritical behavior" ,* Ferroelectrics,99:1,27-44. (1989).

[4] M. J. Haun et al., "*Thermodynamic theory of the lead zirconate-titanate solid solution system, part III: Curie constant and sixth-order polarization dielectric stiffness coefficients",* Ferroelectrics,99:1,45-54. (1989).

[5] M. J. Haun, E. Furman, T. R. Halemane and L. E. Cross, "*Thermodynamic theory of the lead zirconate-titanate solid solution system, part IV: Tilting of the oxygen octahedral",* Ferroelectrics,99:1,55-62. (1989).

[6] M. J. Haun, E. Furman, E. Jang and L. E. Cross, "*Thermodynamic theory of the lead zirconate-titanate solid solution system, part V: Theoretical calculations",* Ferroelectrics,99:1,63-86. (1989).

[7] V. G. Koukhar, N. A. Pertsev and R. Waser, "*Thermodynamic theory of epitaxial ferroelectric thin films with dense domain structures"*, Physical Review, Volume 64, 214103,(2001).

[8] N. A. Pertsev, V.G. Kukhar, H. Kohlstedt and R. Waser, "*Phase diagrams and physical properties of single-domain epitaxial* $Pb(Zr_{1-x}Ti_x)O_3$ *thin films"*, Physical Review B 67, 054107 (2003).

[9] V. G. Kukhar, N. A. Pertsev, H. Kohlstedt and R. Waser, "*Polarization states of polydomain epitaxial* $Pb(Zr_{1-x}Ti_x)O_3$ *thin films and their dielectric properties"*, Physical Review B 73, 214103 (2006).

[10] R. Steenwelle, "*Strain and Composition Effects in Epitaxial PZT Thin Films*", Thesis University of Twente, (2012), ISBN 978-94-6191-293-0.

[11] N. A. Pertsev, A. G. Zembilgotov and A. K. Tagantsev, "*Effect of mechanical boundary conditions on phase diagrams of epitaxial ferroelectric thin films*", Phys.Rev.Lett.80,1988 (1998).

4.Functional properties of poly-domain ferroelectric oxide films.

Abstract:

A numerical and analytical approach are used to investigate the structure and properties of a clamped (001) oriented $PbZr_xTi_{(1-x)}O_3$ (PZT) film near the morphotropic phase boundary MPB (PZT x=0.4, 0.5 and 0.6). The emphasis is on the poly-domain, tetragonal crystal structure with three basic domains, which is a possible improvement on the two-domain structure studied in literature. The analytical solution is used to derive formulas that allow for predictions about the parameters influencing the material properties, such as piezoelectric and dielectric coefficients. Additionally the numerical solutions to the Helmholtz free energy equations are calculated using Matlab in order to predict the structural phase as well as the material properties for the clamped PZT film. Here, external parameters, such as misfit strain, temperature and electric field are varied to reveal their effect on the materials piezoelectric properties.

4.1 Introduction

Perovskites, such as PZT, have been investigated for a long time due to their broad range of physical characteristics[1-3]. In these investigations many material aspects of bulk PZT, especially around the morphotropic phase boundary (MPB), such as the crystals phase, lattice parameters, polarization, piezoelectric coefficients, dielectric coefficients, material stability and poling effects were examined for a wide range of compositions, temperature and electric fields strengths. These were used to obtain values for the material constants[4-9]. The most important material parameters for the present work are the elastic compliances, dielectric stiffness parameters, electrostrictive coefficients, the Curie-Weiss temperature and the Curie-Weiss constant. These material constants are given in the appendix, tables A.3 and A.4, and are used to calculate the energy landscape of the material via the Helmholtz and Gibbs free energy equations developed in chapter 3.

The Helmholtz free energy equations are generally not trivial to solve and usually require a numerical approach to calculate the variables (e.g. polarization and stress components). The result is the overall free energy minimum that corresponds to the most domain structure. These numerical solutions provide a case-by-case results and help to better understand materials properties for a specific situation. In order to get a better understanding of which parameters influence what material property, it is an advantage to solve the equations analytically and derive more simplified equations for estimating material properties.

In this chapter a simplification to the model is suggested in order to allow for an analytical solution to the model. This solution will be used to derive equations for the main material properties such as the piezo electric coefficient. The simplification will be compared to the numerical solution in order to identify the range of conditions under which the analytical solution holds. In addition the Helmholtz free energy equations are solved numerically, which is required to predict the crystal phase structure and allow for various other predictions of material properties.

4.1.1 Unclamped bulk PZT

In this paragraph material properties will be derived for unclamped bulk PZT, described by the Gibbs free energy equation (Eq. 4.1). The simplest energy landscape, using the least variables, is when the material is considered as a stress free, bulk single crystal PZT with an applied electric field in the (001) direction. This material with a tetragonal crystal structure can be modeled using the Gibbs free energy equation (Eq. 3.2) with all stress terms equal to zero (i.e. $\sigma_i = 0$), but including the electric field (Eq. 3.7) energy terms:

$$
\begin{aligned}
&G(\sigma, T) = \\
&+\alpha_1(P_1^2 + P_2^2 + P_3^2) + \alpha_{11}(P_1^4 + P_2^4 + P_3^4) + \alpha_{111}(P_1^6 + P_2^6 + P_3^6) \\
&+\alpha_{12}(P_1^2 P_2^2 + P_3^2 P_2^2 + P_1^2 P_3^2) + \alpha_{123}(P_1^2 P_2^2 P_3^2) \\
&+ \alpha_{112}\left(P_1^4(P_2^2 + P_3^2) + P_2^4(P_1^2 + P_3^2) + P_3^4(P_2^2 + P_1^2)\right) \\
&-E_3 P_3 - 0.5\varepsilon_0 E_3^2
\end{aligned}
\tag{4.1}
$$

If PZT (x=0.4) at 25°C is used as an example we find that the global minimum for $E_3 \neq 0$ is found if $P_1 = P_2 = 0$ and $P_3 \neq 0$, indicating that the lowest energy is found when the material has a tetragonal crystal structure. Assuming $P_1 = P_2 = 0$ one finds the well-known ferroelectric double well potential energy landscape for PZT (x=0.4) at 25°C for different electric field strengths (figure 4.1a). The analytical solution for the lowest energy point can be found from the derivative:

$$
\frac{dG(\sigma, T)}{dP_3} = 0 = 2\alpha_1 P_3 + 4\alpha_{11} P_3^3 + 6\alpha_{111} P_3^5 - E_3 \tag{4.2}
$$

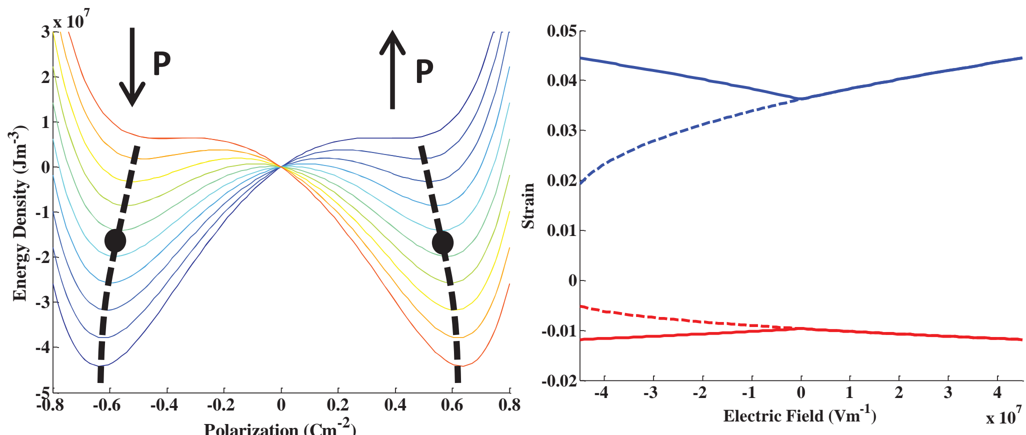

Figure 4.3. (a) Ferroelectric out of plane polarization double well potential for an out of plane electric field ranging between -4.5·10^7 Vm^{-1} (blue) and 4.5·10^7 Vm^{-1} (red). The dashed line shows the stable local minimum values for the polarization. The dot shows the stable local polarization for zero field. (b) Strain of the long (blue) and short (red) axis with a coercive field at zero (solid) and no coercive field (dashed). Both (a) and (b) are at temperature *T*=25°C.

The resulting zero field (E_3=0) polarization is found to be $P_3 = 0.57\mathrm{Cm}^{-2}$ for PZT x=0.4 at *T*=25°C (Fig. 4.3a). Using equation 4.2 the strain of the tetragonal crystal can be found using equations 3.5. Here $S_3^{Model} = Q_{11}P_3^2 = +0.027$ and $S_1^{Model} = S_2^{Model} = Q_{12}P_3^2 = -0.010$ resulting in a tetragonal long and short axis strain difference of $S_{diff}^{Model} = S_3 - S_1 = 0.037$ (Fig. 4.1b). As a comparison our XRD data on PZT (x=0.4) powder gives a value of $a_{long}^{powder} = a_0^{powder}(1 + S_3^{powder})$ =4.150Å and $a_{short}^{powder} = a_0^{powder}(1 + S_1^{powder})$=4.005Å, resulting in a strain difference very similar to the theoretical one, $S_{diff}^{powder} = S_3^{powder} - S_1^{powder}$=0.036. For more information on the basic unit cell lattice parameter (a_0) see section 3.3.1 and 5.3.

For electric field strength values less than about E_3=4.5·10^{7}Vm^{-1} there are two minima. For the global minimum the polarization direction is always aligned with the electric field (this corresponds to the case that the coercive field is zero, E_c=0 Vm^{-1}). The resulting electric field versus strain graph is symmetrical for positive and negative fields (Fig. 4.1b, solid line). If the local minimum is used the polarization does not switch (i.e. E_c>4.5·10^{7}Vm^{-1}). The

polarization direction is static and can be opposite to the electric field. If the polarization is assumed to be positive the resulting electric field versus strain graph is asymmetrical (Fig. 4.1b, dotted line). For E_3>4.5x10^7 Vm^{-1} the local and global minimum are the same and only one solution for the polarization exists (figure 4.2). Although the coercive field should be E_c=4.5·10^7 Vm^{-1} in theory, the value is usually much lower in practice E_c<5·10^6 Vm^{-1} due to crystal imperfections, thermal fluctuations and rotations in the polarization direction. Throughout this chapter, equations are derived that approximate the material properties, which allow for polarization switching. However, the values of these properties (usually at E_3=0 Vm^{-1}) shown in this chapter assume that there is no polarization switch. In chapter 5 the model is used to simulate experimental results where a coercive field is introduced and the effect of the polarization switch is studied.

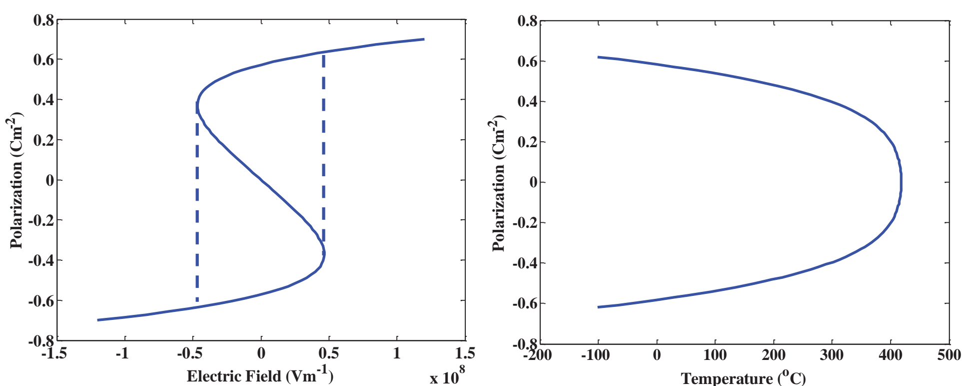

Figure 4.3. P-E loop (a) and P-T plot (b) obtained from equation 4.2 for bulk PZT x=0.4 at T=25°C and E_3=0 Vm^{-1}, respectively. In (a) the dotted line shows the electric fields at which the polarization switch takes place. Between these fields there are three solutions to equation 4.2. The polarization solutions ranging between about -0.4 Cm^{-1} and 0.4Cm^{-1} are saddle points (Fig. 4.3a) and are therefore unstable. In (b) the polarization solution at a given temperature shows that the PZT x=0.4 becomes para-electric at 418.4^{o}C.

Temperature has a large influence on the crystal phase of PZT. At temperatures around 400°C (using $\alpha_1 = (T - \theta)/2\varepsilon_0 C$) it is found that all compositions used in this thesis (0.30 ≤ x ≤ 0.60) have a ferroelectric-para-electric phase transition at the Curie temperature (θ) (which for these compositions is equal to the transition temperature[6]) and become para-electric and the polarization is zero $P = 0$ for $T > \theta$ (Fig. 4.2b), unless the applied electric field exceeds $\alpha_1 P$. Below the Curie temperature equation 4.1 allows for different, stable crystal phases depending on the PZT composition[10].

4.1.2 External parameters of clamped PZT films

To derive the material and structural properties of clamped PZT films the Helmholtz free energy equations must be solved. For this one first requires the external parameters. In this section the external parameters, misfit strain, temperature and electric field, are introduced.

The properties of bulk, unstrained PZT have been studied extensively[11-14]. Piezoelectric materials are however primarily used to either stress or strain another material. This imposes constraints on the deformation of the PZT. The effect of the substrate strain on the film properties is introduced through the misfit strain between film and substrate. In order to achieve a good overview of the changes in the domain structure with changing misfit strain, the misfit strain (see section 3.3) is chosen to be between -0.02 and +0.02 at room temperature. The experimentally accessible misfit strain range (in thermally strained films) by using different substrates, assuming T_d=600°C and measuring around room temperature, is much smaller. The range is defined by the thermal expansion coefficient of the substrate and that of PZT (equation 3.9). Assuming PZT has a thermal expansion coefficient ranging between $\alpha_f \approx 3 - 13 \cdot 10^{-6} K^{-1}$ and the substrate a range $\alpha_s \approx 0 - 11 \cdot 10^{-6} K^{-1}$ (0 for zero thermal expansion glass substrates using nano-sheet bufferlayers[15], about $2.4 \cdot 10^{-6} K^{-1}$ for Si up to $11 \cdot 10^{-6} K^{-1}$ for STO). For $T_d = 600$ °C, one obtains a fairly narrow accessible strain range, $S_m = -0.0046$ to $+0.0075$ (see section 5.4) at room temperature (RT).

One might slightly extend the range at the compressive side by using metal substrates, provided suitable buffer layers can be found. For larger (absolute) strain values one in practice has to resort to bending of substrates.

The temperature of the PZT film will also influence the material structure and properties. At deposition temperature, above the Curie Temperature, the bulk of the PZT film (>>20nm thick) is unstrained and therefore behaves as bulk PZT and is para-electric. When the film is cooled down, it becomes constrained by the substrate causing the substrate and the film to exert a stress on each other. Assuming the substrate does not deform, the film will be under stress due to the misfit strain. Thus, the misfit strain in a particular PZT film is highly dependent on the temperature. Similar to the unclamped bulk PZT, when the clamped PZT films cools down through the Curie temperature the phase of the material will change from the para-electric phase to another crystal phase. This crystal phase depends on the PZT composition but also on the misfit strain. The temperature range used for the model in this chapter is between room temperature (25°C) and deposition temperature (600°C).

The electric field also has an effect on the material structure. An electric field is applied on the film using a capacitor structure with a bottom and a top electrode. A film lacking electrodes will have a depolarizing field, which has a large effect on the film’s polarization and domain structure[16]. In this work we only consider the capacitor setup with shorted electrodes thus largely screening the depolarizing field of the film. When an electric field is introduced, the polarization in all domains changes. A single *c*-domain tetragonal film (section 4.1.3) will increase its out of plane polarization. For a film with only *a*- and *b*-domain the polarization will tilt out of the film plane giving rise to *ac**- and *bc**- domains resulting in the so-called *bc**/*ac**-phase.

4.1.3 Crystal phases in clamped PZT films

The phase and change in phase of a PZT crystal can have a large influence on the properties of the PZT film. Table 4.1 gives all phases that can be found in PZT assuming $P \geq 0$. It is possible that a material in the *c*-phase has multiple domains, one set with the polarization out-of-plane and the other with the polarization in the reverse direction. However, in this work we assume that the polarization is either up or down and the *c*-phase is consequently always in the single domain phase. Different domains can still have different out-of-plane polarization signs as is expected for the *c/b/a*-phase below the coercive field. To more realistically model experimental data by not having all *c*-domains switch at the same field strength one could include separate energy equations for parts of the material with different coercive fields. Note also that the monoclinic phase found by Noheda *et al*[18] is missing. This is because the monoclinic phase cannot be simulated using our approach of the energy function with terms up to the sixth order. The monoclinic phase requires extra polynomial terms.

Table 4.1: The table shows the definition of the different phases used in this work. The polarization vectors and domain information are given for each phase separately. In the *c/bc*/ac** and *ac*/bc**-phases the *a*-domains with an opposite polarization are no longer 180° rotations and can be distinguished through *ac**-, *bc**-, $\overline{ac}$*-, and $\overline{bc}$*-domains. The energy equations of these domains are all still equivalent. A visualization of the unit cells of the different domains is given below.

Phase	c	$c/b/a$	c/bc^{*} $/ac^{*}$	a/b	ac^{*}/bc^{*}	r	p
				Polarization vectors			
'c'-type	$(0,0,P_c)$	$(0,0,P_c)$	$(0,0,P_c)$				
'a'-type		$(P_a,0,0)$	$(P_a,0,P^{*})$	$(P_a,0,0)$	$(P_a,0,P^{*})$		$(0,0,0)$
'b'-type		$(0,P_a,0)$	$(0,P_a,P^{*})$	$(0,P_a,0)$	$(0,P_a,P^{*})$		
'r'-type						(P_1,P_1,P_3)	
Domain fraction	$\phi_c =$ 1	$\phi_a =$ $\phi_b =$ $\frac{1-\phi_c}{2}$	$\phi_{ac*} =$ $\phi_{\overline{ac*}} =$ $\phi_{bc*} =$ $\phi_{\overline{bc*}} =$ $\frac{1-\phi_c}{4}$	$\phi_a =$ $\phi_b =$ $1/2$	$\phi_{ac*} =$ $\phi_{\overline{ac*}} =$ $\phi_{bc*} =$ $\phi_{\overline{bc*}} =$ $1/4$	$\phi_{r_i}=$ $1/4$	$\phi_p =$ 1
Number of Polarization orienta-tions	1	5	5	4	4	4	0
Number of energy functions in the model	1	2	2	1	1	1	1

Phase	c	$c/b/a$	c/bc^{*} $/ac^{*}$	a/b	ac^{*}/bc^{*}	r	p
Number of domains	1	3	5	2	4	4	1
Visualiza-tion of the domains							

4.2 Analytical approach of a clamped tetragonal poly-domain PZT film

To allow for an analytical approach some simplifications are proposed, which are supported by the full numerical model. The numerical analysis discussed in chapter 3, shows that the in-plane stresses are equal $\sigma_{1a} = \sigma_{1c} = \sigma_{2a} = \sigma_{2c} = \sigma_{12}$, and all out-of-plane stresses and shear stresses are zero $\sigma_3^c = \sigma_3^a = \sigma_4^c = \sigma_4^a = \sigma_5^c = \sigma_5^a = \sigma_6^c = \sigma_6^a = 0$. Note that in reality a homogeneous stress might not necessarily apply. Local stresses may arise from the domain structure, giving rise to stress fields in the film. The properties of the film cannot be found analytically unless extra simplifications are made. Here, the "strict polarization condition", where the main polarization vectors are equal $P_3^c = P_1^a = P$ while all other polarization components are zero $P_1^c = P_3^a = P_2^c = P_2^a = 0$ is used to allow an analytical solution. This approach is however only an exact solution for the zero-field situation and deviations in the analytical solution will be compared to the numerical solution in section 4.3. In the numerical results it will be found that the P_3^c and P_1^a are not always equal and that P_3^a is non-

zero when an electric field is applied. In short the analytical assumption is that we are dealing with a *c/b/a* -phase where the main polarization vectors are equal instead of a true *c/bc*/ac**-phase where all polarizations components can and usually do have different values.

4.2.1 Domain fraction (Analytical approach)

In this work the domain fraction, unless indicated otherwise, is synonymous to the *c*-domain fraction (ϕ_c) and indicates the relative proportion of domains in the film. The domain fraction is an important parameter, since different domain types are expected to have different physical properties. Inserting the strain terms (Eq. 3.5) into the domain fraction terms (Eq. 3.12) we obtain the basic domain fraction function requiring polarization, stress and misfit strain terms:

$$\phi_c = \frac{2(s_{11}+s_{12})\sigma_{12}+2s_{12}\sigma_{3a}+(Q_{11}+Q_{12})P_{1a}^2+2Q_{12}P_{3a}^2-2S_m}{(Q_{11}+Q_{12})P_{1a}^2-2(\sigma_{3c}-\sigma_{3a})s_{12}-2Q_{12}(P_{3c}^2-P_{3a}^2)} \qquad (4.3)$$

Although there is no direct electric field term in the formula the polarization components and in-plane stress terms are highly dependent on the electric field, influencing the domain fraction. Using the analytical assumptions this can be simplified to:

$$\phi_c \approx \frac{2(s_{11}+s_{12})\sigma_{12}+(Q_{11}+Q_{12})P^2-2S_m}{(Q_{11}-Q_{12})P^2} \qquad (4.4)$$

4.2.2 Polarization and Stress (Analytical approach)

The polarization of the unit cells of the different domain is an important factor for the dielectric properties of the materials. The in-plane stress is also an important parameter because it gives an indication of the stress exerted on the substrate. Although in this work it is assumed that the substrate is strain free in reality the in-plane stress can give an indication of

the strain the substrate might experience due to the film leading to an estimate for the converse piezoelectric coefficient d_{13}. To obtain the polarization and in-plane stress the energy equation can also be further simplified using the analytical assumptions. Equation 3.5.2 can now be written as:

$$\langle F \rangle_{ac*} \approx \alpha_1 P^2 + \alpha_{11} P^4 + \alpha_{111} P^6 - \phi E P + (s_{11} + s_{12}) {\sigma_{12}}^2 \qquad (4.5)$$

The exact zero field solutions can be found through minimization, giving:

$$\sigma_{12\,E=0} = 0 \qquad (4.6)$$

$$P^2{}_{E=0} = P_s^2 = \frac{-\alpha_{11} + ({\alpha_{11}}^2 - 3\alpha_1 \alpha_{111})^{0.5}}{3\alpha_{111}} \qquad (4.7)$$

Here the saturation polarization (P_s) values correspond to the polarization of the stress-free bulk PZT (P_s^{blk})[4-9]. The importance of the zero in-plane stress is that in the 3D case the field-free domain structure resolves all stress in the film in both in-plane directions, which is an important difference between the 3D and 2D model. In the latter model there is always a non-zero in-plane stress present in the 2-direction, thus orthogonal to the c/a domain structure. The measured out-of-plane remnant polarization of the film (P_3^f) can be obtained using the saturation polarization and equation 4.4 at zero field:

$$P_3^f{}_{E=0} = \phi_{E=0} P_s \qquad (4.8)$$

For a non-zero field, equation 4.5 can be minimized with respect to the stress, simplifying to:

$$\sigma_{12} \approx \frac{E}{(Q_{11} - Q_{12})\, P} \qquad (4.9)$$

and with respect to the polarization:

$$2\alpha_1 P^3 + 4\alpha_{11} P^5 + 6\alpha_{111} P^7 - \frac{(Q_{11}+Q_{12})}{(Q_{11}-Q_{12})} E P^2 \approx \frac{(2S_m - 2(s_{11}+s_{12})\sigma_{12})}{(Q_{11}-Q_{12})} E \quad (4.10)$$

Equations 4.9 and 4.10 are the basic polarization and stress dependencies on the electric field, from which the film properties in the *c/b/a*-phase can be calculated.

4.2.3 Material properties near zero field (Analytical approach)

The influence of an applied electric field on the domain fraction, stress and polarization can be used to obtain the dielectric constant of the PZT film and give an indication of the individual contributions of each domain. The net dielectric constant of the film with top and bottom electrodes, using the strict polarization condition (section 4.2) is:

$$\varepsilon_0 \varepsilon_{33}^f = \left(\frac{\partial P_3^f}{\partial E}\right)_{E=0} \approx \left(\frac{\partial \phi_c P}{\partial E}\right)_{E=0} \approx \left(\frac{\partial \phi_c}{\partial E}\right)_{E=0} P_s + \phi_0 \left(\frac{\partial P}{\partial E}\right)_{E=0} \quad (4.11)$$

To solve this, we first require the derivatives of the σ, P and ϕ_c with respect to E. These can be found using equations 4.9, 4.10 and 4.4 giving:

$$\left(\frac{\partial \sigma}{\partial E}\right)_{E=0} = \frac{1}{(Q_{11}-Q_{12})P_s} \quad (4.12)$$

$$\left(\frac{\partial P}{\partial E}\right)_{E=0} \equiv \varepsilon_0 \varepsilon^{ca} \approx \left(\frac{(Q_{11}+Q_{12})}{(Q_{11}-Q_{12})} + \frac{2S_m}{(Q_{11}-Q_{12})P_s^2}\right) \varepsilon_0 \varepsilon_{33}^* \quad (4.13)$$

$$\left(\frac{\partial \phi_c}{\partial E}\right)_{E=0} \approx \frac{4S_m \left(\frac{\partial P}{\partial E}\right)_0}{(Q_{11}-Q_{12})P_s^3} + \frac{2(s_{11}+s_{12})}{(Q_{11}-Q_{12})^2 P_s^3} \quad (4.14)$$

Here $\varepsilon_0\varepsilon_{33}^* = (6\alpha_1 + 20\alpha_{11}P_s^2 + 42\alpha_{111}P_s^4)^{-1}$ is a dielectric constant of similar functional form as that of an unstrained, single domain, tetragonal bulk PZT $\varepsilon_0\varepsilon_{33}^{bulk} = (2\alpha_1 + 12\alpha_{11}P_s^2 + 30\alpha_{111}P_s^4)^{-1}$ [4-9]. Since $\varepsilon_{33}^* > 0$, $(\partial P/\partial E)_{E=0}$ is negative for a misfit strain when $2S_m < -P_s^2(Q_{11} + Q_{12})$, implying that the polarization in all domains decreases with increasing field in this range. This is again a consequence of the strict polarization conditions. Values for the analytically found parameters have been calculated for PZT (x=0. 5) and PZT (x=0.4) at E=0 and S_m=0, see table 4.2. Note that there is not a single numerically obtained polarization derivative because in the numerical model more than one polarization vector is present.

Table 4.2 Parameters for PZT (x=0.5) and PZT (x=0.4) at E=0 and S_m=0. It shows the analytically (without brackets) and numerically (brackets) obtained values.

	ϕ_c	P_s	$\frac{\partial\phi_c}{\partial E}$	$\frac{\partial\sigma_{12}}{\partial E}$	$\frac{\partial P}{\partial E}$
PZT50/50	0.36 (0.36)	0. 5 Cm^{-2} (0. 5)	5.4x10^{-9} mV^{-1} (8.4x10^{-9})	14 $Nm^{-1}V^{-1}$ (14)	1.2x10^{-9} $Cm^{-1}V^{-1}$ (NA)
PZT40/60	0.47 (0.47)	0.57 Cm^{-2} (0.57)	5.1x10^{-9} mV^{-1} (6.6x10^{-9})	16 $Nm^{-1}V^{-1}$ (16)	8.2x10^{-10} $Cm^{-1}V^{-1}$ (NA)

Using the found parameters $\varepsilon_0\varepsilon_{33}^f$ can be determined. The result for the two parts of equation 4.11 for PZT x=0.4 for E=0 and S_m=0 are:

$$\frac{\left(\frac{\partial\phi_c}{\partial E}\right)_0 P_s}{\varepsilon_0} \approx \frac{0.57 * 5.1 * 10^{-9}}{8.854 * 10^{-12}} = 328 \qquad (4.15)$$

$$\frac{\phi_0\left(\frac{\partial P}{\partial E}\right)_0}{\varepsilon_0} \approx \frac{0.47 * 8.2 * 10^{-10}}{8.854 * 10^{-12}} = 44 \qquad (4.16)$$

ε_{33}^f is then found to be 372. This shows that the polarization change contributes less to the dielectric constant while the effect of the domain

fraction change is an order larger. Note however that the strict polarization condition (section 4.3) has a large influence on $\varepsilon_0\varepsilon^{ca}$. If we drop this approximation the second term in equation 4.11 has to be replaced by the weighted average of the dielectric constants of all domains.

$$\varepsilon_{33}^{f} = \frac{\left(\frac{\partial P_3^f}{\partial E}\right)}{\varepsilon_0} = \frac{\left(\frac{\partial(\phi P_3^c + (1-\phi)P_3^a)}{\partial E}\right)}{\varepsilon_0}$$
$$= \frac{\left(\frac{\partial \phi}{\partial E}\right)(P_3^c - P_3^a) + \phi\left(\frac{\partial P_3^c}{\partial E}\right) + (1-\phi)\left(\frac{\partial P_3^a}{\partial E}\right)}{\varepsilon_0} \quad (4.17)$$

From the numerical study, in which the strict polarization restriction is not used, one finds dielectric constants for each domain individually, see table 4.3. Note that these values are independent of the misfit strain for the *c/b/a*-phase. The values for ε_{33}^{f} for PZT x=0.4 and x=0.5 at $E=0$ are dependent on the misfit strain and are found to be 678 and 1533 at $S_m=0$, respectively. Note that these values include the effect of the domain change on the out-of-plane polarization of the sample.

Table 4.3. Numerically calculated dielectric parameters for poly-domain tetragonal PZT (x=0.5) and PZT (x=0.4) at $E=0$.

	$\varepsilon_{33}^{c} = \frac{\partial P_{3c}}{\varepsilon_0 \partial E_3}$	$\varepsilon_{13}^{c} = \frac{\partial P_{1c}}{\varepsilon_0 \partial E_3}$	$\varepsilon_{33}^{a} = \frac{\partial P_{3a}}{\varepsilon_0 \partial E_3}$	$\varepsilon_{13}^{a} = \frac{\partial P_{1a}}{\varepsilon_0 \partial E_3}$
PZT50/50	-113	0	1706	305
PZT40/60	-17	0	497	186

In first instance one might expect that the ε_{33}^{f} dependence arises from ε_{33}^{c} and $\left(\frac{\partial \phi_c}{\partial E}\right)$ as is suggested by equation 4.11 obtained via the strict polarization approximation. It appears however that ε_{33}^{a} can have a dominant role on ε_{33}^{f} for materials with a significant *a*-domain fraction (equation 4.17) while the *c*-domain contribution (ε_{33}^{c}) is actually negative.

The analytical approach, which requires the strict polarization assumption, is not adequate for finding the dielectric parameters. One requires the numerical analysis to obtain accurate values for these parameters and finally obtain the measured dielectric constant $\varepsilon_0\varepsilon_{33}^f$. The same is true for the dependence of the domain fraction on the applied field, but the approximated value of ϕ_c is still a good indication of the value around zero field (see table 4.2).

4.2.4 Unit cell lattice parameters (Analytical approach)

The strain on the unit cell gives the relative change in unit cell lattice parameters in the relevant direction. The average out-of-plane deformation of the unit cell is the source of the piezoelectric coefficient (d_{33}) of the PZT film. The lattice strains as function of electric field are obtained without (=) and with (≈) the use of the strict polarization condition. We use the assumption that P_{1c}=0, which is confirmed by the numerical analysis:

$$S_1^c = S_2^c = (s_{11}+s_{12})\sigma_{12} + Q_{12}P_{3c}^2$$

$$\approx \frac{(s_{11}+s_{12})}{(Q_{11}-Q_{12})P_s}E + Q_{12}P_s^2 + 2Q_{12}\varepsilon_0\varepsilon_{33}^c P_s E \qquad (4.18)$$

$$S_1^a = (s_{11}+s_{12})\sigma_{12} + Q_{11}P_{1a}^2 + Q_{12}P_{3a}^2$$

$$\approx \frac{(s_{11}+s_{12})}{(Q_{11}-Q_{12})P_s}E + Q_{11}P_s^2 + 2Q_{11}\varepsilon_0\varepsilon_{13}^a P_s E \qquad (4.19)$$

$$S_2^a = (s_{11}+s_{12})\sigma_{12} + Q_{12}P_{1a}^2 + Q_{12}P_{3a}^2$$

$$\approx \frac{(s_{11}+s_{12})}{(Q_{11}-Q_{12})P_s}E + Q_{12}P_s^2 + 2Q_{12}\varepsilon_0\varepsilon_{13}^a P_s E \qquad (4.20)$$

$$S_3^c = 2s_{12}\sigma_{12} + Q_{11}P_{3c}^2$$

$$\approx \frac{2s_{12}}{(Q_{11}-Q_{12})P_s}E + Q_{11}P_s^2 + 2Q_{11}\varepsilon_{33}^c P_s E \qquad (4.21)$$

$$S_3^a = 2s_{12}\sigma_{12} + Q_{12}P_{1a}^2 + Q_{11}P_{3a}^2$$
$$\approx \frac{2s_{12}}{(Q_{11} - Q_{12})P_s}E + Q_{12}P_s^2 + 2Q_{12}\varepsilon_0\varepsilon_{13}^a P_s E \qquad (4.22)$$

$$S_4^c = S_5^c = S_6^c = S_4^a = S_5^a = S_6^a$$
$$\approx 0 \qquad (4.23)$$

The lattice parameters follow from $a_i^x = a_0(1 + S_i^x)$. Because ε_{33}^c is very small (table 4.3) the short and long axes of the c-domain unit cells mainly increase or decrease with the field due to the term arising from the in-plane stress. The long, in-plane axis of the a-domain is elongated by the stress and the piezoelectric effect because the value of ε_{13}^a is significant. The short axes of the a-domain (Eqs. 4.20 and 4.22) respond differently to the stress, but both shorten by the piezoelectric effect. Under the strict polarization conditions similar relations are found but clearly a large difference appears in the applied field dependence of the lattice parameters mainly because the terms depending on ε_{13}^a do not arise in that case. In the approximation, all shear strains are zero but with a non- zero ε_{33}^a appearing in the numerical analysis, these will also become non-zero in the a-domain.

4.2.5 Piezoelectric Coefficients (Analytical approach)

The piezoelectric coefficient is one of the most relevant parameters for piezo electric materials because it indicates the magnitude of deformation of the material due to an applied electric field. The effective piezoelectric coefficient d_{33}^f requires the average out of plane strain dependence on the electric field. The average out of plane strain is given by:

$$\langle S_3 \rangle = \phi S_3^c + (1 - \phi)S_3^a \qquad (4.24)$$

The effective piezoelectric parameter d_{33}^{f} at zero field, without (=) and with (≈) the polarization approximations is:

$$d_{33\,E=0}^{f} = \left(\frac{\partial\langle S_3\rangle}{\partial E}\right)_{E=0} = \left(\frac{\partial\phi}{\partial E}\right)_{E=0}(S_3^c - S_3^a) + \phi_0\left(\frac{dS_3^c}{dE} - \frac{dS_3^a}{dE}\right) + \frac{dS_3^a}{dE}$$
$$= \left(\frac{\partial\phi}{\partial E}\right)_{E=0}(Q_{11} - Q_{12})P_s^2 + 2P_s[\phi_0 Q_{11}\varepsilon_0\varepsilon_{33}^c + (1-\phi_0)Q_{12}\varepsilon_0\varepsilon_{13}^a] + \frac{2s_{12}}{(Q_{11} - Q_{12})P_s}$$
$$\approx \left(\frac{\partial\phi}{\partial E}\right)_{E=0}(Q_{11} - Q_{12})P_s^2 + 2P_s\left(\frac{\partial P}{\partial E}\right)[1 + \phi_0(Q_{11} - Q_{12})] + \frac{2s_{12}}{(Q_{11} - Q_{12})P_s} \quad (4.25)$$

Here we have defined $d_{33}^{c} = \frac{dS_3^c}{dE} = 2Q_{11}\varepsilon_0\varepsilon_{33}^c P_s + \frac{2s_{12}}{(Q_{11}-Q_{12})P_s}$ and $d_{31}^{a} = \frac{dS_3^a}{dE} = 2Q_{12}\varepsilon_0\varepsilon_{13}^a P_s + \frac{2s_{12}}{(Q_{11}-Q_{12})P_s}$ as the individual piezoelectric coefficient of the *c*- and *a*-domains at zero field. The first right hand term of equation 4.25 is the influence of the domain fraction change on the total piezoelectric coefficient, which is only possible through domain wall motion (d_{33}^{DW}). Note that this domain wall motion in practice is frequency dependent due to DW pinning effects. The next two terms are due to the internal piezoelectric coefficients of the *c*- and *a*-domain represented by d_{33}^{c} and d_{31}^{a}, respectively. The values of these piezoelectric coefficients, when using the strict polarization approximation, result in d_{33}^{c}≈-123.08 pmV^{-1} and d_{33}^{a}≈-116.13 pmV^{-1}, respectively. Note that since both signs are negative the unit cells of both the *c*- and *a*-domain decrease in the out-of-plane direction with an increasing electric field. The last term represents elastic deformation due to the in-plane stress and is also negative. The domain wall motion has a positive effect on the average piezoelectric coefficient of the film and is found to be d_{33}^{DW}≈184.65 pmV^{-1} for PZT x=0.4 at zero field. Thus only the domain wall motion gives rise to a net positive longitudinal piezoelectric coefficient.

All other average strains are zero or do not change with applied field ($< S_1 >=< S_2 >= S_m$). The individual in-plane strain values of the *c*- and *a*-domain can however change with applied field. The in-plane stress components are given by equation 4.9 $\sigma_1^c = \sigma_1^a = \sigma_2^c = \sigma_2^a = \sigma_{12} = E/(Q_{11} - Q_{12})P_s$. All other stress components are zero, which is also found numerically. The non-zero piezoelectric coefficients $e_{31}$and e_{32} are obtained from equation 4.9 as:

$$e_{31} = e_{32} = -\left(\frac{\partial \sigma_{12}}{\partial E}\right)_0^S = \frac{-1}{(Q_{11} - Q_{12})P_s} \tag{4.25}$$

The values are independent of the domain fraction and misfit strain and only depend on the saturation polarization and the intrinsic electro-strictive constants (Q_{ij}). The usual expression for e_{31} of a clamped thin film is $e_{31} = d_{31}/(s_{11} + s_{12})$[19]. The difference results from the fact that equation 4.25 considers the domain distribution of the film in detail and expressing all film parameters in terms of microscopic properties, while the usual clamped film result is derived from a model not taking domain formation into account and in principle using averaged properties.

4.3 Numerical Analysis

The analytical approach is used to obtain simplified equations that indicate the general influence between parameters and material properties. To get more information on the material properties using the model and to avoid any simplification, a numerical solution is used. In this section, we compare the results of the analytical approach in section 4.2 with the numerical approach and also investigate the origin of their differences and the influence of higher applied electric fields on material properties. The numerical analysis is performed for the $c/bc^*/ac^*$-phase with the two free energy functions for the *c*- and *a*-domain coupled by the domain fraction as free parameter. The energy minimization of the basic free energy equation (Eq. 3.15) showed that all in plane stresses are equal (σ_1^a=σ_2^a=σ_1^c=σ_2^c=σ_{12}). As a consequence, all other stresses were found to be zero

(σ_3=σ_4=σ_5=σ_6=0). All polarization components of the *c*- and *a*-domains (P_{1c}, P_{2c}, P_{3c}, P_{1a}, P_{2a}, P_{3a}) are independent variables in the free energy function. The poly-domain phase goes over into the single domain c-phase for $\phi_c = 1$, into the polydomain ac^*/bc^*-phase, when $\phi_c = 0$, and into the p-phase, when the polarization components are equal 0 at zero field. The *r*-phase, due to symmetry, can be described with a single free energy function. It can be analytically shown that this phase, as with the $c/bc^*/ac^*$-phase, has a uniform in-plane stress (σ), with all other stresses equal to zero. For all phases, all polarization components are allowed. The tetragonal single domain phase, poly domain phase and rhombohedral phase are analyzed separately for all temperature, strain and electric field values. The minimum energy values of all these phases are compared and the lowest energy value defines the proper phase for the PZT film. The compositions of $PbZr_xTi_{1-x}O_3$ compared here are x=0.4, x=0.5 and x=0.6, which are close to the MPB and show the difference between tetragonal and rhombohedral phases.

4.3.1 PZT phase diagram (Numerical approach)

The resulting phase for the different PZT compositions at T=25°C under varying S_m and E_3, and at E=0 with a varying T and S_m are shown in figure 4.3. Contrary to the 2D model[17] the temperature related figures show fewer phases. The zero field phases for PZT x=0.4 and x=0.5 only consist of *c-, c/b/a-, a/b-* and *p*-phases. With the influence of an electric field the expected phases *c/bc*/ac**- and *ac*/bc**-phases arise. Although any electric field should be enough to initiate some out of plane polarization component the threshold for the boundary was put at 0.006 Cm^{-2} for visual purposes. Only for PZT x=0.6 a r-phase is present, which is expected for PZT with a high Zr content[18]. Note that the misfit strain for the E-S_m (Fig. d-f) is constant because the temperature is constant. In other words, it is allowed to draw a straight line upwards to find what phase the material will be in at a higher applied electric field (Fig. 4.3e), because the value of S_m is constant. The same method does not work for the T-S_m figure because the misfit strain changes with temperature. At the deposition temperature the misfit strain is zero (S_m=0) but at any other temperature it is usually non-zero. What path is taken in the T-S_m figures is uncertain (Fig. 4.3b), however if

both substrate and film have a constant linear thermal expansion coefficient over the temperature range of interest the path can be approximated as a straight line.

The poly domain tetragonal *c/bc*/ac**-phase (including the *c/b/a*-phase) is the only phase with $\phi \neq 1$. From equation 4.4 it is seen that the only region in which this phase can exist in the *T*-S_m figure is between $S_m = Q_{12}P_s^2$, where $\phi_c = 0$, and $S_m = \frac{1}{2}(Q_{11} + Q_{12})P_s^2$, where $\phi_c = 1$. Note that the value of P_s is dependent on the temperature. For the *E*-S_m figures these boundaries are only valid for low electric field strengths. The relation is more complicated at higher fields, but can be found through equation 4.3, requiring knowledge of the other polarization components and the in-plane stress. At the boundary of any tetragonal phase the polarization, stress and domain fraction are continuous giving second order phase transitions, see figure 4.3a-c. For PZT x=0.6 the *r*-phase largely replaces the *c/b/a*-phase. The transition between this phase and the *c/b/a*- and *b/a*- phases are first order phase transitions, which gives rise to large material parameter changes, notably the strain and piezoelectric coefficients.

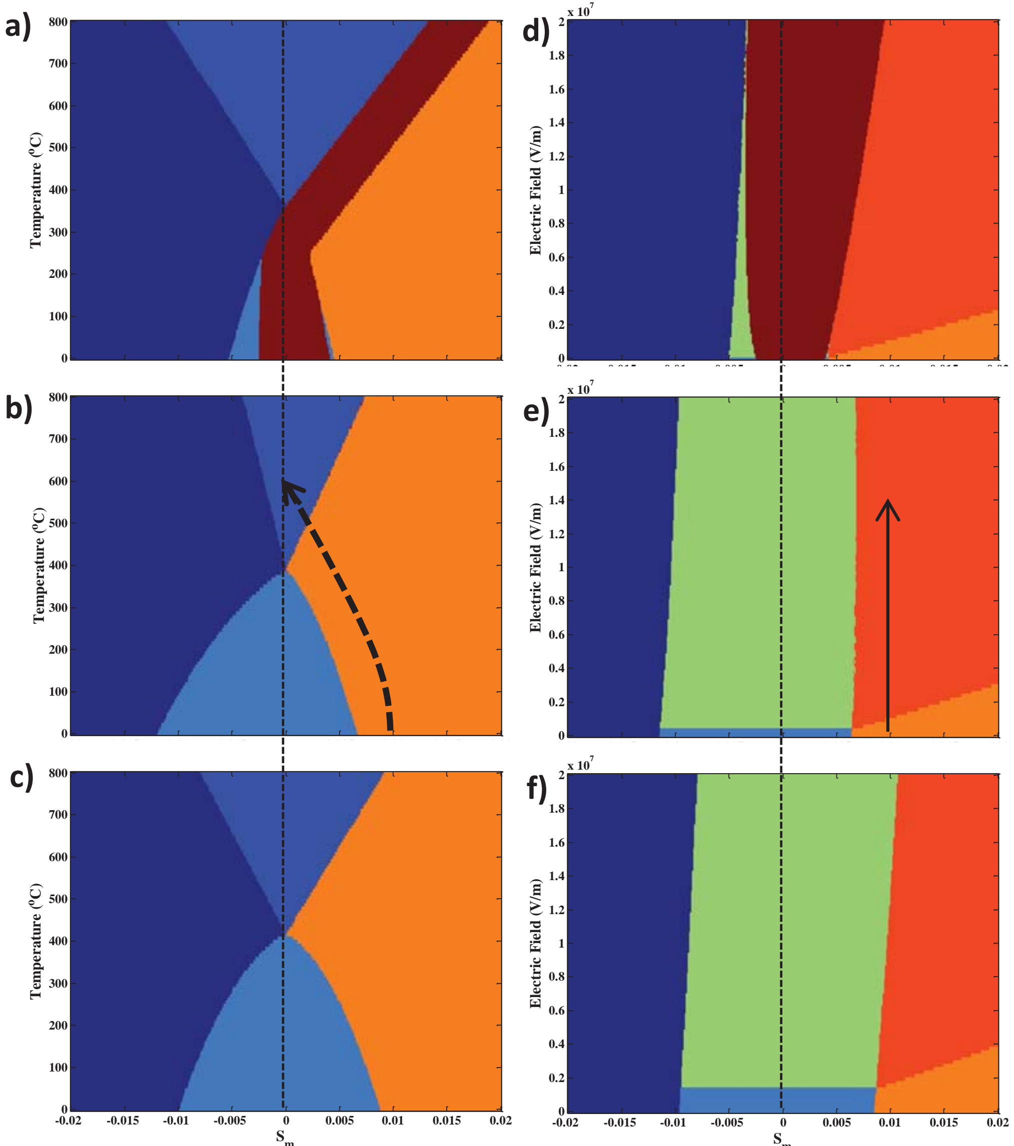

Fig.4.3 (a-c) The Temperature-Strain ($\boldsymbol{T-S_m}$) phase diagrams at zero field and (d-f) the Electrical Field-Strain ($\boldsymbol{E-S_m}$) phase diagrams at room temperature of PZT x=0.6 (a,d), x=0.5 (b,e) and x=0.4 (c,f). The colors represent the *c*-phase (dark blue), *c/b/a*-phase (light blue), *b/a*-phase (orange), *p*-phase (blue), *r*-phase (dark red), *c/ba*/ac**-phase (green) and *ac*/bc**-phase (red). The arrows show an example of the path a film might take through the phase diagrams, assuming that $\boldsymbol{S_m}$=+0.01 at RT. At deposition temperature (600°C) there is no misfit strain. However the exact path depends on the thermal expansion coefficients of the film and substrate. Applying an electric field is represented by a vertical line through the phase diagram.

4.3.2 Domain Fraction and Stress (Numerical approach)

At electric field values of E_3=0 Vm^{-1} and E_3=2·10^7 Vm^{-1} the *c/bc*/ac**- phase transition with the *c*- and *ac*/bc**- phases is continuous in the *c*-domain fraction (Fig. 4.4a). Note that this figure gives the *c*-domain fraction, which is zero for the *b/a*-phase, thus in the free energy equation of *b/*a- the *b/a*-fraction is equal to 1. The change in the *c*-domain fraction at S_m=0 and E_3=0 Vm^{-1} of PZT x=0.4 is slightly underestimated by equation 4.14 where $\left(\frac{\partial \phi_c}{\partial E}\right)_{E=0}$=5.1·10^{-9} mV^{-1}. The numerically obtained domain fraction change is influenced by the misfit strain and ranges linearly between $\left(\frac{\partial \phi_c}{\partial E}\right)_{E=0}$=5.4·10^{-9} mV^{-1} ($\phi_c$=1) and 7.6·10^{-9} mV^{-1} (ϕ_c=0). As predicted analytically by equation 4.6 and 4.9, the 3D model resolves all stress when the PZT film is in the *c/b/a*-phase by adapting the domain fraction. For example, at zero field the energy of all domains are equivalent, therefore if the misfit strain is somehow decreased (i.e. through bending the substrate) the film can reduce the stress caused by this process by decreasing its average in-plane strain. This can be achieved by decreasing the fraction of *a*- and *b*- domain unit cells and increasing the fraction of *c*- domain unit cells. However, the stress rapidly increases when the domain fraction reaches its limits ϕ_c=0 or 1. In the *r*-phase the stress is generally non-zero, but can be partially resolved by a polarization rotation in order to minimize the elastic energy. For finite fields the stress increases the energy, but the total energy is decreased by the electric field term if *E* is parallel to *P*. Note that the electric field energy term can increase with increasing field when the polarization direction is opposite to the electric field direction, which happens just before polarization switching. In that case the energy due to the stress will actually decrease the total energy. The change in stress with applied field is constant over the *c/b/a*-phase and is defined by equation 4.12. At E_3=2.0x10^7 Vm^{-1} the numerically calculated stress change decreases slightly from $\left(\frac{\partial \sigma}{\partial E}\right)$=15.8 Nm^{-1}V^{-1} to 14.6 Nm^{-1}V^{-1} of PZT x=0.4 indicating that equation 4.12 is still accurate.

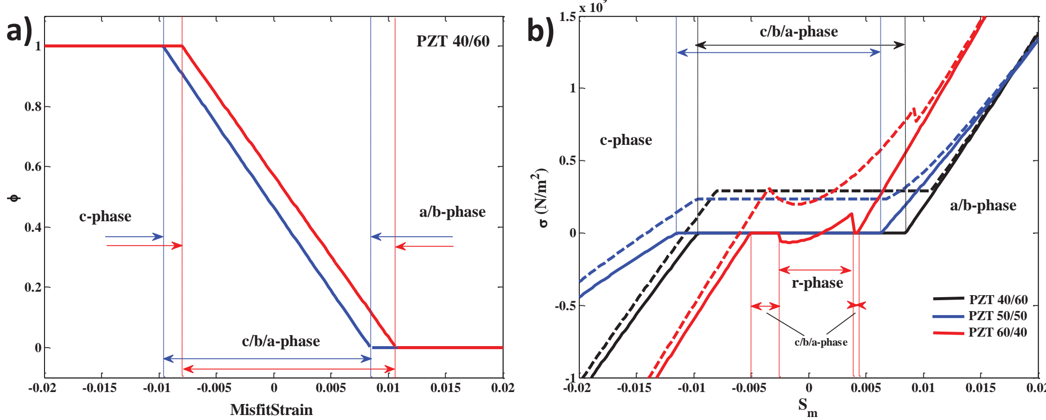

Fig. 4.4 (a) The c-domain fraction ϕ_c for the PZT x=0.4 at E_3=0 Vm^{-1} (blue) and E_3=2·10^7 Vm^{-1} (red) and (b) the in-plane stress σ for the PZT x=0.4, 0.5 and 0.6 as a function of substrate induced strain at E_3=0 Vm^{-1} (solid) and E_3=2·10^7 Vm^{-1} (dashed).

4.3.3 The Unit Cell Polarization (Numerical approach)

The polarization components of the *c* and *a* unit cell lattice parameters of the three PZT compositions at different misfit strains are shown in figure 4.5 for E_3=0 Vm^{-1} and E_3=2·10^7 Vm^{-1} for the *c/bc*/ac**- (and *c/b/a*-) poly-domain phases. The lattice parameters and polarization components, as predicted by equation 4.10 and 4.18-4.23, are equal to those of the bulk phase and independent of the misfit strain because the film has eliminated all stress by changing the domain fraction. With increasing field the stress increases, but also the polarization components change, both affecting the resulting unit cell strain. For all phases the out of plane polarization component increases for increasing electric field except for the *c/bc*/ac**-phase. Although the *a*-domain out-of-plane polarization for this phase increases with increasing field, the *c*-domain polarization actually decreases. The change in polarization has a larger decreasing effect on the out-of-plane strain through the piezoelectric effect of the *c*-domain than the positive strain resulting from the in-plane stress. This causes the out-of-plane strain of the *c*-domain to decrease despite the increase in the in-plane stress. The out-of-plane strain of the *a*-domain of PZT x=0.4 also decreases but slightly increases for PZT x=0.5.

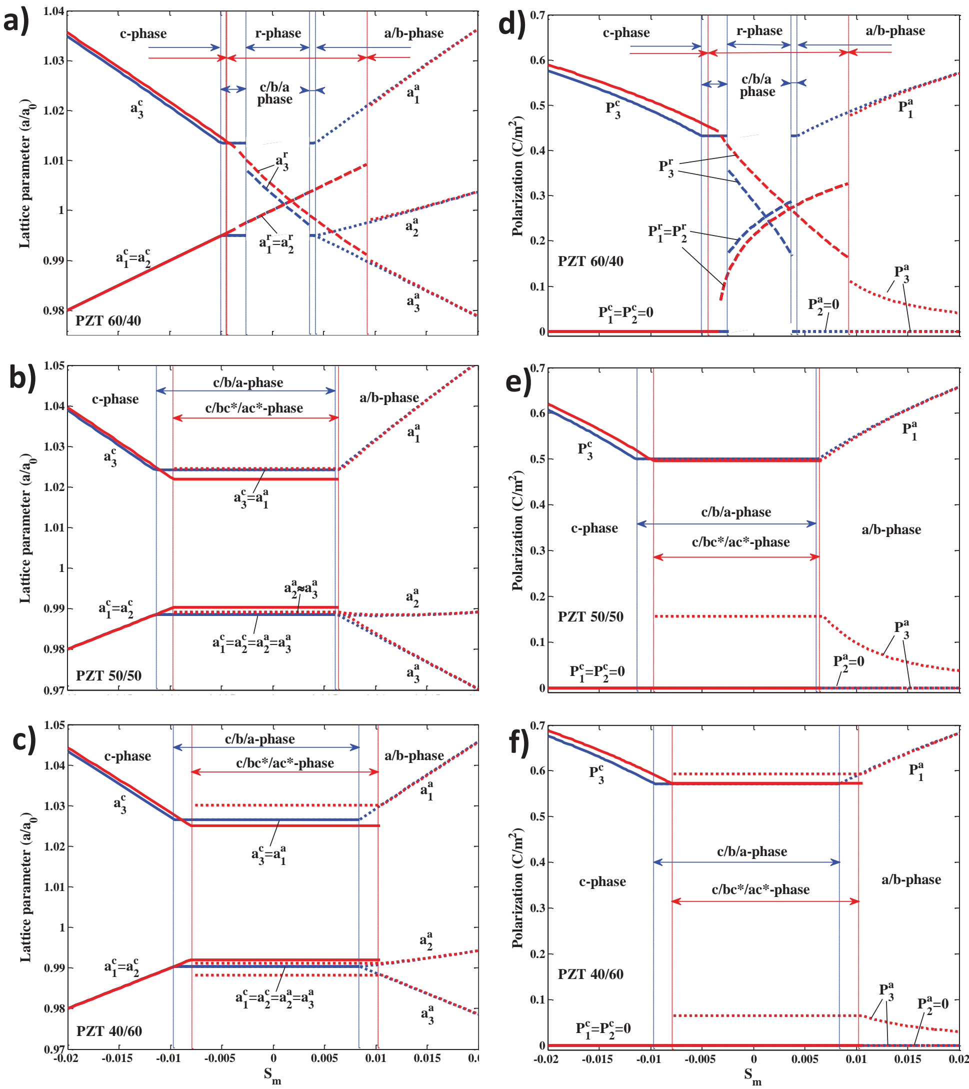

Fig.4.5 The unit cell lattice parameters (a-c) and individual polarization components (d-f) of PZT x=0.6, 0.5 and 0.4 as function of misfit strain at applied fields $E = 0$ Vm^{-1} (blue) and E=2•10^{7} Vm^{-1} (red).

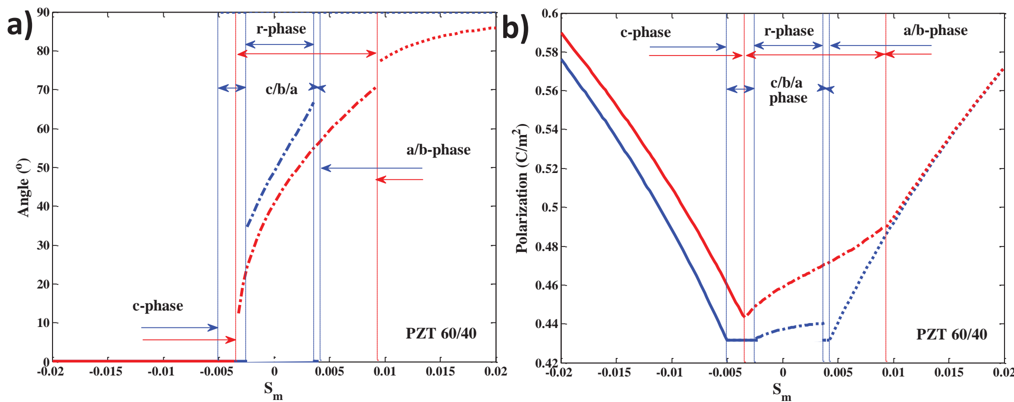

Fig.4.6 Polarization extension and rotation in the r-phase versus strain at $E = 0$ (blue) and E=2•10^7 Vm^{-1} (red)

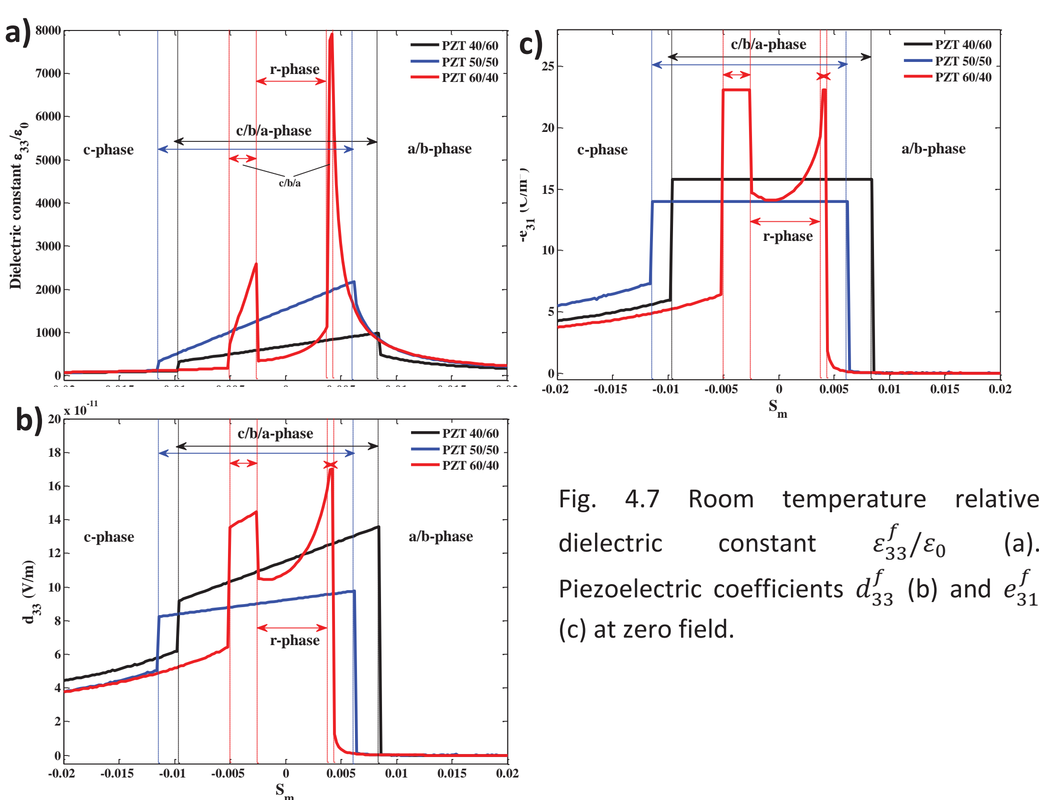

Fig. 4.7 Room temperature relative dielectric constant $\varepsilon_{33}^f/\varepsilon_0$ (a). Piezoelectric coefficients d_{33}^f (b) and e_{31}^f (c) at zero field.

4.3.4 Dielectric constant and piezoelectric coefficients (Numerical approach)

The effective relative dielectric constants, ε_{33}^{f}, of the PZT films as function of S_m are shown in figure 4.7a. For the c/b/a-phase its value increases linearly with the misfit strain, which is due to the decrease in the *c*-domain fraction combined with the large value of ε_{33}^{a}, see table 4.3. Using the numerical approach the first term in equation 4.17, which is due to domain wall motion, $\left(\frac{\partial \phi}{\partial E}\right)(P_3^c - P_3^a)/\varepsilon_0$, is found to be 475 for PZT x=0.5 and 425 for PZT x=0.4 while the terms due to the polarization change equals 1028 and 260 respectively at $S_m = 0$ and $E = 0$. This shows that the domain wall motion is a significant part of the dielectric constant. This explains why ε_{33}^{f} drops abruptly at the *c/b/a*-phase boundary with the other tetragonal phases where the domain wall contribution drops to zero. In the *r*-phase the dielectric constant only originates from polarization rotation and extension.

The piezoelectric coefficient d_{33}^{f} plotted in figure 4.7b can be best understood from equation 4.24. Analytically it is estimated that d_{33}^{f} for PZT x=0.4 is around 170 pmV^{-1} at *E*=0 Vm^{-1} and S_m=0. The numerical results in d_{33}^{f} =115 pmV^{-1}. The largest component comes from the domain wall motion which in equation 4.25 is around 240 pmV^{-1}. As expected from the analytical method the a- and c-domain component are negative with d_{33}^{a} and d_{33}^{c} being -80 pmV^{-1} and -50 pmV^{-1}, respectively. As with the dielectric coefficient there is a drop off of d_{33}^{f} at the boundary of the c/b/a-phase due to the loss of the domain wall motion component. The value nearly drops to zero for the a/b-phase due to the small influence of ε_{33}^{a} on the out of plane strain of the material. For the c-phase the out of plane polarization slightly increases for an increasing field because the effect of the large initial out-of-plane polarization (P_s) on the strain results in a larger d_{33}^{f}than in the case of the *a*-phase, where at zero field P_3^a=0.

4.4 Conclusion

The analytical model described in this chapter is used to estimate the properties of strained (001) PZT film in the *c/b/a*-phase close to zero field, while the numerical model is used to describe any phase over a large electric field and temperature range. For both models the domain wall energy is ignored and is assumed not to affect the PZT film on any scale. It is also assumed that the substrate does not influence the film except on a macroscopic scale through the misfit strain. These assumptions are the main differences with earlier models in literature.

The following conclusions can be made for PZT films under a misfit strain that is expected to hold for most available substrates.

-PZT films at room temperature are always in the poly-domain tetragonal *c/b/a*-phase or the r-phase depending on the substrate misfit strain. Near the MPB (PZT x=0.50) composition the material is found to be in the *c/b/a*-phase. Note however that the introduction of a domain wall energy (chapter 5) to the model can cause the PZT x=0.50 composition to undergo a phase transition

-In the *c/b/a*-phase at zero field the stress in the material is eliminated by shifting the domain fraction. The stress builds up linearly with the application of an electric field independent of the substrate material.

-The analytical approach of the *c/b/a*-phase, which uses the strict polarization assumption, gives rise to some disagreements in the polarization parameters with the numerical method. However, the analytical method can still provide accurate information about the dielectric and piezoelectric properties of the overall PZT film at zero field and also adds insight into the origin of the response of the individual unit cell in the domains.

-The values of the average ε_{33}^{f} and d_{33}^{f} in the *c/b/a*-phase are largely due to domain wall motion and are higher than the *r*-phase values. The piezoelectric coefficients of the individual domains d_{33}^{c} and d_{33}^{a} give a negative contribution to the d_{33}^{f}, indicating that the energy of poly-domain

PZT is most effectively minimized through the variation of the domain fraction.

-The *c*-domain out-of-plane polarization decreases, while the out-of-plane polarization of the *a*-domain increases when the applied electric field is increased with only a minimal effect on the strain of the material.

References

[1] P. Zubko et al., “*Interface Physics in Complex Oxide Heterostructures*”, Annual Review of Condensed Matter Physics vol.2, pp.141 (2011)

[2] P. K. Davies et al., “*Crystal Chemistry of Complex Perovskites: New Cation-Ordered Dielectric Oxides*”, Annual Review of Materials Research vol.38, pp.369 (2008)

[3] H. U. Habermaier et al, “*Thin films of perovskite-type complex oxides*” , H.-U., MaterialsToday 10, pp.34-43 (2007)

[4] M. J. Haun, Z. Q. Zhuang, E. Furman, S. J. Jang and L. E. Cross, “*Electrostrictive Properties of the lead zirconate titanate solid-solution system”*, Journal of the American Ceramic Society, Volume 72,7-1140, (1989).

[5] M. J. Haun, E. Furman, S. J. Jang, L. E. Cross, “*Thermodynamic theory of the lead zirconate-titanate solid solution system, part I: Phenomenology”*, Ferroelectrics,99:1,13-25. (1989).

[6] M. J. Haun, E. Furman, H. A. McKinstry, L. E. Cross, “*Thermodynamic theory of the lead zirconate-titanate solid solution system, part II: Tricritical behavior”,* Ferroelectrics,99:1,27-44. (1989).

[7] M. J. Haun, Z. Q. Zhuang, E. Furman, S. J. Jang and L. E. Cross, “*Thermodynamic theory of the lead zirconate-titanate solid solution system, part III: Curie constant and sixth-order polarization dielectric stiffness coefficients”,* Ferroelectrics,99:1,45-54. (1989).

[8] M. J. Haun, E. Furman, T. R. Halemane and L. E. Cross, "*Thermodynamic theory of the lead zirconate-titanate solid solution system, part IV: Tilting of the oxygen octahedral",* Ferroelectrics,99:1,55-62. (1989).

[9] M. J. Haun, E. Furman, E. Jang and L. E. Cross, "*Thermodynamic theory of the lead zirconate-titanate solid solution system, part V: Theoretical calculations",* Ferroelectrics,99:1,63-86. (1989).

[10] B. Noheda, D. E. Cox and G. Shirane, "Stability of the monoclinic phase in the ferroelectric perovskite $PbZr_{1-x}Ti_xO_3$", Physical review B, vol.63, 014103.

[11] R. Guo, L. E. Cross, S-E. Park, B. Noheda, D. E. Cox and G. Shirane, "*Origin of the High Piezoelectric Response in* $PBZr_{1-x}TixO_3$", Physical review letters, vol.84-23, (2000).

[12] D. E. Cox, B. Noheda and G. Shirane , "*Low-temperature phases in PbZr0.52Ti0.48O3: A neutron powder diffraction study*", Physical review B, vol.71, 134110, (2005).

[13] D. La-Orauttapong et al. **"***Phase diagram of the relaxor ferroelectric* $(1-x)Pb(Zn_{1/3}Nb_{2/3})O_3x\text{-}PbTiO_3$", Physical review B, vol.65, 1441010, (2001).

[14] B. Noheda et al. "*Tetragonal-to-monoclinic phase transition in a ferroelectric perovskite: The structure of* $PbZr_{0.52}Ti_{0.48}O_3$", Physical review B, vol.61-13,(2000).

[15] M. Bayraktar et al. "*Nanosheet controlled epitaxial growth of PbZr0.52Ti0.48O3 thin films on glass substrates*", Applied Physics Letters **105**, 132904 (2014)

[16] Y.M. Jin, Y.U. Wang, A.G. Khachaturyan, J. Li, and D. Viehland. "Conformal miniaturization of domains with low domain-wall energy: Monoclinic ferroelectric states near the morphotropic phase boundaries", Physical Review Letters, 91(19):197601, (2003).

[17] N. A. Pertsev and V. G. Koukhar, "*Polarization Instability in polydomain ferroelectric epitaxial thin films and the formation of heterophase structures*", Physical Review Letters **84**, 3722 (2000)

[18] B. Noheda et al "*A monoclinic ferroelectric phase in the* $Pb(Zr_{1-x}Ti_x)O_3$ *solid solution*", Applied Physics Letters, vol.74-14, (1999).

[19] P. Muralt et al. "Piezoelectric actuation of PZT thin film diaphragms at static and resonant conditions", Sensors and Actuators A 53, pp.397–403, (1996)

5. Determination of the contributions to the piezoelectric coefficient of polydomain 001 tetragonal $Pb(Zr_{40}Ti_{60})O_3$ thin film by XRD methods.

Abstract

It is shown that it is possible to extract the out-of-plane piezoelectric coefficient (d_{33}) of a poly-domain tetragonal $Pb(Zr_{0.4}Ti_{0.6})O_3$ (PZT x=0.4) film from the intrinsic unit-cell characteristics measured with X-Ray Diffraction (XRD) measurements under the application of an electric field. A 740 nm thick PZT (x=0.4) film was grown on a $SrTiO_3$ (STO) substrate with a 65 nm $SrRuO_3$ (SRO) bottom electrode layer and a 65 nm SRO top electrode using pulsed laser deposition (PLD). Next to the d_{33} information the XRD data allows for a detailed investigation into the unit cell deformation, domain fractions and the interaction between the different tetragonal domains in the PZT (x=0.4) film. Additional d_{33} data was gathered using double beam laser interferometry (DBLI). The experimental data was compared to a thermodynamic model for the dense domain structures, see chapter 3, which allows for a detailed understanding of strained ferroelectric thin films.

5.1 Introduction

Piezo-electrics have the ability to convert electrical energy into mechanical energy and visa versa. An important piezoelectric material characteristic is the piezoelectric coefficient (d_{ij}), describing the strain in the material induced by an applied electric field (Eq. 1.1), which is key to most piezoelectric based devices. Coarsely speaking the mechanisms responsible for piezoelectricity in nearly all materials and devices involves the interplay of mechanical, electrical, and compositional effects that are the subject of continuing research for both bulk[1-3], thin film[4-6] and partially clamped island structures[7] of piezoelectric materials. Experimental work has usually been focused on optimizing the material composition and crystal structure leading to a continuous improvement of properties and experimental techniques[8-12]. To further explain the underlying physical properties of the ferroelectric materials the Landau-Ginzburg-Devonshire phenomenological theory is widely used for bulk materials[13-15] and extended to include thin films [16-18]. It is noted that these theories make predictions about not only the piezoelectric coefficient but of nearly any aspect of the material, most notably the polarization, strain and stress, allowing for an in depth analysis of film properties.

Most research has been focused on poly-crystalline PZT with compositions near the morphotropic phase boundary (MPB) due to the interest in the large piezoelectric and dielectric properties found there. Consequently, most models have focused on unclamped bulk PZT. As a result little work has been done on comparing a thermodynamic model and experimental work on clamped films, which are widely used in micro electrical mechanical system.

In this chapter the model for clamped single crystal PZT film is used to predict material properties, which are then compared to experimental data. Although PZT near the MPB is generally used for application purposes, it has been chosen to compare the model results to experiments done on PZT (x=0.4) which has a more tetragonal crystal structure. This is done because PZT with a tetragonal crystal structure allows one to distinguish between the unit cells of different domains using methods such as XRD. This allows

one to gather more information about the individual unit cells in the domains, which improves the comparison to the thermodynamic model. Due to their importance in application, comparison of the measured piezoelectric and dielectric properties with the values predicted by the model is an important step. Ferroelectric measurements and DBLI are used to gain information about the polarization and average strain changes of the film due to an applied field, respectively. The XRD setup also allows for an applied electric field over the film and will give insight into strain change of the individual unit cells of the domains due to an applied field. The proposed model for a clamped PZT film requires a dense, epitaxial, fully clamped, poly-domain, tetragonal $Pb(Zr_{40}Ti_{60})O_3$ (PZT x=0.4) film. A film that fulfills these assumptions to a large extend was grown on a STO (001) single crystal substrate with a SRO top and bottom electrode using pulsed laser deposition (PLD).

5.2 Analytical determination of the average piezoelectric coefficient.

From our model derived in chapter 3 and 4, equations 4.24 and 4.25 predict the average piezoelectric coefficient, $< d_{33} >$. Here, the average is used because the piezoelectric coefficients of the individual unit-cells (d_{33}^{c} and d_{33}^{a}) can differ. Due to the intricate domain structure of the film the macroscopically measured value is the average value. Equation 4.25 can be split into 3 separate parts corresponding to the piezoelectric contribution of the *c*-domains, the *a*-domains and the change in the domain fractions.

$$< d_{33} >= \frac{d\phi_c}{dE}(S_{3c} - S_{3a}) + \frac{dS_{3c}}{dE}\phi_c + \frac{dS_{3a}}{dE}\left(1 - \phi_c\right) \qquad (5.1)$$

Note that apart from an in-plane rotation, all properties of the *a*-domain are equal to the properties of the *b*-domains, see chapter 3. As it can be seen there are three main parts contributing to the average d_{33} of the film, which are referred to as the domain fraction contribution $\left[\frac{d\phi_c}{dE}(S_{3c} - S_{3a})\right]$,

the *c*-domain contribution $\left[\frac{dS_{3c}}{dE}\phi_c\right]$ and the *a*-domain contribution $\left[\frac{dS_{3a}}{dE}(1-\phi_c)\right]$. In this work we obtain experimentally the parameters ($S_{3c}(E)$, $S_{3a}(E)$ and $\phi_c(E)$) separately, which allows us to better understand the source of the average $< d_{33} >$ of the film.

The relevant equations, derived in chapter 4, that are needed to obtain $< d_{33} >$ analytically, are:

$$S_{3c} = s_{11}\sigma_{3c} + 2s_{12}\sigma_{12} + Q_{11}P_{3c}^2 + Q_{12}P_{1c}^2 \tag{5.2}$$

$$S_{3a} = s_{11}\sigma_{3a} + 2s_{12}\sigma_{12} + Q_{11}P_{3a}^2 + Q_{12}P_{1a}^2 \tag{5.3}$$

$$\phi_c = \frac{2S_m^0 - 2(s_{11}+s_{12})\sigma_{12} - 2s_{12}\sigma_{3a} - (Q_{11}+Q_{12})P_{1a}^2 - 2Q_{12}P_{3a}^2}{2(\sigma_{3c}-\sigma_{3a})s_{12} + 2Q_{12}(P_{3c}^2 - P_{3a}^2) - (Q_{11}+Q_{12})P_{1a}^2} \tag{5.4}$$

Here Q_{11} ($8.116\cdot10^{-2}$ m^2C^{-1}) and Q_{12} ($-2.950\cdot10^{-2}$ m^2C^{-1}) are the electrostrictive constants, s_{11}($8.6\cdot10^{-12}$ Pa^{-1}) and s_{12}($-2.8\cdot10^{-12}$ Pa^{-1}) the elastic compliances (see appendix). With the results from chapter 4 an approximation for $< d_{33} >$ of tetragonal PZT x=0.4 around zero field (E_3=0 Vm^{-1}) can be made by using the same assumptions, as were made in chapter 4, using the strict polarization condition (section 4.2) with the strict polarization condition. Further, at E_3=0 Vm^{-1} one has $P_3^c = P_1^a = P_s$, where P_s=0.572 Cm^{-2} for PZT x=0.4. Thus, it is assumed that the polarization of the unit cell does not change under a small applied electric field. Note that this constant polarization assumption works only for approximating $< d_{33} >$ but not for most other parameters. The reason for this is that the largest polarization change ($\frac{\partial P}{\partial E}$) in the numerical solution, table 4.3, arises in P_3^a. This polarization component is however still small and because the influence of polarization on strain is quadratic (Eqs. 4.18-4.22) the actual strain influence is small, although it has a large effect on the out of plane polarization measurements. Most other polarization changes are small, see table 4.3, and can thus be ignored in this approximation. To recapitulate: we use the assumptions and low field approximations: $\sigma_3 = \sigma_{3c} = \sigma_{3a} = 0$, $P_3^a = P_2^a = P_1^c = P_2^c = 0$ and $P_3^c = P_1^a = P_s$. The equation for in-plane

stress is the same as was found in chapter 4: $\sigma_{12} = E/(Q_{11} - Q_{12})P_s$. Equations 5.1-5.4 can now be simplified and used to find the field dependence of the out of plane strains and the *c*-domain fraction.

$$\frac{dS_{3c}}{dE} \approx \frac{2s_{12}}{(Q_{11} - Q_{12})P_s} \approx -88\ (pm/V) \tag{5.5}$$

$$\frac{dS_{3a}}{dE} \approx \frac{2s_{12}}{(Q_{11} - Q_{12})P_s} \approx -88\ (pm/V) \tag{5.6}$$

$$\frac{d\phi_c}{dE} \approx \frac{2(s_{11} + s_{12})}{(Q_{11} - Q_{12})^2 {P_s}^3} \approx 5.1\ (nm/V) \tag{5.7}$$

The combined effect of the strain change of both the *c*- and *a*-domain combined, ($\frac{dS_3}{dE}$), can be calculated without knowledge of the domain fraction:

$$\frac{dS_3}{dE} \approx -88\ (pm/V) \tag{5.8}$$

The effect of the change in the domain fraction is:

$$\frac{d\phi_c}{dE}(S_{3c} - S_{3a}) \approx \frac{2(s_{11} + s_{12})}{(Q_{11} - Q_{12})^2 {P_s}^3}(Q_{11}P_s^2 - Q_{12}P_s^2)$$

$$\approx 183\left(\frac{pm}{V}\right) \tag{5.9}$$

Thus we can approximate for $< d_{33} >$ of PZT (x=0.4) in the *c/b/a*-phase as:

$$< d_{33} > \approx \frac{2s_{12}}{(Q_{11} - Q_{12})P_s} + \frac{2(s_{11} + s_{12})}{(Q_{11} - Q_{12})^2 {P_s}^3}(Q_{11}P_s^2 - Q_{12}P_s^2)$$

$$\approx 2\frac{s_{11} + 2s_{12}}{(Q_{11} - Q_{12})P_s} \approx 95(pm/V) \tag{5.10}$$

This value will prove to be a good indication for the measured average piezoelectric coefficient, as long as ε_{13}^{a} $(= \frac{\partial P_{1a}}{\varepsilon_0 \partial E_3} \approx 0)$ and $\varepsilon_{33}^{c}(= \frac{\partial P_{3c}}{\varepsilon_0 \partial E_3} \approx 0)$ remain small. In the remainder of this chapter this approximation will not

be used for comparing the model predictions to the experimental results, the results from the full numerical model for the *c/bc*/ac**-phase is used.

5.2.1 Model Parameters

As was shown in chapter 4 the model requires a number of input parameters that describe the fully strained, dense epitaxial PZT film. There are four parameters required for the model of which two are material parameters, the film composition ($PbZr_xTi_{1-x}O_3$) and the substrate induced misfit strain (S_m^{model}) (see section 3.32) and two are external factors, temperature (T) and applied electric field (E_3). The influences of these parameters can be found in chapter 4. The coercive field (E_c^{model}) and the basic lattice parameter are two parameters not crucial for the model, but are required to compare its results with the experimentally obtained polarization hysteresis loop and unit cell lattice parameters. Some parameters will be given the superscript "model" to indicate that these values are used in the model and might differ in some way from values found by different methods.

5.2.2 Model Misfit Strain

The misfit strain is a non-trivial parameter to obtain since it depends on the temperature and on the thermal expansion coefficient of both the PZT film and substrate (Eq. 3.9). Note that, for a given substrate material and PZT composition, if the deposition temperature and measurement temperature are the same the resulting misfit strain will also be the same. There are a few methods to estimate the misfit strain, which will be discussed in section 53.3. In this chapter the method of estimating the misfit strain was by fitting the polarization hysteresis loop. The measurement of the PE loop is the most readily available and accurate measurement that can be done on a PZT film.

Figure 5.1 shows the measured polarization loop obtained from a room temperature ferroelectric measurement. To obtain a value for the misfit strain only the remnant polarization has to be fitted. The total measured out of plane polarization P_3= 0.412 ±0.02 Cm^{-2} at zero field. From theory the total out-of-plane polarization is defined by $P_3 = \phi_c P_{3c} + (1 - \phi_c)\, P_{3a}$. The model predicts that P_{3c}=P_s=0.572 Cm^{-2} and P_{3a}=0 Cm^{-2} at zero field, see chapter 4. This results in a *c*-domain fraction of ϕ_c =0.72 ±0.035 . Using equation 5.4 the value of ϕ_c corresponds to S_m^{model} =-0.0046 which is used to model all the experimental data in this chapter.

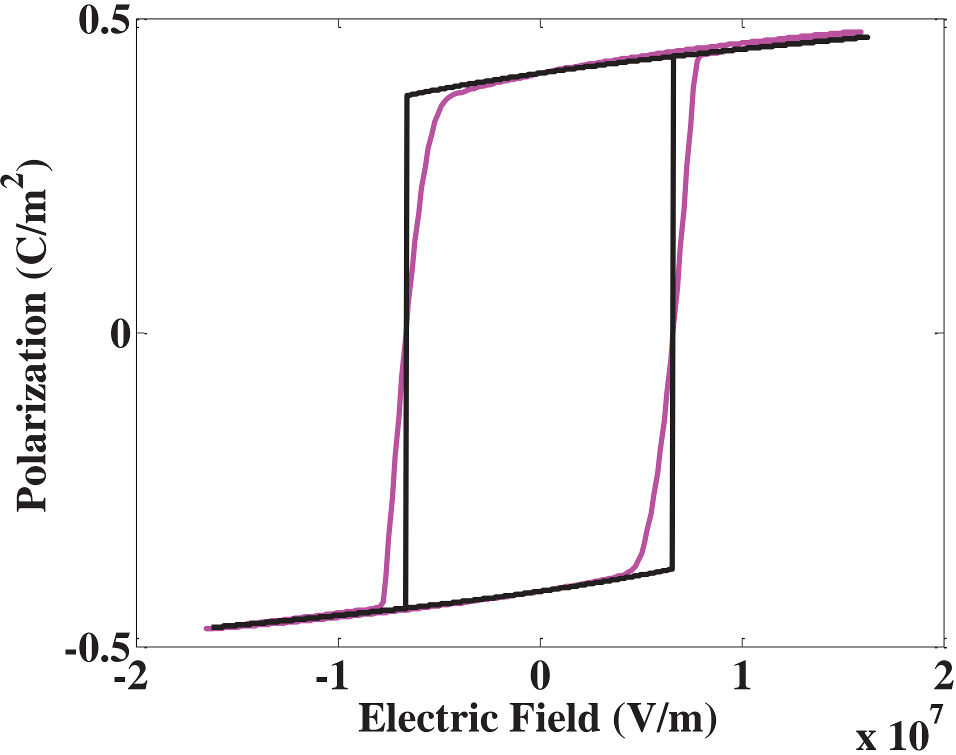

Figure 5.1: The experimental (pink) polarization loop of the STO/SRO/PZT/SRO film capacitor with a 11.04mm^2 top electrode, measured with 100 Hz in the range -12 V and +12 V using an Aixact TF analyzer 2000. The experimental data loop was given a slight offset in order to make the curve symmetrical along the x- and y-axis. The calculated polarization loop based on the model (black) was made using 801 points and a coercive field of ±4.9 V.

The value for E_c^{model} can also be obtained from the polarization hysteresis loop shown in figure 5.1. The experimental coercive field depends on the scan frequency, where a higher coercive field is found for higher frequencies. Because of the long duration of the XRD measurements performed at each voltage step the coercive field applicable to the scan during the XRD measurements is estimated from the PUND measurement (chapter 2). The value found is in the range E_c^{model}=3-4·10^6 Vm^{-1}.

5.3 Basic Lattice Parameter

The model predicts the strains (S_x). Although the strain is closely related to the lattice parameter, one requires the basic lattice parameter (a_0) to estimate the actual lattice parameters. Note that the value of a_0 has no effect on all other predicted material properties since these are usually dependent on the strain. The basic lattice parameter was obtained by two methods. One assumes that the volume is constant for the strained and un-strained unit cells, giving:

$$V_{unit\ cell} = a_1 a_2 a_3 = (a_0^V)^3$$

On the other hand using equation 3.5 and [$a_x = a_0(S_x + 1)$] for the *c/b/a*-phase the volume of the unit cell can be expressed as,

$$V_{unit\ cell} = {a_0}^3(1 + Q_{12}\, P_3^2)(1 + Q_{12}\, P_3^2)(1 + Q_{11}\, P_3^2) = (a_0^V)^3$$

Resulting in a theoretical difference between the estimated and actual basic lattice parameter for PZT x=0.4 of $a_0^V - a_0$ = +0.0022 which is not completely negligible compared to strain values of around +0.0266 and -0.0097 for the long and short axis. In short the polarization changes the volume of the unit cell which, depending on the composition, can have a significant influence on the result of the model.

A method to obtain the basic lattice parameter is to fit the measured lattice parameters of unstrained PZT (powder sample) with the relation:

$$a_{long}^{model} = a_0(1 + Q_{11}\, P_s^2) \tag{5.11}$$

$$a_{short}^{model} = a_0(1 + Q_{12}\, P_s^2) \tag{5.12}$$

Taking a_0 and P_s as free parameters. XRD on PZT (x=0.4) powder gives the lattice parameters a_{long}^{powder} =4.150 Å and a_{short}^{powder}=4.005 Å. This gives as best fit values a_0^{model}=4.0434 Å for $P_s^{powder} = 0.570$ Cm^{-2}, which is slightly less than $P_s^{model} = 0.572$ Cm^{-2}. This difference is small but is a first indication of differences between the theory and experimental data. For the model a value of a_0^{model}=4.0434 Å will be used at *T*=25°C which resutls in a_{long}^{model}=4.150 Å and a_{short}^{model}=4.004 Å at zero field.

5.3.1 Out of plane lattice parameter

Using XRD in combination with an applied electric field the value of the out of plane lattice parameters are obtained at different fields, see figure 5.2. The out-of-plane lattice parameters of the *c*- and *a*-domain at zero electric field are a_{3c} =4.140 Å and a_{3a} =4.022 Å. The values from the model (based on the assumption that $\sigma = \sigma_3 = 0$) are also shown in figure 5.2 and denote a larger strain difference between a_{3c} and a_{3a} that was found experimentally.

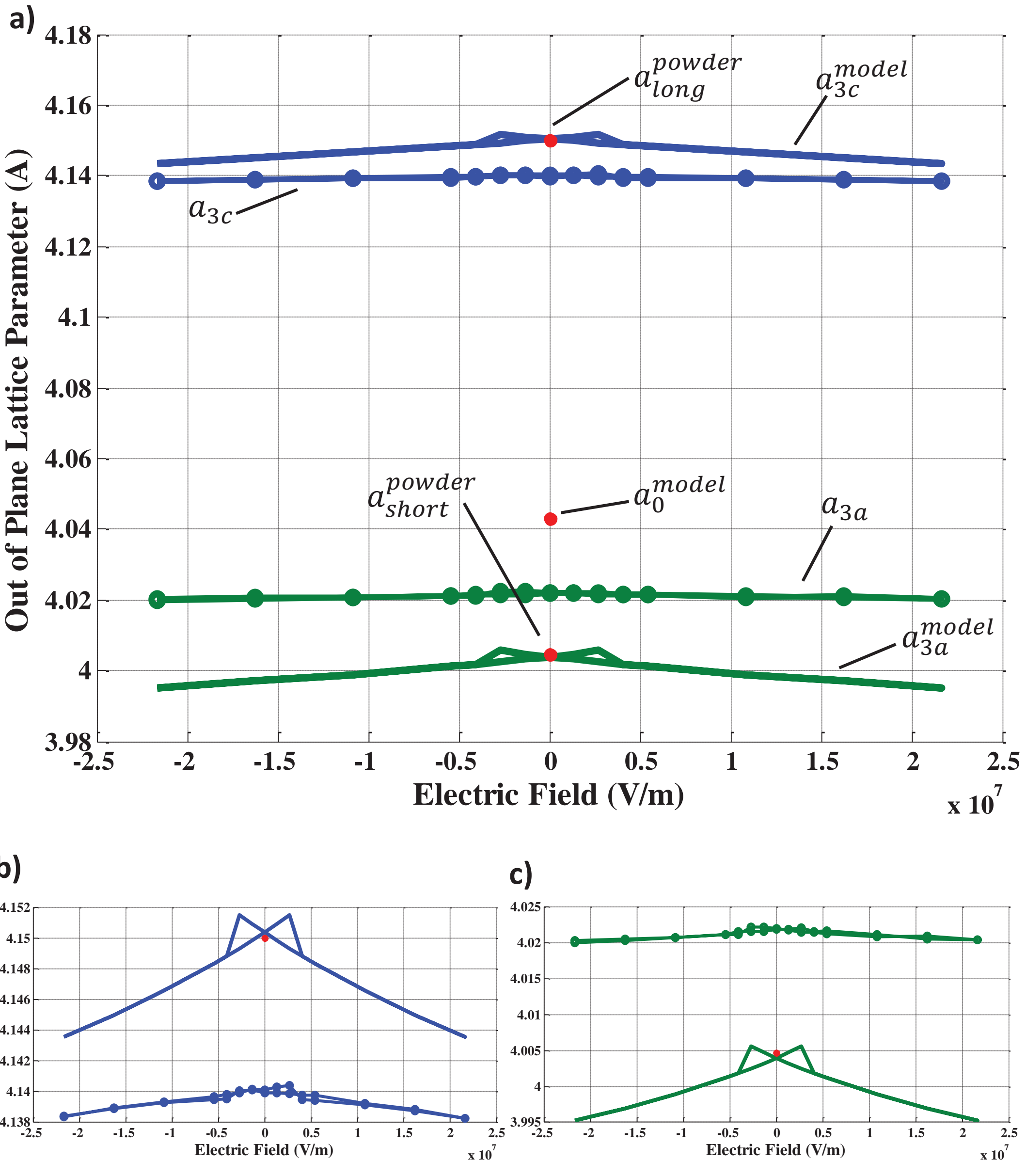

Figure 5.2: (a) The out of plane strain of the *c*-domain unit cells (Blue) and *a*-domain unit cells (Green) obtained from experiment (Points) and the model (Solid line). The red dots at zero field show the lattice parameter results of powder PZT (x=0.4) and the estimated basic unit cell lattice parameter. The model uses a switching field between 2.7-4.0·10^{6} Vm^{-1} in order to let the strain spike coincide with the spike in the experimental data. Although there is a difference in the absolute value of the strain of the experiment and the model, the general trend of decreasing strain can be observed as the applied electric field is increased. A more detailed view of the out of plane strain in the *c*- and *a*-domain are shown in (b) and (c), respectively.

5.3.2 Discussion on the origin of difference between Model and Experiment

Although the general trend in strain is similar for the model and the experimental data, the absolute strain values are noticeably different. In this section the origin of this difference is discussed. In section 5.5 the corrections for the model are analyzed in order to better understand this. In figure 5.2 we find that there is a disagreement in the difference between the *c*- and *a*-domain out of plane lattice parameters for the model and experiment at any applied electric field with a difference at E_3=0 Vm^{-1} of about -0.009 Å and 0.018 Å, respectively. One can think of the following possible causes for the difference in lattice parameters in a powder sample and in a clamped film:

1. The main cause is likely the interaction between the domains in the clamped film, which is a balance between the lattice parameter difference of the domains, causing a tilt between their out-of-plane crystal directions and the stress at the interface with the substrate caused by this tilting. More details of this can be found in chapter 7. The DW between an *a*- and *c*-domain creates a non-zero tilt (ω_{ca}) between the out of plane crystal orientations of the *c*- and *a*-domain. The angle that the *c*-domain (ω_c) and *a*-domain (ω_a) have with the substrate normal depends on ω_{ca} and ϕ_c through the relation $\omega_{ca} = \omega_c + \omega_a$ and $\omega_a(1-\phi_c) = \omega_c\phi_c$. For the film the tilts ω_c and ω_a are constrained by the substrate since any tilt causes a stress in the film. The amount of stress is dependent on ω_{ca}, ϕ_c and on the domain size. The domain size is expected to be determined by the energy balance between this stress energy and the DW energy. Large domains will cause a larger stress at the substrate film interface due to the tilting and the lattice parameters difference that causes the tilting. How exactly these parameters are connected will be discussed in section 5.5. It can be expected that both the DW energy and the stress energy will increase with increasing ω_{ca}. If an energy term proportional to ω_{ca} is added to

the free energy expression we find that the calculated lattice parameters approach the measured values.

2. Another effect that can play a role is the initial epitaxial growth layer of PZT x=0.4 on the SRO/STO. The PZT is expected to initially grow strained before the layer becomes relaxed through the incorporation of defects. If this relaxation is not complete and the energy to create a defect is larger than the energy caused by an in-plane stress at deposition temperature, than residual in-plane stress (σ_{12}) in the film can arise. In the model as used up till now it is assumed that all unit cell are stress free in the *c/b/a*-phase.
3. Changes in the DW pinning and DW energy arising during cooldown can also influence the stress in the film. At the temperature that the film becomes polarized and forms domains (at the Curie temperature) the misfit strain will change upon further cooling. During this cooling DWs have to move or new ones have to be created to keep up with the changing misfit strain S_m and corresponding domain fraction ϕ_c. Since both mechanisms are expected to need an activation energy there should always be a small in-plane stress in the film below the transition temperature that is not yet resolved by the domain structure.
4. Defects arising in the growth of the film can also play a role. Oxygen vacancies created during growth may lead to stress in the film, similar to the way that STO grown on STO can have different lattice parameters.

Since we do not know what is the dominant mechanism we will not attempt to model these mechanisms and introduces them, we will only attempt to estimate the total stress that they are expected to cause at room temperature and at zero field by considering the differences in out-of-plane strain of the powder sample and the clamped film. The strain effect of these mechanisms will be analyzed by introducing a separate out of plane stress for the *c*- (σ_{3c}) and *a*-domain (σ_{3a}) and a uniform in plane stress

(σ_{12}). The model assumes that at E_3=0 both σ_3 =0 and σ_{12}=0. Now we will estimate how much stress has to be applied on the unit cell of the stress free powder sample to obtain the experimental lattice parameters of the film at E_3=0. To achieve this two new variables are introduced:

1. Although the local out of plane stress (σ_3) does not have to be zero, we do know that the average out of plane stress ($< \sigma_3 >$) has to be zero. If not the sample would expand or shrink until it is zero. The equation for the average out-of-plane stress is $< \sigma_3 >= \phi_c \sigma_{3c} + (1 - \phi_c)\sigma_{3a} = 0$. Thus one expects the *c*- and *a*-domains to undergo a negative (compressive) and positive (tensile) out-of-plane stress, respectively, in order to reduce the out of plane strain difference.
2. The effect of an in-plane stress caused by epitaxial growth, DWs or defects is introduced through σ_{12} which will be assumed to be the same for all unit cells $\sigma_{1c} = \sigma_{2c} = \sigma_{1a} = \sigma_{2a}$. If σ_{12} is negative (compressive stress) both the *c*-and *a*-domain out-of-plane lattice parameter becomes larger and visa versa.

Both values will be calculated by finding the best fit at E_3=0. The following formulas describe the effect on the strain when stresses are introduced:

$$S_{3a}^{XRD} = S_{3a}^{powder} + s_{11}\sigma_{3c}\left(\frac{\phi_c}{\phi_c - 1}\right) + 2s_{12}\sigma_{12} \tag{5.13}$$

$$S_{3c}^{XRD} = S_{3c}^{powder} + s_{11}\sigma_{3c} + 2s_{12}\sigma_{12} \tag{5.14}$$

Where S_{3a}^{XRD}, S_{3a}^{powder}, S_{3c}^{XRD}, S_{3c}^{powder} are the strains obtained from the measured lattice parameter with respect to a_0. From these relations we can extract the stresses:

$$\sigma_{3c} = \frac{(S_{3a}^{XRD} - S_{3c}^{XRD}) - (S_{3a}^{powder} - S_{3c}^{powder})}{s_{11}\left(\frac{1}{\phi_c - 1}\right)} \tag{5.15}$$

$$\sigma_{12} = \frac{\left((S_{3c}^{XRD} - S_{3c}^{powder}) - s_{11}\sigma_{3c}\right)}{2s_{12}} \tag{5.16}$$

With inputs, a_0= 4.043 Å, S_{3a}^{powder}= -0.009591, S_{3a}^{XRD}= -0.005312, S_{3c}^{powder} = 0.02635, S_{3c}^{XRD}= 0.02387 and ϕ_c= 0.72 we find the values σ_{3c}= -2.1977·10^8 N/m^2 and σ_{3a}= +5.6512x10^8 Nm^{-2}. The in-plane stress is about a factor 2 to 5 smaller, σ_{12}= +1.0535x10^8 Nm^{-2}. Note that if the domain fraction is less than 0.64 the in-plane stress would be compressive. A positive σ_{12}, hence small tensile stress, is not expected from a substrate with a larger thermal expansion coefficient than that of the film (effect 2) and a smaller unit cell (effect 3). However, the positive stress may have its origin in the crystals growth defects (effect 4). The in-plane stress, which was assumed to be equal to zero in the model, can also be used to give a better estimate for the misfit strain since the fit for the polarization loop was calculated with $\sigma_{3c} = \sigma_{3a} = \sigma_{12} = 0$. A more realistic misfit strain S_m^0 can be found by using equation 5.4. If we assume that P_s does not change from the value estimated by the model then ϕ_c calculated from the polarization loop should be the unchanged, leading to $S_m^0 = S_m^{model} + (s_{11} + s_{12})\sigma_{12}$. From this we find that $S_m^0 = -0.0040$. Note that both S_m^{model} and S_m^0 strongly depend on ϕ_c. Although the value of S_m^0 might be closer to the real value we will continue to use S_m^{model} in the model since the model will not include the estimates of σ_{3c}, σ_{3a} and σ_{12} found in this section.

5.3.3 Electric field and strain:

The calculated average out-of-plane strain change ($\frac{d<S_3>}{dE}$) over the whole positive electric fields is about -79 pmV^{-1} for the *c*-domain and -101 pmV^{-1} for the *a*- domain, while the value from the experiment is about -19 pmV^{-1} for both domains. Figure 5.3 shows the *c*-domain strain change $\frac{dS_{3c}}{dE}$ and the *a*-domain strain change $\frac{dS_{3a}}{dE}$ as function of the applied electric field. The calculated change in strain at the highest electric field is -66 pmV^{-1} for the *c*- domain and -78 pmV^{-1} for the *a*- domain while the experimental values are around -23 pmV^{-1} and -15 pmV^{-1}, respectively.

The model correctly predicts the sign of the $\frac{dS}{dE}$ of both the *c*- and *a*-domains but the values from the experiment are clearly less negative. We speculate that the cause of this difference is the restricted domain wall interaction, which restricts the change in ϕ_c with applied field due to the increased tilt between the *c*- and *a*-domain. The decreased change in domain fraction results in a decrease in the absolute change in out-of-plane strain. Note that there are spikes in the experimental and model data at the electric field step 2.7-4.0·10^6 Vm^{-1} for both *c*- and *a*-domains due to switching of the polarization of *c*-domains. Here, the polarization in the *c*- domains is aligned opposite to the applied field. This increases the energy term corresponding to the c-domain and decreases the *c*-domain fraction, ϕ_c. The model calculations show that as soon as the film switches, this energy contribution changes sign thus resulting in a sudden decrease in the energy term corresponding to the c-domains and leading to a sudden increase in the c-domain fraction. Similar spikes are observed in all XRD measurements when an electric field is applied. It is important to note that these spikes in strain only happen when scanning the field through the coercive field (where the polarization switches sign), making these high apparent piezoelectric values unsuitable for most practical application. The spike would go mostly unnoticed if the $< d_{33} >$ was measured by using a small AC voltage due to the fact that the spike will only occur at the first passing of the coercive field with subsequent sweeps measuring the $< d_{33} >$ at the coercive field corresponding to no polarization switch.

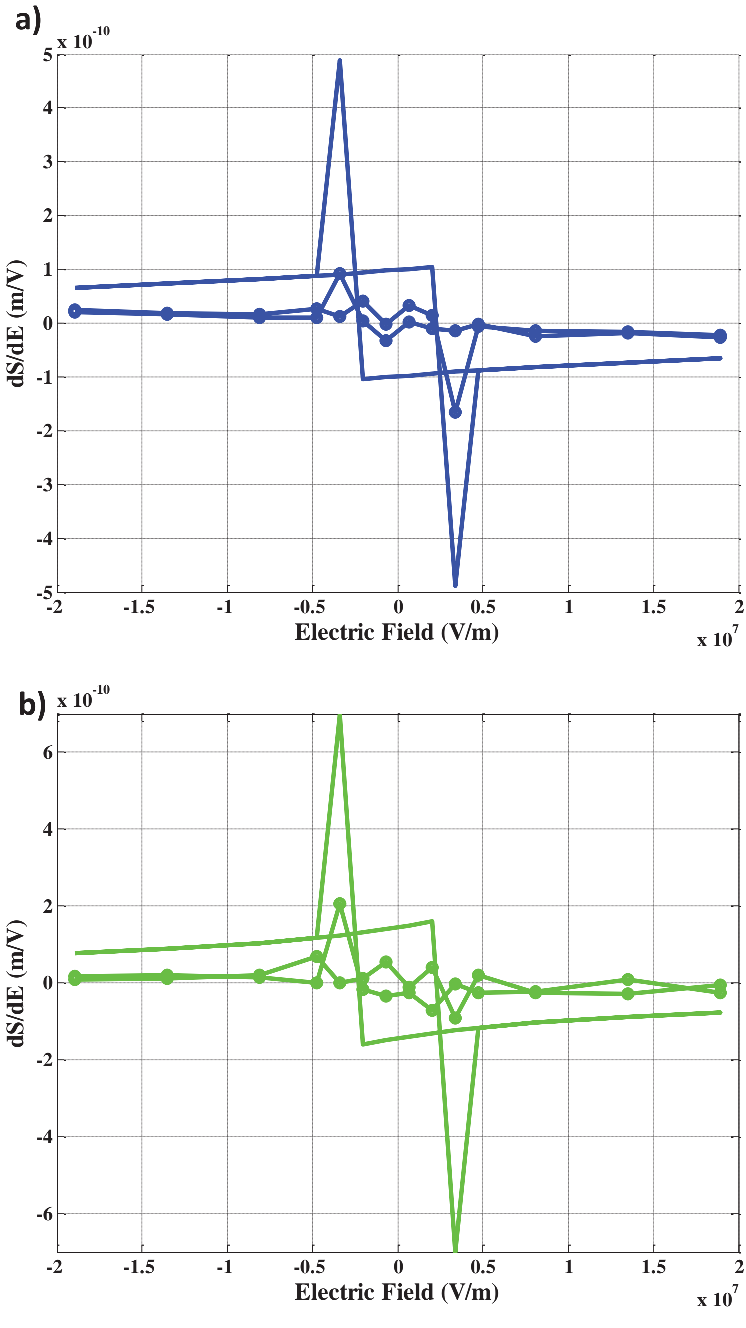

Figure 5.3: The figures show the experimental (dots) and theoretical (solid) $\frac{dS_3}{dE}$ of the *c*- (a) and *a*- (b) domains, respectively.

5.3.4 Domain Fraction

The domain fraction contribution to d_{33} is also determined from the XRD measurements. The absolute domain fraction is obtained by making a ω-χ-scan around the *c*- and *a/b*- domain (004) reflections (Fig. 5.4). The XRD intensities of the two domains are corrected with the structure factor of the bulk lattice. Since this scan takes a long time this correction is only performed to find the initial domain fraction at E_3=0. This value can be compared to the domain fraction obtained from the polarization loop. ϕ_c at different voltages is determined using a ω-scan across the *c*- and *a/b*-domain reflections. This will not give information about the complete intensity, but will show the relative intensity change at different applied electric fields from the measurement at E_3=0. The ω-scan across the *a/b*-domains is centered on the χ value (χ =0) corresponding to the *a*-domain and not the *b*-domain diffraction peaks (Fig. 5.4). Here the angular distance between the *a*- and *b*- domain peaks allows us to collect only data from the *a*-domains. The 4 *c*-domain peaks have a smaller tilt angle compared to that of the *a*-domain, which forces us to use the whole intensity profile of the ω-scan. This might result in a higher measured $\frac{d\phi_c}{dE}$ due to the fact that forward and backward tilted c-domains (Fig. 5.4) (those connected to the *b*-domains) will see a decrease in their χ offset which in turn would correspond to a higher than expected influence of these two c-domains.

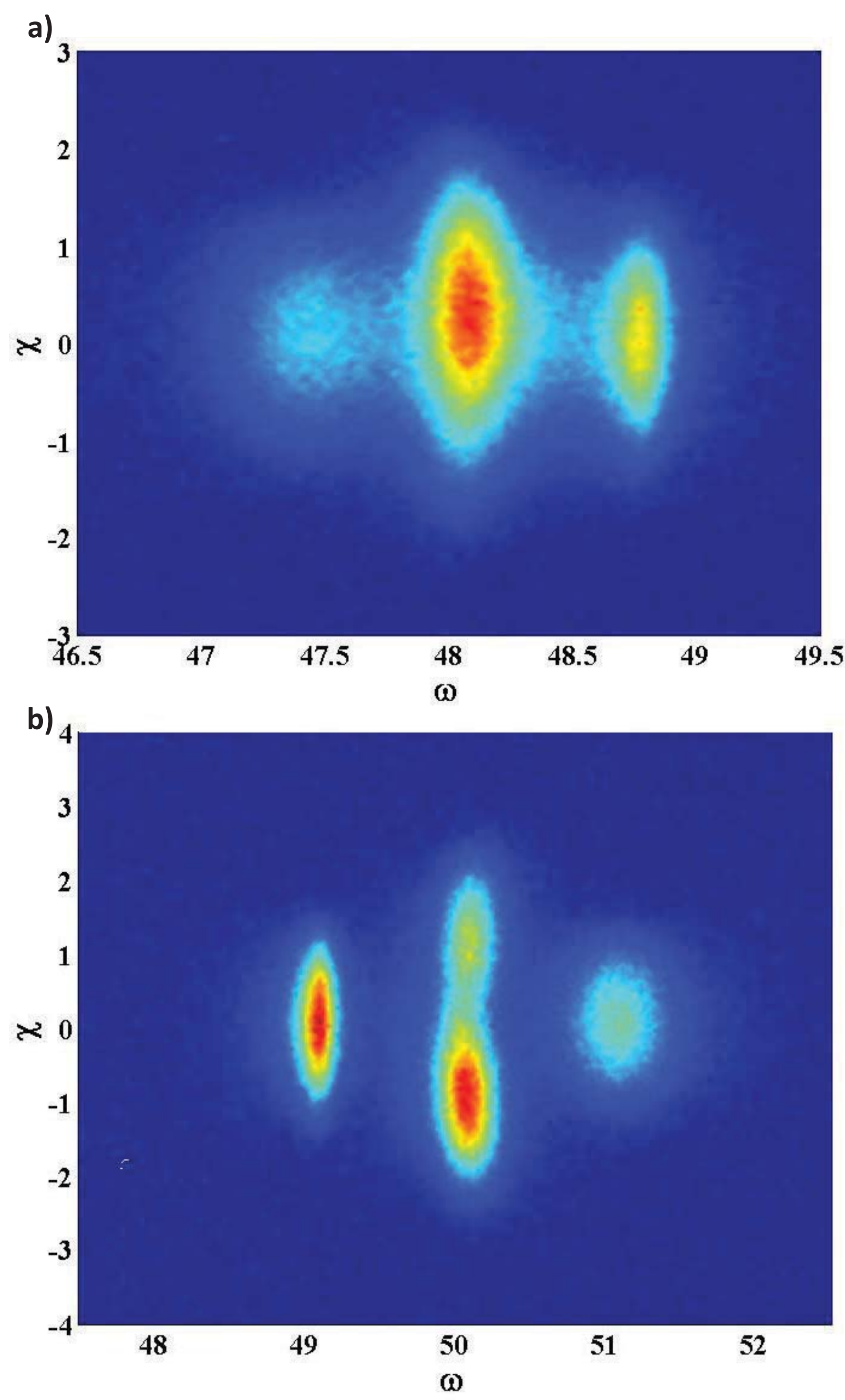

Figure 5.4. XRD ω-χ-scan around the (004) peaks of PZT of a STO/SRO/PZT(x=0.4)/SRO sample. The scan made at (a) $2\theta=96.1^{o}$ shows the *c*-domain diffraction peaks and (b) $2\theta=100^{o}$ shows the *a/b*-domain diffraction peaks. These scans are made after multiple polarization switches, which localizes the peaks (see chapter 7).

Correcting for the background noise and using the structure factor the ω-χ-scan results in a ϕ_c value around 0.62-0.65. There is a slight discrepancy with the value obtained from the polarization loop measurement (0.72 ±0.035 Cm^{-2}). The latter value depends strongly on the bulk polarization value 0.572 Cm^{-2} and the measurement of the area of the capacitor. The former value depends on the structure factor correction, which, may be slightly different in strained compared to bulk (i.e. powder) PZT and also depends on the background noise. Domain fraction estimates with no applied field were also made using TEM data, but the change from a film strained in two directions to a sample that is only 80 nm wide, which is strained in only one direction has a large effect on the domain fraction (chapter 7). In section 5.5 we explore the possible influence of a depolarizing field, which argues that the bulk polarization value might be different from that in PZT films. All together this suggests that the domain fraction calculated through XRD methods is more accurate.

The measurement of the domain fraction during the voltage sweep was performed with a (faster) ω-scan around the 004 peak and was calibrated with the ω-χ scan at zero field. Figure 5.5 shows ϕ_c calculated from the model as obtained from the XRD experiments. The curves are very similar in slopes and switching features, but a significant offset in ϕ_c is observed, which corresponds to the different results in the determination of ϕ_c (E_3=0 Vm^{-1}) from the PE loop (used for the calculated $\phi_c(E_3)$-curve) and for the XRD measurements. The model predicts very well the observed change of ϕ_c with the applied field $\frac{d\phi_c}{dE}$. This is the term that enters the equation for d_{33} (Eq. 5.1). As with the out-of-plane strain of the *c*- and *a*-domains (Fig. 5.3), a spike is observed in the $\phi_c(E_3)$-curve at the electric field range of 2.7-4.0·10^6 Vm^{-1}, which was explained by the switching of the polarization of the *c*-domains at the non-zero switching field.

There are a number of asymmetries that we expect to originate from the initial PZT layer. Because PZT is grown on STO/SRO there is a lattice mismatch which causes strain in the PZT. As the PZT grows thicker defects relax this strain, and the bulk of the grown PZT is largely strain free.

The initial strained PZT layer is polarized through the flexo-electric effect. This fixed polarization is assumed to cause the shift in the switching field to positive fields. This positive shift implies that the initial growth layer has a polarization pointing upwards, corresponding to a negative build in voltage. The initial layer also causes more nucleation points for domains with a similar polarization, which would make the switching transition at the negative applied voltages more smooth and thus decrease the spike height in the domain fraction change in figure 5.5b.

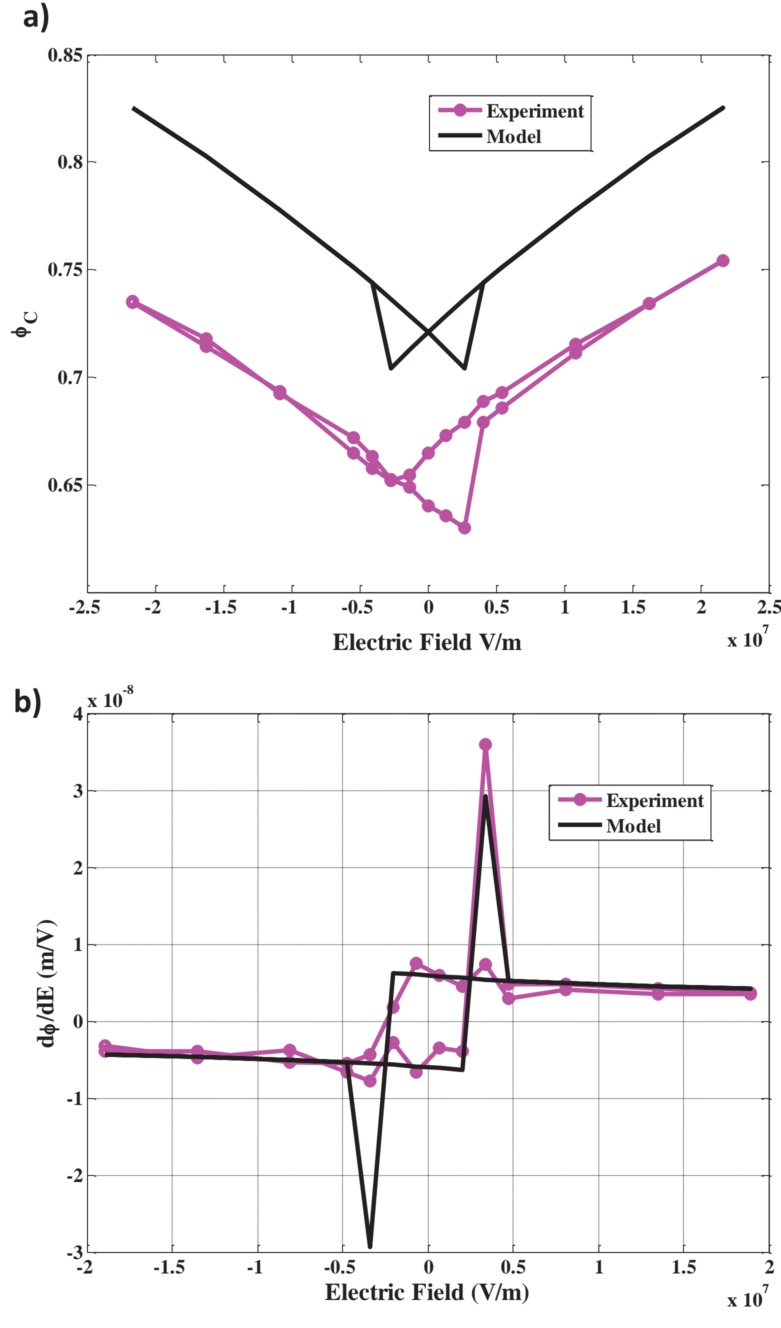

Figure 5.5: (a) The domain fraction obtained by experimental data (pink) and theoretical model (black). (b) The $\frac{d\phi_c}{dE}$ data for both sets.

5.3.5 Resulting d_{33}

From the combined experimental data of the field dependence of the domain fraction and strains the $< d_{33} >$ can be determined using equation 5.1. In figures 5.6a and 5.6b the contribution from the different parts calculated from the numerical model and from experimental measurements are shown, respectively. The domain fraction part $\frac{d\phi_c}{dE}(S_{3C} - S_{3A})$ is given by the blue curve, the c domain part $\frac{dS_{3c}}{dE}\phi_c$ by the red, the a domain part $\frac{dS_{3a}}{dE}(1 - \phi_c)$ by the green and the total $< d_{33} >$ by the black curve.

Although the model and experimental work have some differences the graphs agree on the overall effect of each contribution. The domain fraction part contributes most to the d_{33} while both the *a*- and *c*- domain strain contributions are smaller and negative. The model also predicts the spikes at the switching field observed experimentally.

When looking at the absolute differences of d_{33} between the model and experiment, an overview can be made by using the average of the absolute d_{33}, which gives an idea of the impact of each contribution. The average of the absolute contribution of the domain fraction part is 252 pmV^{-1} for the model and 166 pmV^{-1} for the experiment, while the contributions of the *c*-domain part are 84 pmV^{-1} and 17 pmV^{-1}, respectively, and of the *a*-domain part 41 pmV^{-1} and 10 pmV^{-1}. All experimental values are lower than expected from the model. This is again mainly attributed to the restrained domain motion due to the clamping to the substrate of the domain tilt. Note that d_{33} cannot be expressed in a single value unless the electric field range is specified. This is because d_{33} is not constant versus applied field.

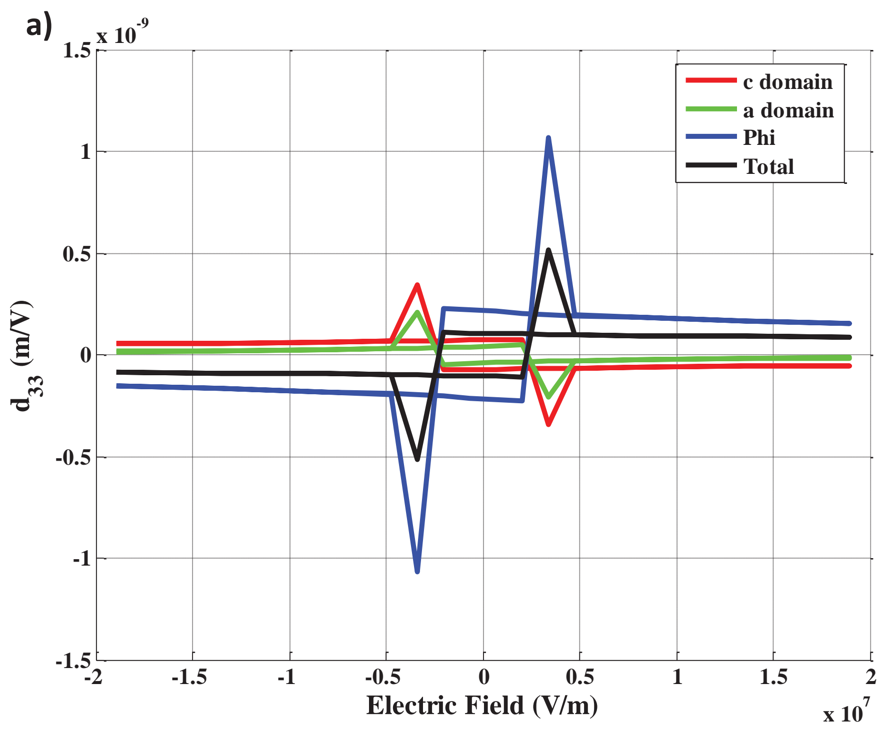

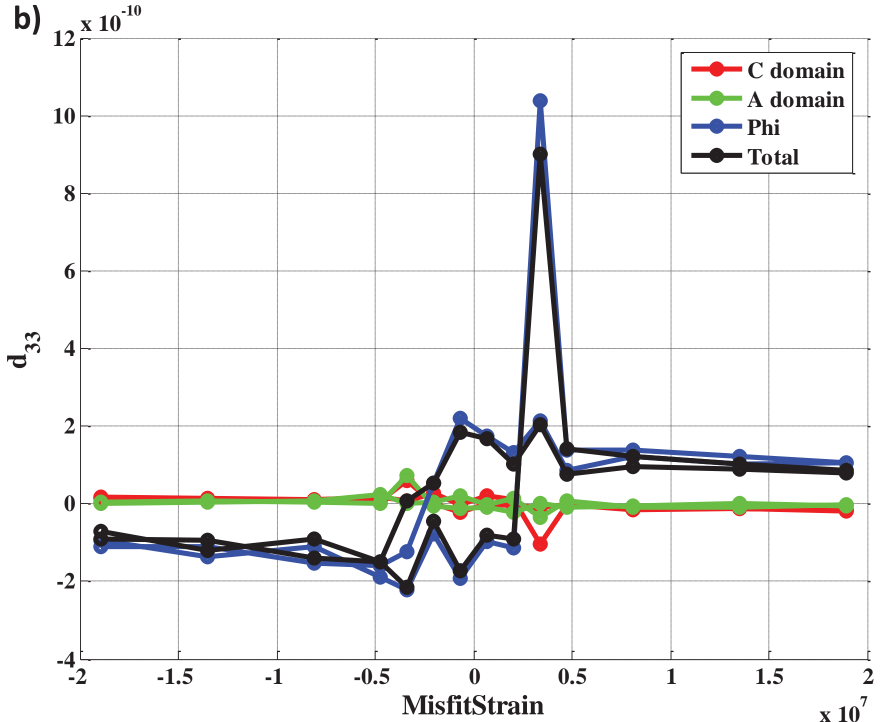

Figure 5.6. In (a) and (b) the separate and total contributions to the d_{33} are shown for the theoretical and experimental work, respectively. The c-domain part (red), a-domain (green) and domain fraction (blue) are given and the resulting $< d_{33} >$ (black) are given.

Adding the individual contributions of both the model and experimental results in the average piezoelectric coefficient, $< d_{33} >$, see figure 5.7. The most important aspect of this figure is the small difference between the model and experimental values. To compare the difference in $< d_{33} >$ between the two methods we compare the part of the d_{33} starting from the highest absolute value of the applied field and returning to zero in order to avoid the spikes in the data when the piezoelectric coefficient switches sign. Going from $2.16 \cdot 10^7$ Vm^{-1} and $-2.16 \cdot 10^7$ Vm^{-1} to zero field in the experimental data results in $< d_{33} >$ values of 102 pmV^{-1} and 106 pmV^{-1}, respectively. From the model data we obtain 96 pmV^{-1} (where $< d_{33}^{E=0} >$=104 pmV^{-1} and $< d_{33}^{E=max} >$=87 pmV^{-1}). Note that the analytical method leading to equation 5.10 predicts a value of 95 pmV^{-1} while the approximation in chapter 4 predicts a value of 185 pmV^{-1}.

Note that one may expect that due to possible domain wall pinning the $< d_{33} >$ obtained by the experiment is smaller than the value obtained by the model for which no domain wall pinning is assumed. A test was done on the model to include an additional energy cost for changing the domain fraction and secondly for changing the tilt angle of the domain with the substrate. Interestingly because of extra stress both these energy costs greatly influence the out of plane strain of both unit-cells and also influence the domain fraction change with the field but the influence on the $< d_{33} >$ is negligible for realistic values of these parameters. This indicates that both DW pinning and domain tilt have an effect on our strain and domain fraction measurements but are too weak to influence the final $< d_{33} >$. That the experiment gives a higher value is expected to happen in part due the uncertainty in the domain fraction obtained from the XRD ω-scans This difference could increase the experimental $\frac{d\phi_c}{dE}$. Another possible cause of the $< d_{33} >$ difference is a change in the structural phase. Around the MPB the $< d_{33} >$ is expected to be high due to phase changes, in our material there could be a phase change in local regions that are on the border between a rhombohedral and tetragonal composition due to strain and compositional inhomogeneities in the PZT.

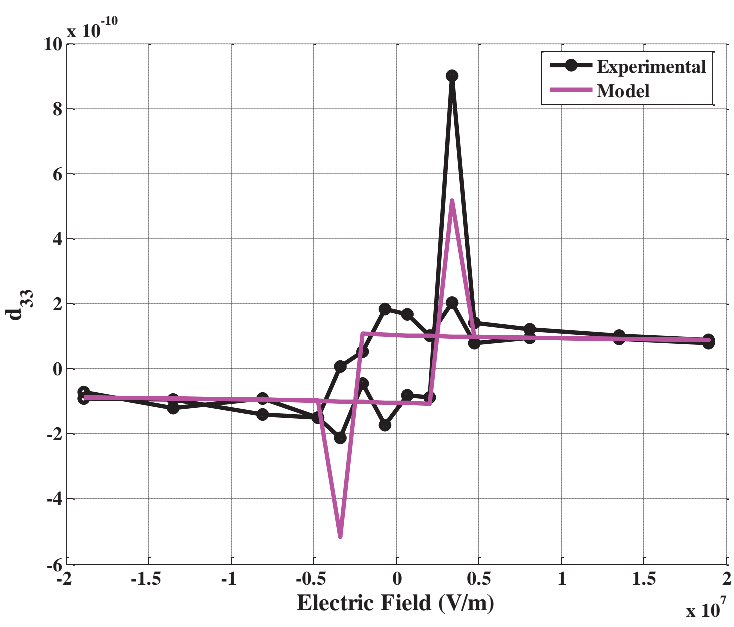

Figure 5.7. Shows the total $< d_{33} >$ obtained though both the experimental data (pink) and the theoretical model (black).

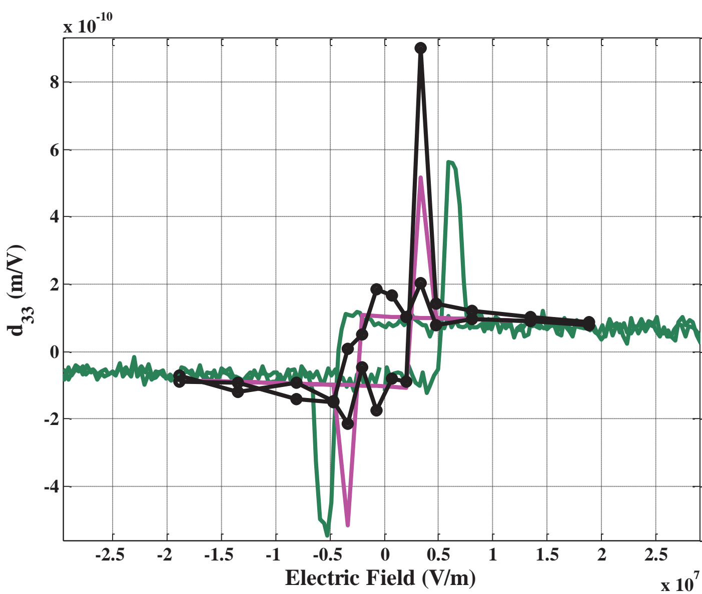

Figure 5.8: Shows the total $< d_{33} >$ obtained though the experimental data (pink) the theoretical model with a switching field at $0.3{\cdot}10^7\,Vm^{-1}$ (black), DBLI measurements (green) which would correspond to the theoretical model, which uses a switching field at $0.62{\cdot}10^7$ Vm^{-1} (blue).

DBLI measurements of $< d_{33} >$ were made on small capacitors (200μm·200μm) on a substrate with a polished and Au coated back surface. The data shows very similar values for $< d_{33} >$ as those obtained by both the model and the XRD experimental data, see figure 5.8. The DBLI data is more stable than the XRD data but it lacks the additional information that is important for better understanding the piezoelectric mechanisms of the film. The DBLI measurement is done with a similar voltage profile as the hysteresis measurement (chapter 2). Here, the thickness of the sample is measured as the voltage increases linearly. This is why the $< d_{33} >$ spike is observed at the coercive field. Note that the type of $< d_{33} >$ measurement is not the same as measurements in which a small AC voltage is applied at different voltage steps. Such a measurement would result in a reduced spike height or no spike at all. The high voltage ramp speed (≈10^4 Vs^{-1}) during the DBLI measurement causes the coercive field (and the location of the spike) to be slightly higher than that observed for the low voltage ramp speed (≈10^{-2} Vs^{-1}) used in the XRD measurement.

5.4 Misfit strain

In this chapter the S_m was obtained by fitting the model to the polarization hysteresis loop. There is another method, based on equation 5.17, which requires the average thermal expansion coefficient difference between the substrate and film, see chapter 2 and 3.

$$S_m = -\Delta T(<\alpha_{Substrate}> - <\alpha_{PZT\ film}>) \quad (5.17)$$

$$<\alpha> = \frac{a_0^{600} - a_0^{25}}{\Delta T\ a_0^{25}} \quad (5.18)$$

Where $-\Delta T = T_d - RT$ with RT the room temperature. Here it is assumed that the PZT is grown at T_d=600°C and that the film is stress free and un-polarized, so that the unit-cell lattice parameter is equal to the basic lattice parameter at this temperature. Note that the PZT film in practice may have some stress from the substrate at 600°. It would be preferable to perform the XRD measurement on PZT powder, but due to the limits of the XRD system used it is only possible to measure on a PZT film. The results of XRD measurements performed on PZT x=0.4 and x=0.2 at 600°C are given in table 5.1. The value of a_0 at 25°C was obtained using the fitting method of section 5.2.2 with the corresponding best fit P_s value also given in the table. Note that the model suggests that the polarization at 25°C of stress free material should be P_s =0.572 Cm^{-2} and P_s =0.701 Cm^{-2} for PZT x=0.4 and x=0.2, respectively.

The linear thermal expansion coefficient of substrates are usually not constant over a large temperature change. Between 600°C and 25° the average linear thermal expansion coefficient are found using XRD, see table 5.2.

Table 5.1. Shows out-of-plane lattice parameters, basic lattice parameter and polarization of PZT x=0.4 and x=0.2 at 600°C and 25°C and the average thermal expansion coefficient $< \alpha >$ over the temperature range.

	a_{3a} (A)	a_{3c} (A)	a_0 (A)	P_s (Cm^{-2})	$< \alpha >$ (10^{-6}K^{-1})
PZT x=0.4 film (T=600°C)			4.065-4.069		
PZT x=0.4 powder (T=25°C)	4.0047	4.150016	4.0434	0.5702	9.29-11.01
PZT x=0.4[19] (T=25°C)	4.0040	4,1500	4.0429	0.5711	
PZT x=0.2 film (T=600°C)			4.0277		
PZT x=0.2[20] (T=25°C)	3.9530	4.1480	3.9980	0.6784	12.92

Table 5.2. Substrate thermal expansion coefficient between 600°C and RT obtained by XRD.

	$SrTiO_3$	$KTaO_3$	Si
Thermal Expansion Coefficient (10^{-6}K^{-1})	10.47	7.65	3.95

Using equation 5.18 the misfit strain for PZT x=0.4 on an STO substrate is found to range between S_m =-0.0007 and +0.0003 while for PZT x=0.2 on STO this value is about S_m =+0.0014. This indicates that the value obtained, for PZT x=0.4 on STO, from the polarization hysteresis loop of S_m =-0.0046 is much lower than would be expected. The cause of this difference will be analyzed in section 5.5.

5.5 Discussion on Model Corrections

The model is able to accurately predict many properties of the PZT film. There are however properties such as the out of plane lattice parameters (a_x) and the c-domain fraction (ϕ_c) for which the model predictions differ noticeably from the experimental values. In this section we change energy terms in the model in order to get an indication of which factors are possible responsible.

5.5.1 Discrepancies

The first discrepancy is the domain fraction that is estimated from the PE loop that is about ϕ_c=0.72 while the XRD data suggest a value between 0.62 and 0.65. The ϕ_c value has a large influence on the tilt of the individual domains (ω_a and ω_c), see chapter 7. The ϕ_c value is very much dependent on the misfit strain (S_m) which was obtained from fitting the polarization loop. S_m can either be chosen to correctly fit ϕ_c from the XRD measurement (0.635) or the total out of plane polarization P_3 (0.412 Cm^{-2}) at zero field, not both. If it is assumed that the ϕ_c deduced from the XRD measurements is correct than one or both out-of-plane polarizations of the individual domains (P_{3a} or P_{3c}) should be higher at zero field. The calculated out-of-plane lattice parameters (a_x) also differ noticeably from the experimentally obtained values, see section 5.3.1. The experimental values suggest a strain difference of S_{diff}=$S_{3c} - S_{3a}$=0.029 while the model suggest a value of 0.036. As was discussed in chapter 3 the values for the polarization and the strain are set values at zero field for the model without corrections.

5.5.2 Corrections

When making additions to a model one should always take care, because everything can be modeled if one uses enough corrections. Here, corrections are introduced which simulate real effects in the film. The correction can subsequently be weakened or strengthened in the model with a coefficient to fit the experimental data. Two considered corrections to the energy are listed below. All corrections were performed on the basic

model (Eq. 3.15). This allows the numerical model to introduce individual out of plane stresses σ_{3a} and σ_{3c}, see chapter 3. Note that none of the corrections below led to a non-zero value for either.

Factor: Energy due to domain tilt differences.

An energy term was added to the free energy equation which represents the stress energy caused by the domain tilts (ω_{ac}, see chapter 7). The added energy is introduced as: $+C_\omega\, \omega_{diff}$. The tilt difference adds energy to the system.

Effect: The term has a large effect on the values of S_{3c} and S_{3a} decreasing the difference between the experimental and model data. The change is caused by an increase of the in-plane stress terms σ_{12} and by the decrease of both P_{3c} and P_{1a}. The unit cells of the *c*- and *a*-domains obtain similar strain values and thus decreases ω_{ca} (Eq. 7.2). The value of P_3 also decreases, requiring an even more negative S_m value in order to achieve the ϕ_c value required to describe the measured remnant polarization. All other parameters are negligibly influenced.

Factor: Energy due to the depolarization field.

The depolarizing field is not included in the energy equation. The free energy equation makes no distinction between the energy cost of an in-plane polarization (P_{1c}, P_{2c}, P_{1a} and P_{2a}) or an out of plane polarization (P_{3c} and P_{3a}) when only top and bottom electrodes are present. These electrodes will decrease the energy of the crystal if the unit cells have an out of plane polarization compared to an in-plane one. The associated energy term was added as $+C_P\ abs(P_3)$. This has the same effect as assuming that the material is subjected to an additional electric field strength out-of-plane.

Effect: The depolarization field factor increases the value of P_3. This is mostly achieved by increasing ϕ_c and rotating the polarization vector in the *a*-domain slightly out-of-plane (P_{3a}), even at E_3=0. Further σ_{12} increases. The term also slightly lowers the piezoelectric coefficient, increases ω_{ac} and has nearly no effect on S_{diff}.

Other energy terms were introduced. An energy term was introduced for the difference between the unit cell strain in the 2-direction for both the *a*- and *c*-domain. This was done because in theory the value of S_{2a} and S_{2c} should be equal at the domain wall. Energy terms simulating logical strain restrictions between the unit cells of domain were also tried. We will not go into details for these corrections. The reason these extra terms are mentioned is that nearly all terms had a negligible effect on the piezoelectric coefficients obtained by the model.

Next we optimized with both domain tilt and depolarizing field effect factors ($C_\omega$and C_P) for the best fit with the experimentally obtained film properties P_3, ϕ_c, ω_{ac} and S_{diff}. After optimization the S_m value was changed from S_m=-0.0046 to S_m==-0.0007 as suggested in section 5.4. The coefficients for the two corrections were adjusted to obtain an optimal fit. Data of some crucial properties are obtained from the original model (1) (using S_m=-0.0007) and can be found in table 5.3. The energy term for the domain tilting is added (2) with C_ω=2.5·10^6 Jm^{-3}degree^{-1}. The energy term for the depolarizing field is also added (3) with a coefficient of C_P=3·10^7 Jm^{-1}C^{-1}.
Using both corrections (3) the differences between the experimental data and the model results have largely been resolved. If both corrections are seen as real the problem of the high P_3 value or a low value of ϕ_c as found experimentally, are explained by an increase in P_{3a} at zero field due to the

Table 5.3: Experimental values and numerical values of the film parameters obtained without (1), with C_ω (2) and with C_ω and C_P (3) at zero field. Experimentally it is not possible to distinguish between the out-of-plane polarization contribution of the individual *c*- and *a*-domain. The in-plane stress of the film is given by σ.

	P_{3c} (Cm^{-2})	P_{3a} (Cm^{-2})	P_3 (Cm^{-2})	ϕ_c
Experimental			0.41	0.635
Model (1)	0.572	0	0.30	0.52
Model (2)	0.574	0.09	0.41	0.66
Model (3)	0.558	0.16	0.42	0.66
	σ (Nm^{-2})	d_{33}(pmV^{-1})	ω_{ac} (^{o})	S_{diff}
Experimental	Null	104	1.70	0.029
Model (1)	0	99	2.02	0.036
Model (2)	4.2x10^{8}	85	2.10	0.037
Model (3)	4.6x10^{8}	92	1.71	0.030

depolarizing field. This allows ϕ_c to remain low in accordance with the XRD data. This also results in a S_m value much closer to that found from other methods, see section 5.4. The domain tilt term has nearly no effect on the ϕ_c but does influence the ω_{diff} and S_{diff} by changing the strain on the unit cells, mostly though the polarization changes. Although the d_{33} value is somewhat reduced, this reduction is small compared to that found from the original model using S_m=-0.0046, which gave d_{33}=96 pmV^{-1}.

With the two corrections we were able to significantly improve the fit of the model to the experimental data. Although both the effect of a depolarizing field and the domain tilting are expected to be present in the PZT film the exact influence is difficult to estimate. If it is expected that the stress caused by the domain wall tilting is only present in the first 50 nm of the film, the domain width is 100 nm and the average domain tilt is 1° (see figure 7.7). With these values it could be estimated that in this layer there would be a maximum out-of-plane strain at the domain wall of around 0.03. This strain correspond to a stress of $4\cdot10^{9}$ Nm^{-2} (see chapter 3) in about 5%

of the PZT film volume, giving an energy term $E = 0.05 \times 0.5 S_{11}\sigma^2$ =3·10^6 Jm^{-3} which, considering that the tilting is around 1.7^o, would make the power coefficient of C_ω=2.5·10^6 very reasonable. The value of the coefficient used for the depolarizing field factor, C_P=3·10^7 Vm^{-1} corresponds to an electric field of that strength and the value of this field is much higher than the externally applied field in the PZT film. The origin of this electric field factor can only explained by an asymmetry in the out-of-plane direction of the film which can only be found in the depolarization field due to the electrodes and the flexo-electric effect in the initial PZT layer.

5.6 Conclusions

In this chapter experimental data are obtain using XRD, ferroelectric and DBLI measurements on a clamped PZT (x=0.4) film. This data is compared to the analytical and numerically predictions made by the thermodynamic model proposed in chapter 3. As a result of the comparison additional energy terms for the model are proposed, which lead to a better understanding of the mechanisms influencing the internal energy of the material and point towards possible improvements for the models. The following conclusions can be drawn from the work done in this chapter.

-Many aspects of an epitaxial poly-domain tetragonal clamped PZT x=0.4 film can be predicted using the model suggested in chapter 3. The model based on the Landau theory of the dense domain structure can be used to give a good indication of what happens in individual unit-cells, such as strain and polarization, and can also produce a good estimate for the maximum average piezoelectric coefficient of the whole sample. One of the most notable predicted characteristics is that the change in the out-of-plane lattice parameter of all unit cells is negative for an increase in electric field, making the intrinsic piezoelectric coefficients (d_{33}^a and d_{33}^c) of these unit cells also negative. But although the intrinsic coefficients are negative, $< d_{33} >$ is positive because the main contribution originating from the domain fraction change ($\frac{d\phi_c}{dE}$) dominates. This indicates that high domain

wall mobility is an important factor for the piezoelectric coefficient. The analytical approach in section 5.2, the numerical model and the data all suggest a value of $< d_{33} >$ at room temperature of around 100 pmV^{-1} for a dense strained epitaxial PZT x=0.4 film on STO grown at 600°C.

-The model also allows for predictions about the material under different DW conditions. We found that with unrestricted DW motion and switching $< d_{33} >$=105 pmV^{-1} at zero field. A single domain film in which the *c*-domain would have a $< d_{33} >$ at least 20% lower, depending on the value of S_m, while a poly-domain film with a constant domain fraction (strong pinning) would have a value about 40% lower. Thus strong DW pinning lowers $< d_{33} >$ significantly. Strong DW pinning also causes the change in out-of-plane strain due to an electric field change to be more positive for both domains ($d_{33}^{c}$and d_{33}^{a}), than is expected for an unstrained unit cell. In the case of unrestricted DW motion the strain in the unit cell might above a given field essentially remain constant while the $< d_{33} >$ becomes only dependent on the domain fraction change. The model predicts that if the misfit strain is within the region ($-0.01 < S_m^{model} < +0.008$) (where ϕ_c is between 0 and 1) $< d_{33} >$ is between 90 and 140 pmV^{-1} at zero field. When the misfit stain is lower than -0.01 the film switches to a film with a single *c*-domain state ($\phi_c = 1$) and d_{33} decreases to 60 pmV^{-1}, while a misfit strain higher than about +0.008 will lead to a film with only a and b domains ($\phi_c = 0$) lowering the d_{33} to nearly zero.

-Adding an energy term caused by a strained film-substrate interface due to the tilting of the domains, and a small depolarization energy term, gives better fits for all parameters. This suggest that the tilting of the domains due to the domain walls play a large role in the observed difference in the out-of-plane strain of the unit-cells of strained and unstrained PZT. The added depolarization term suggests that the out-of-plane polarization of both the *a*- and *c*-domain in a capacitor system is much larger than expected for bulk PZT.

References

[1] S. E. Park and T.R.Shrout, ”*Ultrahigh strain and piezoelectric behavior in relaxor based ferroelectric single crystals*”, Journal of Applied Physics 82(4):1804-1811, (1997).

[2] R. Guo, L. E. Cross, S-E. Park, B. Noheda, D. E. Cox and G. Shirane, “*Origin of the High Piezoelectric Response in* $PBZr_{1-x}TixO_3$”, Physical Review Letters, vol.84-23, (2000).

[3] B. Noheda et al. “*Tetragonal-to-monoclinic phase transition in a ferroelectric perovskite: The structure of* $PbZr_{0.52}Ti_{0.48}O_3$”, Physical review B, vol.61-13,(2000).

[4] G. Catalan, J.Seidel, R.Ramesh and J.F.Scott, “*DW nanoelectronics*”, Reviews of modern physics 84, (2012).

[5] G. Catalan et al.”*X-ray diffraction of ferroelectric nanodomains in pbtio3 thin films*”, Integrated Ferroelectrics. 92, 1, p. 18-29 12 p., (2007).

[6] Dal-hyun do et al., “*In situ x-ray probes for piezoelectricity in epitaxial ferroelectric capacitors*”, Integrated Ferroelectrics Vol. 101 , Iss. 1,2008

[7] Zhengkun Ma et al., ”*Effect of 90° domain movement on the piezoelectric response of patterned PbZr0.2Ti0.8O3 /SrTiO3 /Si heterostructures*”, Applied Physics Letters 87,072907, (2005).

[8] Xiao-hong Du et al”*Crystal orientation dependence of piezoelectric properties of lead zirconate titanate near the morphotropic phase boundary*”, Applied Physics Letters, vol 72-19, (1998).

[9] J. T. Reszat et al.,"*Analysis of intrinsic lattice deformation in PZT-ceramics of different compositions*", J. European Ceramic Society 21, 1349-1352, (2001).

[10] B. Noheda et al., "*A monoclinic ferroelectric phase in the* $Pb(Zr_{1-x}Ti_x)O_3$ *solid solution*", Applied Physics Letters, vol.74-14, (1999).

[11] D. E. Cox et al."*Universal phase diagram for high-piezoelectric perovskite systems*", Applied Physics Letters, vol 79-3, (2001).

[12] C. Vecchini et al., "*Simultaneous dynamic electrical and structural measurements of functional materials*" , Review of Scientific Instruments. 86(10):103901. (2015) doi: 10.1063/1.4931992.

[13] M. J. Haun, Z.Q.Zhuang, E.Furman, S.J.Jang and L.E.Cross, "*Electrostrictive Properties of the lead zirconate titanate solid-solution system"*, J. American Ceramic Society, Volume 72,7-1140, (1989).

[14] F. Jona and G. Shirane, "*Synthesis, Structural, and Electrical Properties of Pure* $PbTiO_3$ *Ferroelectric Ceramics*", Ferroelectric Crystals, MacMillan, New York, NY, USA, (1962).

[15]. A. J. Bell and L. E. Cross,"*A phenomological gibbs function for* $BaTiO_3$ *giving correct e-field dependence of all ferroelectric phase changes*" Ferroelectrics 59, 197, (1984).

[16] V. G. Koukhar, N. A. Pertsev, and R. Waser, "Thermodynamic theory of epitaxial ferroelectric thin films with dense domain structures", Physical Review B 64, 214103, (2001).

[17] N. A. Pertsev, V.G. Kukhar, H.Kohlstedt and R.Waser, "*Phase diagrams and physical properties of single-domain epitaxial* $Pb(Zr_{1-x}Ti_x)O_3$ *thin films"*, Physical Review B 67, 054107 (2003).

[18] V. G. Kukhar, N. A. Pertsev, H. Kohlstedt and R. Waser, "*Polarization states of polydomain epitaxial* $Pb(Zr_{1-x}Ti_x)O_3$ *thin films and their dielectric properties"*, Physical Review B 73, 214103 (2006).

[19] Primary reference: *Calculated from ICSD using POWD-12++* Structure: Frantti, J., Lappalainen, J., Eriksson, S., Lantto, V., Nishio, S., Kakihana, M., Ivanov, S., Rundlof, H., *Jpn. J. Appl. Phys. Part 1*, 39, 5697, (2000). Obtained from Highscore+.

[20] Primary reference: *Calculated from ICSD using POWD-12++* Structure: Frantti, J., Lappalainen, J., Eriksson, S., Lantto, V., Nishio, S., Kakihana, M., Ivanov, S., Rundlof, H., *Jpn. J. Appl. Phys. Part 1*, 39, 5697, (2000). Obtained from Highscore+.

6. Determination of the origin of high piezoelectric coefficients in clamped dense (001) single crystal PZT films.

Abstract:

In this chapter we investigate the origin of high dielectric and piezoelectric properties in dense (001) single crystal $PbZr_xTi_{1-x}O_3$ (PZT) both in bulk and thin films using the thermodynamic model developed in chapter 3 and 4. The piezoelectric properties of PZT films are determined with XRD measurements with the goal of determining the effect of different misfit strains and compositions. In order to obtain a large misfit strain from different substrates, but retain identical crystal growth using PLD, $SrTiO_3$ and $SrTiO_3$/Si are chosen as substrate materials. The effect of columnar growth on the piezoelectric properties of PZT is explored through PLD growth of PZT x=0.52 on platinized silicon and $KCa_2Nb_3O_{10}$ (CNO) nanosheets on silicon substrate[1].

6.1 Introduction

Ferroelectric $PbZr_xTi_{x-1}O_3$ (PZT) with compositions near the morphtropic phase boundary (MPB) has been studied extensively because of the large piezoelectric and dielectric properties. For bulk (unclamped) polycrystalline PZT at room temperature the MPB is found near a PZT composition of x=0.52. The MPB is on the boundary between compositions which give a tetragonal and rhombohedral crystal structure[2-7], see figures 1.2. Many attempts to explain the crystallography and piezoelectric properties at the MPB have done. These include the coexistence of rhombohedral and tetragonal domains[8-11], a monoclinic crystal phase[5][7] and the existence of nanoscale domains[12][13].

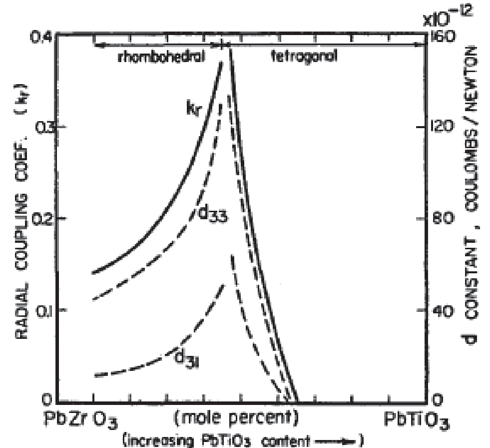

Figure 6.1: The effect of composition on the piezoelectric (d_{33} and d_{31}) coefficients and the electro mechanical coupling facto (k_p) [14].

The individual piezoelectric response of individual tetragonal and rhombohedral unit cells in a bulk PZT system has been approached phenomenologically[15-21]. The lack of large bulk single crystal PZT samples has made studying of the individual phases more difficult. However, work on materials such as $(1\text{-}x)PbZn_{1/3}Nb_{2/3}O_3(x)PbTiO_3$ (PZN-PT)[22], which exhibits a similar MPB as PZT and can be made in larger single crystals, has allowed for experimental confirmation of predictions made by the phenomenological model for unclamped bulk crystals. Similar to unclamped

bulk PZT, clamped single crystal PZT film also exhibits a change in piezoelectric properties for different compositions. However, the value of the piezoelectric coefficients for dense clamped single crystal films are not nearly as high and do not necessarily coincide with the values for the same as they do for bulk unclamped PZT[25].

The better understand the possible cause of the piezoelectric and dielectric properties the phenomenological model presented in chapter 3 is used to predict and explain these properties for PZT ranging from x=0.3 to 0.6 in both the unclamped bulk and clamped film single crystal states. In this model only the tetragonal and rhombohedral solutions are considered. Only these two phases are compared because the presented model predicts that at RT no other phases are expected to be present in the film (figure 4.3). The origin of high piezoelectric properties is analyzed with special emphasis on the influence of misfit strain, the rotation of polarization in the unit cell and the effect of phase changes on the average out-of-plane strain of the PZT crystal. PZT film with x=0.50 and x=0.55 are grown on both STO and STO/Si substrate to test the influence of composition and misfit strain on the piezoelectric properties. Furthermore, the effect of PZT films with a columnar structure grown on platinized silicon and $KCa_2Nb_3O_{10}$ (CNO) nano-sheets is also studied and compared to the model to better understand the properties of partially clamped PZT.

6.2 Bulk single crystal PZT

6.2.1 Polarization rotation

The average piezoelectric coefficients $< d_{33} >$, $< d_{31} >$ and the relative dielectric constant $< \varepsilon_{33} >$ of bulk (i.e. unclamped) single domain PZT (001) crystals of different compositions in the *c*- or *r*-phase were calculated using the model derived in chapter 3. The values are given (table 6.1 and 6.2) for an applied field in the (001) direction for a small (0-10^5 Vm^{-1}) and large (0-10^7 Vm^{-1}) field range. At zero field the simulations show a $< d_{33} >$ ranging between 103 pmV^{-1} and 326 pmV^{-1} for PZT in the tetragonal *c*-phase. PZT with x=0.60 is in the rhombohedral *r*-phase and shows a much higher value

of $< d_{33} >$=761 pmV^{-1}. This is due to the fact that the zero-field polarization of the rhombohedral unit cell is not parallel to the electric field direction. This causes the polarization to rotate in the out-of-plane direction with increasing fields strengths, greatly increasing the value of $< P_3 >$ and $< \varepsilon_{33} >$ and consequently $< S_3 >$ and $< d_{33} >$ through equation 3.5.

If an electric field is applied parallel to the polarization of the rhombohedral unit cell (i.e. the PZT crystal is oriented to have the crystal (111) direction along the 3-direction) the $< d_{33} >$ and $< \varepsilon_{33} >$ of PZT with x=0.60 drops to around 94 pmV^{-1} and 257, respectively. However, for the same field alignment, in case of PZT with a tetragonal crystal structure the electric field will now rotate the polarization towards the (111) PZT crystal direction resulting in much higher dielectric and piezoelectric values, table 6.1. Note that as long as most of the polarization is still along the [001] (or [010], or [100]) axis of the tetragonal crystal structure the material is still considered tetragonal.

The effect of the orientation of the single crystal on the piezoelectric and dielectric properties indicates the main difference between a dense bulk single crystal PZT and bulk polycrystalline PZT. The properties of the latter are the average of the properties of randomly oriented PZT crystallites in which the polarization in some crystallites will and others will not experience a rotation due to the applied field. If the average $< d_{33} >$ for bulk PZT with an electric field along the (001) and (111) direction serves as a simplified model for randomly oriented bulk poly-crystalline PZT it would indicate that the highest piezoelectric properties are to be found between PZT x=0.50 and x=0.60 (table 6.2), which corresponds to experimental measurements[14][23].

6.2.2 Phase change

Phase changes can have a very large effect on the average piezoelectric and dielectric properties due to the abrupt change in polarization orientation. Although one should only consider a PZT unit cell to be tetragonal if its polarization is only in one of the three polarization direction (e.g. $P_3 \neq 0$ and $P_1 = P_2 = 0$) in this chapter, to allow for a better overview, a unit cell with a small additional polarization in the other orientations is still considered to be tetragonal and considered a phase change (e.g. $P_3 \neq 0$, $P_1 \ll P_3$ and $P_2 \ll P_3$ is tetragonal) . This differentiation is possible due to the observed abrupt change in the polarization, which is considered to be the phase change. For example, PZT with x=0.40 with an applied field in the [111] direction has the polarization components (P_3, P_2, P_1) equal to (0.55,0.16,0.16) at the phase switch field E_3^{Phase}≈6.4·10^7 Vm^{-1} (along the (111) direction), where the components abruptly change to (0.33,0.33,0.33). The former is still considered tetragonal in our case while the latter is rhombohedral. For a phase change from the rhombohedral to a tetragonal crystal structure with an electric field along the (001) direction of an analogous reverse transition is observed.

The values of $< d_{33} >$, $< d_{31} >$ and $< \varepsilon_{33} >$ over an electric field range between 0 Vm^{-1} and 2·10^7 Vm^{-1} are given in table 6.2. Bulk (001) single crystal PZT with x=0.60 goes through a phase change from the *r*-phase to the *c*-phase at higher fields E_3^{Phase}≈0.2·10^7 Vm^{-1}. At this phase change the value of $< S_3 >$ abruptly jumps from around +0.0029 to +0.0139. This causes the $< d_{33} >$ of PZT x=0.60 to remain high (745 pmV^{-1}, see table 6.2) although the average $< d_{33} >$ of the PZT single crystal drops to around ≈138 pmV^{-1} once PZT x=0.6 is in the tetragonal *c*-phase. A similar stepwise change of the piezoelectric properties due to crystal orientation with changing electric field had been found in large single crystal PZN-PT[22].

In the model only the rhombohedral phase in a bulk (001) single crystal occurs for PZT x=0.60. It can change to the tetragonal phase for a field applied in the (001) direction. A similar, but reverse phase change can be found for the other compositions. These are initially tetragonal but with a high enough field applied in the (111) direction will become rhombohedral,

see table 6.2. All these phase changes correspond to an abrupt out-of-plane strain change. If the model is forced to accept only a rhombohedral or a tetragonal crystal structure the corresponding S_3 value of a bulk (001) single crystal can be found in table 6.3. Note that this change in phase is not a ferroelectric switch since the phase and polarization will change back when the applied electric field is removed.

One should however consider that the energies of the rhombohedral and tetragonal phase (at zero field) are necessarily nearly equal near the MPB composition. The difference in energy at zero field for PZT x=0.3 , x=0.4, x=0.45, x=0.5, x=0.55, x=0.6 between the tetragonal and rhombohedral phase is 17.1, 6.5, 3.4, 1.5, 0.4 and $-0.4 \cdot 10^6$ Jm^{-3}, respectively. Noheda *et al.*[24] found from experiment that at x=0.55 the material is still in the *r*-phase. This suggests that the actual energy offset is at least $0.4 \cdot 10^6$ Jm^{-3} (i.e. the actual energy cost of the tetragonal phase compared to the rhombohedral phase is higher than our model currently suggests). Due to the small difference in energy between the two phases for near MPB compositions one has to consider that the material either contains both phases or an intermediate phase. For this intermediate phase the monoclinic phase has been considered[5].

If an electric field allows one to switch between the two phases the $< d_{33} >$ can become arbitrarily large at the phase change field strength due to the fact that the model will assume that all the material will change phase at the same field strength (thus at the same time when the field is scanned). This will not happen in a realistic situation for various reasons, for example due to imperfections in the crystal, a local variation in the composition and pinning sites. But, if a bulk single crystal of PZT can be made largely defect free the out-of-plane strain change due to the phase change should be in a narrow field range and result in an extremely large piezoelectric coefficient for this particular field strength. Note that unlike the ‘single use’ large piezoelectric properties found in chapter 5 due to the ferroelectric polarization switch of the *c*-domains, this effect will be reversible around this electric field strength allowing this large piezoelectric effect to be useful in applications. Also note that the model does not give

rise to a mixed phase or transition phase, such as the monoclinic phase, between the tetragonal and rhombohedral phases. Such a transition phase would likely reduce the abrupt out-of-plane strain change and lower the maximum attainable piezoelectric properties found by the model.

Table 6.1. Modeled properties of bulk, unclamped (001) and (111) single domain crystals at T=25°C. The values are obtained in the electric field range E_3=0 to 10^5 Vm^{-1}, the electric field orientation is given in on the left side of the table. The piezoelectric coefficient, $< d_{33} >$, is defined from the average strain change over this electric field range. The polarization of the domain is assumed to have a component in line with the electric field to avoid polarization switching.

(001)	PZT (x=0.30) *c*-phase	PZT (x=0.40) *c*-phase	PZT (x=0.45) *c*-phase	PZT (x=0.50) *c*-phase	PZT (x=0.55) *c*-phase	PZT (x=0.60) *r*-phase
$< d_{33} >$ pmV^{-1}	103	162	235	326	225	761
$-< d_{31} >$ pmV^{-1}	33	59	100	155	97	370
$< \varepsilon_{33} >$	115	197	281	381	338	1766.3
(111)						
$< d_{33} >$ pmV^{-1}	65	127	209	420	665	93
$< \varepsilon_{33} >$	183	397	656	1269	2403	257

Table 6.2. Modeled properties of bulk, unclamped (001) and (111) single domain crystal at T=25°C. The values are averages obtained over the electric field range E_3=0 to $2x10^7 Vm^{-1}$. The piezoelectric coefficient, $< d_{33} >$, is defined as the average strain change over this electric field range. The polarization of the domain assumed to already be in line with the electric field to avoid polarization switching. The electric field required for a phase change is given by E_3^{Phase}. Rhombohedral PZT (x=0.6) changes from the *r*-phase to the *c*-phase for an electric field in the (001) orientation. Tetragonal PZT (x=0.3, x=0.4, x=0.45, x=0.50 and x-0.55) changes from the *c*-phase to the *r*-phase for an electric field in the (111) orientation.

Electric field along (001)	PZT (x=0.30)	PZT (x=0.40)	PZT (x=0.45)	PZT (x=0.50)	PZT (x=0.55)	PZT (x=0.60)
$< d_{33} >$ pmV^{-1}	97	147	205	274	191	745
$< -d_{31} >$ pmV^{-1}	31	53	87	130	82	360
$< \varepsilon_{33} >$	108	174	236	304	272	1228
E_3^{Phase} $x10^7 Vm^{-1}$						0.2
Electric field along (111)						
$< d_{33} >$ pmV^{-1}	62	118	196	627	500	82
$< \varepsilon_{33} >$	168	334	519	1272	1279	215
E_3^{Phase} $x10^7 Vm^{-1}$	18.5	6.4	3.3	1.3	0.2	

Table 6.3. Modeled strain properties of bulk, unclamped (001) single domain crystal PZT in the *r*-and *c*-phase. The values are obtained at T=25°C and E=0 Vm^{-1}. Here the model was forced to give a tetragonal crystal structure for PZT x=0.6 and a rhombohedral unit cell for PZT x=0.55 and PZT x=0.50. ΔS_3 gives the change in out-of-plane strain if the unit cell changes from the *r*-phase to the *c*-phase and ΔG gives the corresponding energy density difference. Here the phase shown in bold is the phase at zero field.

	PZT (x=0.50) *c*-phase	PZT (x=0.50) *r*-phase	**PZT (x=0.55) *c*-phase**	PZT (x=0.55) *r*-phase	PZT (x=0.60) *c*-phase	**PZT (x=0.60) *r*-phase**
$S_1=S_2$	-0.0115	+0.00032	-0.0072	+0.00072	-0.0050	+0.00118
S_3	+0.0242	+0.00032	+0.0167	+0.00072	+0.0135	+0.00118
ΔS_3	+0.0239		+0.0160		+0.0123	
ΔG	$+1.5x10^6$		$+0.4\ x10^6$		$-0.4\ x10^6$	

6.2.3 Dense clamped PZT film

Similar to the bulk (001) single crystal material, the model predicts that the highest piezoelectric and dielectric constants of a clamped (001) single crystal film are attributed to a phase change. The electric field-strain ($E - S_m$) phase diagrams of PZT x=0.50 (Fig. 4.3d) does not show a rhombohedral phase, because it arises at an electric field strength as high as $4{\cdot}10^7$Vm^{-1}. For PZT x=0.60 (Fig. 4.3e) the material is mainly in the *r*-phase at zero field and shows an abrupt phase change in a small range of misfit strains. Figure 6.3 is the phase diagram of PZT x=0.55, which shows a wide range of misfit strains where the material changes from a tetragonal to a rhombohedral phase starting around an electric field strength of $0.4{\cdot}10^7$ Vm^{-1}. At 25°C an increasing electric field will generally push nearly all tetragonal compositions from a tetragonal phase into a rhombohedral phase (Figs. 6.2a-d). Here it is also shown (Figs. 6.2e-h) how the phase diagrams changes if a reasonable (see section 5.5.2) extra energy term of the order of +10^6 Jm^{-3}, is added, for example arising for the domain tilting expected in poly-domain films in the *c/ac*/bc**-, *c/b/a*-, *b/a*- and *bc*/ac**-phases. The average piezoelectric, dielectric and remnant polarization properties of a PZT x=0.40, x=0.50, x=0.55 and x=0.60 films, between 0 and $2{\cdot}10^7$ Vm^{-1} are shown in figure 6.4, 6.5 and 6.6, respectively. The piezoelectric value is generally lower than the theoretical values found for the bulk single crystal (Table 6.2) and range from 70-160 pmV^{-1} for attainable misfit strains values, which range from around S_m=-0.005 to +0.005 (Section 3.3). The average piezoelectric coefficient of any dense single crystal PZT film should therefore be expected to lay within this range of piezoelectric properties over this electric field range. Note that unlike bulk polycrystalline PZT (Fig. 6.1) the model predicts that the piezoelectric properties of clamped film PZT with a near MPB composition (near PZT x=0.50) do not appear to be higher than those of PZT x=0.4 or x=0.6. This is also supported by experimental data shown in table 6.4 [25], showing that all experimental $< d_{33} >$ values are within the range of 50 pmV^{-1} and 105 pmV^{-1} for a variety of misfit strains.

Similar to the bulk single crystal, higher piezoelectric properties are expected to be found at the phase change boundary. Interestingly the average out-of-plane strain change $< \Delta S_3 >$ is not constant along the boundary. For PZT x=0.55 there is actually a decrease in $< \Delta S_3 >$ at the boundary between the *c/b/a*-phase and the *r*-phase at around S_m=-0.032 and E_3=2·10^7 Vm^{-1} when the electric field is increased. Here the $< S_3 >$ of the *c/b/a*-phase and the *r*-phase is +0.0098 and +0.0095, respectively, giving $< \Delta S_3 >$=-0.0003. Near the *b/a*-phase at S_m=+0.047 and E_3=2·10^7 Vm^{-1} the value of $< S_3 >$ is -0.0070 and abruptly increases to -0.0063 when entering the *r*-phase, giving $< \Delta S_3 >$ =+0.0007. This shows that at the boundary between the tetragonal and rhombohedral phase the abrupt average out-of-plane strain change can be negative for low misfit strains while, as the misfit strain is increased, the abrupt average out-of-plane strain change at the boundary also increases, which results in an overall positive strain change for larger values of the misfit strain (figure 6.3). A similar out-of-plane strain difference ($< \Delta S_3 >$) along the boundary of the two phases can be found for PZT x=0.60 and x=0.50. Note, however, that the latter does not show an *r*-phase until an electric field strength E_3>4·10^7 Vm^{-1}. This is partially responsible for the general increase in $< d_{33} >$ and $< \varepsilon_{33} >$ when the misfit strain is increased towards S_m=+0.005. This corresponds with experimental data shown in table 6.4 indicating that a lower substrate thermal expansion coefficient (i.e. higher misfit strain) leads to larger piezoelectric and dielectric properties.

Similar to the bulk single crystal, in theory, an arbitrarily high value of the piezoelectric coefficient can be achieved if a crystal were exactly on the phase change boundary between the tetragonal and rhombohedral phase. In a similar ideal situation the piezoelectric properties can also be arbitrarily negative if the right misfit strain is chosen. Note again that a transition phase, such as a monoclinic phase, would 'smooth out' the phase boundary location and reduce the theoretically possible high piezoelectric properties. If, for example, this smoothing would occur over an electric field range of 10^6 Vm^{-1} then the contribution from the abrupt strain change due to the phase transition (assuming $< \Delta S_3 >$ =+0.0007) would be about 700 pmV^{-1}.

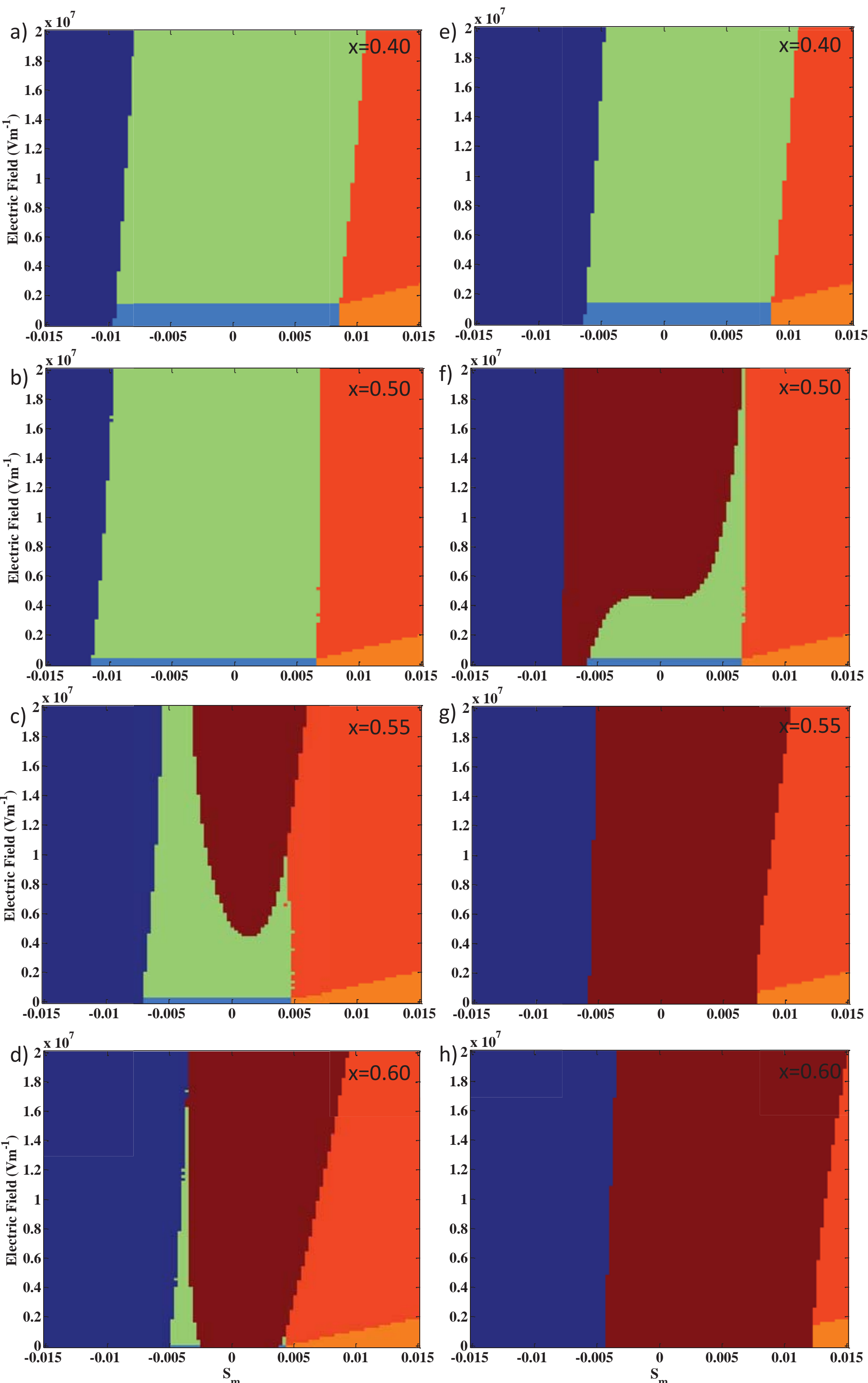

Figure 6.2: Electrical Field-Strain ($E - S_m$) phase diagrams at room temperature of PZT composition close to the MPB. (e)-(h) increased energy term of 10^6 Jm^{-3} (derived from the stress found in the sample in chapter 5) for poly-domain PZT phases such as the *c/ac*/bc**-, *c/b/a*-, *b/a*- and *bc*/ac**- phases. See fig. 6.3 for color information.

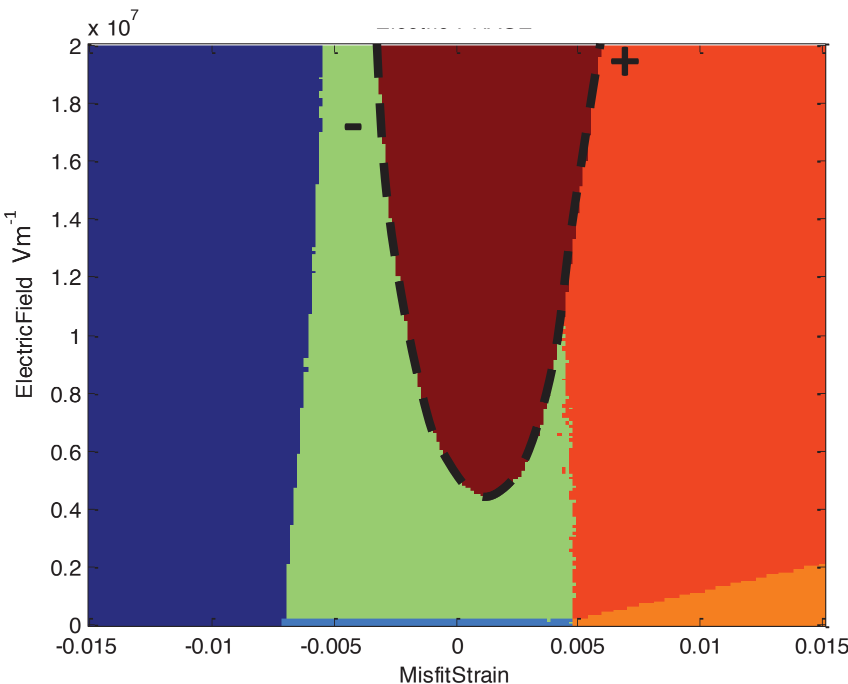

Figure 6.3: Electrical Field-Strain ($E - S_m$) phase diagrams at room temperature of PZT 55/45. The colors represent the *c*-phase (dark blue), *c/b/a*-phase (light blue), b/a-phase (orange), *r*-phase (dark red), *c/ba*/ac**-phase (green) and *ac*/bc**-phase (red). The dotted line shows the region where a first order phase transition is present where the out-of-plane strain abruptly changes. The minus and plus sign indicates the location where the abrupt $< \Delta S_3 >$ change value, due to the phase change, on the dotted line is negative and where it is positive. Along the dotted line this value slowly changes between the positive and negative ends as the misfit strain changes. All other phase transitions in this figure are second order phase transitions.

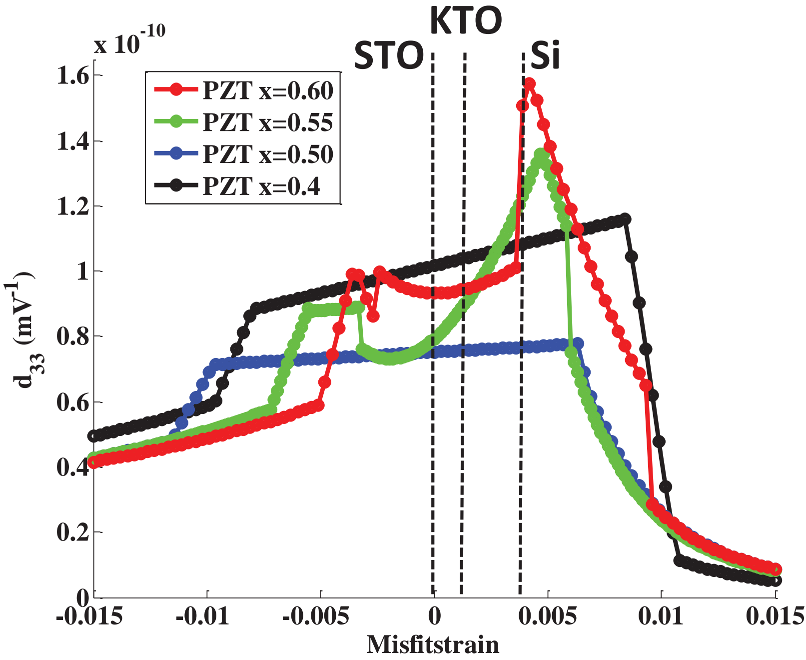

Figure 6.4: Average piezoelectric coefficient $< d_{33} >$ of PZT x=0.6 (red), x=0.55 (green), x=0.5 (blue) and x=0.4 (black) films at T=25°C between E_3=0 and $2{\cdot}10^7$ Vm^{-1}. The black dotted lines represent the misfit strain from different substrate materials (STO (S_m≈0), KTO (S_m≈0.0014), Si (S_m≈0.0035)) assuming that all PZT compositions have a thermal expansion coefficient between 600°C and RT of about 10^{-5} K^{-1} (see section 5.4).

Table 6.4: The table shows remnant polarization P_r, the relative dielectric constant $< \varepsilon_{33} >$ and the piezoelectric coefficient $< d_{33} >$ obtained by Steenwelle *et al.*[25]. Additional information about the thermal expansion coefficient is given in chapter 5.

	Si			KTO			DSO			STO		
Thermal Expansion Coefficient (K^{-1})	$3.95{\cdot}10^{-6}$			$7.65{\cdot}10^{-6}$			$8.7{\cdot}10^{-6}$			$10.47{\cdot}10^{-6}$		
Composition	0.4	0.5	0.6	0.4	0.5	0.6	0.4	0.5	0.6	0.4	0.5	0.6
$< d_{33} >$ (pmV^{-1})	101	105	70	94	100	63	83	95	57	72	90	50
$< \varepsilon_{33} >$	600	610	300	370	520	290	450	405	158	350	315	125
P_r (Cm^{-2})	0.344	0.229	0.230	0.372	0.316	0.237	0.397	0.359	0.269	0.497	0.406	0.275

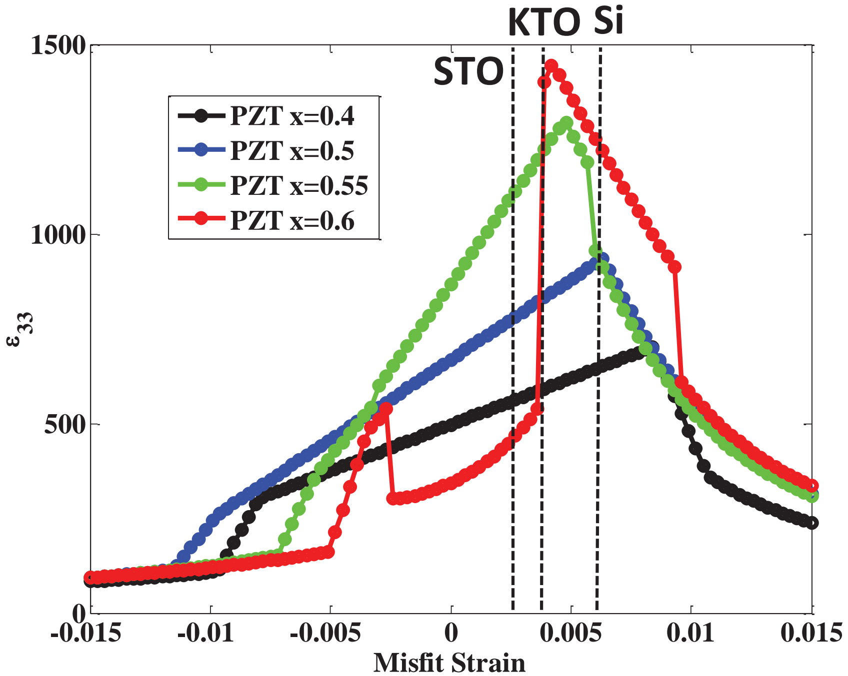

Figure 6.5: Average relative dielectric constant $< \varepsilon_{33} >$ of PZT x=0.6 (red), x=0.55 (green), x=0.5 (blue) and x=0.4 (black) films at T=25°C between E_3=0 and 2x10^7 Vm^{-1}.

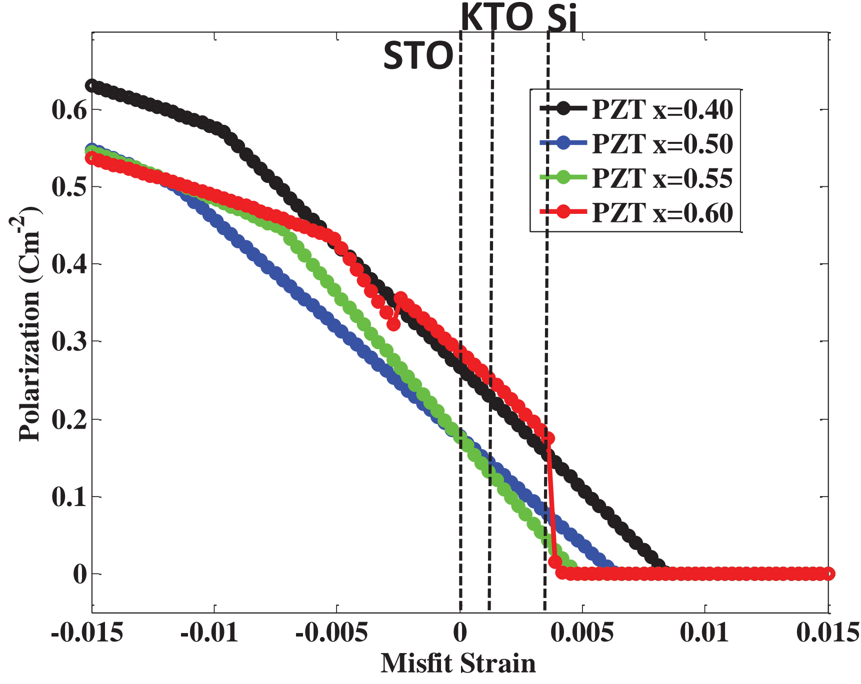

Figure 6.6: Remnant polarization of PZT x=0.6 (red), x=0.55 (green), x=0.5 (blue) and x=0.4 (black) films at T=25°C and E_3=0.

6.3 Experimental comparison

6.31 Misfit strain in dense clamped PZT film.

The abrupt average out-of-plane strain change at the tetragonal-rhombohedral phase boundary can in theory result in an arbitrarily large $< d_{33} >$ value. However, in real world samples inhomogeneities in the PZT composition, crystal defects, pinning sites and possible transition phases will all result in a less well defined phase boundary, similar to the coercive field in a polarization loop, which is generally not a single, well-defined value. The general trends in the piezoelectric properties should however be predictable. For PZT x=0.50 and x=0.55 a higher misfit strain due to a change in substrate should lead to a higher $< d_{33} >$ (Fig. 6.4), as long as the misfit strain is in the range S_m=-0.005 to +0.005. It also suggests that on average $< d_{33} >$ is higher for PZT x=0.55 compared to that for x=0.50.

Four samples were prepared, two with PZT x=0.55 ($Pb(Zr_{55}Ti_{45})O_3$) and two with x=0.5 ($Pb(Zr_{50}Ti_{50})O_3$). In order to have a sufficient difference in misfit strain Si and STO were chosen as substrate material for their large difference in average thermal expansion coefficients. The expansion coefficients were measured between 25°C and 600°C using XRD and found to be $< \alpha_{STO} >\approx$ 10.47·10^{-6} K^{-1} and $< \alpha_{Si} >\approx$3.95·10^{-6} K^{-1} resulting in a misfit strain difference of about 0.0037. In order to exclude the influence of growth conditions the silicon was first coated with a few nanometers thick buffer layer of (001) crystalline STO grown using molecular beam epitaxy (MBE). On top of the STO, a 85nm thick film of SRO bottom electrode was grown using PLD. On this about 900 nm of the piezoelectric material PZT ($Pb(Zr_{50}Ti_{50})O_3$ or $Pb(Zr_{55}Ti_{45})O_3$) was grown with again a 85nm SRO top electrode. The top electrode was covered with 100nm of sputtered gold in order to improve the conductivity of the top electrode and as a protection and adhesion layer for wire bonding. The top electrode was then etched to an area of 4.9x2.4mm, allowing for a contact point to the bottom electrode. The large area capacitor allows for XRD measurements.

To measure the average out of plane strain of the unit cells, 2θ-ω XRD scans were made around the (004) peak of PZT. The scans were made at steps of 1 V between 0 V and 20 V. Figure 6.7 shows the average out-of-plane strain, $< \Delta S_3 >$, compared to the zero field value, versus the applied electric field. The average $< d_{33} >$ of the films over the full electric field range can be found in table 6.4.

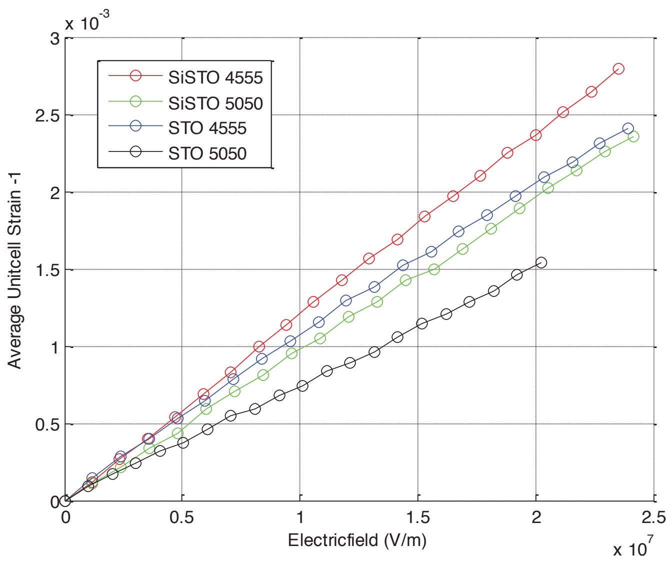

Figure 6.7. *Shows the out of plane strain against the applied electric field for each PZT film.*

Table 6.5. *The average* $< \boldsymbol{d_{33}} >$ *of the PZT films between 0V and 20V.*

	Si/STO PZT x=0.55	Si/STO PZT x=0.50	STO PZT x=0.55	STO PZT x=0.50
$< d_{33} >$ (pmV^{-1})	119	97	101	76

In section 5.4 it was calculated that the misfit strain of PZT on STO was between S_m^{STO} =-0.0007 and +0.0003 for this we estimate that the misfit strain due to the Si substrate to be in the range from S_m^{SiSTO} =-0.0030 to +0.0040. The piezoelectric properties (table 6.5) show a slight trend. The value of $< d_{33} >$ tends to be larger for Si/STO as compared to STO by about 20 pmV^{-1} . This difference can be expected for PZT x=0.55 on the

misfit strain range (Fig. 6.4). Because of the linear change in piezoelectric properties with changing misfit strain, PZT x=0.50 is expected to show an increase in $< d_{33} >$ of 1.4 pmV^{-1} over a misfit strain difference of +0.0035 based on a single phase state over the whole field range. The larger observed difference in $< d_{33} >$ of 20 pmV^{-1} suggests that PZT x=0.50 undergoes a phase change, which, as for PZT x=0.55, is expected to result in a larger piezoelectric coefficient difference.

The measured piezoelectric properties as function of applied field of PZT x=0.50 are generally lower than PZT x=0.55 by about 24 pmV^{-1}. If it is assumed that PZT x=0.50 does experience a phase change, similar to PZT x=0.55, then it should be expected that the piezoelectric properties of PZT x=0.50 are about 14 pmV^{-1} lower, as is suggested by the linear change in $< d_{33} >$ found around S_m=-0.005 in figure 6.4. It is similarly expected that PZT x=0.40 has a larger $< d_{33} >$ compared to PZT x=0.50. The $< d_{33} >$ obtained from measurements on PZT x=0.40 in chapter 5 ($< d_{33} >$=102-106 pmV^{-1}) is 28 pmV^{-1} larger than PZT x=0.50 in accordance with the predicted difference (Fig. 6.4).

6.3.2 Columnar PZT growth

Generally only films which are fully clamped are considered in this work. However, it is possible to create a film with a columnar structure such that the columns are hardly connected with each other. This allows most of the film to be free of the substrate induced misfit strain. Such films are not or hardly restrained by the substrate and will therefore have little mechanical effect on the substrate when under an applied field. Because of this such films are impractical for any application, which uses the in-plane piezoelectric coefficient d_{31}. Due to the lack of a substrate induced in-plane strain the grains in the film can be considered as bulk, unclamped PZT, but with all PZT grains aligned in the same crystal direction. Therefore one might expect that the properties of such a film approach the piezoelectric properties predicted in table 6.1 and 6.2 for an unclamped (001) single crystal material.

The average piezoelectric coefficient of PZT x=0.52 on CNO/Si and Pt/Si are measured to be in the range 376-471 pmV^{-1} and 372-383 pmV^{-1}, respectively. The range originates from the difference between the average out-of-plane strain from the voltage increase compared to the voltage decrease, indicating an change in the crystal structure. The values are larger than those predicted by the model for bulk single crystal PZT x=0.50 and x=0.55 without a phase change. This suggests that PZT x=0.52 to experiences a phase change from the tetragonal to the rhombohedral phase as is seen for PZT 0.60 (Fig. 6.2). Note that the values are larger than those found in bulk polycrystalline PZT[23], where the highest $< d_{33} >$ was found to be 233 pmV^{-1} in PZT x=0.52.

6.4 Discussion

In this chapter it has been shown that it is possible to explain the origin of high piezoelectric properties using the phenomenological model derived in chapter 3 on the basis of a phase change between the tetragonal and rhombohedral phases and a small spatial inhomogeneity in the free energy allowing for these phases to both be present in the PZT material.

A high piezoelectric property in bulk polycrystalline PZT can have its origin in both the rotation of the polarization, aligning to the applied electric field, and the change in phase from a rhombohedral phase to a tetragonal phase, or visa versa. Due to the random crystal orientation of grains in poly-crystalline PZT the highest piezoelectric properties are found on the boundary between the two phases, the MPB, near PZT x=0.50. But it should be expected that for single crystal bulk PZT the high piezoelectric properties will be found more towards lower Zr PZT compositions for an applied field along the (111) crystal direction of the film, while for a higher Zr composition a high piezoelectric coefficient is obtained for crystals with an electric field along the (001) crystal direction. In short one should try to achieve a complete but reversible phase change for all unit cells in the PZT, which either requires a completely tetragonal or completely rhombohedral crystal (at zero-field) depending on the applied field orientation. Although bulk single crystal PZT is difficult to obtain the effect could be observed in thin film samples using columnar growth. It is therefore suggested that for (001) oriented PZT columnar films, PZT with a higher Zr composition than that of the MPB should be used (i.e. PZT x=0.60-0.70).

6.5 Conclusion:

A number of conclusions can be drawn about the origin of high piezoelectric and dielectric properties of both bulk and thin film PZT with compositions in the range of x=0.40 to x=0.60.

-The piezoelectric and dielectric properties of PZT films are generally higher as the misfit strain is increased to a higher positive value. Ideally the highest properties at zero field are found for a material on the boundary between the *c/b/a*- and *b/a*-phase at zero field, so that an applied electric field will cause the film to change to the *r*-phase .

-An electric field applied along the (001) crystal orientation for bulk single crystal PZT will push the material into the tetragonal phase. However, an applied electric field along the (001) orientation for clamped PZT films will push the crystal to the rhombohedral phase.

-For (001) PZT films, a gradual phase change boundary between the tetragonal and rhombohedral phase can be better defined (over narrower electric field range) by, for example, improving the crystal quality. It should be possible to use the phase boundary to achieve very high piezoelectric properties (in this field range) employing the out-of-plane strain change predicted for the transition between the tetragonal and rhombohedral phase. As opposed to bulk PZT a negative piezoelectric coefficient could be obtained in PZT film on substrates with a low misfit strain (Fig. 6.3) by using the same out-of-plane strain change at the phase boundary.

References:

[1] H.Yuan et al., "*Synthesis of KCa2Nb3O10 crystals with varying grain sizes and their nanosheet monolayer films as seed layers for piezoMEMS applications*". ACS applied materials & interfaces, 7 (49). 27473 - 27478. ISSN 1944-8244, (2015)

[2] B. Ja_e, W. Cook, and H. Ja_e. *Piezoelectric Ceramics*. Academic Press, London, "*Ferroelectric behaviors dominated by mobile and randomly quenched impurities in modified quenched lead zirconate titanate ceramics edition*", 1971.

[3] B. Noheda and D. E. Cox, "Bridging phases at the morphotropic boundaries of lead oxide solid solution, Phase Transitions",79:1-2,5-20,DOI:10.1080/01411590500467262, (2006).

[4] B. Noheda et al., "New features of the morphotropic phase boundary in the Pb(Zr1−xTix)O3 system", Ferroelectrics, 237:1, 237-244, DOI: 10.1080/00150190008216254, (2000).

[5] B. Noheda, D. E. Cox and G. Shirane, "*Stability of the monoclinic phase in the ferroelectric perovskite* $PbZr_{1-x}Ti_xO_3$", Physical review B, vol.63, 014103.

[6] B. Noheda, "*Structure and high-piezoelectricity in lead oxide solid solutions*", Current Opinion in solid state and materials science, vol.6,issue 1, p.27-34, (2002).

[7] B. Noheda et al. "*A monoclinic ferroelectric phase in the* $Pb(Zr_{1-x}Ti_x)O_3$ *solid solution*", Applied physics letters, vol.74 14, (1999).

[8] W. Cao and E. Cross. "*Theoretical model for the morphotropic phase boundary in lead zirconate-lead titanate solid solution*". Phys. Rev. B., 47(9):4825, 1993.

[9] G. Rosetti, W. Zhang, and A. Khachaturyan. "*Phase coexistence near the morphotropic phase boundary in lead zirconate titanate (PZT) solid solutions*". Appl. Phys. Lett, 88(7):072912-072912-3, 2006.

[10] J. Ouyang and A.L. Roytburd. “*Theoretical modeling of coexisting tetragonal and rhombohedral heterophase poly-domain structures in lead zirconate titanate ferroelectric films near the morphotropic phase boundary*”. Acta Mat., 54(20):5565-5572, 2006.

[11] P.G Lucuta. “*Ferroelectricdomain structure in piezoelectric ceramics*”. Journal of the American Ceramic Society, 72(6):933-937, 1989.

[12] Y.M. Jin et al., “*Conformal miniaturization of domains with low domain-wall energy: Monoclinic ferroelectric states near the morphotropic phase boundaries*”. Physical Review Letters 91(19):197601,2003.

[13] M. Davis. “*Picturing the elephant: Giant piezoelectric activity and the monoclinic phases of relaxor-ferroelectric single crystals*”. J. Electroceram., 19(1):25-47, 2007.

[14] B. Jaffe, R. S. Roth and S. Marzullo, “*Piezoelectric Properties of Lead Zirconate-Lead Titanate Solid-Solution Ceramics*”, Journal of Applied Physics 25, 809 (1954).

[15] M. J. Haun, Z. Q. Zhuang, E. Furman, S. J. Jang and L. E. Cross, “*Electrostrictive Properties of the lead zirconate titanate solid-solution system”*, J. American Ceramic Society, Volume 72,7-1140, (1989).

[16] M. J. Haun, E. Furman, S. J. Jang, L. E. Cross, “*Thermodynamic theory of the lead zirconate-titanate solid solution system, part I: Phenomenology”*, Ferroelectrics,99:1,13-25. (1989).

[17] M. J. Haun, E. Furman, H. A. McKinstry, L. E. Cross, “*Thermodynamic theory of the lead zirconate-titanate solid solution system, part II: Tricritical behavior”,* Ferroelectrics,99:1,27-44. (1989).

[18] M. J. Haun, Z. Q. Zhuang, E. Furman, S. J. Jang and L. E. Cross, “*Thermodynamic theory of the lead zirconate-titanate solid solution system, part III: Curie constant and sixth-order polarization dielectric stiffness coefficients”,* Ferroelectrics,99:1,45-54. (1989).

[19] M. J. Haun, E. Furman, T. R. Halemane and L. E. Cross, “*Thermodynamic theory of the lead zirconate-titanate solid solution system, part IV: Tilting of the oxygen octahedral”,* Ferroelectrics,99:1,55-62. (1989).

[20] M. J. Haun, E. Furman, E. Jang and L. E. Cross, “*Thermodynamic theory of the lead zirconate-titanate solid solution system, part V: Theoretical calculations”,* Ferroelectrics,99:1,63-86. (1989).

[21] T. Yamamoto, ”*Crystallographic, Dielectric and Piezoelectric Properties of $PbZrO_3$-$PbTiO_3$ System by Phenomenological Thermodynamics*”, Japanese Journal of Applied Physics vol.37 (1998), p.6041-6047.

[22] Seung-Eek Park and Thomas R.Shrout,”*Ultrahigh strain and piezoelectric behavior in relaxor based ferroelectric single crystals*”, Journal of Applied Physics 82, 1804 (1997).

[23] D. A. Berlincourt, C. Cmolik and H. Jaffe, ”*Piezoelectric Properties of Polycrystalline Lead Titanate Zirconate Compositions*”, PROC.IRE, vol.48 (1960), p.220-229.

[24] B. Noheda et al. “*The monoclinic phase in PZT: new light on morphotropic phase boundaries*”, arXiv:cond-mat/0002409 [cond-mat.mtrl-sci], (2000).

[25] R. Steenwelle, “Strain and Composition Effects in Epitaxial PZT Thin Films”, Thesis University of Twente, (2012), ISBN 978-94-6191-293-0.

7. Domain wall structure and motion in dense clamped tetragonal (001) PZT films.

Abstract:

Domain walls (DWs) are a well-known phenomena in any poly-domain material. As was mention in chapters 3 and 4 our model relies upon the fact that the stress caused by the misfit strain can be resolved by the formation of a combination of *c*-, *b*- and *a*- domains. This makes it important to understand how these domains of a clamped tetragonal $PbZr_xTi_{1-x}O_3$ (PZT) film interact with the substrate and each-other and how the domain structure of the film is organized. In addition it is also of interest to understand how this domain structure responds to an applied electric field, since DWs will have to move in order to accommodate the domain fraction change observed in chapter 5.

In this work we will focus on the origin and effect of 90° DWs in tetragonal PZT x=0.20, x=0.37 and x=0.40 films originating from the misfit strain of the film with the substrate. Samples of $SrTiO_3$(STO)/Sr_2RuO_4(SRO)(≈80nm) /PZT(≈800nm) are made using pulsed laser deposition (PLD) with either a SRO, platinum (Pt) or no top electrode. The structure of 2D films (i.e. films clamped in one in-plane direction) are analyzed using transmission electron microscopy (TEM) and compared to the structure of the full 3D films (films clamped in two in-plane directions) using X-ray diffraction (XRD), atomic force microscopy (AFM) and piezo force microscopy (PFM). The interaction between regions with different domain tilts, the initial domain reconstruction and polarization switching mechanics are explored.

7.1 Introduction

Ferroelectric materials can, and usually do, divide into regions with different polarization orientations[12]. Such regions are referred to as domains and the boundaries between these domains are called DWs[1][6][7][8][10]. Unclamped ferroelectric single crystals can lower their total energy by forming domains to reduce the depolarizing field, similar to the formation of domains in magnets due to the demagnetizing field [1][2]. For fully clamped ferroelectric single crystal films with a bottom and top electrode the main origin of domain formation is not the depolarizing field but the relaxation of stress in the film by random nucleation of domains during cooling.

All crystal phases, except for the *p*- phase (table 4.1) due to the lack of an anisotropy in polarization, can and usually do have multiple domains. The *c*-phase, for example, has *c*-domains with its polarization out of or into the plane of the film. Any single crystal with multiple polarization domains must have DWs at their domain boundaries. DWs are specified by the rotation of the polarization across them. For example, for the *c*-phase the domains have an opposite polarization giving 180° DW. A *b*/*a*-phase has 90° DWs between the *b*- and *a*-domain. Note that 180° DW can still exist in the b/*a*-phase between two similar domains, for example the a^+/a^- where the + and – sign indicates opposite polarization directions.

The domain structure and the corresponding DWs are important for the properties of bulk unclamped PZT and clamped PZT films. It is predicted by the model in chapter 4 and measured in chapter 5 that the domain fraction change has a large contribution to the overall piezoelectric and dielectric properties of PZT in the *c/b/a*-phase. For the domain fraction to change the domain structure in the PZT single crystal has to change as well. This can only occur if either new DWs are created or if existing DW can move. In addition, the model proposed in chapter 3 requires a local *c/b/a* domain structure in order to relax the stress in the bulk of the PZT which has its origin in the misfit strain between the film and substrate. Although the *c/a* or *c/b* domain structure is mostly understood, the structure of the *c/b/a*

domain structure has not been explored and will require a better understanding of the DWs present in these clamped PZT films.

In this chapter the aim is to get a better understanding of the domain structure and DWs in the c/b/a-phase of tetragonal PZT. To achieve this, the structure of tetragonal PZT will first be studied through TEM measurements This will allow for a detailed analysis of the structure of individual unit cells, the domain wall structure and the effect of the interface between film and substrate of different domains on this structure. The TEM sample preparation results in a 2D crystal, which is clamped in only 1 direction compared to the 3D crystal of PZT films, which are clamped in 2 directions. Nonetheless the information about the domain structure obtained with TEM will be used, in combination with PFM measurements, in order to better understand the large scale statistical information gathered using X-ray diffraction (XRD) of full (3D) PZT films. The change in the domain structure due to an electric field can also be studied during XRD measurements but cannot be accompanied with TEM data due to the fact that the TEM setup used does not allow for an applied electric field during measurements. To allow for a better understanding of the effect of an electric field on the domain structure, the statistical XRD data will be accompanied with local data obtained using AFM measurements on PZT films with thin top electrodes. These measurements are done on dense, clamped, tetragonal $PbZr_xTi_{1-x}O_3$ (PZT) x=0.20, x=0.37 and x=0.40. Samples of $SrTiO_3$(STO)/ $SrRuO_3$(SRO) (≈80 nm)/PZT(≈800 nm) are made using pulsed laser deposition (PLD) with either a SRO or a platinum (Pt) top electrode, which are used for XRD and AFM measurements, or no top electrode, which is required for PFM measurements. Finally the information gathered about the domain structure will be compared to the domain structure predicted by the model to give insight into possible limitations of the model. Because the current model is based on the assumption that there is no interaction between domains apart from the mechanism of area filling by tuning the domain fraction.

7.1.1 DWs in PZT films with a tetragonal crystal structure

In this chapter we study the tetragonal *c*/*b*/*a*-phase as it is observed in PZT x=0.2, 0.37 and 0.4. Due to the nature of tetragonal ferroelectric materials only 90° and 180° DWs are expected in single crystal thin films. This is because the polarization in each unit cell is equal and due to symmetry there are 6 main polarization orientations, resulting in either 90° or 180° DWs. Due to the importance of stress relaxation our focus will be on the 90° DWs (Fig. 7.4), especially between the *c*- and the *a*- or *b*-domains, since these DWs are required for the different domains to coexist. In our model 180° DWs are not included in order to explain the domain structure of our samples since the +/- direction of the polarization does not affect the strain state of the crystal, except close to the coercive field. In practice 180° DWs will be present during domain polarization switching when the mechanism of switching requires some *c*-domains with an upwards polarization to coexist with domains with a downwards polarization[3]. DWs are also likely to be present at the film-substrate interface due to the initial cube on cube growth of the PZT film. Due to the stress gradient and possible flexo-electric effects this initial layer may have a pinned out-of-plane polarization, even when the rest of the PZT film has switched to an opposite polarization. For our work, the 90° DW is crucial due to the need for coexisting *c*-,*b*- and *a*-domains in the *c*/*b*/*a*-phase, required to relieve the stress, caused by the misfit strain of the film with the substrate.

7.1.2 DWs in unclamped bulk tetragonal PZT

The basic structure of the 90° DWs in tetragonal PZT is formed by the connection between two alternating domains, for example alternating *c*- and *a*-domains (*c*/*a*/*c*/*a*/*c*/*a*), referred to as a *c*/*a* domain region. A schematic of a DW in the *c*/*a* domain region can be readily found in literature[4] (Fig. 7.1).

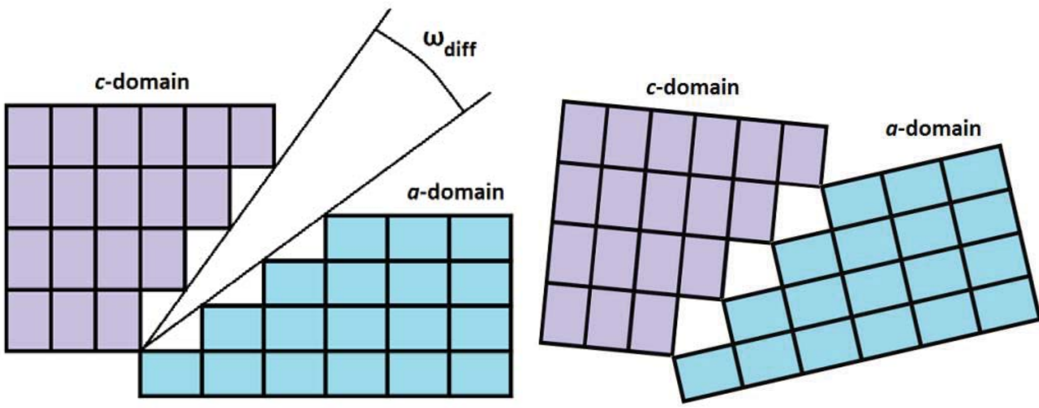

Figure 7.1: An unclamped single crystal with *c*- and *a*-domain will, (a) in theory, have an offset angle between the atoms in the unit cells, which does not allow for a continuous lattice. At the DW in the poly-domain film the domains tilt (b) to allow for a continuous crystal lattice. The deformed unit cells at the DW are the origin of the domain wall energy. Note that the tetragonal nature of the unit cells is exaggerated (chapter 5).

The domains in tetragonal PZT are connected along a DW at about 45° to the polarization direction. Although a 90° DW can in theory have any angle with respect to the polarization direction, in ferroelectric materials one is generally limited to either a 180° DW along the polarization orientation or a 90° DW at 45° to the polarization orientation. The cause of this is that in ferroelectric materials the polarization results in an electric displacement field which has to be continuous over the DWs in order to make the DW uncharged[11]. If the displacement field is not continuous the DW will be charged, which results in an increase in the free energy, similar to the nature of depolarizing fields. For 180° DWs parallel to the polarization direction the displacement field is zero. For 90° DWs the displacement field is continuous across the DW if the components of the polarization vectors at both sides of the DW, that are orthogonal to the DW, are equal, see figure 7.2. Both domains are part of the same single crystal structure the atomic structure of the unit cells of the domains at both sides of the DW must therefore be continuous [5]. To make this possible the unit cell diagonals (101) in the tetragonal crystal structure in both domains are required to have the same length and direction in the DW. In stress free PZT the *c*- and *a*-domain unit cells have identical lattice parameters and only the polarization direction of the unit cell changes across the *c/a* DW, so that the

long axis of the *a*- and *c*-domain will no longer be at an exactly 90° angle, see figure 7.1b. For a relaxed tetragonal crystal structure the angle difference (ω_{diff}) is calculated using the long and short unit cell lattice parameters in the bulk of the domains[5]:

$$\omega_{diff} = 90^o - 2\,\mathrm{atan}\left(\frac{a_{3a}}{a_{3c}}\right) \quad (7.1)$$

Where a_{3c} and a_{3a} are the out-of-plane ((001) or the 3-direction) lattice parameters of the unit cells in the *c*-domain and *a*-domain, respectively. To recapitulate: the polarization orientations of the *c*-domain (001) and *a*-domain (100) are in the 3- and 1- direction, respectively. This polarization is the origin of the strain in the lattice parameter (eq. 3.5) of both domains, making a_{3c}=a_{1a} the long axis and a_{1c}=a_{2c}=a_{2a}=a_{3a} the short axis if the unit cell is relaxed. If the unit cell is not relaxed the strains in any direction are not necessarily equal. For a small ω_{diff} the following approximation for the angle can be used:

$$\omega_{diff} = \frac{90^o}{\pi} * \left(1 - \left(\frac{a_{3a}}{a_{1a}}\right)\right)\left(1 - \left(\frac{a_{1c}}{a_{3c}}\right)\right) \quad (7.2)$$

Note that this equation ignores any shear strains (eq. 3.5) and also the fact that the diagonal lengths and the in-plane strains (S_2^a and S_2^c) should be equal at the DW. The model of chapter 3 does not include any microscopic effects from DWs, but can still be used to approximate ω_{diff} through equation 7.2. In the absence of an electric field the model predicts an angle of ω_{diff}=2.02^o for PZT x=0.4 and ω_{diff}=2.87^o for PZT x=0.20. According to the model the application of an electric field of E_3=2.0·10^7 Vm^{-1} has a very small effect on ω_{diff}, it increases the tilt by approximately 0.06^o.

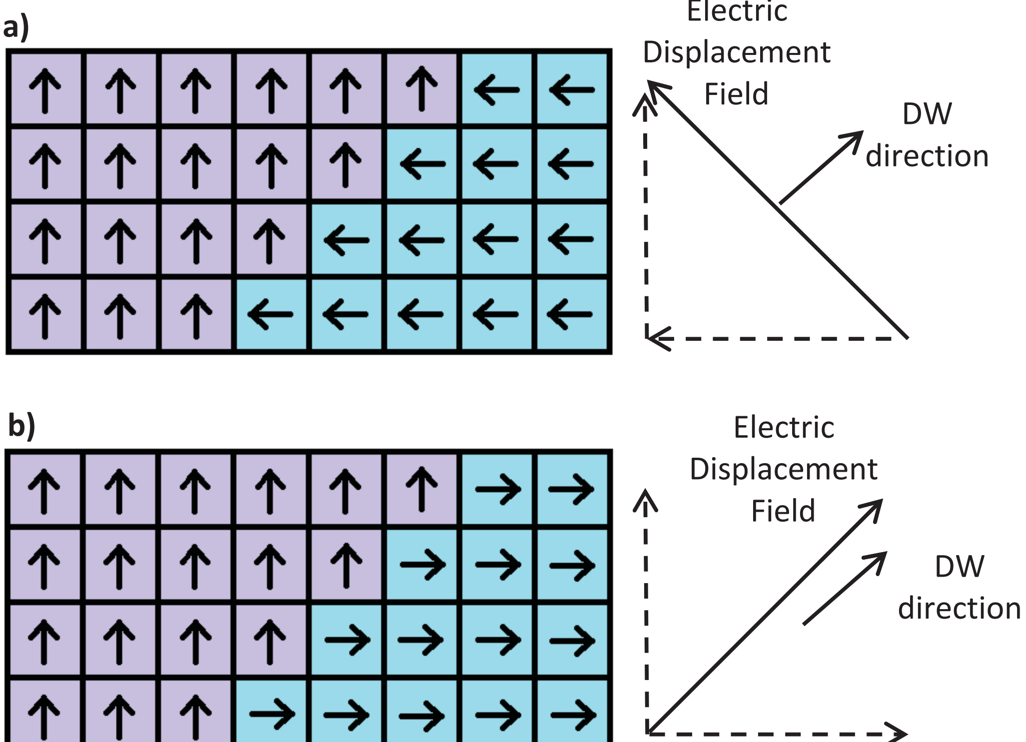

Figure 7.2: Unit cell polarization orientation with respect to a 90° domain wall angles at 45° to the polarization. (a) An uncharged domain wall where the displacement field is perpendicular to the DW direction. (b) A charged domain wall where the displacement field is along the DW direction. The free energy of the charged domain wall is higher than that of the uncharged domain wall.

7.1.3 DWs in clamped tetragonal 2D PZT films.

In TEM measurements the films are constraint in one direction by the substrate, and will be referred to as a 2D film, see figure 7.3b. Here the thickness (or depth) of the TEM sample is much smaller than the height. The result is that the majority of the film is not constrained by the substrate in the depth. The lack of average stress in the major part of the 2D film results in the boundary conditions $<\sigma_2>=<\sigma_3>=0$. Note that the substrate also has a reduced thickness in the 2D film system, which can allow the otherwise stiff substrate to buckle in order to further reduce the stress in the film. A full film will be referred to as a 3D film, when both in-plane

directions of the film are constrained by the substrate and only the out-of-plane direction has no average out of plane stress, $<\sigma_3>$=0.

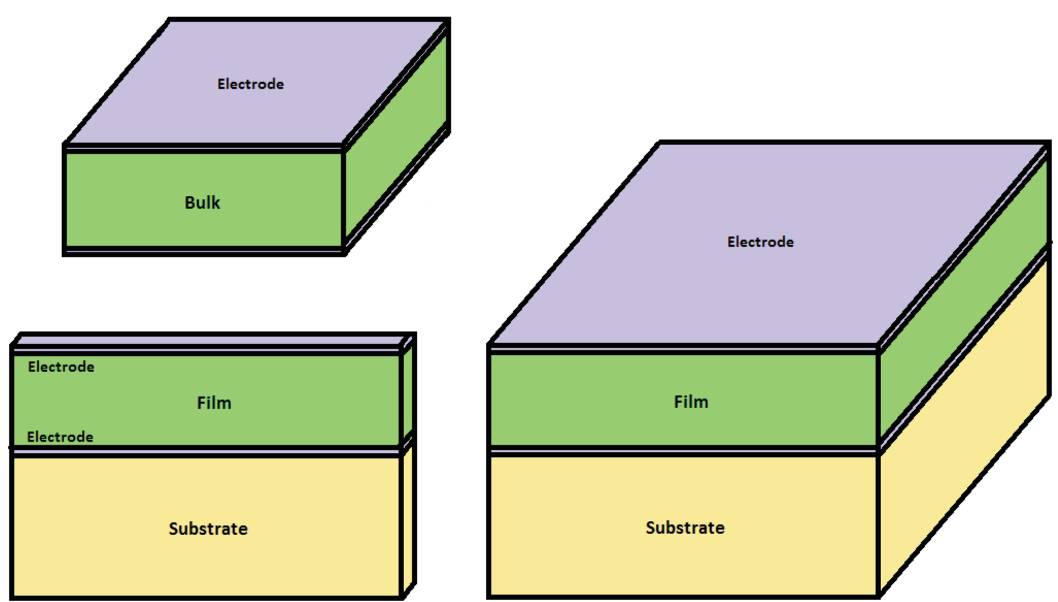

Figure 7.3: (a) Shows a bulk unclamped PZT film. (b) Shows a "2D film" which is constrained in only one direction, the 1-direction (100). (c) Shows a "3D film" which is constrained in both in-plane directions, the 1-(100) and 2-direction (010). PZT (green), electrodes (purple), substrate material (yellow).

The model proposed in chapter 3 does not include local effects at the substrate film interface. Only the average strain over the length (2D) or in the plane (3D) of the film is constrained by the substrate. The type of DW in clamped, tetragonal PZT 2D films are therefore considered to be the same as in bulk, tetragonal PZT. Therefore ω_{diff} can be described by the same equations as in the case of bulk crystal (Eqs. 7.1 and 7.2). We assume that only *c*- and *a*- domains are present in 2D films. This is only true for some systems. When the film relaxes the stress in the (100) direction only *a*-domains and either *c*- or *b*-domains are required. This is because in the relaxed state *c*- and *b*-domains are equivalent with respect to the strain in

the (100) direction, $S_1^b = S_1^c$. In theory the film could either be in a *b/a*-phase, *c/a*-phase or a combination of both. In reality there are a number of reasons why one might expect that the *c/a*-phase has a lower free energy. The depolarization energy of a 2D film would be higher for b-domains than *c*-domains, especially since the films considered here have a bottom electrode so that the depolarization field of *c*-domains is largely screened. The unit cells at the interface with the substrate are still constrained by the substrate reducing the energy cost of the domain with the lowest misfit strain in the (010) direction. It was shown in chapter 5 that the *c*-domain is dominant in PZT x=0.4 on STO indicating that this domain has the lowest misfit strain. Because of these two effects the model of clamped tetragonal PZT 2D films will only take the *c/a*-phase into account and no *b/a*-domain structure. Using TEM it will be shown in section 7.2.3 that this is true for the films considered in this chapter.

The total angle difference, ω_{diff}, does not give any information about the actual angle or tilt between the out-of-plane axis of the substrate and either the *a*- or *c*-domain, ω_a and ω_c, respectively. This can be approximated using the *c*-domain fraction, ϕ_c (see chapter 3), of the film, determined by the mechanical boundary conditions set by the substrate, see figure 7.4. This can be approximated using:

$$\omega_{diff} = \omega_c \left(1 + \frac{\phi_c}{\phi_a}\right) = \omega_a \left(1 + \frac{\phi_a}{\phi_c}\right) \tag{7.3}$$

Both types of domains have an offset from the substrate plane and they must be tilted in opposite directions, see figure 7.4. In this work it was chosen to indicate this by giving the *a*-domain a negative tilt angle and the related c-domain a positive tilt angle (see fig 7.4a). Although a uniformly tilted film, in which the DWs are all tilted to the right (45°) (c/a) or all tilted to the left (-45°) (c'/a'), would have a lower energy, because of the lack of stress at the intersection of both domain regions, both tilts are likely to be present in the 2D film due to the random nucleation of the domain structure during cooling. In this work a domain with the opposite tilt compared to another will be referred to as a *c'*- or *a'*- domain, which

together form a *c′/a′* domain region. Finally we note that equation 7.3 depends on the ϕ_c which is highly dependent on the misfit strain and thus on the substrate material.

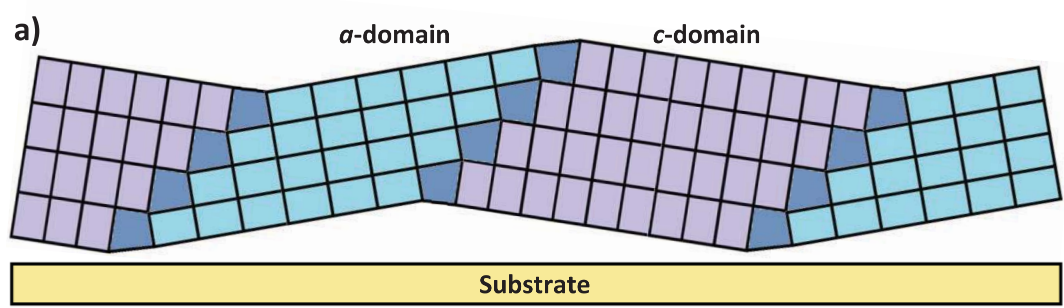

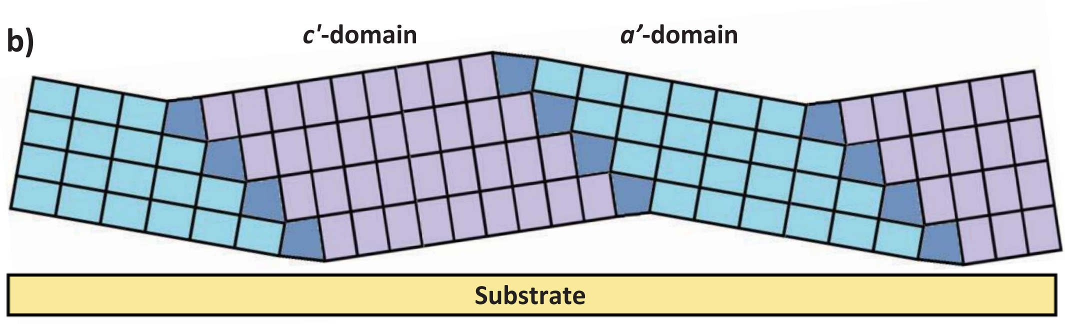

Figure 7.4: (a) The figure shows that the bulk of the film has *c*- and *a*- domain which will on average follow the orientation of the substrate. The average angle of the unit cells must on average be zero with respect to that of the substrate. Therefore angles ω_c and ω_a are dependent on the fraction of the domains according to equation 7.3. (b) shows the same system for *c′*- and *a′*-domains with DW tilted to the left. At the interface a clamped layer is needed in order to have the single crystal connected to the substrate (figure 7.11).

The connection between the domain fraction and thermal misfit strain in 3D films, discussed in section 3.3, is slightly different from that in 2D films. The thermal misfit strain is still defined by equations 3.9 and 3.10 but equation 3.12 simplifies to:

$$1 + S_m = \phi_c(1 + S_{1c}) + \left(1 - \phi_c\right)(1 + S_{1a}) \tag{7.4}$$

In using equation 3.10 the domain fraction can be describe in terms of lattice parameters:

$$\phi_c = \frac{(1+S_m)-(1+S_{1a})}{(1+S_{1c})-(1+S_{1a})} = \frac{\left(\frac{a_{PZT}^{600}a_{STO}^{RT}}{a_{STO}^{600}}\right)-(a_{1a})}{(a_{1c})-(a_{1a})} \tag{7.5}$$

7.2 TEM analysis of 2D films

TEM is used to gain information about the nanoscale structure of the films. A sample with a highly tetragonal crystal structure was prepared for TEM imaging, because of its predicted clear DW structure. A 1µm thick PZT film with a composition of x=0.2 and a 100nm thick SRO bottom electrode was grown on a STO substrate using PLD. Due to the preparation process for TEM two sample areas can be observed, see figure 7.5. One sample has an area with no top electrode (sample A), which was not switched, another area had a 50nm Au top electrode (sample B) and was switched repeatedly (>100x) before the TEM sample was prepared. Here it was investigated what the effect is of polarization switching on the domain structure.

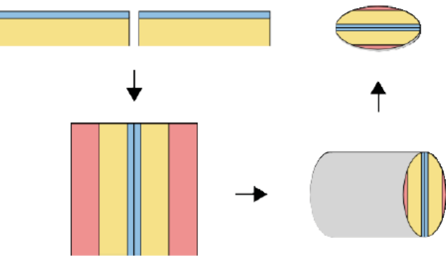

Figure 7.5: TEM sample preparation process. Two samples surfaces are connected using epoxy glue and ground down to a thickness range of 65-100 nm.

The TEM analysis has shown that the sample is a single crystal film with no visible grain boundaries over a range >100 μm. From figure 7.7 it is seen that both samples are in the c/*a*-phase, showing clear 90° DWs, with a thickness in the range of 1-3 unit cells. No *b*-domains were observed. By slightly tilting the incoming electron beam it was possible to obtain a slight overall contrast difference between *a*-domain and *c*-domain areas. It was only possible to focus on one type of *a*-domain at a time. Figure 7.7a therefore only shows one direction of *a*-domain tilting, while the *a'*-domains are indistinguishable from the *c*- and *c'*-domains. Both types of tilting are present in sample A and B with each *c/a* and *c'/a'* domain regions consisting of about 10-20 domains extending over a length of about 1-3μm. Most domains extend from the bottom to the top of the PZT film. Only at the boundary between *c/a* and *c'/a'* domain regions do domains end on other domains.

7.2.1 Tilting and the domain fraction

TEM allows one to observe the unit cell orientation of the PZT film (Fig. 7.6), from a statistical analysis of multiple TEM figures using a 2D Fourier transform (FFT) (Fig. 7.6b). Away from the boundary between a *c/a* and *c'/a'* domain region the ω_{diff} tilt was found to range between 2.2^o-2.8^o, while it was predicted to be 2.87^o for PZT x=0.2. The 2D FFT allows one also to extract the unit cell lattice parameters a_{1a}, a_{1c}, a_{3a} and a_{3c} of the 2D film, table 7.1. In chapter 5 we found that the two short and two long axes of the *a*- and *c*-domains are not equal, indicating that the PZT unit cells are not completely stress free. The TEM measurements also show that the lattice parameters (and the unit cell diagonals) are not equal in the *c*- and *a*-domains. The domain fraction was calculated by estimating the area covered by all *a*- and *c*-domains in the TEM figures. Within the physical size of the figures it generally shows between 4 and 8 domains, which results in a ϕ_c=0.65-0.75 depending on the figure with an average value of ϕ_c=0.71. The domain fraction was also estimated from the lattice parameters using equation 7.5. This equation requires a value for the misfit strain, which was obtained from XRD (as will be discussed in section 7.3.2) and the measured

lattice parameters a_{600}^{STO}=3.930 Å, a_{RT}^{STO}=3.906 Å,a_{600}^{PZT}=4.031 Å. The equation results in an estimate of ϕ_c=0.68. TEM data was also used to compare the *c*- and *a*-domain tilting from the average surface, ω_a=0.8° and ω_c=1.8°. When using equation 7.3 the estimates for ω_a and ω_c are approximately 0.83° and 1.77°.

At the boundary between the oppositely tilted c/*a*- and *c'/a'*-domain regions the *a*- and *a'*-domains can be seen to intersect, see figure 7.7b. Due to the different tilt angles, the *a/a'* boundary has to give rise to some stress in the material. This can be seen in the left top of the TEM image in figure 7.7b. Here the *c*-unit cells of the left and right tilted c/*a*-area has to gradually rotate the long axis and thus the polarization between the *c*-domain and *c'*-domain, see figure 7.7c. This can be considered as a wide, low energy DW between the c- and c'-domains. The result of this DW is that the unit cells in this area are clamped, giving rise to the visible half circle clamped PZT at the top of the sample seen in figure 7.7b.

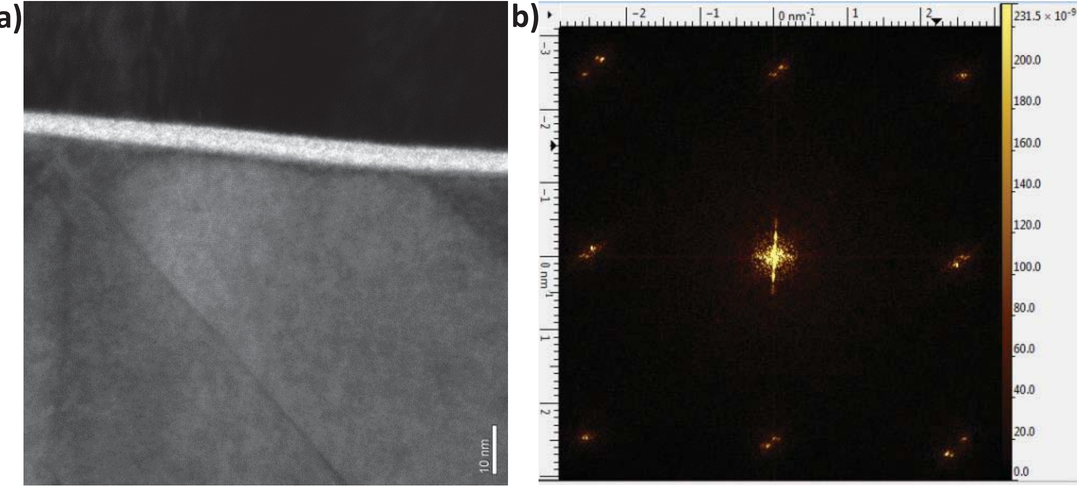

Figure 7.6: (a) A TEM image of sample B showing the PZT interface with Au (white). Two DWs are visible between the *c/a*- domain regions. The unit cells of the PZT are visible. (b) The FFT of image (a) revealing the regular crystal structure and allows one to obtain information on the average unit cell lattice parameters and domain tilting.

Table 7.1: Unit cells lattice parameters of the 2D films deduced from TEM measurements. The domain fraction, ϕ_c, ω_{diff}, ω_a and ω_c are obtained from the TEM and also estimated from the lattice parameters using equation 7.2, 7.3 and 7.5.

	a_{3c}	a_{1c}	a_{3a}	a_{1a}
TEM (±0.025 Å)	4.107Å	3.945 Å	3.933 Å	4.137 Å
	ϕ_c	ω_{diff}	ω_a	ω_c
TEM	0.65-0.75	2.2°-2.8°	1.8° (±0.1°)	0.8° (±0.1°)
Estimated	0.68	2.6°	1.77°	0.83°

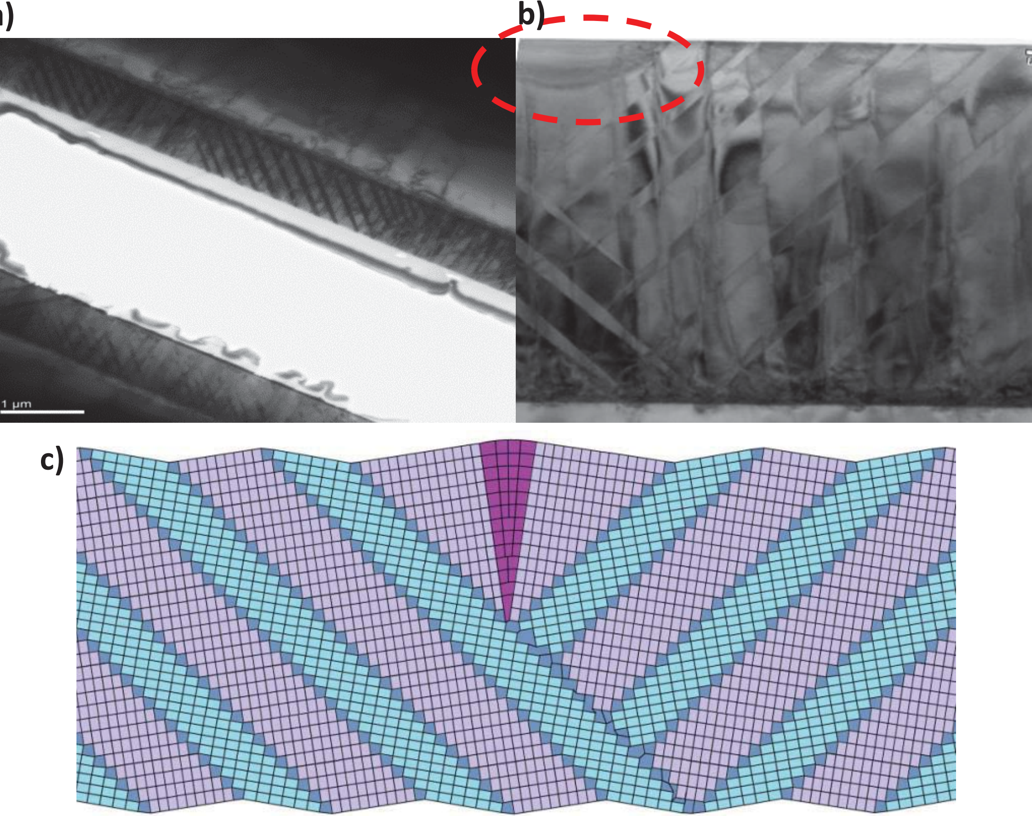

Figure 7.7: (a) TEM image showing both sample A (top) and sample B (bottom) showing *c/a*-domain regions. (b) Close up of the domain structure over the whole PZT film thickness. Here *c/a*- and *c'/a'*-domains are interacting at their boundary. At the top a large clamped *c/c'*-domain is visible in the red circle. (c) A rough visual representation of the unit cell structure at the boundary between *c/a*- and *c'/a'*-domains. The dark purple area represents the strained *c*-domain unit cells.

At the *c/a* and *c′/a′* boundary the *a*-domain ends when it intersects with another *a′*-domain. The *a*-domain predominantly ends by narrowing into a needle shaped domain till it interacts with the a'-domain, see figure 7.8a-b. At these intersections the *c*-domain orientation also needs to rotate to adjust to the *c′*-domain similar to that seen in figure 7.8b.

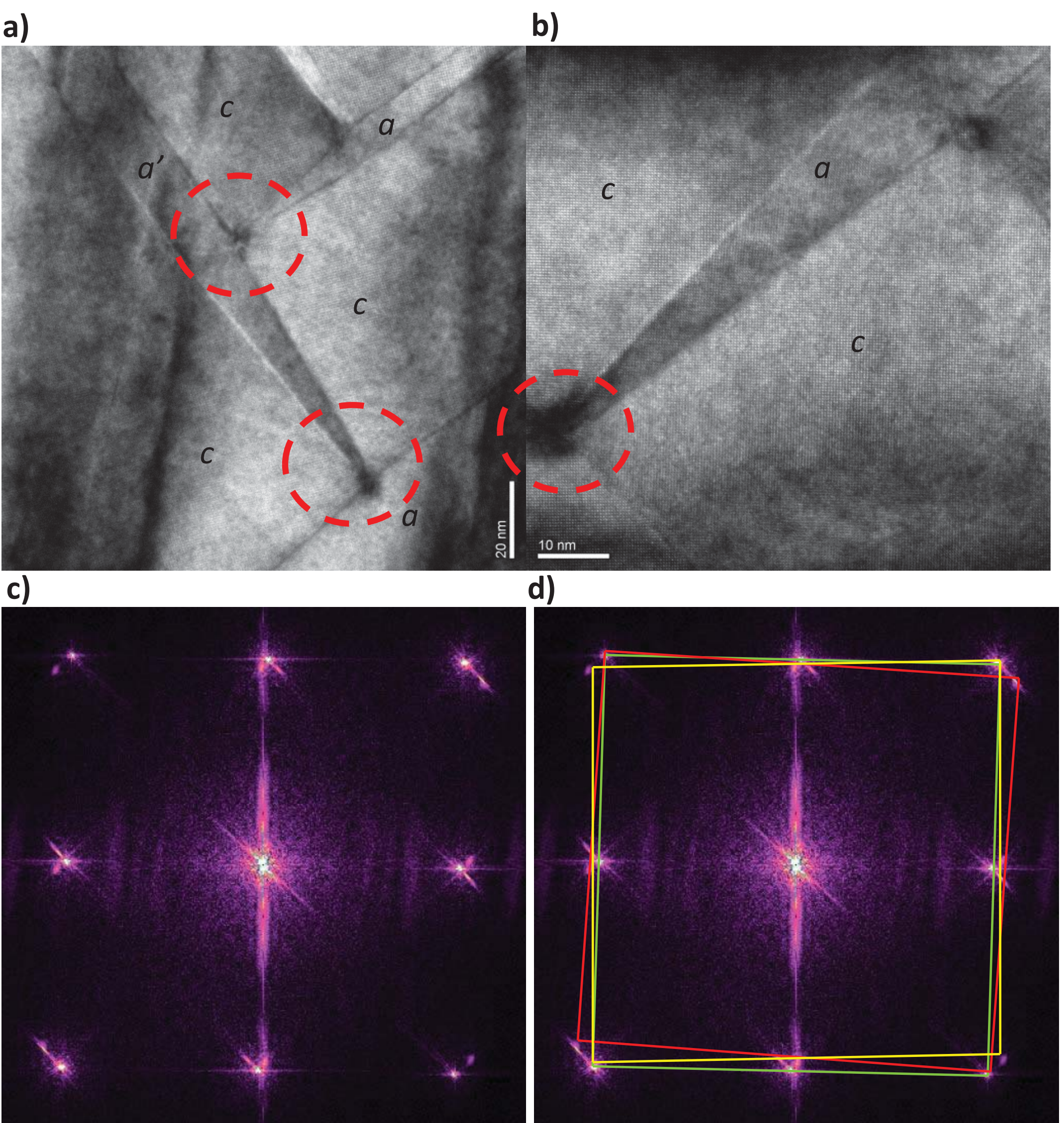

Figure 7.8: (a) TEM image with unit cell resolution of the intersection between the *c/a*- and *c′/a′*-domain regions showing needle *a*-domain narrowing (red circles). (b) Zoom in on the needle structure. (c) 2D FFT of figure (b). (d) shows three unit cell structure indicating 3 domains. The red and yellow tetragonal structure show the tilt of the *a*- and *a′*-unit cells, respectively. The green structure is the c-domain unit cell found near the boundary. The c-domain has only one tilt.

FFT analysis of figures 7.8b is presented in figure 7.8c-d. These figures show that only one *c*-domain orientation is present and that both the *a*- and *a*'-domain are tilted nearly equally from it, see table 7.2. This indicates that at the intersection the *c*-domain is oriented nearly perfectly out-of-plane. Note that the *c*- and *c'*-domains away from the boundary are both tilted away from the out-of-plane direction. This is likely the cause of the spreading out of the *c*-domain in the ω-direction as was observed in XRD data (figure 7.12). This *c*-domain with zero tilt is expected to only be present due to the local influence of *a*- and *a'*-domains. Due to the length of the *a*-domain this would indicate that the *a*-domains have a slightly different tilt, ω_a, at the intersection than away from it.

Table 7.2:Tilts information on both the in-plane and out-of-plane crystal directions of the *a*- and *a'*-domains compared to the in-plane and out-of-plane crystal directions of the *c*-domain, obtained from figure 7.8d.

Error ±0.3^o	Out-of-plane tilt offset	In-plane tilt offset
a-domain	+1.9	+2.1
a'-domain	-1.8	-2.7

For sample B, which was switched and has a top electrode, the PZT has triangular shaped areas near the top electrode. This effect is missing in the PZT sample without a top electrode, see figure 7.9a. This triangular area is usually found in the *c*-domain. When figure 7.9b is analyzed using the 2D-FFT it is found that the area has no different unit cell structure from the rest of the *c*-domain, see figure 7.9c. As discussed in the work by Peng Gao *et al.*[3] it can be interpreted as a *c*-domain with the opposite polarization giving a 180° DWs that are visible in this way in the TEM data. No other differences were found between sample A and B.

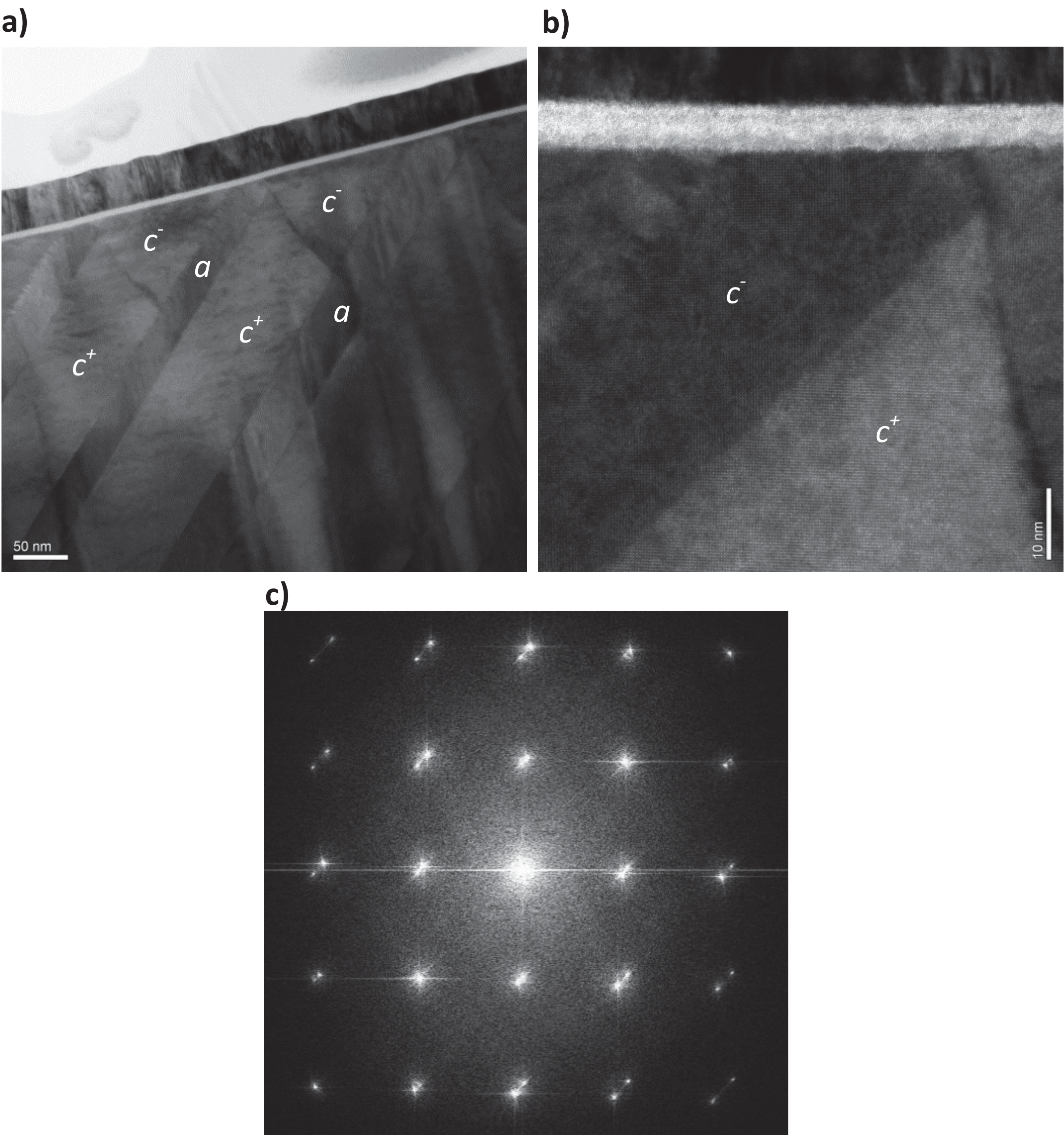

Figure 7.9: (a) TEM image with unit cell resolution near the top electrode of sample B. The figure shows a triangular structure at the end of the *c*-domain. (c) 2D FFT of the zoomed in TEM image (b). The 2D FFT only shows that only *c*- and *a*-domains are present in near this triangular area.

7.2.2 Discussion on 2D films

DWs are necessary to reduce the stress in and with that the energy of the film. However, due to the deformation of the unit cells at the 90° DWs (Figs. 7.1b and 7.3), the energy of the film is also slightly increased. The energy associated with the deformation of the unit cell at the DW is the DW energy, E_{DW}. Because of the DW energy an unclamped tetragonal single crystal (for which the depolarizing field is negligibly small) would be in the lowest energy state when it has only a single domain. The domain size would therefore ideally be as large as the crystal.

A clamped 2D film is in the poly-domain *c/a*-phase and therefore has 90° DWs. The model of chapter 3 can estimate the domain tilt, but gives no information about the size of the domains. Unlike an unclamped bulk single crystal an extra energy term can be introduced that accounts for the elastic energy cost due to the strain at the interface between the film and substrate E_{IFS} (Fig. 7.5). Because this energy is related to the interface layer that forms the connection between the substrate-film interface and the domains in the bulk of the film, it is independent of film thickness. It is dependent on the domain tilts (ω_c and ω_a), domain widths and on the in-plane strain difference with the basic unit cell lattice parameter. The balance between E_{DW} and E_{IFS} results in a film thickness dependent domain size, which explains the local DW pattern observed. These energy terms are not added to the model due to the lack of information about the quantitative contribution of these terms making the addition to the model solely a fitting parameter. From the dependence of the domain size on the thickness it is predicted that as the sample is grown thicker, domain sizes will grow.

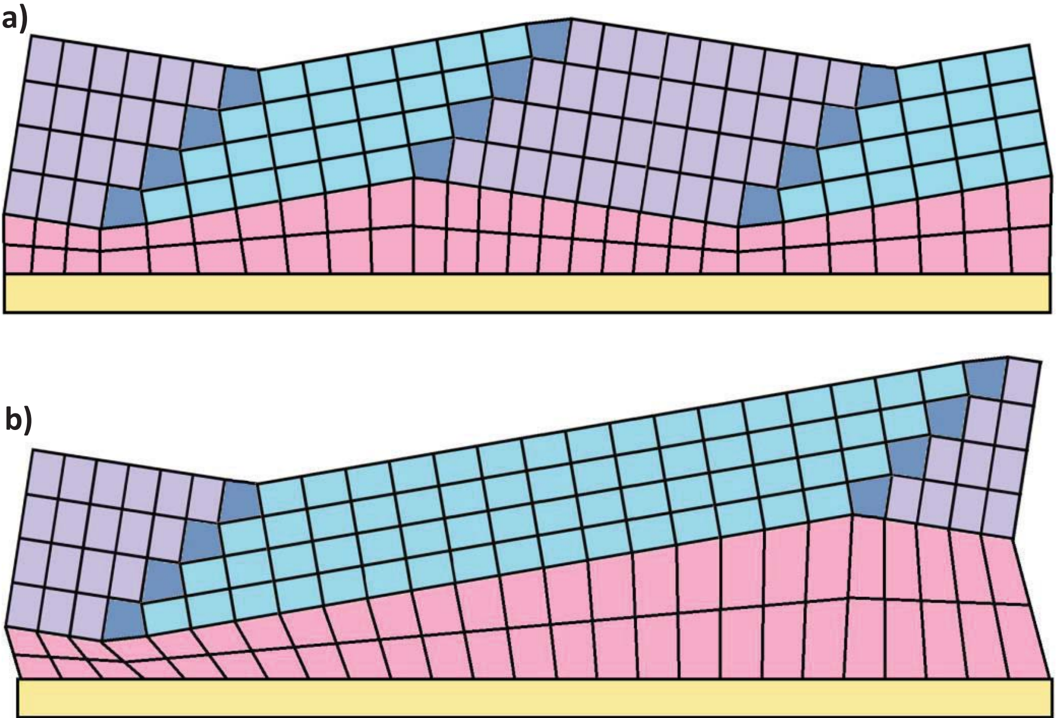

Figure 7.10: A visual representation of DWs (dark blue) and the clamped PZT interface layer (pink). (a) Smaller domains leading to more domain walls and a less clamped interface layer. (b) Larger domains with less DWs but a more strained interface layer leading to a lower E_{DW} and higher E_{IFS} compared to (a).

7.3 3D PZT films

7.3.1 DWs in clamped tetragonal 3D PZT films.

Samples analyzed with TEM are necessarily thin (65-100 nm). The main difference in the domain structure between 2D and 3D films is the lack of *b*-domains in the first, due to the zero in-plane stress. A 3D film analyzed with AFM, see figure 7.11, shows a complicated maze-like structure with a 4 fold symmetry indicating that both c/b and c/a DWs are present. The origin of the large difference can be understood through the domain tilt (Fig. 7.4 and 7.5). No *b/a* DWs are visible in AFM scans, which would show up as lines at 45° to the *c/b* and *c/a* DWs. In PFM images some indications for *b/a* DWs are found, see section 7.3.6. The largescale lack of *b/a* domains indicates that, as with the TEM sample, the *c*-domain is dominant (ϕ_c>ϕ_a=ϕ_b). The high ϕ_c results in a lower *c*-domain tilt (Eq. 3) making the presence of a DW

in which the tilt change is that between *c*- and *c'*-domains (as is visible In the TEM picture) more likely than a DW between *a*- and *a*'- or *b*- and *b*'-domains. All domain types are found close to each other and therefore it is expected that all 4 tilt directions (*c/a*- *c'/a'*-, *c/b*- and *c'/b'*-domains) of the *c*-domains are present, including all the transitional rotation orientations in between them. The film can be seen as consisting of *c/a*- *c'/a'*-, *c/b*- and *c'/b'*-domain regions with the *c*-domain functioning as the "malleable" unit cell allowing them to be connected at their boundaries.

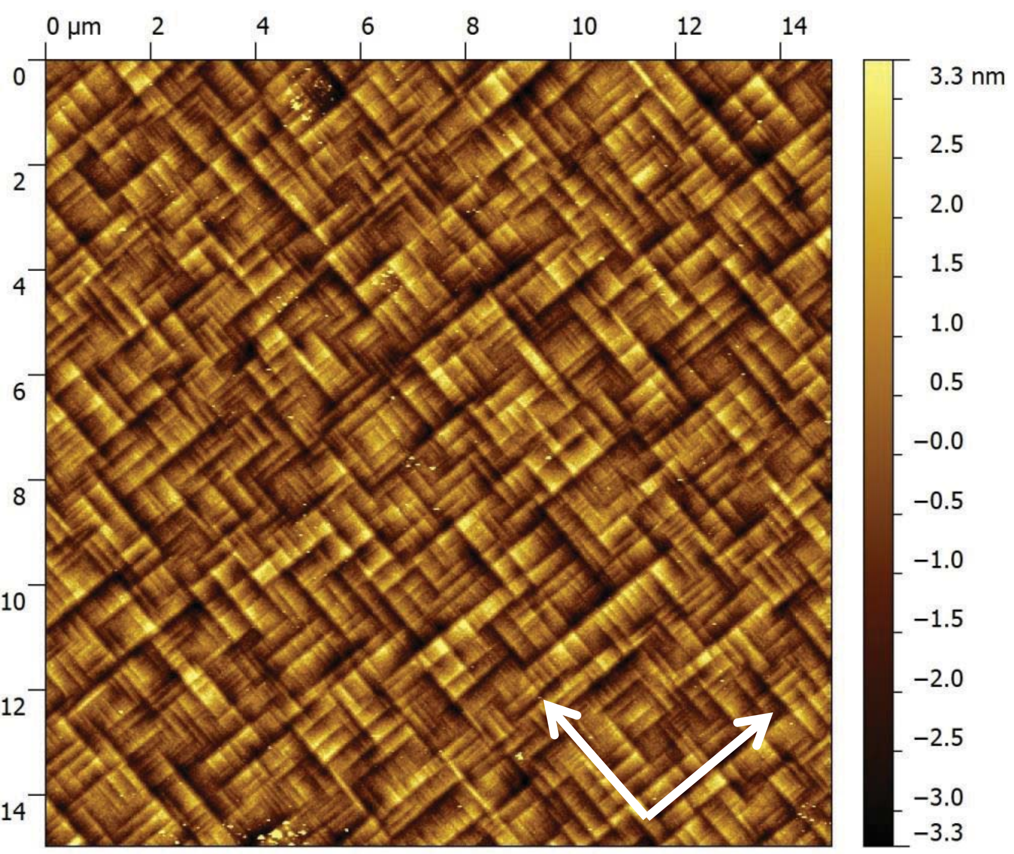

Figure 7.11: (a) AFM data on a 3D PZT (x=0.2) film. The STO/SRO(80 nm)/PZT(800 nm) sample is oriented such that the 010 (2-direction) and 100 (1-direction) crystal direction (red arrows) is oriented at 45°.

7.3.2 Domain structure observed using XRD

Due to the large area and need for statistical information about the domains XRD is an ideal analysis method. The domain fraction, tilting and lattice parameters can be readily obtained for most tetragonal PZT configurations, see figure 7.12, and table 7.3. In some samples XRD can give an indication for what types of DWs are present, figure7.11e. The diffraction pattern show lines connecting *a*- and *c*-domains with opposite tilting angles, as is expected for the *c/a* DWs. Lattice parameters and tilt angles obtained from XRD are given in table 7.3. Due to the symmetry the *a*- and *b*-domains lattice parameters are identical, but the in-plane lattice parameters should be interchanged. The *c*-domain fraction can be found using the lattice parameters (ϕ_c^l), equation 3.12, and independently from equation 7.3 using the measured tilt angle (ϕ_c^ω).

Table 7.3: In-plane and out-of-plane lattice parameters obtained from XRD measurements of 3D PZT (x=0.4) and (x=0.2) films on STO.

PZT (x=0.4)	(001) out-of-plane	(100) In-plane	(010) In-plane
STO	3.905	3.906	3.906
c-domains	**4.146**	4.020	4.020
a-domains	4.021	**4.149**	4.018
STO 600°C	3.928	3.928	3.928
PZT 600°C	4.068	4.068	4.068
	ω_{diff}	ω_a	ω_c
	1.7^o	1.0^o	0.66^o
	ϕ_c^ω	ϕ_c^l	
	0.60	0.60	
PZT (x=0.2)			
STO	3.906	3.906	3.906
c-domains	**4.150**	3.992	3.992
a-domains	3.967	**4.151**	3.972
STO 600°C	3.929	3.930	3.930
PZT 600°C	4.031	4.031	4.031
	ω_{diff}	ω_a	ω_c
	2.4^o	1.71^o	0.70^o
	ϕ_c^ω	ϕ_c^l	
	0.71	0.79	

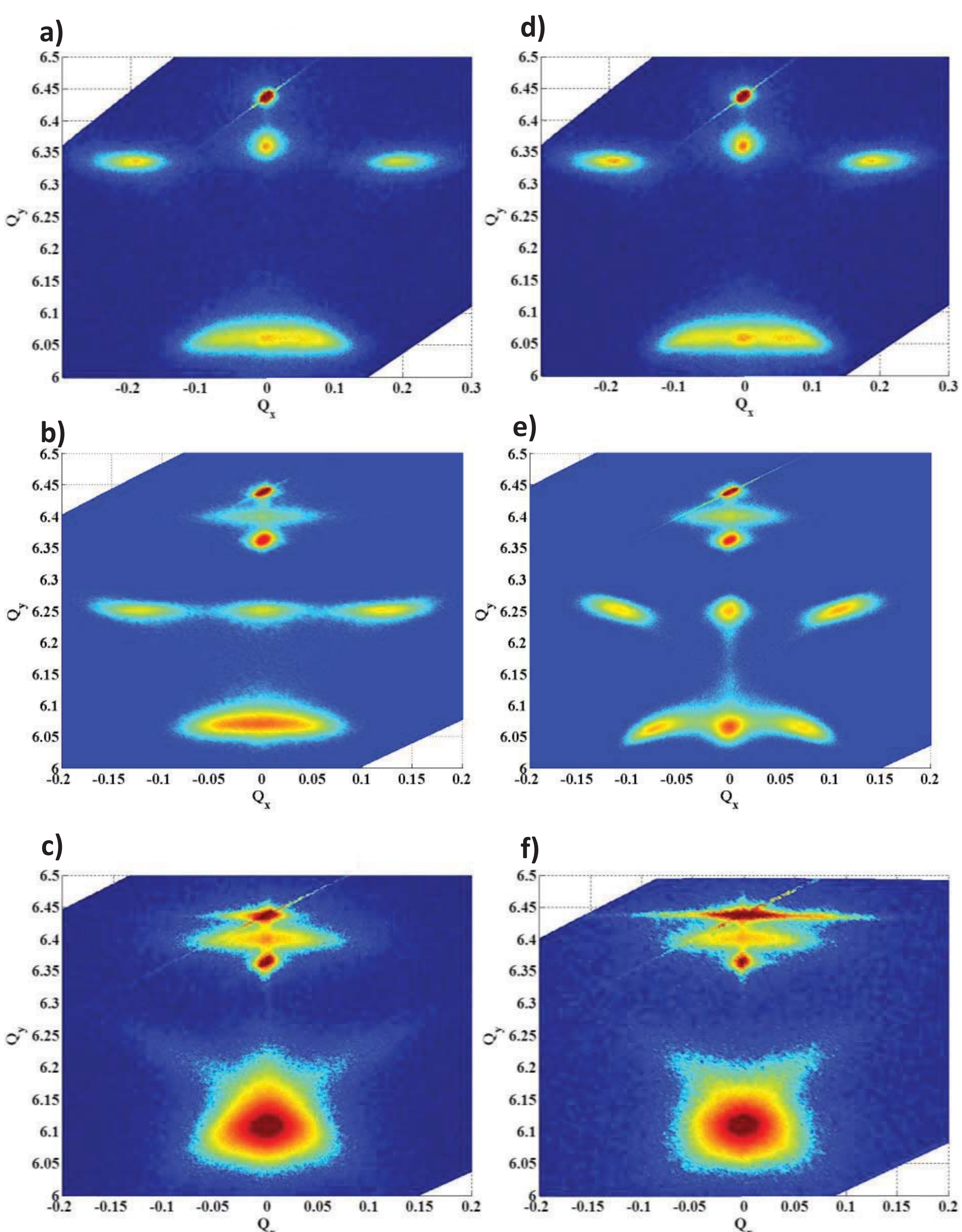

Figure 7.12: Reciprocal Space Map scan of the (004) peaks of STO/SRO/PZT(x=0.2,0.4 and 0.5)/SRO (a-c) before any electrical measurements were performed and (d-f)) after 200+ polarization cycles. For all figures the diffraction peaks represent, from top to bottom, the STO peak, the SRO top electrode, the SRO bottom electrode, the three a-domain peaks and the (three) c-domain peak(s). All map scans are aligned to have the (100) direction on the Q_x axis.

7.3.3 Polarization switching and domain reconstruction

In the course of several XRD experiments in combination with an applied electric fields it was noticed that the XRD patterns undergo permanent changes due to the applied fields. This effect is most notable for PZT x=0.4, figure 7.12b and 7.12e, where the *c*- and *a*-domain peaks move and become more localized, making the different *c*-domain peaks clearly visible. The same effect is seen in PZT x=0.2 but not as pronounced as for the x=0.40 sample. The XRD pattern of PZT x=0.5 also shows some changes. The cause of this change has been investigated, using a fresh sample STO/SRO(80 nm)/PZT x=0.4 (800nm)/SRO(80 nm)/Au(150 nm), by applying different applied fields strengths while performing the XRD measurement. A linear voltage run was done from 0→-0.5→ +0.5→-0.5→0 Volts (below the expected coercive field of 2.5 V) with ω-scans performed on the *c*- and *a*-domain diffraction peaks. The measurements were done after the voltage cycle was completed 1,2,5,10,20 and 50 times (last run 200 times) . This was repeated for a voltage cycle going from 0→-4→ +0.5→-4→0 V so that only one coercive field is crossed and thus not allowing for polarization back switching. Neither voltage run showed any change in the domain structure, figure 7.13. The voltage run was repeated with 0→-4→ +4→-4→0 Volts so that both coercive fields are exceeded. In this case the XRD pattern shows clear changes for both domain reflections, see figures 7.13. A clear path develops between the reciprocal space maps in figure 7.12 upon repeated cycling which saturates between 10 to 20 polarization switching cycles. The switching process has a clear influence on the domain structure indicating that DWs are not static during the initial switching process. The reconstruction of the domains to domains showing clearer and narrower XRD peaks, suggests a change to larger, more uniformly stressed domain regions, with each region becoming more identical with respect to the unit cell tilts or out-of-plane lattice parameters, or both. It is likely that DWs move in such a way that the total energy is lowered by creating more stress free unit cells. This can be achieved by removing locally oppositely tilted domains (e.g. *c/a/c'/a'/c/a* → *c/a/c/a/c/a*), see figure 7.14. The reconstruction cannot be reversed using an applied field, but a new (different) initial condition can be created by heating the sample above the Curie temperature.

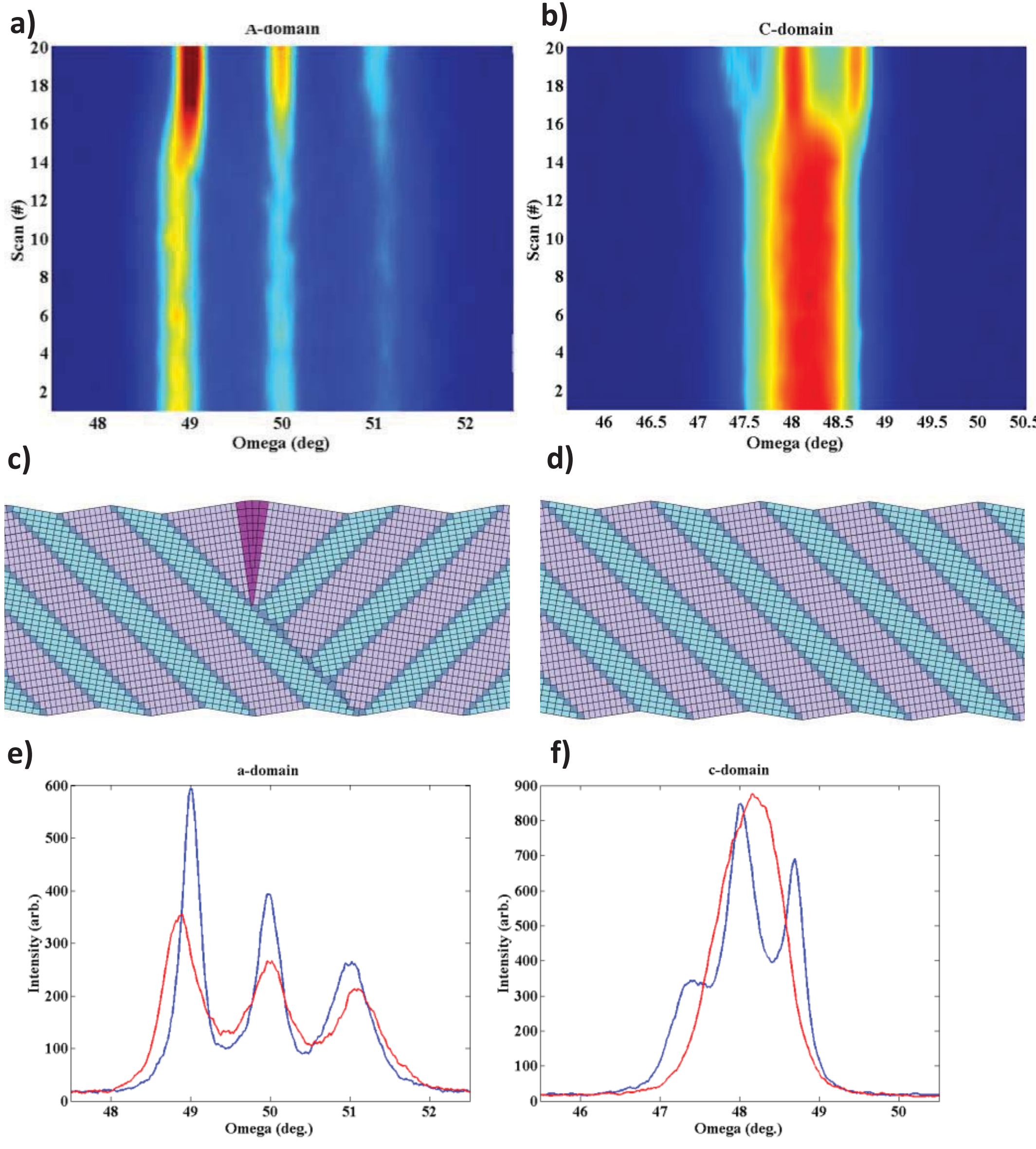

Figure 7.13. Omega scans at the a-domain (a) and c-domain (b) peaks after applied electric fields. Three sets of scan were made with every set using an increasing number of "voltage cycles" starting with 1x, 2x, 5x, 10x, 20x, 50x with only the third set going up to 200x with the last scan. The "voltage cycles" of the sets were for the first/second/third set applying -0.5/-4/-4 V then increasing to +0.5/+0.5/+4 V and decreasing again to -0.5/-4/-4 V and ending at 0/0/0 V. Scan 1 is before an applied voltage, the first set consists of scans 2-7 where the voltage is below the coercive field, the second set of scans 8-13 only crosses the negative coercive field so there is no continuous polarization switching, the third set of scans 14-20 crosses both coercive fields and continuously switches the polarization. In the scan it shows that the domains don't change unless the polarization is actually switched back and forth. Visualization showing a *c/a*- and *c'/a'*-domain (c) and a single *c/a*-domain (d) region. It is suggested that the XRD peak narrowing, due to polarization switching, could be explained by the samples transition from a more stressed (c) towards less stress (d) film structure. XRD omega scan at the a- (left) at 2-θ=100° c-domain (right) at 2-θ= 96.1^{o}. The red line is the sample before any electrical measurements and the blue is after a large number (200+) of polarization switches.

DW motion[9] is not only present during initial reconstruction. The difference between *c*- and *a*-domain peaks can be observed at zero field when approached from either coercive field, see figure 7.14. The difference in the red and blue curves clearly shows that the domain structure is different after cycling to either positive or negative (larger than $|E_c|$). Especially the *a*-domain reflection show a change from a larger *a*- to a larger *a'*- tilted domain fractions. This change is not permanent and can be observed for every half cycle. As with the initial reconstruction the domain reconstruction for the PZT (x=0.4) film is much clearer than for the PZT x=0.2 and 0.5 films for which the omega scan changes are very small.

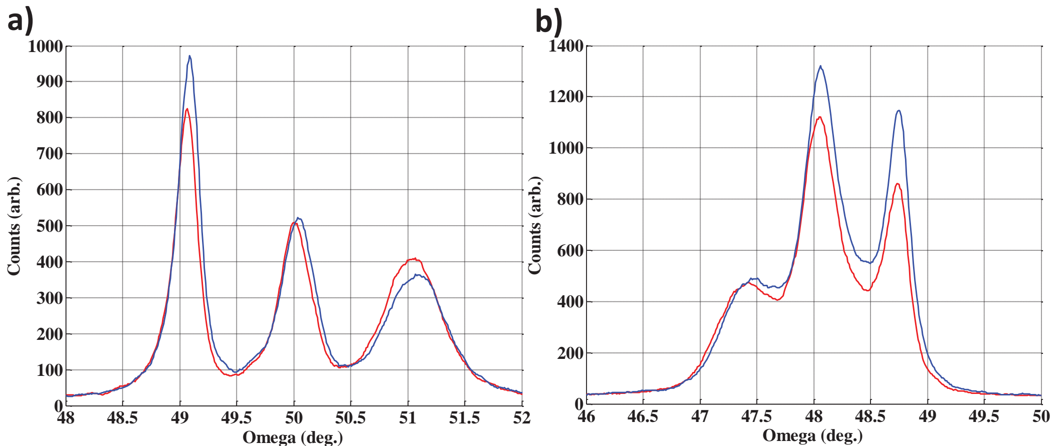

Figure 7.14: XRD omega scan of a PZT x=0.4 film at the *a*- (a) at 2-θ=100° *c*-domain (b) at 2-θ= 96.1°. The red (blue) lines in the data are obtained at zero applied field after the coercive field exceeded with a negative (positive) voltage applied on the top electrode compared to the bottom electrode.

Values for ω_{diff}(=ω_a-ω_c), ω_a and ω_c as a function of the applied field can be determined from the XRD ω-scans. The asymmetry in peak intensity between the left and right tilted peaks can only be explained through the STO miscut as this is the only source for any in-plane anisotropy. On this large scale it is unlikely to arise at random during the reconstruction process. The values for ω_a and ω_c are obtained using the average values for the left and right tilted peaks and are compared to what is predicted by the model with a misfit strain of -0.0046, see figure 7.15. The values ω_a and ω_c are obtained from the model using equation 7.2 and are dependent on the

domain fraction and thus on the applied field. The value of ω_{diff} is however independent of the domain fraction (Eq. 7.3) but influenced by the lattice parameters.

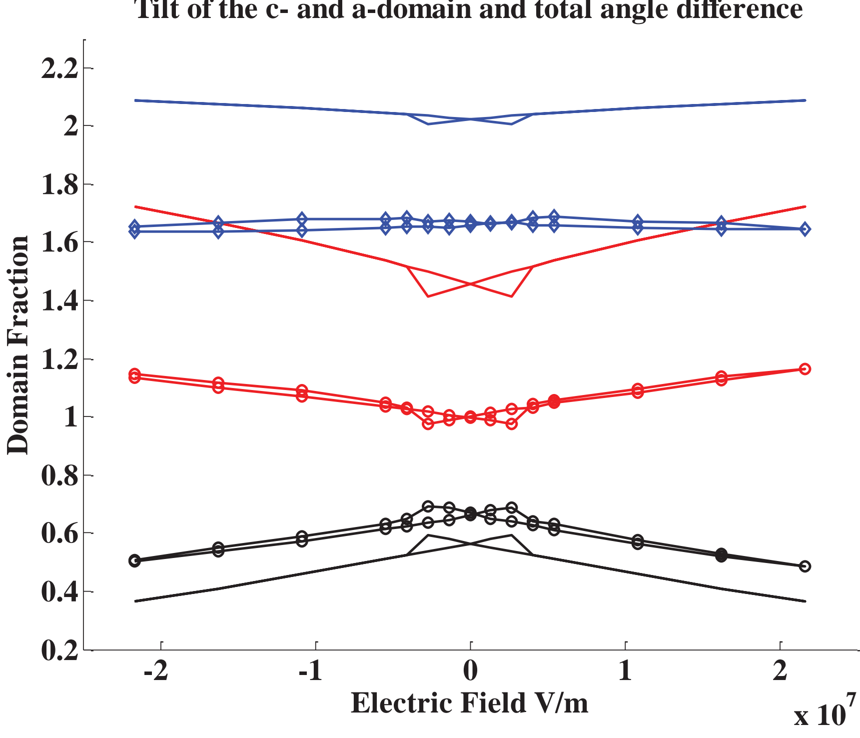

Figure 7.15. Tilts of domains obtained from ω-scans are marked, $\boldsymbol{\omega_{diff}}$ (blue), $\boldsymbol{\omega_{a}}$(red) and $\boldsymbol{\omega_{c}}$(black). The unmarked lines are the values calculated using the model (Sm=-0.0046).

The change in the XRD diffraction pattern due to polarization switching in PZT x=0.4 films indicates that there is some change in the tilting of the domains, requiring a change in the domain structure. Any change in the domain structure and locations of the DW is visible on the sample surface. PZT films were grown on STO/SRO(100 nm) using PLD with a thin (<5nm) Ti/Pt as a top electrode (Ti was used as an adhesion layer between the Pt metal and oxide). The thin top electrode film allows for the application of an electric field, while still allowing for AFM measurements to follow domain pattern changes (Fig. 7.16*a*-f). An electric field above the coercive field was applied for 1 s and subsequently removed. The film is scanned at E_3=0 Vm^{-1} after each switching step. Figures 7.16a,c and e are made after

the application of a positive field step (0^+ measurement), while figure 7.1b,d and f are made after a negative field step (0^- measurement). The data shows that there are differences in the domain structure between the 0^- and 0^+ measurements. The change due to polarization switching is completely reversible and no large differences were found in the domain structure between all 0^- measurements and between all 0^+ measurements. Measurements were also done with an applied field, but these resulted in a blurred figure which was similar to the sign of the corresponding 0^- and 0^+ measurements. In the 0^+ and 0^- measurements of the PZT x=0.37 sample an overall change in the AFM pattern is noticed after every switch namely the occurrence of spots. These spots continue to grow upon cycling until the entire domain structure is lost. The height difference measured with AFM does not indicate delamination as the blurred spots follow the average height of the domain structure. Although on might attribute this observation to the metal electrode smearing out over the film it is also possible that it is related to domain reconstruction as is observed in XRD through the narrowing of the diffraction peaks (Fig. 7.12e). Similar measurements done on a PZT x=0.2 film did not show any change in the surface domain structure and no blurred spots were found, coinciding with the lack of domain reconstruction for this composition.

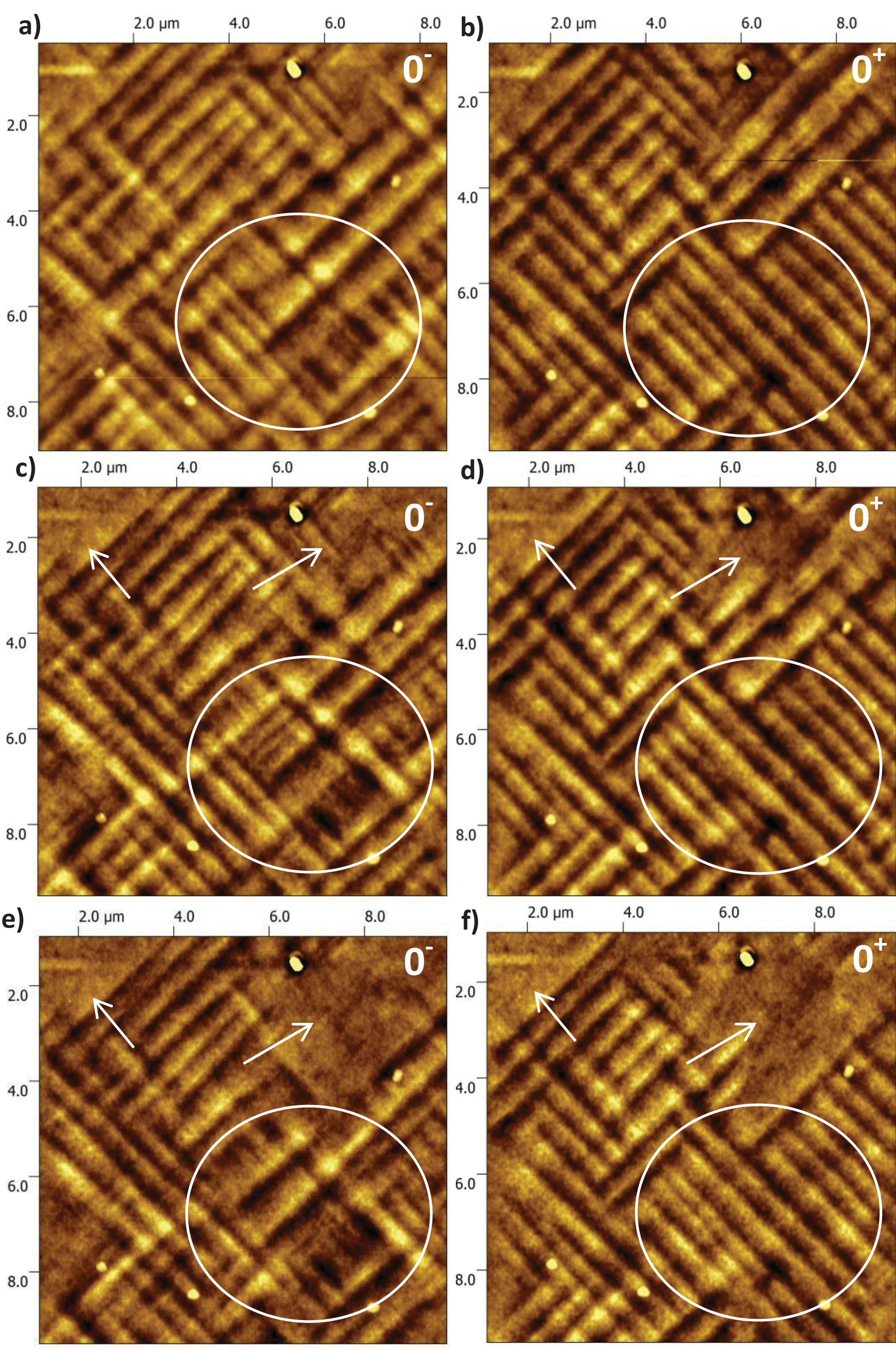

Figure 7.16: Domain structure obtained at zero field using AFM measurements. Figures (a), (c) and (e) are 0^- measurements and (b),(d) and (f) are 0^+ measurements.

7.3.4 PFM: Surface structure

All surface measurements up until now have only given information about the height profile of the surface. Observation of the polarization orientation in combination with a height profile is achieved using piezo force microscopy (PFM)[12]. Most details about the polarization of the domains can be obtained from the in-plane tilt of the cantilever, while bending of the cantilever in the surface normal direction gives information about the height profile. Measurements were done on a sample composed of STO/SRO(100 nm)/PZT x=0.4(1 um). Figure 7.17 (a) shows the height profile of a 5µmx5µm area of the PZT surface. Figures 7.17 (c) and (d) show the in-plane phase amplitude, corresponding to the polarization, of the same area, obtained with the cantilever along the horizontal direction (b) and vertical direction (c). The angle difference allows us to distinguish between the *a*- and *b*-domains due to the different in-plane response to the electric field of the PFM tip. The lighter areas show the regions with a higher response corresponding to an in-plane polarization perpendicular to the cantilever while darker regions show a lower response. Consequently the lighter areas in figure 7.17c correspond to what we will refer to as *a*-domains while lighter areas in figure 7.17d correspond to *b*-domains.

The measurement shows clear large (≈0.2 µm x 2 µm), referred to here as "macro-domains", uniformly polarized domains, with more numerous smaller features (≈0.1 µm x 0.4 µm), referred to here as "micro-domains" (Figs. 7.17 b and c). These micro-domains overlap with similar small features seen in the AFM height profile of the same film. Note that these features are also seen in AFM and PFM data for the other tetragonal PZT films (x=0.2 and x=0.37). The distance between the micro-domains of all tetragonal PZT films coincide with the domain distance seen in TEM data, which was found to be about 100nm for a PZT (x=0.2) film. This indicates that the micro domain structure is the *c/b* and *c/a* domains structure we observe in TEM and corresponds to the tilted domain in the XRD data. This is supported by the observation that DWs at 45° to the (100) or (010) orientation can be found in the macro domains in figure (e), indicating the presence of *b/a* DWs. These DWs appear to originate from the line structure of the micro-domains indicating that *b*- or *a*-domains are present.

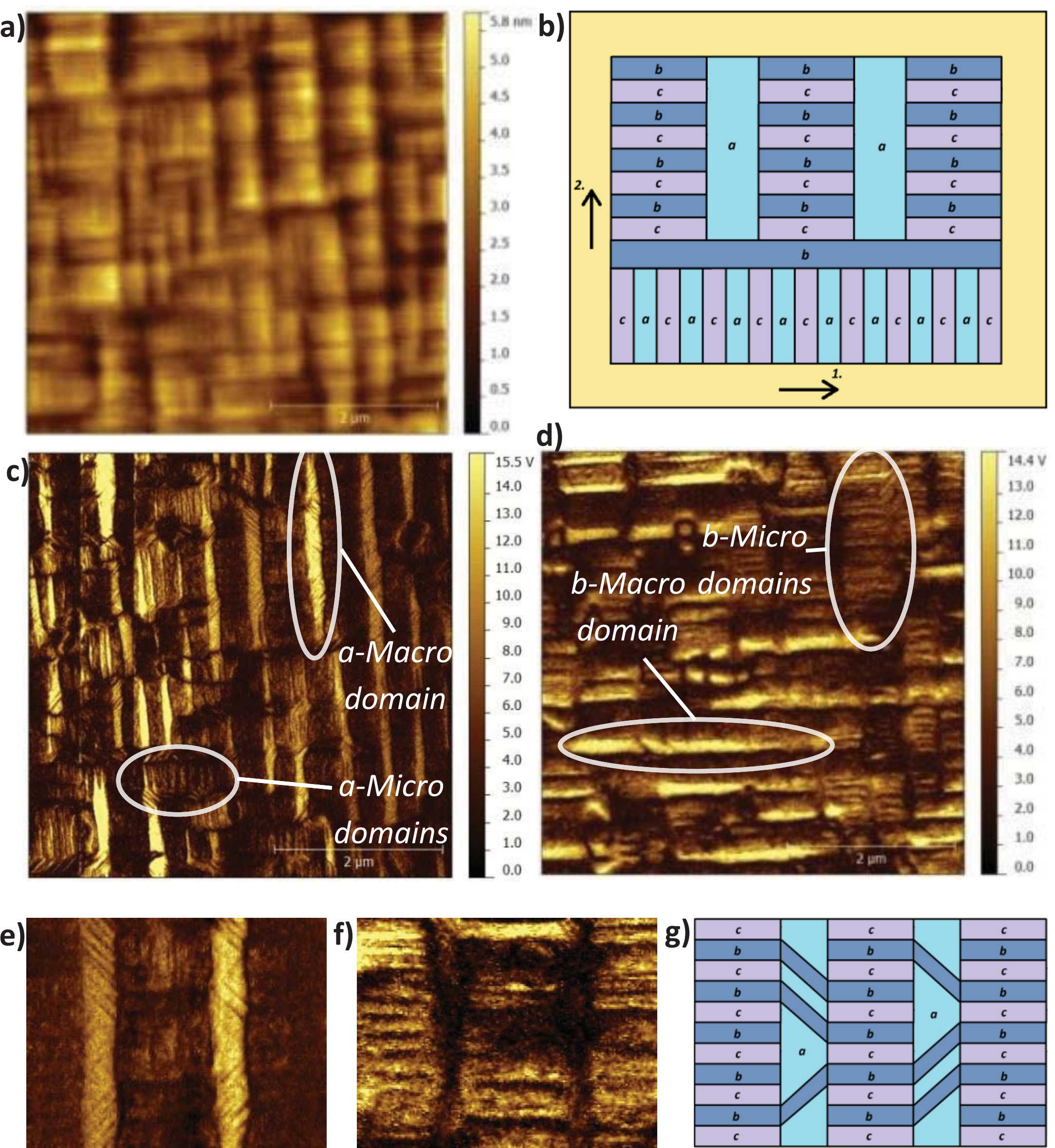

Figure 7.17: PFM data of a 5 µmx5 µm area of a STO/SRO(100nm)/PZT x=0.4(1um) sample. (a) Height profile. (b) Top view visualization of the micro domain structure showing the possible interface between the *c/b*- and *c/a*- domain regions through domain tilts of 45° in both the (100) and (010) orientation. (c) In-plane amplitude data highlighting the polarization orientation of *a*-domain. The circles area show the larger (Marco) *a*-domain and the smaller (Micro) *c/a*-domain structure. (d) In-plane amplitude where the PFM cantilever was rotated 90°, highlighting the polarization orientation of *b*-domain. The circles area shows the larger (Marco) *b*-domain and the smaller (Micro) *b*-domains structure. (e) and (f) show identical zoomed in areas of (c) and (d), respectively. (e) shows structures oriented in the (110) (or equivalent) orientations indicating the presence of a *b/a*-domain region with *b/a* DWs in the macro domain. (f) The micro domain structure indicates alternating c/b domains between the macro domain structure. (g) Visualization of the suggested domain structure of (e) and (f).

7.4 Discussion

The domain structure of a 2D film is found to have a clear *c/a*- or *c'/a'*-domain structure with domains walls oriented at 45° with respect to the substrate plane. The introduction of *c/b*- and *c'/b'*- domain regions in 2D films, which are required to reduce the stress induced by the misfit strain in 3D films, is not trivial.

The 45° angle of the 90° DWs is still expected for the 3D film domain structure. However the DW angle for the *c/a*-, *c'/a'*-, *c/b*- and *c'/b'*- domain regions all have DWs in different 45° orientations. In 2D films the interface between *c/a*- and *c'/a'*- domain regions gave rise to stress visible in the TEM data. For 3D films the intersections between domain regions are expected to be more numerous, because of the intricate domain structure observed in AFM for a 1µm thick film. For example, to reduce the stress from these DW intersections between *c/a*- and *c/b*- domain regions it is proposed that the 90° DWs in the *c/a*-domain region are not only tilted at 45° (in the polarization orientation (001)) but also at 45° to the other in-plane orientation (010) in order to not intersect with the c/b- domains regions.

The interaction, in such a domain structure, due to the tilt of the unit cells of the individual domains is however still unclear. XRD data shows that *a*-domains and *b*-domains, and their corresponding *c*-domain, of the tetragonal PZT films are always tilted in the (100) and (010) direction, respectively. At any location where the *b*- and *a*- domains interact the slight tilt difference of the unit cells in the structure would, over the thickness of the sample, imply a large crystal mismatch. This would be easily resolved if the *a*- and *b*- domain unit cells were tilted in both the (010) and (001) direction allowing for an interaction between the domains over the full film thickness and allowing for a continuous single crystal structure. However, in this case the XRD data would show a tilt in the (110) (or equivalent) directions, which is not observed. XRD data of PZT (x=0.4) also does not indicate the presence of any intermediate domain region as was observed in the 2D films. This intermediate region would be seen as a connection

between either the diffraction peaks of differently tilted *c*-domains or between the *a*- and *b*-domains similar to the connection seen between the *c*- and *a*- domain observed in figure 7.12e. At the moment it is unclear how both *c/a*- and *c/b*- domains with different unit cell tilts over the full thickness of the 3D film and a continuous single crystal structure can coexist. Further investigation of this domain structure would be possible if one can gather information of about the unit cell tilt locally, on the scale of the micro domains.

Additional information could be obtained if one could add the energy terms corresponding to the domain tilting and related stress in the film due to the substrate clamping to the model. This would be of special interest to the result of the model around the MPB composition (x=0.5), because of the effect it would have on the phase change boundary between tetragonal unit cells and rhombohedral unit cells. If the energy terms were known it could also allow the model to indicate at what critical thickness certain domains would arise[5].

Out-of-plane polarization switching of the film during XRD measurements has shown that the 3D PZT (x=0.4) film undergoes an (irreversible) initial reconstruction of the domains. In AFM it can also be observed that the domain structure changes between two states when the polarization is switched. Both these domain structure reconstructions can only be achieved through some DW motion in the material. Note that in AFM it is observed that a significant part of the film is not changed upon polarization switching. Here the switching mechanism for both the static and reconstructing domain structure will be proposed. For the static domain structures it is likely that the process is similar as is measured in [3], initially a part of the *c*-domain at one of the interfaces switches, and a needle like switched domain with 180° DWs grows until an *a*- or *b*-domain is reached. The *a*- and *b*- domains will likely switch their polarization to avoid a charged *c/a* or *c/b* domain wall (Fig. 7.18b). As this process continues the polarization of all domains would be switched with all DW remaining static. If the sample reconstructs the domain structure it implies that the *c/a* and *c/b* DWs move upon switching. One possible gradual process to achieve this

movement would be to have similar needle-like switching of the *c*-domains at the interface. If the *c*-domains switch polarization direction and the adjacent *a*-domains do not (Fig. 7.18e), the DW will have to change their angle in order to avoid charged DWs. Although some charged DWs will be present (see yellow interface), as the process continues, theoretically no charged DW are required and the angle of the DWs in a large region can be changed. Note that this movement would allow not only switching between c/a- and c'/a'- domain regions but also between *c/a*- and *c/b*- domain regions. This switching mechanism might be tested using TEM in combination with an applied electric field similar to that done by[3], only then on a region similar to that seen in figure 7.7, where a strained area is present and a change in the DW angle would not result in additional stress in the 2D film.

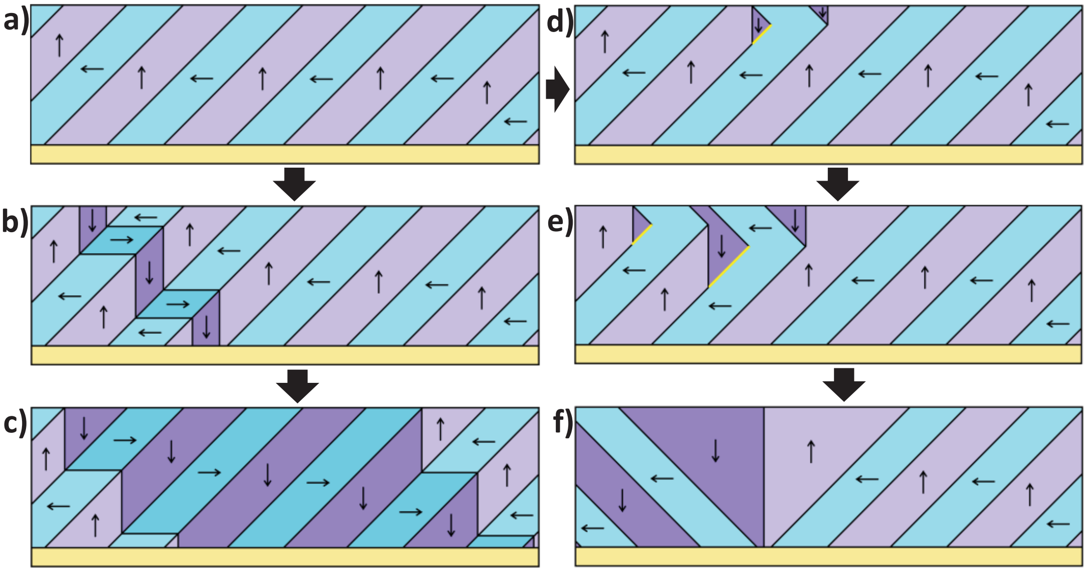

Figure 7.18. Side-view visualization of the domain structure of the PZT film showing a *c/a*-domain region during polarization switching. Possible switching mechanism for a static (or pinned) DW of a *c/a*-domain region (a)-(b)-(c) and a polarization switching mechanism allowing for a DW tilt change coinciding with a change in the unit cell tilt of the *a*- and *c*-domains.

7.5 Conclusion

Experiments have been done on 1 um thick clamped, dense, tetragonal PZT (001) films epitaxially grown on STO substrates with a SRO bottom electrode using PLD deposition. Two types of samples were analyzed: a TEM sample, clamped in one in-plane direction (2D sample) and a clamped film, clamped in two in-plane directions (3D sample).

-A 2D film has only one direction in which there is a misfit strain which is solved by tetragonal domain formation. The *c*-domain has a smaller and the *a*-domain has a larger in-plane strain compared to the misfit strain. Therefore the film can release the stress caused by the misfit strain by creating an alternating *c*- and *a*-domain pattern which can be observed in TEM. These domains are about 100nm wide and are approximately at 45° inclined with respect to the surface normal of the film. Due to the 2D nature of the film no *b*-domains are required nor observed. The *a*- and *c*-domain pattern has a non-90° angle between the long axes of the two domains, that can be described by equations 7.1 and 7.2. The transition between the oppositely tilted *c/a*- and *c'/a'*-regions requires the *c*-domain to rotate its out-of-plane orientation between the *c*- and *c'*- tilt or have a static angle in between the two tilts. Only the *c*-domain is found to change its tilt which is likely due to the smaller tilt difference between the *c*- and *c'*-domains compared to the tilt between the *a* and *a'*-domains as predicted by equation 3. The equations shows that the tilt of the domains depends on the domain fraction, indicating that the misfit strain between the film and substrate influences the tilting between the domain regions.

-3D films present a more complicated picture, which can be observed using AFM, that shows a mazelike domain structure with a 4-fold symmetry. XRD data indicates the presence of a similar tetragonal domain structure for 3D films as was found for 2D films with the addition of *c/b*- and *c'/b'*-domain regions next to the c/a and *c'/a'*-domain regions. It is suggested by the model that the different domains are necessary to release the stress on the film in both in-plane orientations.

-The interaction between the different domain regions can be studied using piezo force microscopy (PFM). PFM images have shown that in the 3D films there are marco- and micro-domains, where the micro-domains coincide with the domain pattern seen in TEM. The size of the micro-domain (about 0.1µm by 0.4µm) suggests that the stress in the film is relaxed locally. This indicates that the film is better described through a c/b/a phase instead of a c/a-phase supporting that the model presented in chapter 3 is an improvement over the model presented in literature for clamped films[10].

-The composition of tetragonal PZT has a noticeable influence on the domains polarization switching mechanisms. PZT x=0.2 shows a static DW structure during switching similar to that observed by [3] both in AFM and XRD measurements. PZT x=0.4 shows a largely static DW structure, but also shows clear initial domain reconstruction in XRD and a recurring domain structure change between out-of-plane polarization switches.

References

[1] G. Catalan, J. Seidel, R. Ramesh and J. F. Scott, "*DW nanoelectronics*", Reviews of modern physics 84, (2012).

[2] D. Griffiths, "*Introduction to Electrodynamics*", Addison Wesley; 3 edition, (30 Dec. 1998)

[3] Peng Gao et al., "*Atomic-scale mechanisms of ferroelastic domain-wall-mediated ferroelectric switching*", Nature Communications 4-2791, (2013).

[4] A. H. G. Vlooswijl, G. Catalan and B. Noheda. "*Comment on "Nanometer resolution piezoresponse force microscopy to study deep submicron ferroelectric and ferroelastic domains*", Applied Physics Letters 94, 162903 (2009)]", Citation: Applied Physics Letters 97-046101, (2010).

[5] C. Kittel, "*Thickness of DWs in ferroelectric and ferroelastic crystals*", Solid State Communications Vol. 10, (1972).

[6] J. S. Speck and W. Pompe, "*Domain configurations due to multiple misfit relaxation mechanisms in epitaxial ferroelectric thin films. l. Theory*", Journal of Applied Physics 76, 466, (1994).

[7] Peng Gao et al., "*Ferroelastic domain switching dynamics under electrical and mechanical excitations*", Nature Communications 5-3801, (2014).

[8] P. Marton, I. Rychetsky and J. Hlinka, "*DWs of ferroelectric BaTiO3 within the Ginzburg-Landau-Devonshire phenomenological model*", Physical Review B 81, 144125 (2010)

[9] T. Tybell et al. "*DomainWall Creep in Epitaxial Ferroelectric* $Pb(Zr_{0.2}Ti_{0.8})O_3$ *Thin Films*", Physical Review Letters 89-9, 2002.

[10] N. A. Pertsev and A. Yu. Emelyanov,"*Domain–wall contribution to the piezoelectric response of epitaxial ferroelectric thin*

Films", Applied Physics Letters 71-3646, (1997).

[11] M. Y. Gureev, A. K. Tagantsev and N. Setter, "*Structure and Energy of Charged DWs in Ferroelectrics*", IEEE Application of ferroelectrics, (2009).

[12] Y.Ivry, D.Chu, C.Durkan, "*Nanometer resolution piezoresponse force microscopy to study deep submicron ferroelectric and ferroelastic domains*", Applied Physics Letters 94-162903, (2009).

Appendix

Table A.1: Glossary

Term	*Symbol*	*Unit*
Gibbs free energy	G_0	J
Gibbs free energy density	G	Jm^{-3}
Enthalpy	H	J
Temperature	T	K
Entropy	S_e	JK^{-1}
Pressure	P	Nm^{-2}
Volume	V	m^3
Internal energy	U	J
Helmholtz free energy	F_0	J
Helmholtz free energy density	F	Jm^{-3}
Strain	S	
Stress	σ	Nm^{-2}
Polarization	P	Cm^{-2}
Elastic compliances constants	s	m^2N^{-1}
Dielectric stiffness constants	α_x α_{xx} α_{xxx}	mF^{-1} m^2F^{-2} m^3F^{-3}
Electrostrictive constants	Q	m^4C^{-2}
Curie-Weiss temperature	ϑ	K
Vacuum Permittivity	$\varepsilon_0 = 8.854\text{x}10^{-12}$	Fm^{-1}
Curie-Weiss constant	C	K

Table A.2: Name and abbreviation of materials used in this work.

Material	*Chemical Formula*	*Abbreviation*
Strontium Titanate	$SrTiO_3$	*STO*
Lead Zirconate Titanate	$PbZr_xTi_{1-x}O_3$	*PZT*
Potassium Tantalate	$KTaO_3$	*KTO*
Strontium Ruthenate	Sr_2RuO_4	*SRO*
Platinum	*Pt*	*Pt*
Gold	*Au*	*Au*
Titanium	*Ti*	*Ti*

Table A.3: Material constants obtained from Haun et al[1] and Yamamoto[2]. Note that for values of $x \geq 0.90$ and $x \leq 0.20$ the value of the Curie-Weiss temperature (T_0 *or* ϑ) is not equal to the transition temperature.(T_c). Also note one needs to consider O-octahedral rotation in the low temperature rhombohedral phase (figure 1.2), which requires tilt angle related coefficients. At temperatures about RT this is significant for PZT compositions with $x \geq 0.70$.

$PbZr_xTi_{1-x}O_3$	*x=0.60*	*x=0.55 (Interpolated)*	*x=0.50*
s_{11} $\cdot 10^{-12}\ m^2N^{-1}$	*8.8*	*9.65*	*10.5*
s_{12} $\cdot 10^{-12}\ m^2N^{-1}$	*-2.9*	*-3.3*	*-3.7*
s_{44} $\cdot 10^{-12}\ m^2N^{-1}$	*24.6*	*26.65*	*28.7*
Q_{11} $\cdot 10^{-2}\ m^4C^{-2}$	*7.260*	*8.46*	*9.660*
Q_{12} $\cdot 10^{-2}\ m^4C^{-2}$	*-2.708*	*-3.654*	*-4.600*
Q_{44} $\cdot 10^{-2}\ m^4C^{-2}$	*6.293*	*7.2415*	*8.190*
α_1 $\cdot 10^7\ mF^{-1}$	*-7.904*	*-6.3955*	*-4.887*
α_{11} $\cdot 10^7\ m^2F^{-2}$	*13.62*	*9.192*	*4.764*
α_{12} $\cdot 10^8\ m^2F^{-2}$	*2.391*	*2.063*	*1.735*
α_{111} $\cdot 10^8\ m^3F^{-3}$	*2.713*	*2.0245*	*1.336*
α_{112} $\cdot 10^8\ m^3F^{-3}$	*12.13*	*9.129*	*6.128*
α_{123} $\cdot 10^8\ m^3F^{-3}$	*-5.690*	*-8.584*	*-2.894*
T_C (K)	*364.3*	*378.45*	*392.6*
C $\cdot 10^5$ K	*2.424*	*3.335*	*4.247*

Table A.4: Material constants obtained from Haun et al.[1] and Yamamoto[2].

$PbZr_xTi_{1-x}O_3$	*x=0.45 (Interpolated)*	*x=0.40*	*x=0.30*
s_{11} $\cdot 10^{-12}$ m^2N^{-1}	*9.55*	*8.6*	*8.4*
s_{12} $\cdot 10^{-12}$ m^2N^{-1}	*-3.25*	*-2.8*	*-2.7*
s_{44} $\cdot 10^{-12}$ m^2N^{-1}	*24.95*	*21.2*	*17.5*
Q_{11} $\cdot 10^{-2}$ m^4C^{-2}	*8.888*	*8.116*	*7.887*
Q_{12} $\cdot 10^{-2}$ m^4C^{-2}	*-3.7750*	*-2.950*	*-2.480*
Q_{44} $\cdot 10^{-2}$ m^4C^{-2}	*7.450*	*6.710*	*6.356*
α_1 $\cdot 10^7$ mF^{-1}	*-6.6135*	*-8.340*	*12.47*
α_{11} $\cdot 10^7$ m^2F^{-2}	*4.189*	*3.614*	*0.646*
α_{12} $\cdot 10^8$ m^2F^{-2}	*2.484*	*3.233*	*5.109*
α_{111} $\cdot 10^8$ m^3F^{-3}	*1.5975*	*1.859*	*2.348*
α_{112} $\cdot 10^8$ m^3F^{-3}	*7.3155*	*8.503*	*10.25*
α_{123} $\cdot 10^8$ m^3F^{-3}	*-3.4785*	*-4.063*	*-5.003*
T_C (K)	*405.5*	*418.4*	*440.2*
C $x10^5$ K	*3.4555*	*2.664*	*1.881*

References:

[1] M. J. Haun, Z. Q. Zhuang, E. Furman, S. J. Jang and L. E. Cross, "*Thermodynamic theory of the lead zirconate-titanate solid solution system, part III: Curie constant and sixth-order polarization dielectric stiffness coefficients",* Ferroelectrics,99:1,45-54. (1989).

[2] T. Yamamoto, "*Crystallographic, Dielectric and Piezoelectric Properties of $PbZrO_3$-$PbTiO_3$ System by Phenomenological Thermodynamics*", Japanese Journal of Applied Physics vol.37 (1998), p.6041-6047.

Summary

The work described in this thesis is focused on the characterization and understanding of epitaxial, clamped, dense $PbZr_xTi_{1-x}O_3$ (PZT) films. An introduction to Piezoelectricity and Piezoelectric materials such as PZT is given in **Chapter 1**.

In **Chapter 2** the fabrication of epitaxial films and how these films are characterized is explained. The fabrication steps needed to create a capacitor structure with an epitaxial PZT film on $SrTiO_3$ (STO) and $KTaO_3$ (KTO) single crystal substrates with a top and bottom conductive $SrRuO_3$ (SRO) electrode using PLD are shown.

In **Chapter 3** a thermodynamic model is developed, which is used to simulate properties of clamped PZT films throughout this work. It is shown that the new model, which allows for a more general domain interaction between different domains, is an improvement on existing models for predicting material characteristics. Free energy equations for single- and poly-domain films are given, which allow us to simulate the material properties of epitaxial, clamped, dense PZT films.

In **Chapter 4** the free energy equations are used to analytically derive PZT films properties, which are compared to numerical calculations. Here it is shown that the equations can be used to derive the piezoelectric coefficients, stress, strain, polarization and crystal phase of PZT. An analytical approximation is given that provides a relationship between important parameters allowing for a more simplified prediction of material parameters.

Experimental work done on tetragonal poly domain $PbZr_{40}Ti_{60}O_3$ films is described in **Chapter 5**. X-ray diffraction measurements done with an applied field are used to measure the intrinsic piezoelectric coefficients of individual domains. It is shown that the intrinsic piezoelectric coefficient of the domains in the PZT film is negative while the average piezoelectric coefficient of the film is positive. This result was predicted by the model.

An alternative explanation for the origin of high piezoelectric coefficients using the thermodynamic model is discussed in **Chapter 6**. The model is used to explain the high piezoelectric characteristics of both film and bulk PZT found at the morphotropic phase boundary (MPB) using the characteristics of the rhombohedral and the tetragonal crystal phase or the phase change between them. The model also predicts that in principle arbitrarily high piezoelectric coefficients can be obtained in defect free films. The value of the coefficient is highly dependent on the misfit strain, which can be tuned using different substrates.

In **Chapter 7** the structure of the domains and domain walls (DWs) in tetragonal PZT is explored. Data obtained using transmission electron microscopy shows that 2D films exist out of a c/a, c'/a' domain structure. X-ray diffraction and piezo force microscopy on 3D films show a complex *c/a, c'/a', c/b, c'/b'* domain structure which reconstructs when an electric field is applied or when the out-of-plane polarization is switched. The complex domain structure can be explained as a mixed micro- and macro-domain structure, that on average is described by the domain structure required by our new thermodynamic model.

Samenvatting

Het focus van het werk in dit proefschrift ligt op het karakteriseren en begrijpen van epitaxiale, geklemde en dichte $PbZr_xTi_{1-x}O_3$ (PZT) films. In **hoofdstuk 1** wordt piëzo-electriciteit en piëzo-elektrische materialen zoals PZT geïntroduceerd.

In **hoofdstuk 2** wordt de fabricage van epitaxiale films en hoe deze films worden gekarakteriseerd toegelicht. De fabricage stappen die nodig zijn om een condensator van epitaxiale PZT film te maken op $SrTiO_3$ (STO) en $KTaO_3$ (KTO) substraten met een top en bodem geleidende $SrRuO_3$ (SRO) elektrode met behulp van PLD, worden getoond.

In **hoofdstuk 3** wordt een thermodynamisch model ontwikkeld dat wordt gebruikt om eigenschappen van geklemde PZT films te simuleren. Hier wordt aangetoond dat dit nieuwe model, die een meer algemene interactie tussen domeinen toelaat, een verbetering is op bestaande modellen voor het voorspellen van materiaal eigenschappen. Vrije energie vergelijkingen voor mono- en poly- kristallijne films worden gegeven die het mogelijk maken om deze eigenschappen van epitaxiale, geklemde en dichte PZT films te simuleren.

In **hoofdstuk 4** worden de vrije energie vergelijkingen analytisch benadert en vergeleken met numerieke berekeningen. Hier worden de vrije energie vergelijkingen gebruikt om de piëzo-elektrische coëfficiënten, spanning, rek, polarisatie en kristal fase van PZT te geven. Ook wordt een analytisch oplossing gegeven die het mogelijk maakt om een relatie tussen belangrijke parameters te simplificeren.

Experimenteel werk aan tetragonale poly-domein $PbZr_{40}Ti_{60}O_3$ films wordt getoond in **hoofdstuk 5**. Röntgendiffractie metingen in combinatie met een aangelegd elektrisch veld worden gebruikt om de intrinsieke piëzo-elektrische coëfficiënten van de individuele domeinen te bepalen. Deze metingen laten zien dat de intrinsieke piëzo-elektrische coëfficiënten van

beide domeinen negatief zijn maar dat de gemiddelde piëzo-elektrische coëfficiënt van de film positief is. Dit resultaat wordt voorspeld door het model.

Een alternatieve uitleg voor de oorsprong van hoge piëzo-elektrische coëfficiënten wordt besproken in **hoofdstuk 6**. Het nieuwe model wordt gebruikt om de hoge piëzo-elektrische karakteristieken van bulk en film PZT, die gevonden wordt in PZT met composities rond de morphotropic fase grens, uit te leggen met behulp van de karakteristieken van de romboëdrische en tetragonale kristal fase en de fase overgang tussen beide. Het model voorspelt ook dat een arbitrair hoge piëzo-elektrische coëfficiënten gevonden kan worden bij PZT films zonder afwijkingen. De waarde van de piëzo-elektrische coëfficiënt is sterk afhankelijk van de misfit rek, welke sterk gestuurd kan worden door het gebruik van verschillende substraten.

In **hoofdstuk 7** wordt de structuur van de domeinen en domeingrenzen in geklemde en tetragonale PZT films onderzocht. Experimentele gegevens verkregen via transmissie elektronen microscopie laat zien dat 2D films opgebouwd zijn uit c/a, c'/a' domeinen. Röntgendiffractie en piëzo force microscopie laten zien dat 3D films een complexe *c/a, c'/a', c/b, c'/b'* domein structuur heeft die een reconstructie laat zien als de polarisatie wordt omgekeerd door het aanleggen een elektrisch veld. De complexe domein structuur kan begrepen worden door een mix van een micro- en macro- domein structuur, die gemiddeld beschreven kan worden door een domein structuur die vereist wordt door ons thermodynamische model.

Acknowledgements:

This thesis is the result of four years of research on the structure and properties of epitaxial $PbZr_xTi_{1-x}O_3$. However, the research alone does not tell the complete story of these four years. In this part I would like to express my gratitude to all the people, who have made these years into a wonderful and unforgettable stage in my life.

First of all, I would like to thank my supervisor *Guus Rijnders*. Fresh out of student life I was not really sure what I wanted to do and I don't remember exactly why but I didn't think a PhD would fit me. However, after meeting you, I was quickly looking forwards to joining the IMS group as a PhD researcher. I am thankful that in those four years I have been able to learn a lot from you not only on our field of research but also on many unrelated topics during our or the groups discussions at the coffee table. I would also like to thank *Evert Houwman*, without whom I would have not been able to write down '2017' in my thesis. I relished all the technical and theoretical discussions concerning my research we have had over the years, on which half my work is now based. I also thank my supervisor *Gertjan Koster*, who had to endure the many questions I had concerning X-ray diffraction and also for the help with writing the thesis. Here, I would also like to thank *Bernard*, *André, Mark*, *Frans*, *Igor, Hans, Marion*, *Jose*, *Dominic*, *Laura*, for all your help and advice over the years.

I also have to thank my colleagues for enduring my endless series of questions. I think, the most interesting and helpful moments in my PhD have been during the IMS coffee breaks, which always seemed to start a little earlier and end a little later than planned. The beauty of these breaks for me was the discussions, which continued until either *André* knew the answer (if there was one), if *David* finally took out his phone and looked it up on Wikipedia or if *Karin* wanted us to switch to a different topic. For this great and interesting atmosphere I have to thank all my colleagues at the University. This atmosphere usually trailed along as we returned to our office, where I have also really enjoyed the continuing discussions *Peter*, *Ruud* , *Jaap* and I had there. Here, I would like to assure *Guus* that at least

half of these were in some way relevant to one of our research projects, probably. Only in the lab in between the laser pulses was it ever really quite, at least until *Alexander* and *Thomas* decided to join my work. I would like to express my gratitude to you both for helping me with my research. I would especially like to thank *Thomas* for all the great philosophical discussions we had while waiting for the film layers to be grown. I would also like to acknowledge *Rik,* who first thought me XRD and *Minh*, *Alim*, *Nirupam, Kees* and *Huiyu* for helping me with the small PLD and supplying many samples crucial for my work. The IMS football team, the conferences and the Frimibo are all memorable moments in these last four year for which I have all my colleagues to thank. In return for this, I hope I have also added something to your time here, although I'm not sure if the journal clubs about Bell's inequality and the quantum entanglement were very successful.

Many things in the labs can't be done alone. That is why I would like to thank *Mark Smithers*, *Rico Keim* and *Frank Roesthuis* for their help over the years. *Mark*, I really appreciate that you were always there to defend the IMS honour on the field and that you pushed the HRSEM to the limit in order to try to detect the slope of the microscopic domains in my samples. *Rico,* seeing the atomic structure of the epitaxial PZT film had a great influence on my understanding of the domain structure and without your help I would be missing most of my images and would not have been able to explain or visualize most of my work. *Frank*, thank you for your help with realigning the small PLD and fixing the "giant laser" whenever it was needed.

And of course I have to thank my friends Tieskuh?&Eliane, Theo&Marta, Theo&Elea en Jasper&Miriam. I think of everyone, you had the least faith in my PhD choice. I always seem to lag behind a little and it appears that I am now the last of our group to leave the UT nest. But although we are now spread across the time zones I will look forward for having the group back together again.

Doing a PhD is probably the closest one can stay to their student life, which is probably one of the reasons I enjoyed it so much. Life as a student at

Patio 26 was one of the greatest times I've had in my life and I have mostly Koen&Yvonne, Pim&Ianthe, Marco&Sabrina, Kaj&Evita and Maarten to thank for this. I don't think I will ever be able to completely get used to not having so much free time and fun, which I have had with you guys over the years. Now, that I am no longer at the Patio, I want to thank Joost, Hielke, Thijs and Gerto for continuing the board game tradition.

Ziakachek, of all the people you have supported me the most. Whether it was listening to me talk about the adventures of the communist princess while you're falling asleep or getting me to focus back on work what needs to be done, I could always count on you to be there for me. I am also very happy I got *Wilfred* to "force" you work with me ☺. I would also like to thank your sister, *Dasha*, for helping with the cover, showing us Saint Petersburg and, of course, for translating the many conversations I had with my new Russian family, *Elena*, *Victor*, *Valentina* and *Gennady*, and allow me to have a great time visiting Taganrog and the black sea.

Last but not least, I would like to thank my family. *Paul*, *Helene*, *Bart*, *Rob*, *Jiajia*, *Alicia*, *Lena* and *Evelyn*. Without your support I would not have been able to do this work. You gave me a warm place to go to in the "sunny south" Brabant, or Vietnam during the cold winters in Twente. I am not sure if I was ever any good at explaining my work or other aspects of physics in which I was interested, but I appreciate that you have always shown interest in what I was doing.

As Time Goes By:

“From a low point in chaos we were all born.
The time was bright and lasted quite long.
But we drifted apart, became lonely and red.
Only far far away could we still see our past.
The last of us died and turned from dark into light.
Time stretched the light red until nothing was left.”

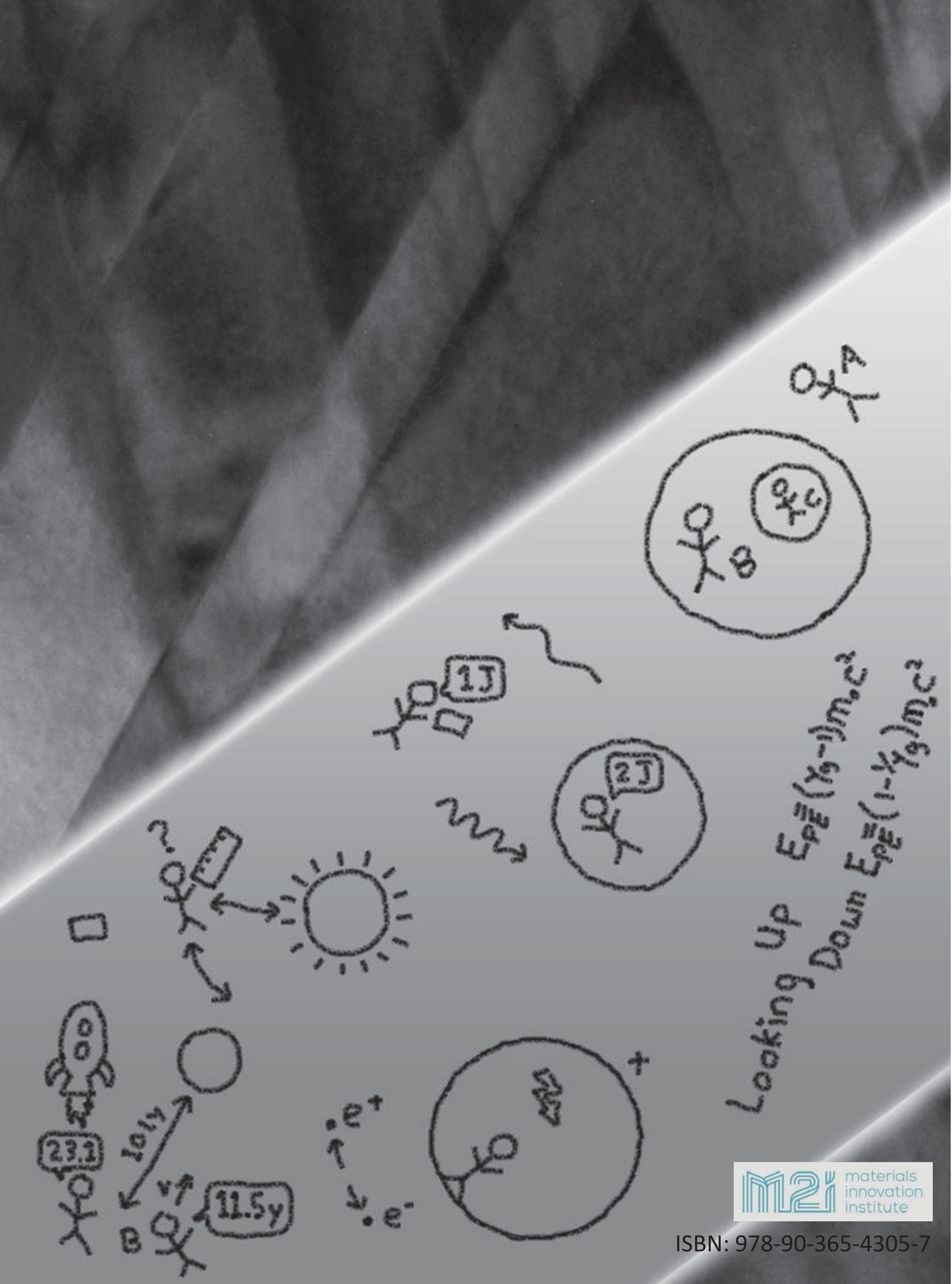

ISBN: 978-90-365-4305-7